Investigation on Photophysical Properties in Nanoscale Metal-Organic Frameworks and Conjugated Microporous Polymers

A Thesis Submitted for the Degree of

Doctor of Philosophy

By

Venkata Suresh Mothika

Chemistry & Physics of Materials Unit (CMPU)

Jawaharlal Nehru Centre for Advanced Scientific Research

(A Deemed University)

Bangalore-560064

December, 2015

Dedicated to My Parents

DECLARATION

I hereby declare that the matter embodied in the thesis entitled "**Investigation on Photophysical Properties in Nanoscale Metal-Organic Frameworks and Conjugated Microporous Polymers**" is the resultant of the investigations carried out by me at the Molecular Materials Laboratory, Chemistry and Physics of Materials Unit, Jawaharlal Nehru Centre for Advanced Scientific Research (JNCASR), Banglore, India under the supervision of **Prof. Tapas Kumar Maji** and that it has not been submitted elsewhere for the award of any degree or diploma.

In keeping with the general practice in reporting the scientific observations, due acknowledgement has been made whenever the work described is based on the findings of other investigators. Any omission that might have occurred due to oversight or error in judgement is regretted.

……

Venkata Suresh Mothika

Date:
Place:

CERTIFICATE

I hereby certify that the work described in this thesis entitled "**Investigation on Photophysical Properties in Nanoscale Metal-Organic Frameworks and Conjugated Microporous Polymers**" has been carried out by **Mr. Venkata Suresh Mothika** under my supervision at the Molecular Materials Laboratory, Chemistry and Physics of Materials Unit, Jawaharlal Nehru Centre for Advanced Scientific Research (JNCASR), Banglore, India and that it has not been submitted elsewhere for the award of any degree or diploma.

……

Dr. Tapas Kumar Maji

(Research Supervisor)

Date:

Place:

ACKNOWLEDGEMENTS

First and foremost, I wish to express my sincere gratitude to my research supervisor Prof. Tapas Kumar Maji for his kind support, guidance, suggestions and invaluable encouragement he has given to me all through the course of this investigation. I shall remain ever thankful to him for giving me enough freedom to work on my area of interests.

I thank Prof. C. N. R. Rao FRS, who has been a constant source of inspiration for me. I would also like to thank him as the Chairman, NCU for allowing me to use the facilities of the centre.

I would like to thank Prof. Balasubramanian Sundaram, Chairman, CPMU, for his generous support and encouragement throughout my stay in JNCASR. I also thank him for providing the infrastructure and facilities to carry out my research work.

I am thankful to Prof. T. N. Guru Row, Prof. A. Sundaresan, Prof. Tapas Kumar Maji, Dr. Sridhar Rajaram for their excellent courses that has been extremely helpful to this study.

I would like to thank Prof. C. N. R. Rao, Prof. Sundaram Balasubramanian, Prof. Swapan K. Pati, Prof. Subi J George, Prof. Tapas Kundu, Prof. H. S. Atreya (IISc), Dr. A. B. Patel (CCMB), Prof. S. K. Das (HCU), Mr. B. Satyanarayana, Ms. A. Bandyopadhyay, Mr. Snehajyoti Chatterjee, Dr. Rahul Modak, Mr. Vivek Tiwari for their valuable discussions and fruitful collaborations.

I would like to specially thank Dr. Ranjani Viswanatha and Mr. Gopalkrishna Murthy for life time measurements, Dr. Rajesh Ganapathy and Dr. Manasa for rheological measurements

I am grateful to all my lab mates Dr. Prakash Kanoo, Dr. Sudip Mohapatra, Dr. K. Jayaramulu, Dr. Ritesh Haldar, Dr. Arpan, Mrs. Anindita, Ms. Nivedita, Ms. Papri, Mr. Syamntak, Ms. Komal, Ms. Sohini. I am also thankful to SRF students Ms. Anangsha De for working with me on different research projects.

I thank the timely help of technical staffs namely Mrs. Selvi (FESEM), Mrs. Usha (TEM), Mr. Basavaraj (AFM), Mr. Mahesh (NMR), Mr. Vasu (UV/PL/IR), Mr. Anil (PXRD), Shivakumar (HRMS), for their help with the various characterization techniques.

It is a pleasure to thank all my JNC friends who supported me both at sports and technical aspects Nagarjun, Diwakar, Venki, Umesh, Satti, Vijay, Yugandar, Ganga, Karteek, Murthy, Lingampalli, Malli, Ramana, Arjun, Sunil, Anand, Saraiah, Shiva, Rajashekar, Pandu, Debu, Venkat, Ankit, Subbu, Ramakrishna, Pramoda, Rajanna, Jiaul, Dheeraj, Avinash, Avijit, Gopal, Dheeraj and many more for their support and encouragement have been an indispensable in my Ph.D. life. I thank all my well-wishers and those who have helped me directly or indirectly.

I specially thank Dr. Sridhar Rajaram for his suggestions and technical discussions at my early stage of PhD. Also special thanks to Arjun, Ramana and Nagarjun for helping me out in various data analysis and suggestions.

I thank Administrative Staff, Hostel Staff, Mess Workers, House Keeping Staff and Security for providing and maintaining the various facilities that have been helped me immensely.

Special thanks to my parents and family members for their love, blessings and affection on me. This thesis is a minor recognition to my parents and family for their love and support.

PREFACE

The thesis is organized into four chapters emphasizing the photophysical properties of luminescent materials mainly nanoscale metal-organic materials, conjugated microporous polymers and hydro/organogels for applications in light-harvesting, bimodal imaging, molecular sensing, tunable emission including white light and catalysis

Chapter 1 provides an introduction to metal-organic frameworks (MOFs), different photophysical processes in MOFs and importance of scaling down bulk MOFs to nanoscale MOFs and their applications in sensing, light-harvesting, bimodal imaging etc. In the second part, it discuss recent developments in conjugated microporous polymers (CMPs) and their various applications in light-harvesting, catalysis, sensing, color tunability and gas storage

Chapter 2 deals with alkoxyalkyl(C8)-oligo-(*p*-phenyleneethynylene)dicarboxy late (OPE) derived nanoscale metal-organic frameworks (NMOFs) and consists of two subchapters. ***Chapter 2A*** deals with rational design approach and construction of nanovesicles and toroids of supramolecular ordered luminescent porous coordination polymer {Zn(OPE)·$2H_2O$} derived from alkoxyalkyl (C8)-oligo-(*p*-phenyleneethynylene) dicarboxylate(OPE)/ Zn^{II}. The ZnOPE nanoflakes (6hrs) undergo morphology transformation to vesicles and toroids with increasing reaction time to 24 and 36 hrs. ZnOPE showed efficient light-harvesting properties in nanoflakes and nanovesicles through Försters resonance energy transfer (FRET) process. ***Chapter 2B*** describes coordination driven self-assembly of OPE with a paramagnetic metal ion (Gd^{III}) to form highly ordered nanoscale porous coordination polymer with nanorod morphology. Excellent physiological stability, strong luminescence properties and paramagnetic behaviour of these nanorods exploited in optical and MRI imaging applications.

Chapter 3 deals with tetraphenylethene (TPE) derived luminescent materials and consists of three subchapters. ***Chapter 3A*** delineates synthesis of a tetraphenylethene (TPE) conjugated microporous polymer (CMP) and its framework induced emission (FIE) has been exploited for light harvesting applications by encapsulating a suitable acceptor dye. The polymer shows high surface area (854 m^2g^{-1}) with a pore size of 1 nm. By replacing the linker with varied amounts of acceptor (fluorenone) in the polymer a series

of donor-acceptor CMPs have been synthesized. All the polymers show selective CO_2 uptake properties and pore size is tunable by changing the fluorenone content. Controlling the fluorenone content in the polymer, the emission color and band gap is finely tuned where the emission is governed by intramolecular charge transfer (ICT) and inter-chain energy transfer between TPE and fluorenone segments in the polymer. ***Chapter 3B*** deals with photomodulation in metal-organic hydrogels to achieve pure white light emitting soft hybrid material. Self-assembly of anionic metal-organic cubes (MOC; derived from Imidazoledicarboxylate and Ga^{III}) and cationic dialkylammonium tetraphenylethene gelator (TPEQA) forms hydrogel with strong AIE emission with appreciable quantum yield. Loading MOC-TPEQA hydrogel with rhodamine 6G (Rh6G) results in strong orange emission due to efficient energy transfer from TPEQA to Rh6G. This composite on photoirradiation for 5 min shows strong white light emission due to conversion of TPE molecules to diphenylphenanthrene (DPP). This white light emitting material is highly transparent and easily coated on flexible substrates. ***Chapter 3C*** deals with design and synthesis of aggregation induced emission (AIE) active tetraphenylethene based low molecular weight gelator (LMWG) and its self-assembly with metal ion to form coordination polymer gel (CPG). LMWG self-assembles through H-bonding and forms 1D nanofibers. Coordination of metal ion transforms the nanofibers morphology into nanotubes. Also, the combined effect of AIE and matrix coordination induced emission (MCIE) in CPG results tunable emission in gel state.

Chapter 4 describes reversible/selective sensing and sequestration of F^- ion from aqueous solutions (THF/H_2O or DMSO/H_2O) using a Lewis acidic boron based conjugated microporous polymer (BMOP) derived from tris(4-bromo-2,3,5,6-tetramethylphenyl) boron and diethynylbiphenyl linker. Intramolecular charge transfer (ICT) between linker to empty p_π orbital on boron results strong green fluorescence in the polymer. Addition of F^- ion solution to BMOP obstructs ICT and leads to the turn-on blue emission selectively in presence of other anions. Strong B-F interactions also facilitate complete removal of F^- ion from solution.

Table of Contents

Chapter 1 1

Introduction 1

1.1 Porous materials 3

1.2 Metal-organic frameworks (MOFs) 3

1.3 Nanoscale metal-organic frameworks (NMOFs) 5

1.3.1 Synthetic methods of NMOFs 7

1.3.2 Applications of NMOFs 10

1.3.2.1 Gas storage, and catalysis 10

1.3.2.2 Luminescence: Colour tunability, sensing and light-harvesting 12

1.3.2.3 Biomedical applications 17

1.4 Conjugated microporous polymers (CMPs) 20

1.4.1 Applications of CMPs 24

1.4.1.1 Gas storage/capture, separation 25

1.4.1.2 Luminescence: Colour tunability, sensing and light-harvesting 27

1.4.1.3 Heterogeneous catalysis 32

1.5 Scope of the work 34

1.6 Outlook 35

1.7 References 36

Chapter 2A 43

MOF Nanovesicles and Toroids: Self-Assembled Porous Soft-hybrids for Light Harvesting 43

2A.1 Introduction 47

2A.2 Experimental section 48

2A.2.1 Materials 48

2A.2.2 Physical measurements 48

2A.2.3 Synthesis of {Zn(OPE)·2H_2O} (1) 48

2A.2.4 Preparation of {Zn(OPE)-DSMP} (2) 49

2A.3 Results and discussion 49

2A.3.1 Structural characterization 49

2A.3.2 Photophysical studies and light-harvesting 55

2A.4 Conclusion 58
2A.5 References 58
Chapter 2B 61
Oligo(*p*-phenyleneethynylene)-Derived Porous Luminescent Nanoscale Coordination Polymer of Gd^{III}: Bimodal Imaging and Nitroaromatic Sensing 61
2B.1 Introduction 65
2B.2 Experimental section 66
2B.2.1 Materials 66
2B.2.2 Physical measurements 66
2B.2.3 MRI imaging studies 67
2B.2.4 Cell culture and Immunofluorescence in cell line 67
2B.2.5 Synthesis of $\{[Gd(OPE)(NO_3)(H_2O)_2]\cdot H_2O\}$, (NMOF-1) 68
2B.3 Results and discussion 68
2B.3.1 Structural characterization 68
2B.3.2 SEM and TEM studies 72
2B.3.3 Photoluminescent properties of NMOF-1: Bimodal imaging 73
2B.4 Conclusions 77
2B.5 References 78
Chapter 3A 81
Framework Induced Emission and Bang Gap Engineering in Donor-Acceptor Conjugated Microporous Polymers 81
3A.1 Introduction 85
3A.2 Experimental section 86
3A.2.1 Materials 86
3A.2.2 Physical measurements 86
3A.2.3 Synthesis of tetrakis(4-bromophenyl)ethene 87
3A.2.4 Synthesis of 2,7-biphenyl-9H-fluoren-9-one 87
3A.2.5 Synthesis of TPE-CMP-1 87
3A.2.6 Synthesis of TPE-CMP-F0 87
3A.2.7 Synthesis of TPE-CMP-F1 88
3A.2.8 Synthesis of TPE-CMP-F2 88
3A.2.9 Synthesis of TPE-CMP-F3 88

3A.3 Results and discussion....88
3A.3.1 Structural characterization and morphology....88
3A.3.2 Thermal stability and porosity....92
3A.3.3 Photophysical studies....94
3A.4 Conclusion....99
3A.5 References....100
Chapter 3B....101
Highly Processable Self-assembled White-Light Emitting Nanoscale Metal-Organic Soft Hybrids....101
3B.1 Introduction....105
3B.2 Experimental section....107
3B.2.1 Materials....107
3B.2.2 Physical measurements....107
3B.2.3 Synthesis of the metal-organic cube, $[Ga_8(ImDC)_{12}][Me_2NH_2]_{12}\cdot 24H_2O$ (1)....107
3B.2.4 Synthesis of 1,2-bis{4-[4-(*N*,*N*-diethylammonium)ethoxy]phenyl} -1,2-tetraphenylethene dibromide hydrochloride (TPEQA)....108
3B.3 Results and discussion....108
3B.3.1 Structural description of metal-organic cube (MOC)....108
3B.3.2 MOC-TPEQA hybrid gel formation....110
3B.3.3 Energy transfer and white light emission....112
3B.3.4 Processibility....117
3B.4 Conclusions....118
3B.5 References....118
Chapter 3C....121
High aspect ratio, processable coordination polymer gel nanotubes based on an AIE-active LMWG with tunable emission....121
3C.1 Introduction....125
3C.2 Experimental section....126
3C.2.1 Materials....126
3C.2.2 Physical measurements....126
3C.2.3 Synthesis of ligand (L)....127
3C.2.4 Titration of L with Eu(III) ion in methanol....128

3C.2.5 Synthesis of L gel....129
3C.2.6 Synthesis of CPG....129
3C.3 Results and discussion....129
3C.3.1 Structure and AIE property of L....129
3C.3.2 Synthesis and characterization of L gel and CPG....132
3C.3.3 Photophysical properties of L gel and CPG....136
3C.4 Conclusion....138
3C.5 References....138
Chapter 4....141
Highly Luminescent Microporous Organic Polymer with Lewis acidic 'Boron' Sites on the Pore Surface: Ratiometric Sensing and Capture of F^- Ions....141
4.1 Introduction....145
4.2 Experimental section....146
4.2.1 Materials....146
4.2.2 Physical measurements....146
4.2.3 Computational details....147
4.2.4 Synthesis of 1,4-dibromo-2,3,5,6-tetramethylbenzene....147
4.2.5 Synthesis of tris(4-bromo-2,3,5,6-tetramethylphenyl)boron....147
4.2.6 Synthesis of 4, 4′-diethynylbiphenyl....148
4.2.7 Synthesis of BMOP....148
4.3 Results and discussion....149
4.3.1 Synthesis and characterization....149
4.3.2 Photophysical Studies....152
4.3.3 Fluoride sensing and capture....154
4.4 Conclusion....160
4.5 References....161

Chapter 1

Introduction

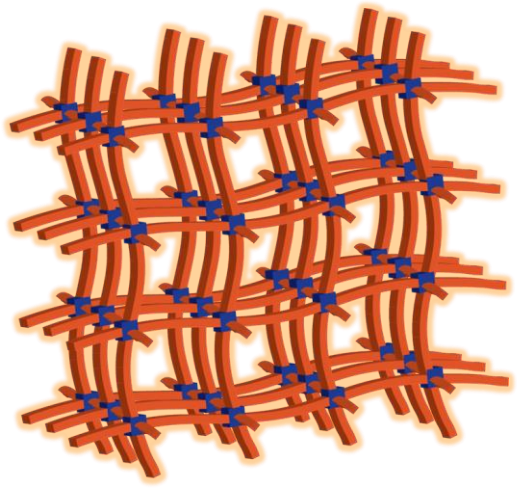

1.1 Porous materials

Porous materials are one of the most widely studied research areas of the recent times due to their wide potential in gas storage, separation, catalysis and energy related applications.[1] Traditionally, porous materials are either organic based materials like graphene, disordered carbon or inorganic such as zeolites, silica. They possess high surface area and profound applications in gas storage, purification, catalysis, however they lack in diversity of building blocks since the main constituents seldom differed from C, Si, Al or chalcogens.[2] Also, targeted synthetic approach of these porous materials for specific function is difficult. A functional porous material can be realized when the pore surface of the material have specific physical or chemical functionality on its pore wall and accessible surface area. Recently, two important class of materials namely, metal-organic frameworks (MOFs) or porous coordination polymers (PCPs) and porous organic polymers (POPs) have received tremendous attention, as they exhibit porosity and high surface area as shown by the conventional porous materials. In addition, the framework structure of these materials can be finely tuned/tailor made for a specific function like molecular sensing, selective gas storage, light harvesting and catalysis.[3]

1.2 Metal-organic frameworks (MOFs)

MOFs are prepared by the assembly of inorganic metal ions or metal-oxygen clusters (called secondary building unit, SBU) and bridging organic linkers having different binding sites. MOFs are extended polymeric structures with intriguing network topologies.[4] Transition metal ions and lanthanides are commonly used as inorganic nodes and their oxidation state and coordination number play a pivotal role to direct the structure of MOFs. The final geometry is also dependent on reaction solvent, temperature and organic ligands used.[5] Usual geometries of the central metal ions found in MOFs are linear, T- or Y-shaped, tetrahedral, square planar, square pyramidal, trigonal-bipyramidal, octahedral, trigonal-prismatic, pentagonal-bipyramidal forms. Organic linkers generally contain metal binding functional groups such as COOH, SO_3H, pyridine etc.[6] Synthetic organic chemistry methods allows functionalization of these organic linkers with various groups such as OH, F, CONH, NH_2 or structure directing alkyl chains. Organic linkers can be predesigned or post-synthetically modified to modulate property of MOF. Possible lists of organic linkers are shown in Figure 1. MOFs are highly crystalline, possess periodic structures and emerged as functional porous materials harnessing functions of both inorganic components (metal ions) such as magnetism, redox behaviour,

luminescence (in case of lanthanides) and properties like fluorescence, molecular sensing, and energy transfer stemming from organic components. Also, their remarkable surface area has accelerated applications in gas storage, separation, drug delivery and catalysis.

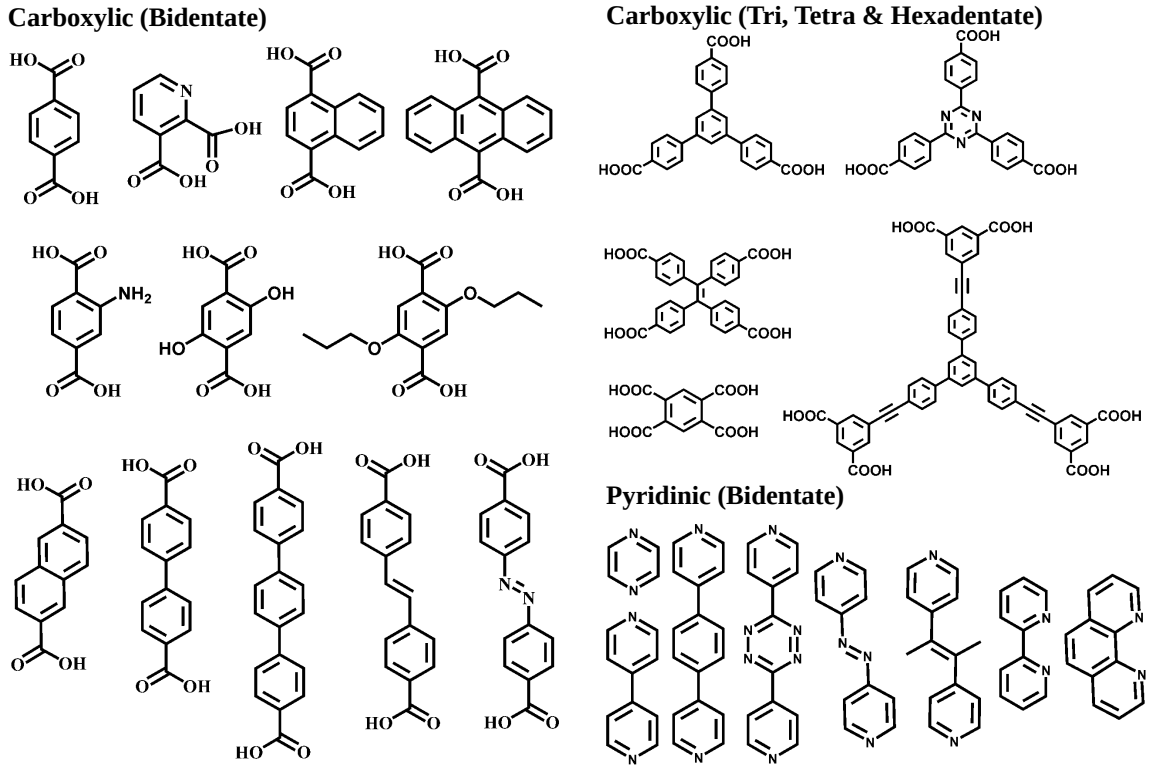

Figure 1. List of organic bridging linkers used for the preparation of MOFs.

Limitless combination of metal ions/clusters and diverse organic linkers provided great opportunity to construct enormous amount of new metal-organic frameworks. Yaghi *et al.* reported a series of IRMOFs keeping metal cluster constant and varying the organic linker from bdc to tpdc (Figure 2).[7] Octahedral $Zn_4O(CO_2)_6$ SBU and rigid dicarboxylate linkers form non-interpenetrated 3D porous MOF, and organic linkers are further augmented to have different functional groups. Ferey *et al.* reported highly porous chromium(III) dicarboxylate MOFs called MIL-53, 101 (MIL: Materials Institute Lavoisier) with excellent surface areas upto 4100 m^2g^{-1}.[8] Zeolitic imdiazolate frameworks (ZIFs) are another interesting class of MOF materials constructed from tetrahedral metal ions (Fe^{2+}, Co^{2+}, Cu^{2+}, Zn^{2+}) and imdiazolate organic linkers. ZIF-8 and ZIF-11 consists of Zn^{2+}, 2-methylimidazolate and benzimidazolate are most stable and permanently porous MOFs.[9] Apart from these, there are several MOFs exhibiting very high surface areas *e.g.* NU-110 (NU- Northwestern University) exhibit surface area of

7140 m^2g^{-1}, while MOF-177: 5640 m^2g^{-1}, MIL-101: 5900 m^2g^{-1}, UMCM-2: 6000 m^2g^{-1} and MOF-210: 6240 m^2g^{-1}.[10]

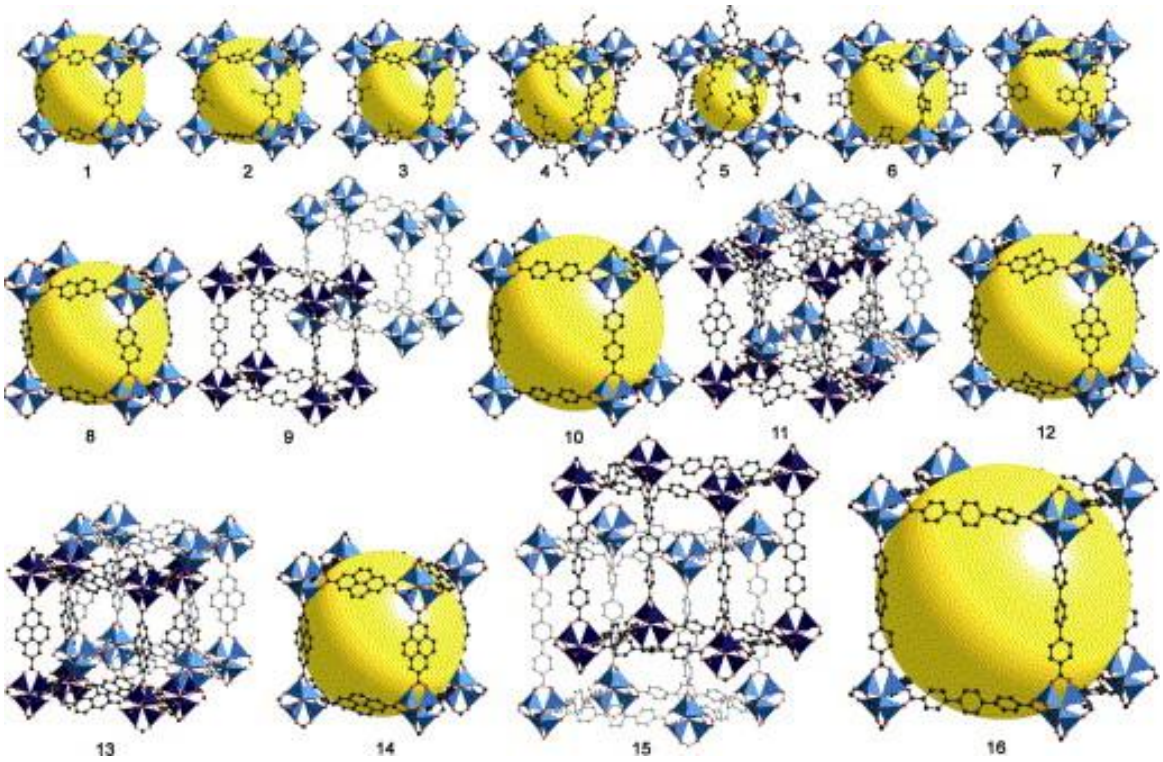

Figure 2. A series of isoreticular MOFs (IRMOFs) sharing same cubic topology. Linkers differ both in functionality of pendant groups (IRMOF-1 to -7) and in length (IRMOF-8 to -16). Expansion of the linkers increases the internal void space (represented by yellow spheres); it also allows the formation of catenated phases (IRMOF-9, -11, -13 and -15). This figure has been reproduced with permission from reference no. 7a.

1.3 Nanoscale metal-organic frameworks (NMOFs)

Scaling down bulk MOF materials to nanoscale regimes is a fruitful strategy to develop new materials with novel and improved properties over bulk materials especially for technological and biomedical applications including solar cells, optoelectronics, catalysis and drug delivery.[11a] Inorganic-organic hybrid nanomaterials or nanoscale metal-organic materials resulted from the self-assembly of inorganic (metal ions) and organic components are rapidly growing and they are superior compared to nanomaterials containing either purely organic or inorganic compositions in terms of modularity in structures and properties. Bulk MOFs showed promising applications in gas storage, separation, catalysis and optoelectronics.[3] However, bulk nature of MOF solids completely restricts their applications especially in cell imaging, diagnostics or as delivery vehicles due to poor internalization into cells.[11b] On the other hand, MOFs with

nanoscopic dimensions typically possess sufficiently small sizes to cross the cell-membrane. With well-defined shape, nanosized, morphological architectures, they disperse well in aqueous media or organic solvents and can be easily coated on large area substrates. Combined with high surface area to volume compared to bulk MOFs, NMOFs show enhanced and unique properties especially in sensing, gas sorption and size dependant electronic, optical properties.[11a] MOF nanostructures with different sizes and morphologies fabricated by various methods have been reported in literature by several groups (Figure 3). In this thesis I will be discussing synthesis of NMOFs of various nanomorphologies using ligand design approach and their applications in bimodal imaging and light-harvesting.

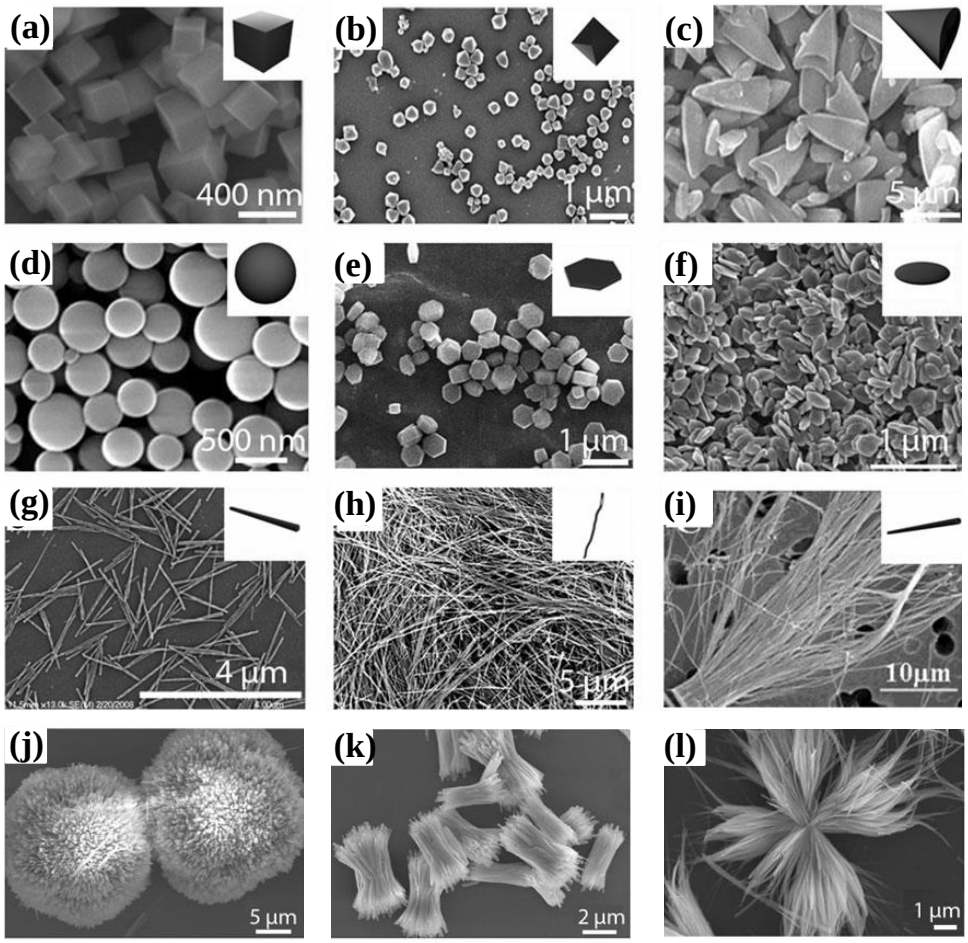

Figure 3. Metal-organic nanostructures with various morphologies and their SEM images: (a) Cubic, (b) octahedral, (c) arrow-like particles, (d) spheres, (e) hexagonal lumps, (f) plate-like particles, (g) rods, (h) fibres, (i) tubes, (j) urchin-like, (k) bundle-like, and (l) flower-like superstructures. This figure has been reproduced with permission from reference no. 11a.

1.3.1 Synthetic methods of NMOFs

With the first example of synthesizing nanoscale coordination polymer by Mann *et al.* the field of nano coordination polymers or NMOFs got great attention and several strategies have been reported to realize variety of MOF nanostructures. They include (i) emulsion method: Growth and supramolecular assembly is confined by forming nanoreactors using surfactant, (ii) coordination modulation method: Rate of crystal growth is perturbed and inhibited by addition of metal binding modulator, (iii) controlled precipitation by addition of poor solvent, (iv) solvo/hydrothermal method, (v) microwave heating and (vi) ultrasound (Figure 4).[11a]

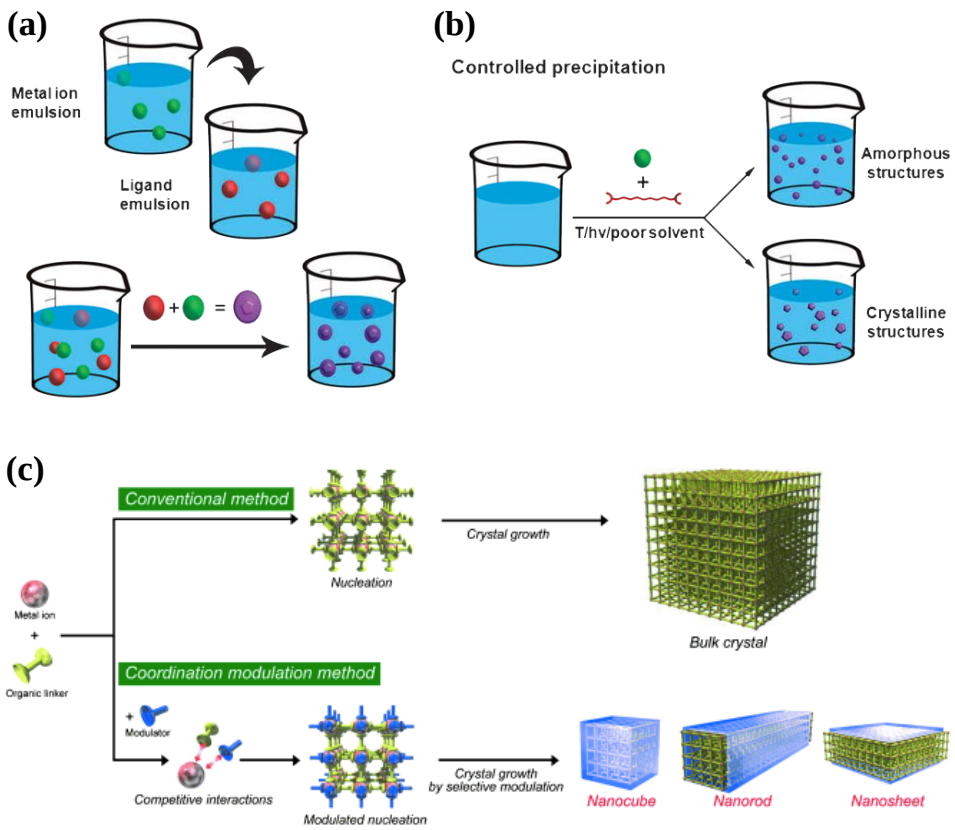

Figure 4. Synthetic methods of MOF nanostructures. These figures have been reproduced with permission from reference no. 11a, 13a.

Nano emulsion method involves surfactant stabilized nano droplets (50-1000 nm) or nano reactors which directs growth of the metal-organic nanostructure. Initially metal ion precursor and organic linker are dissolved in a solvent and then dispersed in a surfactant solution individually. Now mixing of these dispersions, followed by application of external stimuli like temperature, light or microwave radiation leads to form metal-organic nanostructures inside droplet. First example of emulsion method to

prepare coordination polymer nanostructures was reported by Mann *et al.* using water-in-oil microemulsion method where clusters of Prussian blue cubic nanocrystals were prepared by photo reduction of $[Fe_2(C_2O_4)_3]^{3-}$ to Fe^{2+} followed by reaction with $[Fe(CN)_6]^{3-}$.[12a] Lin *et al.* reported synthesis of Mn^{2+} NMOFs using micro emulsion method.[12b] Heating a microemulsion of $MnCl_2$ and $[NMeH_3]_2$(BDC) prepared using CTAB/1-hexanol/n-heptane/water in a 1:1 ratio at 120 °C in a microwave oven formed nanorod like structures of Mn^{II} NMOF. While replacing the ligand with Na_3(BTC), nanoparticles of NMOF were found to be formed under similar reaction conditions. Recently, Maspoch *et al.* reported spray-drying strategy to prepare various types of NMOFs and their assembly into hollow superstructures.[12c]

Coordination modulation is another well studied approach to prepare NMOFs. Kitagawa *et al.* reported synthesis of $[\{Cu_2(ndc)_2(dabco)\}_n]$ nano crystals by using monocarboxylic acid modulator.[13a] This method involves regulating rate of framework extension and crystal growth by addition of competitive modulator with similar functionality as that of organic linker. By increasing the amount of acetic acid added rate of crystal growth decreases and MOF nanorods with increasing aspect ratio are formed due to the inhibition of growth in [100] direction. Similarly, formation of $[Cu_3(btc)_2]_n$ nanostructures was observed by using *n*-dodecanoic or lauric acid modulator.[13b] Zhang *et al.* reported formation of nanoscale $[Dy(BTC)(H_2O)]$ MOF using sodium acetate modulator and by controlling the pH of the reaction medium.[13c] Horcajada, Gref *et al.* reported synthesis of NMOFs using microwave radiation where simple mixing of Fe^{3+} metal ions and multi topic ligands like BDC or BTC in solvent followed by heating above 100 °C led formation of MOF nanostructures. [13d] Ni and Masel *et al.* reported synthesis of IRMOF-1, 2 and 3 using microwave radiation by simple mixing of Zn^{2+} metal ions and BDC ligands.[13e] Solvothermal synthesis is also regular approach to prepare the nanoscale MOFs; Ahn *et al.* reported miniaturization of MOF-5 to nanoscale. [13f]Another very important approach is poor solvent assisted precipitation of MOF nanoparticles. This method is divided into two types (i) use of poor solvents which dissolve the building blocks but the metal-organic polymers are insoluble, (ii) addition of a poor solvent externally to precipitate the metal-organic polymer formed in other solution. Wang *et al.* reported monodispersed spherical particles of Pt(IV) metal ions and *p*-phenylenediamine. [13g] Oh and Mirkin *et al.* reported infinite coordination polymer particles using ether or pentane as poor solvent from Zn^{2+}, Cu^{2+} or Ni^{2+} and binaphthyl bis-metallotridentate

Schiff base in pyridine.[13h]

Fabrication of 2D membranes and thin films of MOFs by controlling the supramolecular self-assembly of inorganic and organic components is another exciting approach. Mallouk *et al.* reported layer-by-layer synthesis of metal-organic polymers by controlled self-assembly of Zr^{4+} metal ions and 1,10-decanebisphosphonate (DBP) on a Si surface. [14a]In this approach the Si surface functionalized with phosphonate-terminated monolayer is exposed to a solution of $ZrOCl_2$ and DBP resulting multilayer metal-organic films with desired thickness. Another technique is growing thin films by directing the

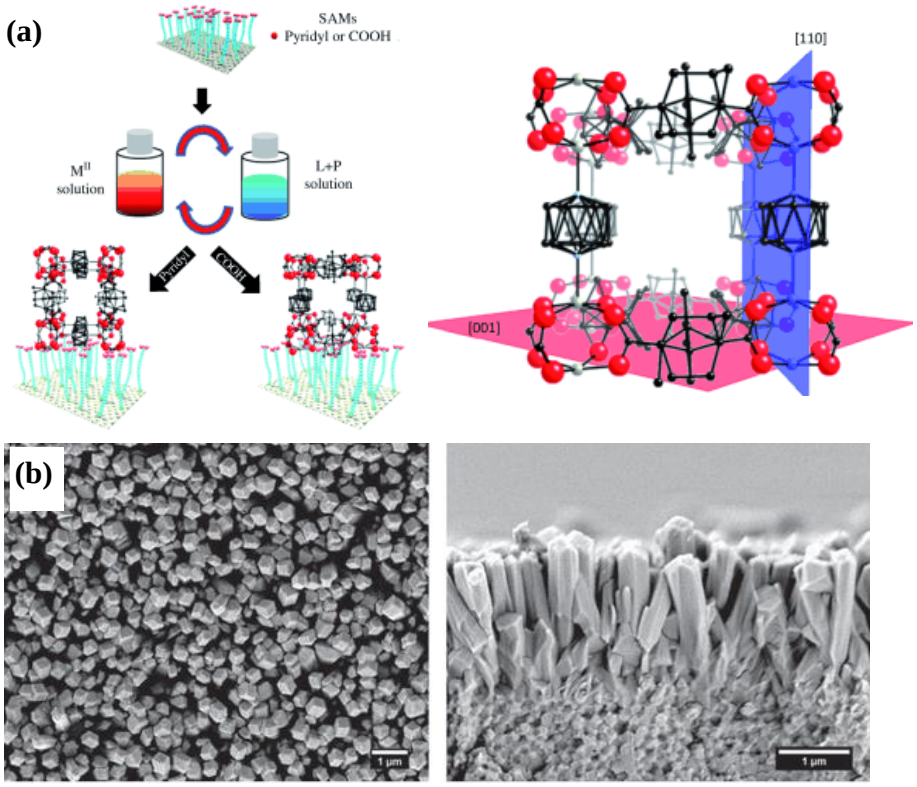

Figure 5. (a) Left: Schematic illustrations of oriented growth in (001) orientation on pyridyl-terminated (PPMT) and (110) orientation on COOH-terminated (MHDA) SAMs on gold substrates. Right: Two principle growth directions of $[\{Zn_2(cam)_2\text{-}(dabco)\}_n]$. (b) SEM top (left) and cross-section (right) views of ZIF-7 membranes obtained after microwave assisted secondary growth. These figures have been reproduced with permission from reference no. 14b, d.

growth of NMOFs on surfaces using self-assembled monolayers (SAMs) appended on substrates. In these approach substrates *e.g.* Au is functionalized with SAMs containing terminal COOH, OH which will act as nucleation points and by immersing substrates into a solution of metal ions and ligand, the growth of NMOF occurs directionally. Fischer *et al.* reported growth of surface MOFs (SURMOF) $[\{Zn_2(cam)_2(dabco)\}_n]$ (cam: (+)-

camphoric acid and dabco: 1,4-diazabicyclo(2.2.2)octane) in (110) and (001) orientation on Au substrate coated with mercaptohexadecanoic acid and 4,(4-pyridyl)phenyl) methanethiol (Figure 5).[14b] Woll *et al.* reported controlled formation of non-interpenetrated MOF (IRMOF) from [Zn_4O] clusters and 4,4′-biphenyldicarboxylic acid linkers.[14c] Growth of zeolitic imdiazolate framework membranes especially ZIF-7 membranes was shown by Caro *et al*.[14d]

1.3.2 Applications of NMOFs

1.3.2.1 Gas storage, and catalysis

MOF are not only structurally divergent, they also possess high porosity and surface area which makes them potential candidates for gas storage and catalysis. Ease of modulating the organic linker using synthetic organic chemistry, pore surface of MOF can be modulated from a non-polar to highly polar nature which is quite essential along with high surface area for gas storage applications especially H_2 and CO_2. Hupp *et al.* reported mesoporous NU-100 with excellent H_2 uptake capacity of 9.95 wt% at 77 K and 56 bar (Figure 6) and other noteworthy reports are PCN-12: 3.05 wt% at 77 K and 1 atm, MOF-505: 2.59 wt % at 77 K and 1 atm and HKUST-1: 2.54 wt % at 77 K and 1 atm.[15a-b] Mg-MOF-74 is one remarkable example showing excellent CO_2 storage capacity of

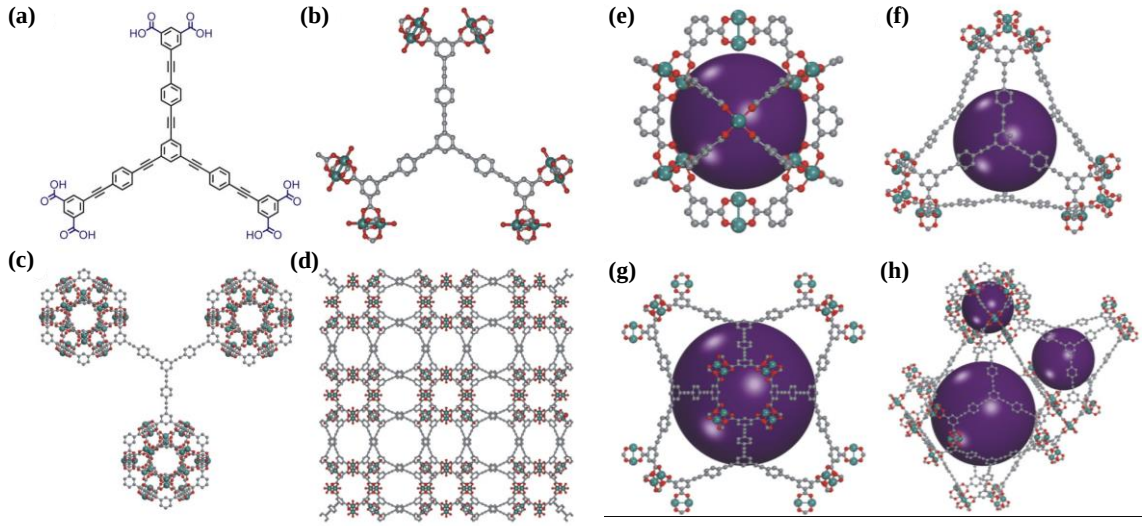

Figure 6. Structural features of NU-100. (a) Schematic of the chemical structure of LH_6. (b)-(h) Representations of the single-crystal X-ray structure of NU-100: LH_6 connecting six paddlewheel units (b), cubaoctahedral building blocks (c) and different cages in NU-100 (e–h). Hydrogens and disordered solvent molecules are omitted for clarity. Carbon, grey; oxygen, red; copper, teal; Purple, representation of the largest spheres that can fit within the cages. This figure has been reproduced with permission from reference no. 15a.

27.5 wt% at 298 K. Zaworotko *et al.* have demonstrated fluorinated MOFs with excellent performance to separate CO_2 from N_2 at ambient condition.[15c-d]

MOFs are highly insoluble in aqueous or organic solvents and their well-defined pores with catalytically active functional sites makes them potential candidates for size and shape selective heterogeneous catalysts. Catalytically active sites generally obtained during synthesis or by post-synthetic modification. One of the earlier example is HKUST-11, $[Cu_3(btc)_2(H_2O)_3]$ contains large cavities (6 Å) and unsaturated Cu^{2+} Lewis acid sites (on removal of water molecules coordinated), which showed catalytic cyanosilylation of benzaldehyde or acetone. While Kitagawa *et al.* have reported Knoevenagel condensation in an amide functionalized coordination polymer.[16]

Miniaturization of bulk MOFs to nanoscale had opened door to develop new class of nanoscale metal-organic materials with diverse structures, properties of metal-organic materials along with additional advantages of nanomaterials. Most important outcome of

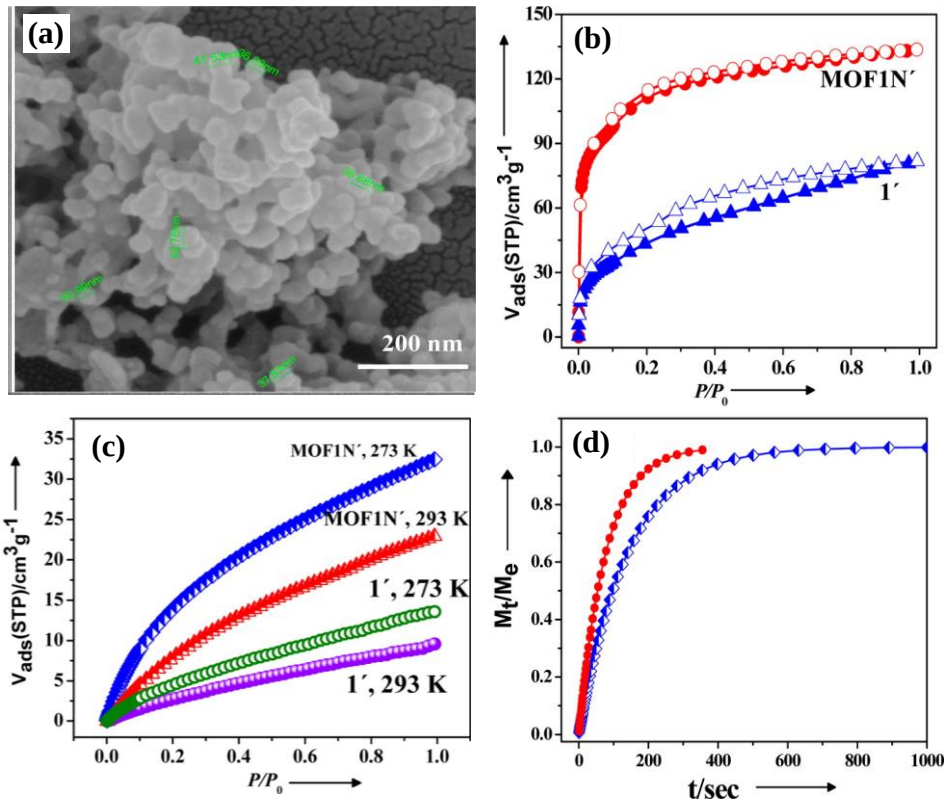

Figure 7. (a) FESEM images of MOF1 nanospheres (MOF1N). (b) CO_2 adsorption isotherms (at 195 K) of bulk MOF (1′) (blue triangle) and MOF1N′ (red circle). (c) CO_2 adsorption isotherms of 1′ and MOF1N′ measured at 273 and 293 K. (d) Kinetics of adsorption of water on 1′ (blue square) and MOF1N′ (red circles) at 298 K showing higher mass diffusion in MOF1N′ compared to bulk phase 1′. This figure has been reproduced with permission from reference no. 17a.

scaling down MOF to nanoscale is their increased surface area to volume ratio which would have effect on their gas storage properties because of the lesser diffusion barrier. Kitagawa *et al.* reported fabrication of nanorod like structures of $[\{Cu_2(ndc)_2(dabco)\}_n]$ (ndc = 1,4-naphthalene dicarboxylate; dabco = 1,4-diazabicyclo [2.2.2]octane) MOF using coordination modulation method.[13a] These nanorods showed enhanced surface area compared to bulk MOF and also improved CO_2 storage capacity over bulk counterparts. Similarly, Maji *et al.* reported synthesis of nanoscale interpenetrated MOF $\{[Zn_2(bpdc)_2(azpy)]\cdot 2H_2O\cdot 2DMF\}_n$ (bpdc = 4,4′-biphenyldi carboxylic acid, azpy = 4,4′-azobipyridine) by using coordination modulation method. MOF nanospheres showed remarkably higher CO_2 storage capacity compared to bulk MOF crystals due to lesser diffusion barrier at nanoscale as supported by the adsorption kinetics(Figure 7).[17a] Groll *et al.* showed fabrication of coordination polymer nanocrystals of $[Zn(ip)(bpy)]_n$ (ip=isophthalic acid, bpy=4,4′-bipyridyl) using inverse micro emulsion method combined with ultra-sonication. Nanocrystals showed a similar solvent adsorption capacities as that of bulk MOFs however the shape of the isotherms changes drastically and the adsorption kinetics increase dramatically.[17b] Oh *et al.* reported NMOFs based on In^{3+} metal ions and BDC organic linkers that showed excellent H_2 and CO_2 uptake capacities upto 140 mL/g and 333 mL/g at 77 K and 195 K respectively.[17c]

1.3.2.2 Luminescence: Colour tunability, sensing and light-harvesting

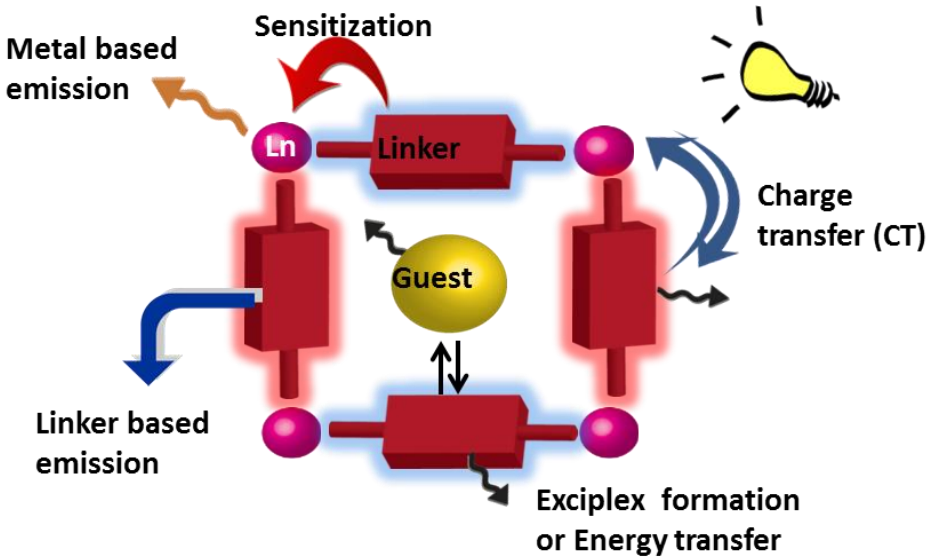

Figure 8. Schematic showing possible emission pathways in a porous metal-organic framework constructed from metal ion nodes (pink balls) and organic linkers (wine red) with encapsulated guest molecules.

Coordination driven self-assembly of these porous hybrid structures facilitate an ordered arrangement of chromophores that improves the exciton hoping over large arrays of chromophoric units and ordered porous channels allow easy orientation of confined guest molecules for better energy transfer efficiencies. In contrast to pure organic assemblies where weak interactions play major role in forming higher ordered structures, metal coordination directed hybrid assemblies' leads to rigid and thermally stable macromolecular structures and are often retain chromophoric ordering when transferred to substrates. This thesis focuses on nanoscale metal-organic frameworks or nanoscale coordination polymers for applications like light-harvesting and bimodal imaging as they provide high solution processability and useful in device fabrication.

Photophysical properties of MOFs are extensively studied as they provide excellent platform for the fabrication of diverse solid state luminescent materials by incorporating large variety of organic chromophores as linkers. Well defined pore size and shape in MOFs provide platform for size selective recognition or sensing of specific analytes with easy signal read out through host-guest interactions such as charge transfer, electron transfer or energy transfer (Figure 8). Also, MOFs provide long range ordered spatial organization of chromophoric linkers through metal coordination in three-dimensional fashion which reduce aggregation thus enhanced emission intensity and quantum yields. Furthermore MOFs can act as excellent platform as light-harvesting antennas based on strut to strut or host-guest energy transfer. Luminescence in MOFs might be associated with inorganic components (metal ions): trivalent lanthanide metal ions especially Eu^{3+}, Tb^{3+} and Dy^{3+} show sharp and narrow band emission when connected to a suitable organic ligand through sensitization or antenna effect. For this process, strong vibronic coupling between the linker and metal ion is required which leads to excitation energy transfer from linker to excited state of the metal ions thereby radiative relaxation results in characteristic lanthanide emission. Maji *et al.* reported porous Tb^{3+} mucicate frameworks, $\{[Tb_2(Mu^{2-})_3(H_2O)_2]\cdot 4H_2O\}_n$ with strong Tb^{3+} emission at 485, 545, 585, 620 nm, where the mucicate ligand acts as antenna or sensitizer for Tb^{3+}.[18a] Controlled doping of Eu^{3+} in Tb^{3+} mucicate framework emission output changed due to energy transfer between Tb^{3+} and Eu^{3+} and emission colour is finely tuned. Chen *et al.* studied lanthanide emission in $\{Eu(BTC)(H_2O)\cdot 1.5H_2O\}$, where BTC ligand coordinated to Eu^{3+} acts as sensitizer.[18b] Desolvated framework obtained on removal of coordinated water molecules showed characteristic Eu^{3+} emission at 590, 616

and 698 nm. Interestingly, the emission of desolvated Eu^{3+}-MOF was observed to show excellent sensitivity to DMF and acetone. On exposure to DMF the emission intensity of MOF gradually increases while to acetone fluorescence quenching is observed. The emission changes and sensing properties were attributed to the replacement of weakly coordinated 1-propanol molecules by DMF and acetone. Emission in MOF may also be realized due to charge transfer (metal to ligand or ligand to metal) interactions between metal ion and the linker. It may be due to linker when the ligand is chromophoric in nature. The emission may be also due to encapsulation of chromophoric guest molecules which shows strong emission. In some cases, formation of excimer or exciplex occurs due to host-guest interactions between organic linker and the guest molecules encapsulated and show large red shifted emission with longer life times. Kitagawa *et al.* reported such interesting example, $[Zn_2(bdc)_2(dpNDI)]_n$, (bdc=1,4-benzene dicarboxylate, dpNDI= N,N′-di(4-pyridyl)-(1,4,5.8-naphthalenediimide)) having redox active naphthalenediimide

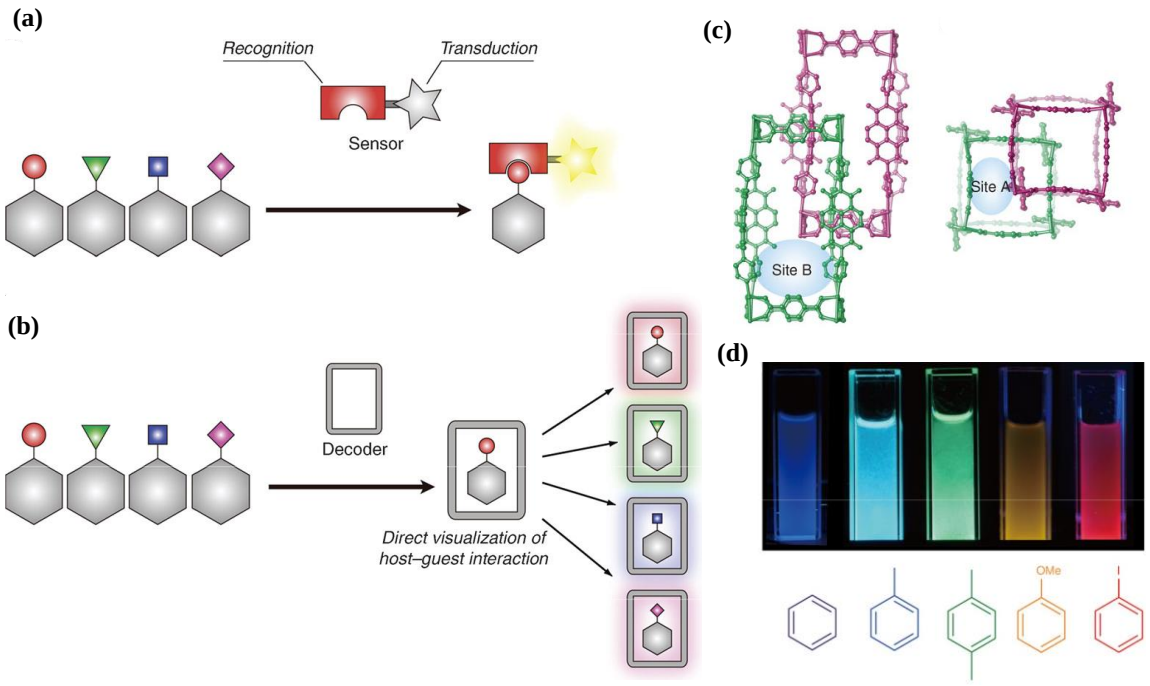

Figure 9. (a) Schematic showing the conventional molecular sensing: a recognition part and a transduction part. (b) Molecular decoding materials accommodate chemically diverse analytes and differentiate between them by displaying a signal that corresponds to each analyte. (c) View of two different sites in two-fold entangled structure of $[Zn_2(bdc)_2(dpNDI)]_n$, and (d) emission of different VOCs included framework under UV light. This figure has been reproduced with permission from reference no. 19a.

components was observed to show multicolour emission on inclusion of aromatic guests.[19a] Emission colour strongly dependent on the substituent on the guest molecules

and enhanced exciplex formation (dpNDI: guest) along with charge transfer features (Figure 9). This is termed as molecular decoding where single host system distinguishes class of molecules with varied fluorescence read-out signal. Excited state intramolecular proton transfer (ESIPT) is another interesting process observed to show emission in MOFs, Maji *et al.* reported a Mg(II) and dihydroxy terephthalic acid (DHT) based frameworks, $\{Mg(DHT)(DMF)_2\}_n$ where the linker show ESIPT properties. In polar solvents the proton transfer is quite facile and emission colour changes by varying the polarity of solvents like DMF, methanol, water due to stabilization of ESIPT process.[19b]

Nature's photosynthesis process also known as light-harvesting is one of the efficient approaches that harvests solar light energy. Many artificial light-harvesting antennas have been developed to mimic this natural process using various approaches like self-assembled porphyrins, organogel scaffolds, dendrimers and polymers.[20]The high efficiency of the energy migration in natural systems is due to their well-ordered chromophore organization at longer distances. MOFs having high crystallinity provide such long range ordered arrangement of chromophores; further the inorganic components make the chromophoric linkers well-separated without any aggregation.[21] The inherent porosity could encapsulate acceptor molecules and provides an interface between donor scaffold and the reaction center. Resonance energy transfer phenomenon is essentially driven by rapid transfer of excited energy of donor to an acceptor non-radiatively. This phenomenon was suggested by Theodor Förster and is known as Förster Resonance Energy Transfer (FRET). Energy transfer from the excited molecule occurs *via* coupling of the dipole moments of the donor and acceptor through columbic (electrostatic) interaction. The extent of energy transfer is dependent on the distance between the donor/acceptor (FRET occur in the range of 30-100 Å) and spectral overlap between emission of donor and absorption of acceptor. As MOFs are highly ordered the organization of donor and acceptor are easily controlled and hence the energy transfer can be efficient. Hupp *et al.* was first studied efficient strut-to-strut energy transfer in bulk MOFs constructed from the porphyrin and boron dipyromethane (bodipy) building blocks.[22a] In another report, CdSe/ZnS core/shell quantum dots (QDs) doped MOFs are studied for light-harvesting applications with excellent energy transfer efficiencies (>80%) where the energy transfer occurs from QD to porphyrin units (Figure 10).[22b,c] However they are bulk crystalline in nature and possess limited solution processability. In an approach by Lin *et al.* a photoactive microscale MOF derived from $\{M[4,4'\text{-}(HO_2C)_2\text{-}$

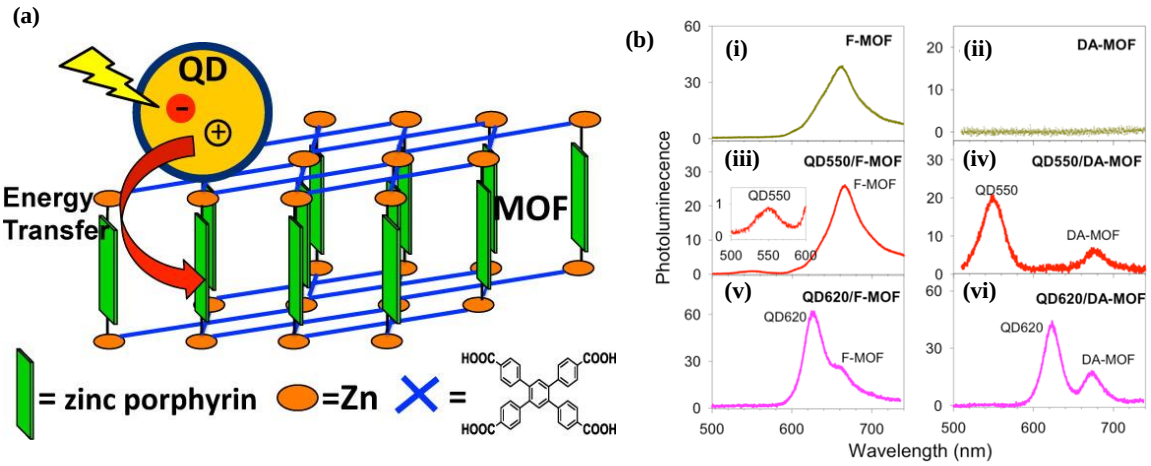

Figure 10. (a) Schematic diagram of a QD–MOF complex: The CdSe/ZnS QDs are sensitized on the MOF surface through the amine-Zn interaction. (b) Emission spectra of the MOFs and QD–MOF complexes at λ_{ex} = 400 nm: (i) F-MOF; (ii) DA-MOF; (iii) QD550–F-MOF; (iv) QD550–DA-MOF; (v) QD620–F-MOF; (vi) QD620–DA-MOF. This figure has been reproduced with permission from reference no. 22b.

bpy]$_2$bpy}$^{2+}$, (M=Ru^{II}, Os^{II}) building blocks connected by metal-carboxylate bonds demonstrated to show facile long range energy transfer to the in-situ doped Os^{II} trap sites.[23a] Exciting [**LRu**Zn] ·2DMF·4H$_2$O resulted in Ru^{II}*-Ru^{II} energy hops and increasing the level of Os^{II} from 0-2.6 mol% led to growth of Os^{II} emission with simultaneous decay in Ru^{II}* showing controlled site-site energy transfer from Ru^{II} to Os^{II}. Recently, an elegant study of resonance energy transfer between two chromophoric struts in a nanoscale MOF is carried out by Uvdal *et al.*[23b] Synthetic diversity of organic chromophores allow pathways to construct complicated MOF structures with desired emission outputs. Lanthanide metal ion (Ln= Gd, Eu, Yb) directed self-assembly of H$_2$**L1** in DMF at 140 °C showed to form disk like particle with highly ordered hexagonal porous structure and doping with another chromophoric linker, H$_2$**L2** of similar molecular length formed disk like morphology (Figure 11). Sufficient spectral overlap between absorbance of H$_2$**L2** with emission of H$_2$**L1** provided facile resonance energy transfer from **L1** to **L2** within in NMOF, when Gd-**L1** doped with 2 mol% of **L2** excited at 360 nm immediate quenching of **L1** emission with a concomitant appearance of emission from **L2**. Interestingly, Gd-**L1**-**L2** exhibit intense white light emission as the emission spans entire visible region. Similar strategies of light-harvesting in nanoscale metal-organic materials via noncovalent approach of dye encapsulation was observed by Uvdal *et al.*[23c] Nanoscale coordination polymer(NCP) particles derived from fluorine cored pi-conjugated dicarboxylate ligand and Ln^{3+} metal ions shows linker based blue emission at

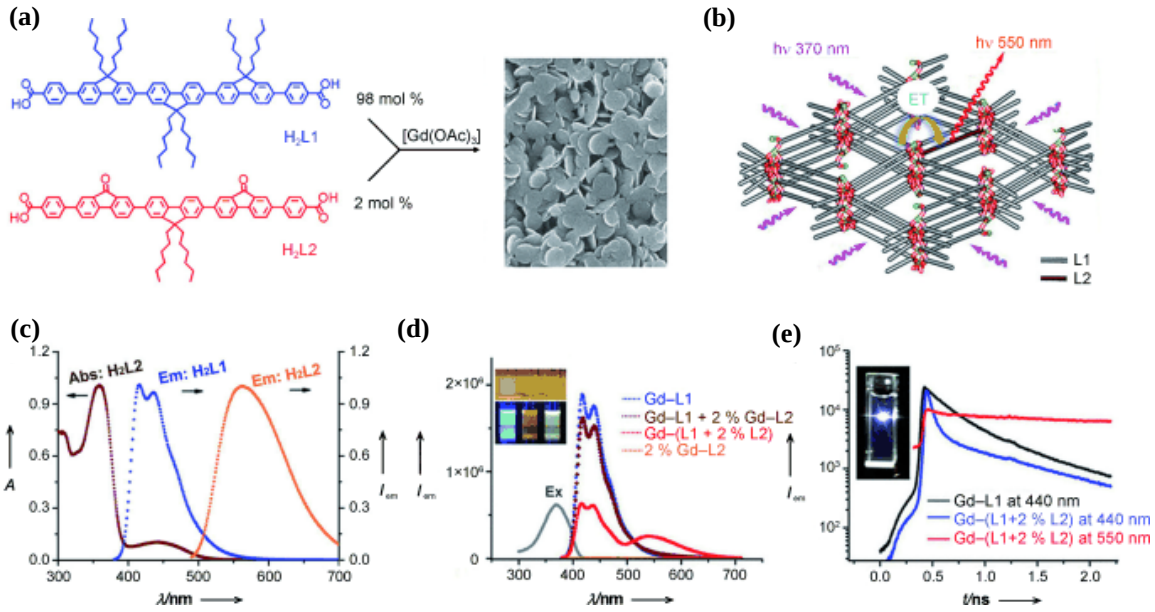

Figure 11. Synthesis and light harvesting study of multicomponent nanoparticles: (a) Illustration showing the preparation of Gd–L1–L2 multicomponent nanoparticles. (b) Schematic representation of the energy transfer in long-range ordered MOFs. (c) Normalized absorption and emission spectra of H_2L1 and H_2L2 in DMF. (d) Emission spectra of Gd–L1, Gd–L1 mixed with 2 mol% Gd–L2, Gd–(L1+2 mol% L2), and Gd–L2 nanoparticles. The grey curve is the excitation spectrum of Gd–(L1+2 mol% L2) nanoparticles; inset (from left to right): photo images of Gd–L1, Gd–L2, and Gd–L1–L2 nanoparticles in daylight (upper row) and under an ultraviolet lamp (365 nm; bottom row). (e) Time-resolved fluorescence decay of Gd–L1, Gd–L2, and Gd–(L1+2 mol% L2). Inset: photo image of Gd–(L1+2 mol% L2) nanoparticles under excitation by laser (370 nm). This figure has been reproduced with permission from reference no. 23b.

480 nm which would sufficiently overlap with the absorbance of the dyes D1 and D2. In this study, temperature controlled guest encapsulation leads to the formation of NCP composites Gd-L1-D1 and Gd-L1-D2. Gd-L1-D1 NCP composite prepared at 20 °C showed complete quenching of L1 emission at 480 nm with a concomitant emission appearance at 580 nm while it is even stronger for NCPs prepared at 140 °C. These results clearly indicate that the specific interaction between donor and acceptor is necessary for energy transfer to occur. Energy transfer is feasible and facile by coordination induced organization of donor moieties and electrostatic interactions between negatively charged carboxylate and dye molecules.

1.3.2.3 Biomedical applications

Nanoscopic dimensions of the MOFs are sufficiently smaller to cross the cell-membrane and they can be internalized into cells for potential imaging and drug delivery

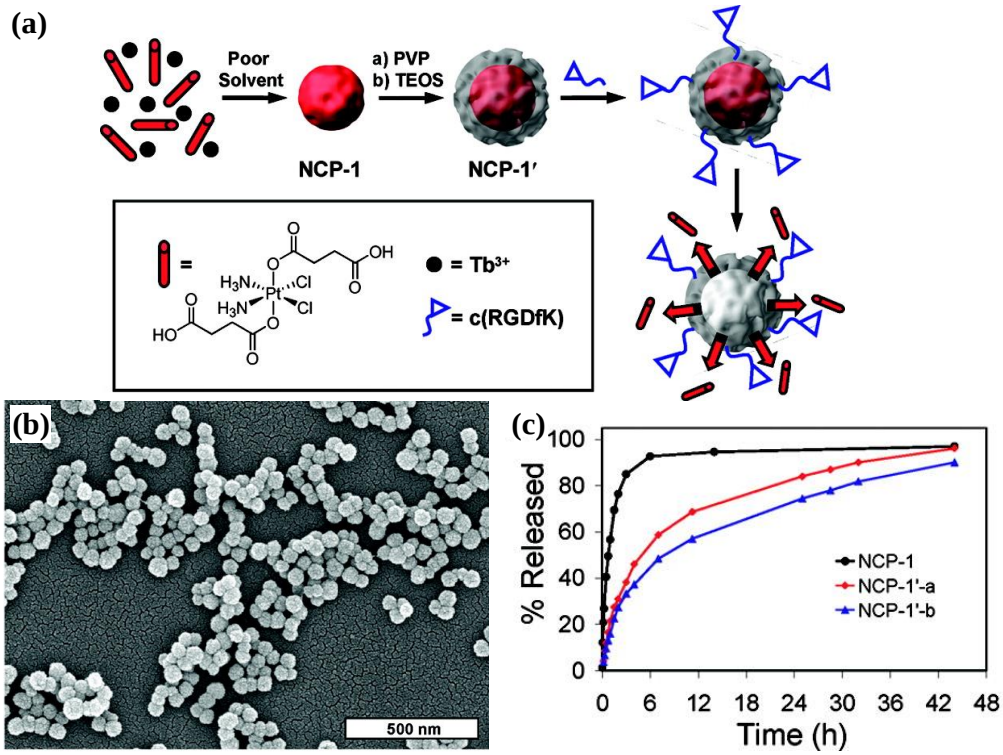

Figure 12. (a) Schematic showing the synthesis of nanocoordination polymer (NCP) containing *cis*-platin prodrug. (b) SEM image of nanospheres of NCP and (c) release profiles for as-synthesized NCP-1, silica coated NCP-1 (NCP-1′-a, and NCP-1′-b) obtained by plotting the % Pt released against time. This figure has been reproduced with permission from reference no. 24a.

applications. Limitless combination of metal ions and organic linkers diverse NMOFs can be perceived with exceptionally high surface areas, large pore sizes and are highly potential for loading and controlled release of drug molecules. Uniform dimensions and morphologies of NMOFs make them highly dispersible in aqueous medium and possess improved biocompatibility compared to bulk MOFs. Therefore NMOFs act as excellent delivery vehicles. Drug molecules are incorporated into NMOF structures either by encapsulation into pores of the MOF matrix or the drug molecules itself act as building block. Lin *et al.* reported synthesis of NMOF of Tb^{3+} containing anticancer prodrug *cis*-platin (*c*,*c*-*t*-$Pt(NH_3)_2Cl_2(succinate)_2$, DSCP) as organic building block for construction of NMOF (Figure 12) by using poor solvent assisted precipitation method.[24a] Similarly, covalent attachment of *cis*-platin prodrug in iron(III)-carboxylate NMOF was reported.[24b] Horcajada *et al.* reported non-covalent loading of therapeutic drug molecules into iron-carboxylate NMOFs prepared by solvothermal synthesis. NMOF showed excellent loading capacities for busulfan drug and showed similar cytotoxicity assay as that of free drug in several cell lines. NMOF also showed to load variety of antitumoral

drugs like DOX, cidofovir and azidothymidine triphosphate.[24c] NMOF loaded with above drugs showed controlled and progressive release of drug molecules and in-*vitro* anticancer efficiencies.

NMOFs constructed from highly paramagnetic metal ions such as Gd^{3+}, Mn^{2+} are highly potential candidates for magnetic resonance imaging (MRI) imaging applications. Further adding luminescence property to these MRI active NMOFs would provide targeted imaging applications. Having smaller sizes, excellent biocompatibility and diversity in building blocks, NMOFs provide unique opportunities in multimodal imaging applications. Lin *et al.* reported reverse micro emulsion method to prepare nanorods of $\{Gd(BDC)_{1.5}(H_2O)_2\}$ from $GdCl_3$ and bis(methylammonium)benzene-1,4-dicarboxylate for MRI imaging applications (Figure 13). Gd(BDC) nanorods of 100 nm length and 40 nm diameter in 0.1 % xanthan gum showed exceptionally high longitudinal *R1* and transverse *R2* relaxivities of 35.8 s^{-1} and 55.6 s^{-1} per mM of Gd^{3+}.[25a] Nanorods showed inverse dependent *R*1 and *R*2 values, with increasing length of nanorods the relaxitivity

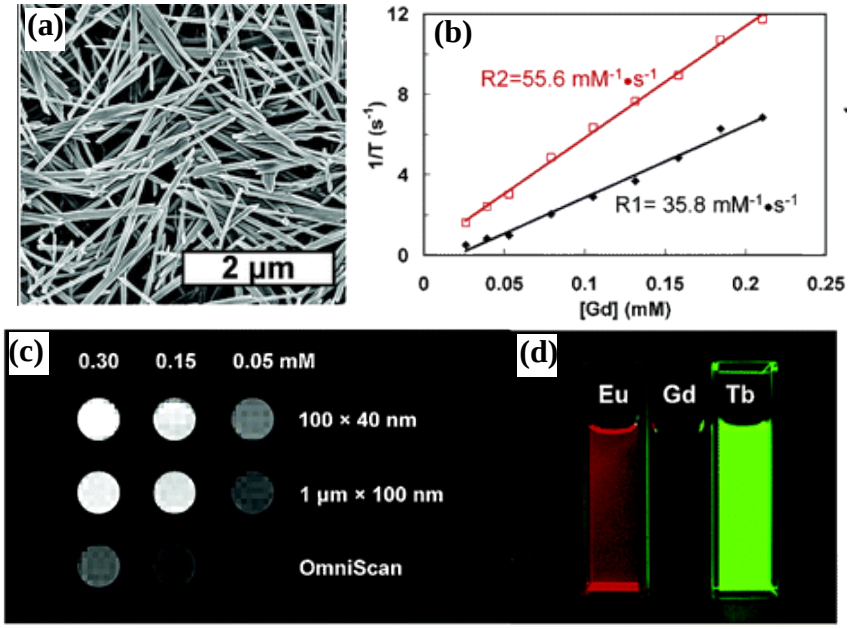

Figure 13. (a) SEM images of $Gd(BDC)_{1.5}(H_2O)_2$ (**1**) nanorods synthesized. (b) *R*1 and *R*2 relaxivity curves of **1** of 100 nm in length by 40 nm in diameter. (c) *T*1-weighted MR images of suspensions of **1** in water containing 0.1% xanthan gum. (d) Luminescence images of ethanolic suspensions of **1**, **1a** (**1** doped with 5 mol % of Eu^{3+}), and **1b** (**1** doped with 5 mol % of Tb^{3+}). This figure has been reproduced with permission from reference no. 25a.

values decreased gradually due to decrease in surface to volume ratio thereby decrease in interaction of Gd^{3+} with water protons. Further incorporation of Tb^{3+} and Eu^{3+} through

external doping during the synthesis, luminescent nanorods was achieved which are highly potential for multimodal imaging applications. Similarly, nanoparticles of $[Gd_2(bhc)(H_2O)_6]$ (bhc=benzenehexacarboxylic acid) showed excellent *R*2 values of 122.6 s^{-1} per mM of Gd^{3+}.[25b]

1.4 Conjugated microporous polymers (CMPs)

The field of porous materials has seen tremendous development starting from conventional porous materials such as zeolites, porous silica to well defined metal-organic frameworks (MOFs).[26] Recently, porous organic materials ranging from disorder to ordered structures like hyper cross-linked polymers (HCPs),[27] porous organic polymers (POPs),[28] conjugated microporous polymer (CMPs),[29] polymers of intrinsic porosity (PIMs),[30] covalent organic polymers (COPs),[31] covalent triazine frameworks (CTFs)[32] and covalent organic frameworks (COFs)[33] have received immense attention over inorganic porous materials, especially due to light weight, easy synthesis, strong covalent linkages and availability of large synthetic diversity for different building blocks. Among the porous organic materials, conjugated microporous polymers (CMPs) constructed by linking purely π-conjugated building units starting from simple benzene to higher arenes are unique for different functionalities.[29a] Pioneered by Cooper *et al.* field of CMPs has received significant attention[34] worldwide with tailor made synthetic diversity for targeted function. Extended electronic communication and semiconducting behaviour due to long range conjugation in 3D amorphous polymeric network resemble conventional conjugated polymers. CMPs poses high porosity in contrast to linear conjugated polymers which leads to additional functions like gas storage, separation, catalysis, sensing, tunable emissions and light-harvesting.[29a]

CMPs are constructed from organic nodes and linkers. Organic node is generally an aromatic molecule contains three or more reactive groups (C_3, C_4 and C_6) especially bromide, iodide cyanide, aldehyde, amine, and linker contains at least two reactive (C_2) functional groups as like node (Figure 14). Combination of building blocks such as $C_2 + C_3$, $C_2 + C_4$, $C_2 + C_6$; $C_3 + C_3$, $C_3 + C_4$, $C_3 + C_6$; $C_4 + C_6$ results in formation of 3D porous polymeric CMP network with accessible surface area and nanoporosity. Porous polymers obtained from these diverse building blocks thus contain specific functional groups such as amine, fluoride or hydroxy anchored to the pore surface, hence polymer show diverse properties. From the synthetic point of view, metal catalysed coupling reactions, like

Suzuki-Miyura coupling, Sonogashira coupling, Yamamoto coupling, cyclotrimerization, Ulman coupling, Schiff-base condensation are key reactions used for the synthesis of wide range of CMPs. Mainly small halogenated arenes are used as coupling precursors (Figure 15).

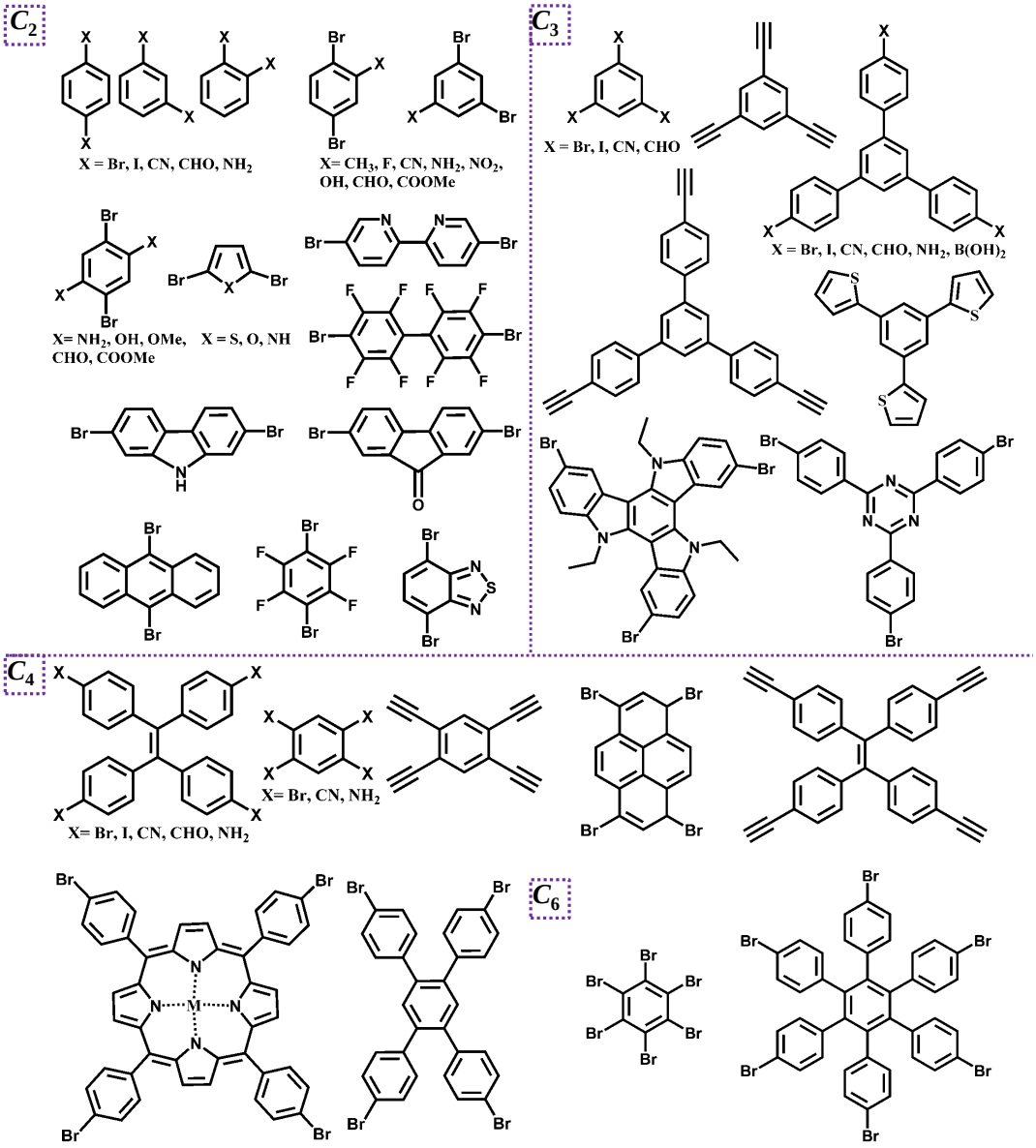

Figure 14. Set of organic nodes and linkers use to build 3D conjugated microporous polymers.

The synthetic strategies are quite similar to conventional linear conjugated polymers. Formation of covalent bonds mainly C-C, C-N between building blocks and their growth in three-dimensional direction results in 3D porous polymeric network. Kinetically controlled polymerization and irreversibility of covalent bonds leads to amorphous nature to CMPs. Besides, they possess irregular 3D pores of different sizes. In

general, appropriate monomers of interest are mixed in a suitable solvent generally anhydrous dimethylformamide (DMF), tetrahydrofuran (THF) or toluene along with suitable metal catalyst and heated at desired temperature for required period of time. The insoluble polymer gets precipitated, washed with several solvents and dried under vacuum. The complete removal of metal catalysts impurities and monomers or other impurities is done by performing Soxhelet extraction with solvents like methanol, THF *etc.* and finally highly pure CMPs are obtained. Poor crystallinity and insoluble nature of CMPs allows its structural characterization using only few methods like Fourier transform infrared (FTIR) spectroscopy, solid state ^{13}C NMR, X-ray photoelectron spectroscopy (XPS) and elemental analysis. As CMPs do not yield single crystals, an in-depth understanding of the structure is not possible by X-ray diffractometer; however, molecular simulation methods add advantage to model the possible structure of CMP. The modelled structure is validated by calculating nitrogen adsorption isotherms and accessible surface area.

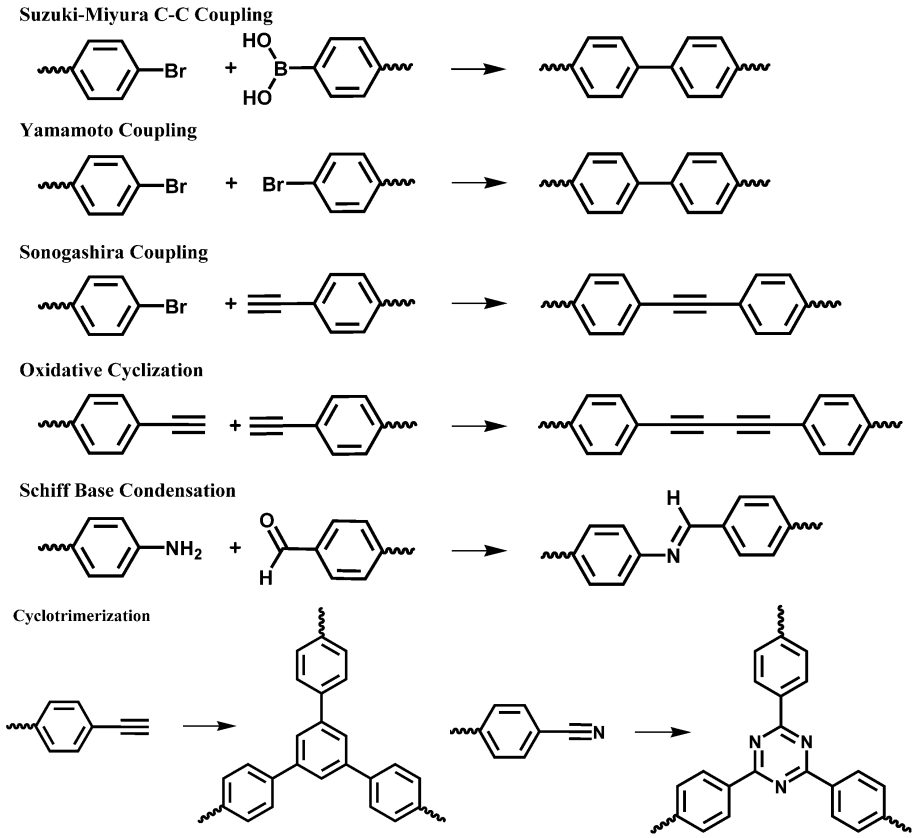

Figure 15. Schematic reactions for the synthesis of CMPs from versatile building blocks.

From porosity perspective, CMPs are mainly microporous in nature and surface area is tunable over wide range by judicious choice of organic building blocks. As like

MOFs, the pore volume and surface area of CMPs can be controlled by changing molecular length of the linker or node. For example Cooper *et al.* reported series of CMPs[35a] by changing linker length and keeping the node (1,3,5-triethynylbenzene) constant. CMP-0, CMP-1 and CMP-2 with tunable surface areas 1018, 834 and 634 m^2g^{-1}

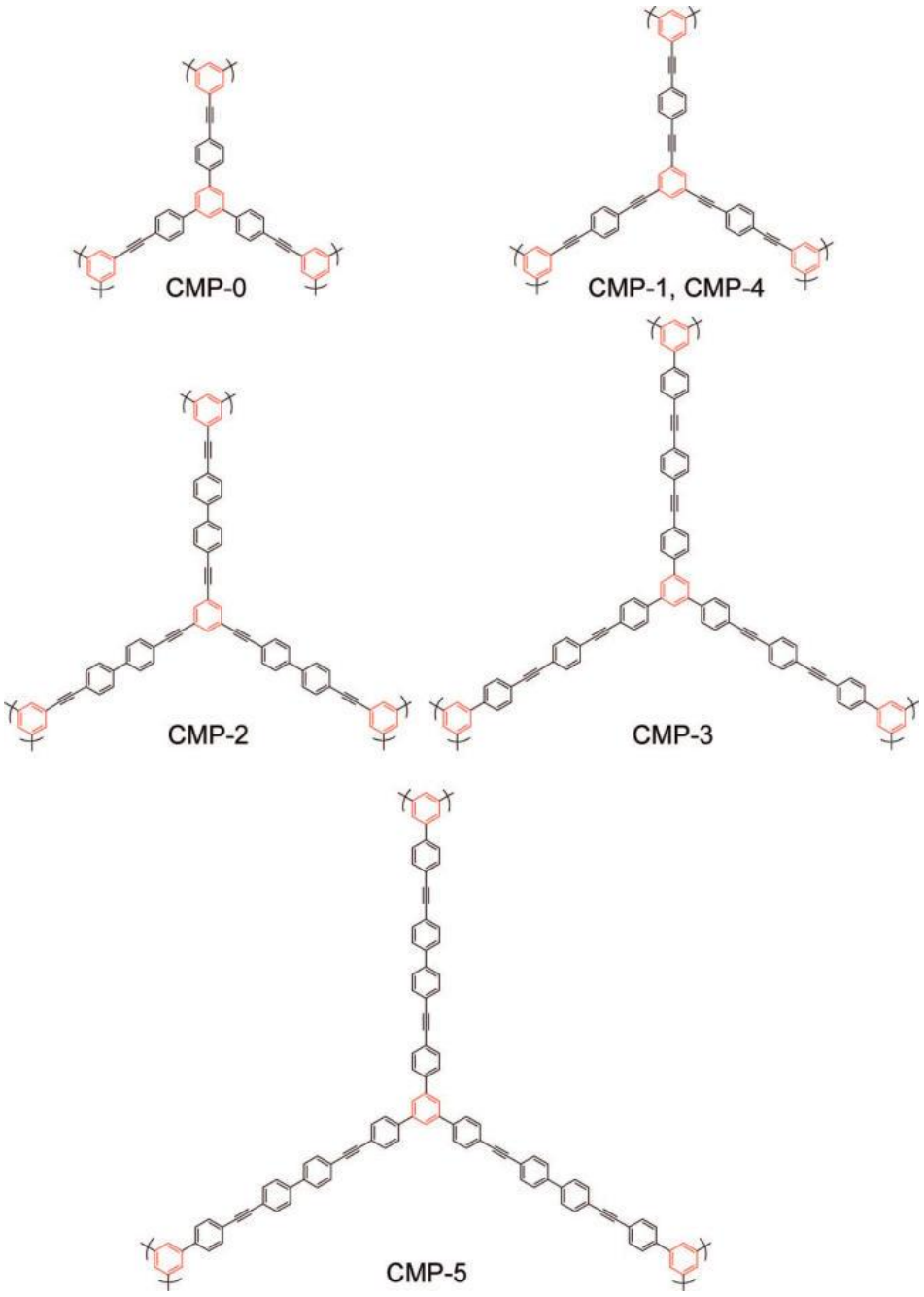

Figure 16. Representative molecular structures for networks CMP-0-5. This figure has been reproduced with permission from reference no 35a.

are realized (Figure 16). While, having constant three connecting node 1,3,5-tris-(4-iodophenyl) benzene and varying linker length two polymers namely CMP-3 and CMP-5 with different surface areas 522 and 512 m^2g^{-1} are reported. These investigations imply

BET surface area decreases with increasing molecular length of linker while it increases with increasing connectivity of linker from C_2 to C_3. Han *et al.* reported porous conjugated polycarbazoles (CPOPs)[35b] by oxidative coupling reaction with as high surface area as 2440 m^2g^{-1}. Therefore increase in length of the linker increase surface area to an optimized level and it starts decreasing due to interpenetration or intercalation effects at high molecular length. Similarly, NCMPs reported by Cooper *et al.* observed to show a decrease in surface area from 1108 to 546 m^2g^{-1} with increasing linker length.[35c] Also it is shown that connectivity and surface area of the CMPs are strongly affected by the choice of the reaction solvent.[35d] On the other hand, Jiang *et al.* showed conformational locking of the linker can affect the surface area of CMP.[35e]

1.4.1 Applications of CMPs

Synthetic diversity of organic building blocks provides large variety of CMPs with modularity in surface area, porosity. It is also possible to systematically functionalize the pore surface of CMPs through post-synthetic modification or by pre-designing the building blocks with diverse functional groups. Having excellent diversity

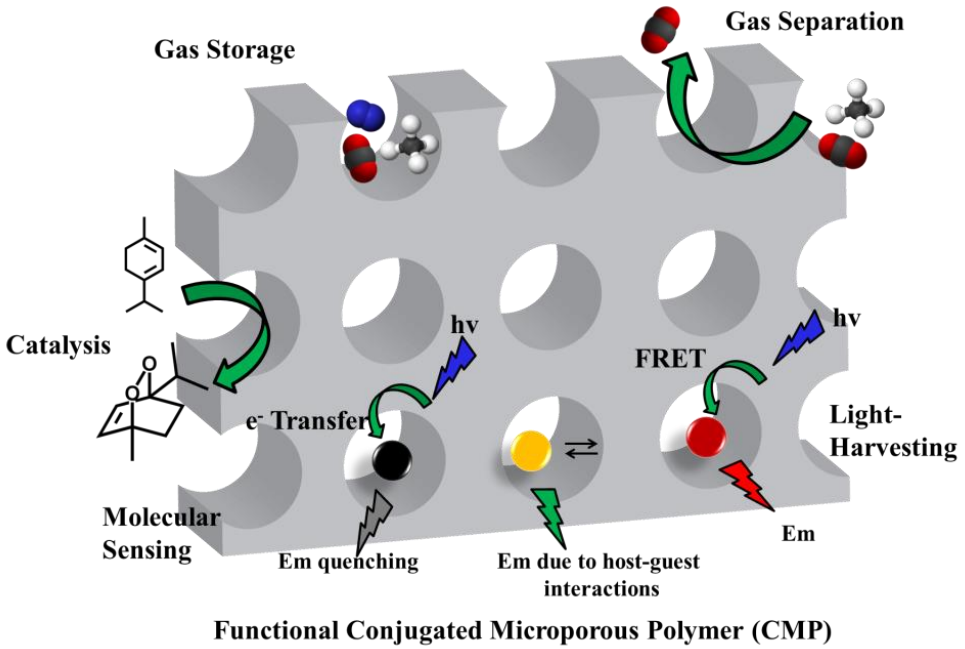

Figure 17. Functional CMP and its possible applications.

in structure, CMPs show versatile applications in gas storage, separation, catalysis. Further, unique π-conjugation present along the polymer chains of CMP harness strong luminescence thereby potential in molecular sensing, light-harvesting, band gap tuning and other luminescence based applications. The schematic shows a functional CMP for

versatile applications (Figure 17). This thesis mainly discusses molecular sensing and bang gap engineering in CMP.

1.4.1.1 Gas storage/capture, separation

Characterized by the intrinsic microporosity and high surface area, CMPs have been extensively studied for gas storage applications. BCMBP reported by Cooper *et al.* shows gravimetric H_2 storage capacity of 3.68 % at 15 bar and 77.3 K with a isosteric heat of adsorption of 6-7.5 kJ/mol.[36a] Deng *et al.* reported an elegant strategy of improving H_2 uptake, where Li^+ ions are doped into CMP matrix for excellent H_2 uptake capacity of 6.1 wt% at 1 bar and 77 K.[36b] BCMBP was also found to exhibit 5.2 $mmolg^{-1}$ of methane uptake at 20 bar and 298 K.[36c] Zhou *et al.* reported high surface area porous polymer networks (6461 m^2g^{-1}) with methane storage capacities of 389 mgg^{-1} at 55 bar and 295 K.[36d] Among the rapidly growing research interests of gas storage, selective CO_2 adsorption and its sequestration is one of the important and environment related problem. Post combustion effluents like flue gas comprise 3-15 % CO_2 and nearly 70 % N_2, while landfill gas contains nearly equal ratio of CO_2/CH_4. The high performance CO_2 adsorbents should generally have ultra micropores with high surface area which provides large amount of low pressure adsorption due to stronger adsorption potential. Besides, functionalization of pore surface with highly polar pendant groups like NH_2, COOH, OH, F within the micropores enhance the adsorbate-adsorbent interaction and allow selective capture of CO_2 over other gases. Cooper *et al.* reported tuning of CO_2 uptake properties in CMPs[37a] by changing polarity of the functional groups on the pore surface from CH_3,

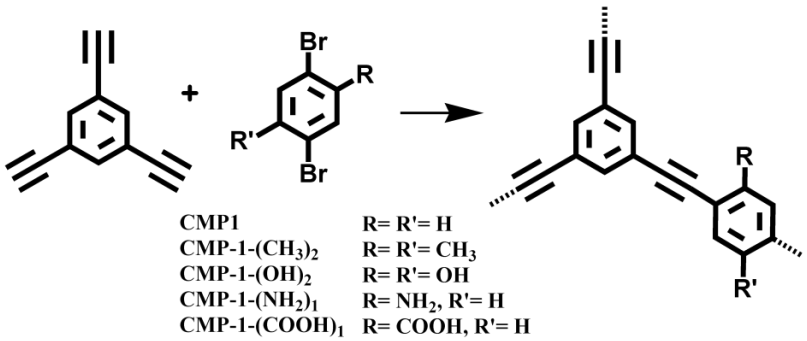

Figure 18. Synthesis of functionalised CMPs using (i) DMF, NEt_3, $Pd(PPh_3)_4$, CuI, 100 °C, 72 h. This figure has been reproduced with permission from reference no 37a.

NH_2, OH to COOH (Figure 18). CMP-1-$(OH)_2$ observed to show higher CO_2 uptake (1.07 $mmolg^{-1}$ at 1 bar and 298 K), while lowest uptake (0.94 mmol g^{-1}) is observed for CMP-1-$(CH_3)_2$ (Figure 19). Isosteric heat of adsorptions are found to be higher (32.6-21.6 kJ

mol^{-1}) for COOH appended CMP and lower for methyl substituted CMP. So the results clearly indicate the chemical composition of pore has greater impact on CO_2 uptake properties. Similarly George *et al.* reported selective adsorption of CO_2 over N_2 in polyphenylene porous organic polymers, where the large aromatic π-clouds and polar end functional groups are shown to affect CO_2 selectively over N_2.[37b]

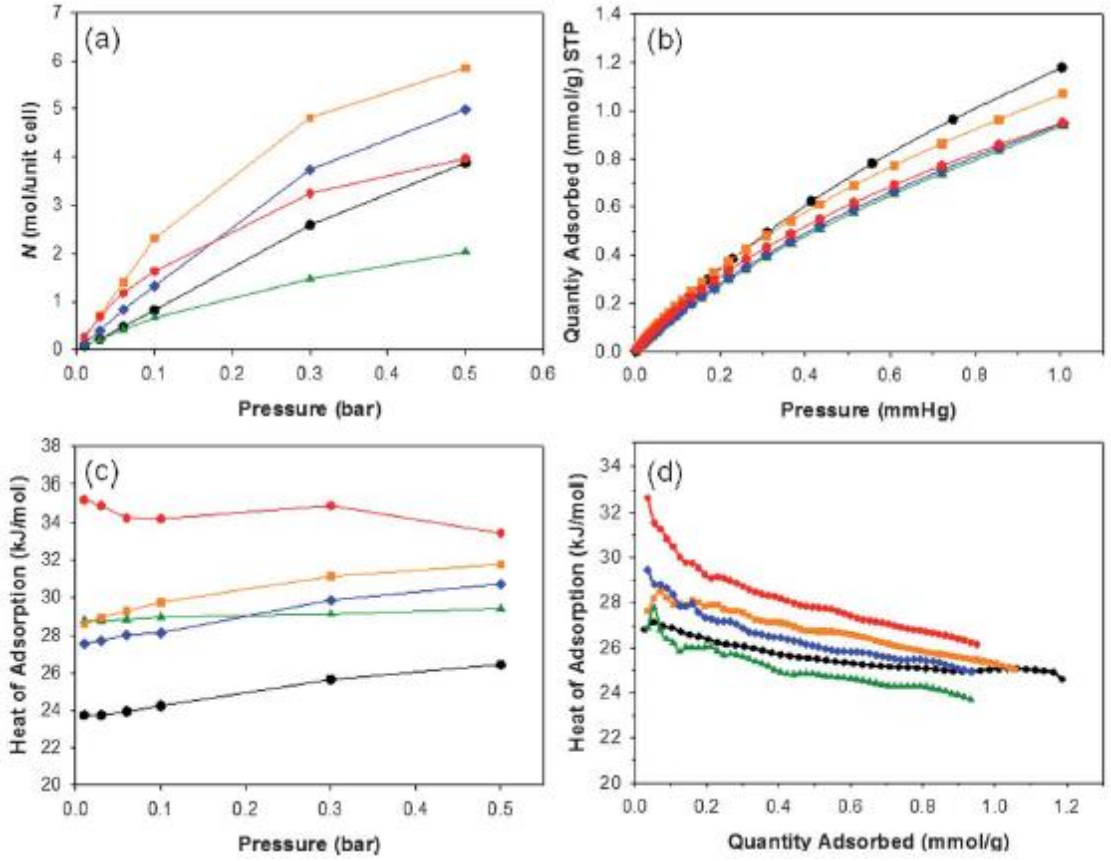

Figure 19. (a) Calculated CO_2 isotherms at 298 K for substituted MIL-53 frameworks, and (b) measured CO_2 isotherms for CMP networks. (c) Calculated isosteric heats of adsorption for CO_2 in substituted MIL-53 frameworks, redrawn from ref. 46 and (d) measured for CMP networks. Colour-coding is as follows: Unsubstituted networks (black); $–(CH_3)_2$ (green); $–(OH)_2$ (orange); $–NH_2$ (blue) and –COOH (red). This figure has been reproduced with permission from reference no 37a.

Separation and capture of gases or harmful vapours is industrially important. For example, separation of CO_2 from CH_4 is industrially important to increase the net heat of fuel combustion. Yang *et al.* reported phosphine oxide containing porous polymers (TEPO) for selective CO_2 adsorption[38a] with relatively high adsorption capacities of 8.4 wt% at 273 K and 1 bar. Deng *et al.* reported metal-salen containing polymers (Co/Al-CMP) to capture and convert CO_2 at ambient conditions. Co-CMP and Al-CMP observed to show 79.3 mgg^{-1} and 76.5 mgg^{-1} CO_2 uptake at 1 atm and 298 K.[38b]CMPs also show

potential in capture of carcinogenic or harmful gases which are industrially relevant. Jiang *et al.* reported porphyrin containing CMPs for exceptional amine capture at room temperature.[38c] ZnP-CMP found to show an uptake capacity of 2.2 g_{amine} per g_{CMP} for n-butyl amine and 2.7 g_{amine} per g_{CMP} for n-hexyl amine. It also showed excellent capacities for secondary amines such as dibutyl amine (2.3 g_{amine} per g_{CMP}) and diisobutyl amine (1.6 g_{amine} per g_{CMP}).

1.4.1.2 Luminescence: Colour tunability, sensing and light-harvesting

π-Conjugation extended over large arrays of 3D polymeric network structure of CMP harness high photoluminescence with excellent quantum yields comparable to inorganic components. Flexibility in incorporating desired chromophores within the CMP frameworks covalently or non-covalently allows fine tuning of emission through host-guest interactions. Not only the conjugation effect, occurrence of host-guest interactions such as charge transfer, energy transfer or electron transfer may lead to changes in luminescence properties of the CMPs. Cooper *et al.* reported highly soluble luminescent pyrene CMPs showing cyan emission at 478 nm and is attributed to the extended pyrene conjugation in CMP.[39] Jiang *et al.* reported systematic porosity and luminescence changes in the CMPs with reaction time. [40a] Recently, Thomas *et al.* reported charge-transfer exhibiting tetrathiafulvalene (TTF) CMPs where the TTF shows strong electron donating character.[40b] Recently Liu *et al.* reported luminescent CMP by conjugating triarylborane and triphenylamine building blocks through C-C linkage where the intramolecular charge-transfer (ICT) from triphenylamine to triarylborane result in emission.[40c]

Copolymerization is one efficient technique used to tune the emission properties of CMPs. Cooper *et al.* reported band gap engineering in series of pyrene based CMPs (YPy, YDPPy, YDBPy) by changing the extent of conjugation length by using π-linkers of varying conjugation.[40d] The emission properties are finely tuned from red (620 nm) to orange (602 nm) and yellow (545, 582 nm) in solid state (Figure 20). Interestingly, band gap of these pyrene networks were found to be decreased from 1.84 to 2.37 eV. Similar conjugation dependant emission tuning is also observed in core-shell CMPs reported by Jiang *et al.,* where polyphenylene CMP (PP-CMP) core polymerized with controlled shell thickness of polytetraphenylethene CMP (TPE-CMP) by changing molar ratio of monomers (TBTPE/TBB) from 0.125-0.4 the emission maxima is tuned from 435 nm (PP-CM) to 518 nm (TPEs-PPc-CMP@4).[41a] Similar emission colour tuning is also

observed in other TPE based CMPs.[41b] Weber *et al.* showed emission colour tuning in spirobifluorene CMPs by changing the monomer ratios of 1,4-benzene diboronic acid and 2,5-thiophene boronic acid.[41c]

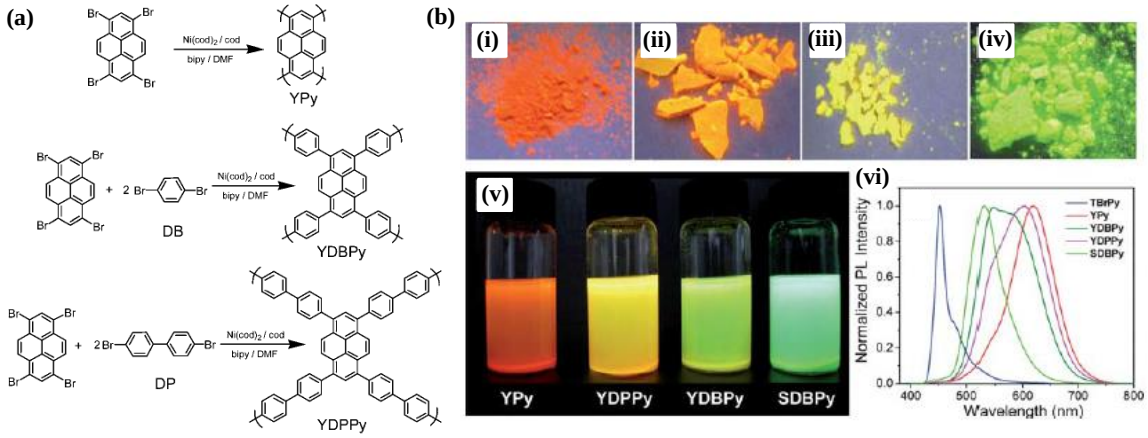

Figure 20. (a) Synthetic routes to luminescent CMPs showing notional network structures. The actual structures of these statistical copolymers will be more complex than represented. (b) Photographs of the polymers under irradiation with UV light (λ_{ex}=365 nm) in the solid state, (i) YPy, (ii) YDPPy, (iii) YDBPy, and (iv) SDBPy; (v) Photographs of suspensions of the polymers in THF (10 mg/10 mL); (vi) Photoluminescent spectra of the monomer TBrPy and the resulting polymers measured in solid state powder (λ_{ex} = 360 nm). These figures have been reproduced with permission from reference no 40d.

CMPs are three dimensional polymeric structures with interconnected micropores, extended conjugation and host-guest interaction between polymer and guest leads to diverse phenomena which alter the emission properties of CMP. These specific changes in photophysical properties of CMP can be signature for the nature of analyte present, and it provides excellent platform to design molecular sensory systems. Magnitude of changes strictly depends on the ability of the polymer to interact with analyte at low concentrations of analyte species. CMPs are studied as luminescent sensors due to strong photoluminescence behaviour and amenable pore sizes to host various analyte molecules. Jiang *et al.* reported molecular sensing (Figure 21) of electron rich and electron deficient arenes using polycarbazole CMP (TCB-CMP; S_{BET}= 1280 m^2g^{-1}; Pore size of 0.8-1.5 nm).[41d] On exposure to electron deficient arenes such as 2,4-dinitrotoluene (2,4-DNT, 40 %), 1,4-benzoqunone (BQ, 80 %) etc. TCB-CMP observed to show significant fluorescence quenching with time. Remarkably, TCB-CMP showed fluorescence enhancement when exposed to electron rich vapours. Interestingly, TCB-CMP found to

show fluorescence on/off sensing properties when exposed to NB and toluene alternatively over several cycles. Electron transfer process from CMP to nitroaromatics

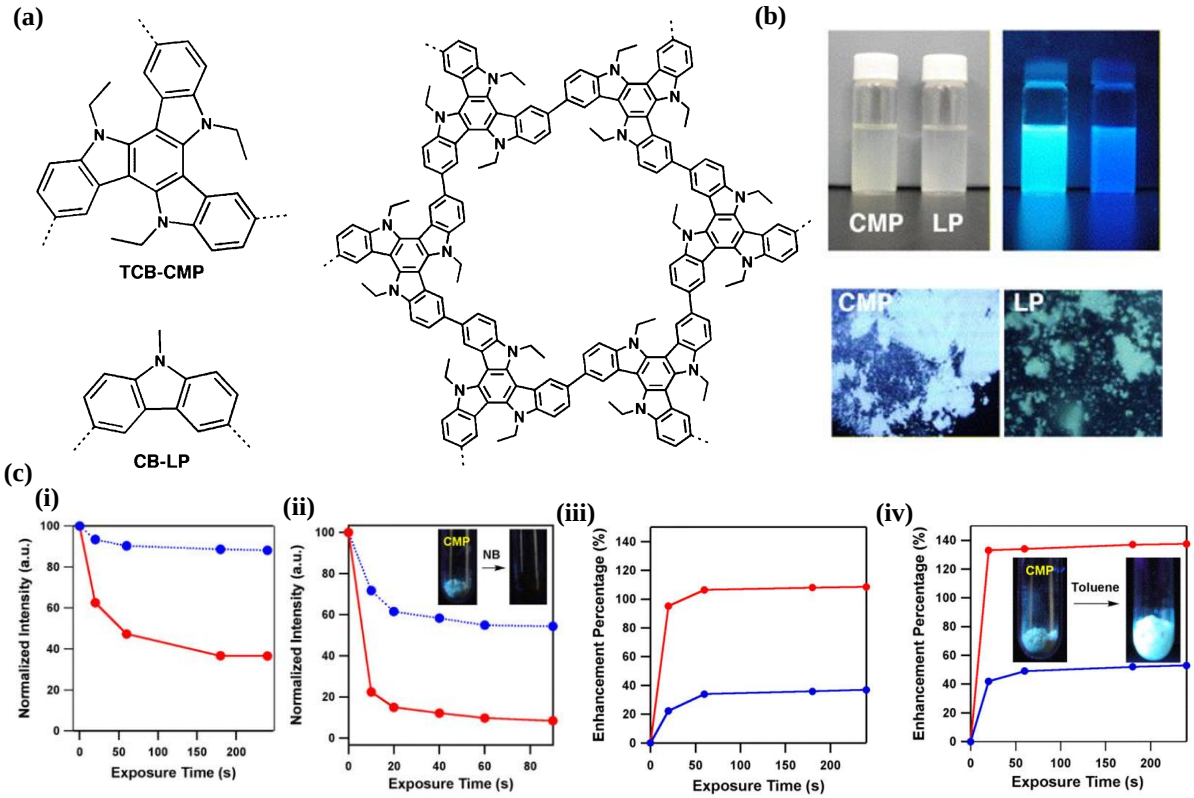

Figure 21. Schematic representations of (a) the carbazole-based CMP (TCB-CMP) and the linear polymer analogue CB-LP and elementary pore skeleton of TCB-CMP containing TCB Units. (b) Images of TCB-CMP and CB-LP (left) in PEG and (right) under a UV lamp and fluorescence microscopy images of solid samples of TCB-CMP and CB-LP. (c) Loss of fluorescence intensity of TCB-CMP (red ●) and CB-LP (blue ●) at 25 °C upon exposure to vapours of (i) DNT, (ii) NB, and fluorescence enhancement of TCB-CMP (red ●) and CBLP (blue ●) upon exposure to vapours of (iii) benzene, and (iv) toluene. Inset in (iv): luminescence images of CMP in the presence and absence of toluene under a handheld UV lamp. These figures have been reproduced with permission from reference no 41d.

through host-guest interactions is claimed to be responsible for the fluorescence quenching of CMP. Similarly, polycarbazole CMP films were studied for sensing of dopamine, metal ions and hydrochloric acid.[42a] Fluorescence response of carbazole CMPs to electron deficient/rich arenes were also reported by Zhang *et al*.[42b] Molecular sensing of nitroaromatics using triphenylene CMPs is recently reported by Pan *et al*. Hypercrosslinked CMPs based on triazine building blocks were studied for sensing and removal of mercury ions.[42c]

CMPs with inherent porosity (<2 nm), continuous aromatic units throughout the polymer network makes them highly potential in light emitting diodes, electroluminescent materials and artificial light-harvesting systems. Highly dense aromatic polymer scaffolds with remarkable surface area could harvest and transfer energy to an appropriate reaction center with appreciable efficiency. In contrast to pure organic assemblies, where the donor or acceptor molecules are susceptible to aggregation thereby deplete energy transfer efficiency, CMPs with confined and interconnected micropores surrounded by large number of energy donor units facilitate excellent spatial confinement of acceptor molecules with no possibility of aggregation and enhance energy transfer efficiency.

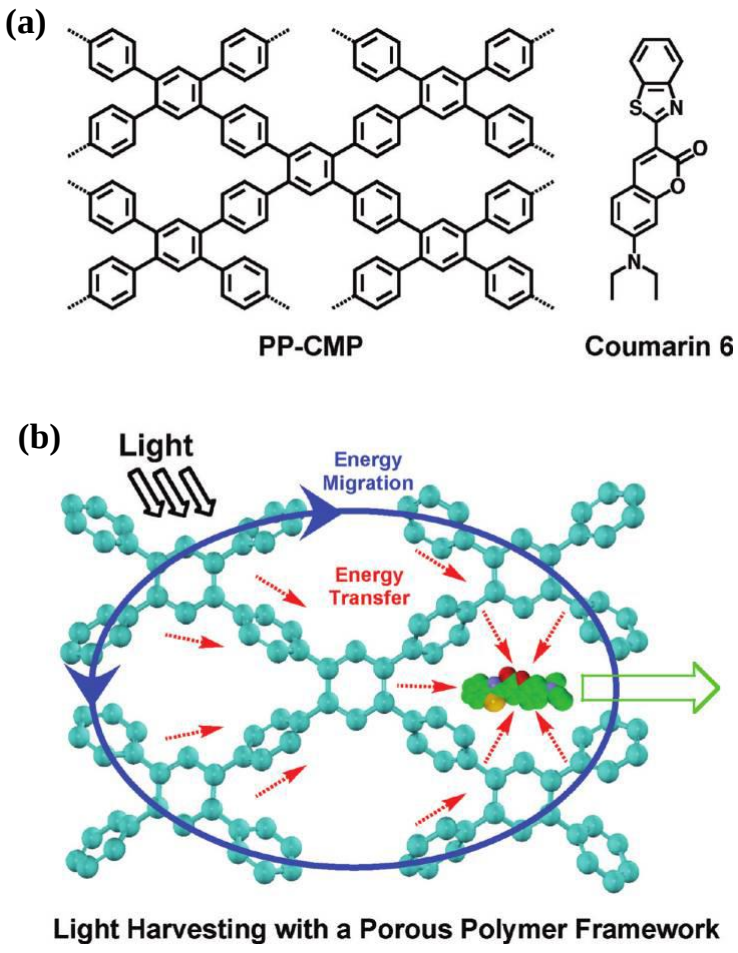

Figure 22. (a) Structure representation of PP-CMP and coumarin 6 and (b) schematic representation of energy funnelling from PP-CMP to spatially confined coumarin 6. This figure has been reproduced with permission from reference no 42d.

First report of non-covalent encapsulation of acceptor molecules in CMPs for light-harvesting applications is demonstrated by Jiang *et al.*, PP-CMP (SBET = 1083 m^2/g; Pore diameter= 1.56 nm) synthesized by Suzuki cross coupling reaction between benzene diboronic acid (BDBA) and tetrabromobenzene (TBB) found to show strong blue

luminescence at 443 nm (Q= 23 %). Energy transfer occurs from PP-CMP to encapsulated acceptor dye molecules Coumarin-6 through Försters resonance energy transfer mechanism due to significant spectral overlap between PP-CMP emission and Coumarin-6 absorption (Figure 22, 23).[42d] At 2.9 mol% of dye doping, PP-CMP showed strong emission at 497 nm and emission at 443 nm was observed to be quenched completely and the emission colour of the compound changes to green.

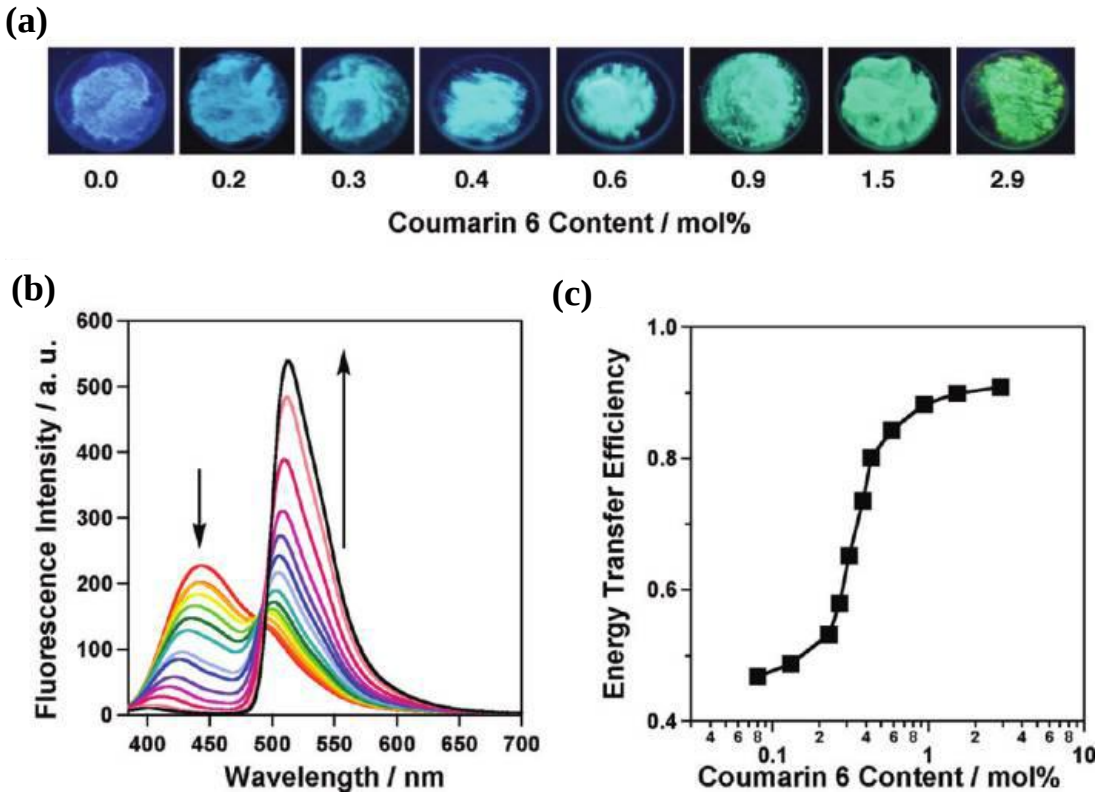

Figure 23. (a) Fluorescence images of solid samples of PP-CMP⊃coumarin 6 upon excitation at 363 nm. (b) Fluorescence spectral change of PP-CMP⊃coumarin6 with different coumarin 6 contents upon excitation at 363 nm. (c) Plot of quantum efficiency of energy transfer from PP-CMP to coumarin 6 versus coumarin 6 content. This figure has been reproduced with permission from reference no 42d.

More recently, Jiang *et al.* reported electro-oxidative coupling based deposition of CMPs on an electrode surface which was studied for cascade energy transfer process by non-covalent encapsulation of donor acceptor dyes.[42e] This thesis details clear understanding of photophysical properties of CMPs mainly intramolecular charge transfer in triarylborane CMPs for molecular sensing and inter chain energy transfer and charge transfer in fluorenone CMPs for band gap engineering applications.

1.4.1.3 Heterogeneous catalysis

Facile post synthetic modification and extraordinary hydrolytic stability of CMPs make them potential in heterogeneous catalysis applications. Cooper *et al.* reported metal-organic CMPs[43a] where the CMP is post synthetically modified with catalytically active metal sites (CpIr) and studied for its catalytic activity towards reductive amination of carbonyl compounds. Deng *et al.* reported salen-Co/Al catalyst appended CMPs[38b] for the conversion of CO_2 to propylene carbonates under mild conditions. Recently, Thomas *et al.* reported an anionic CMP constructed from triarylborane building blocks, [43b] where the Li^+ cations are replaced by catalytically active manganese(II) bipyridine complexes and studied for oxidation of styrene (Figure 24).

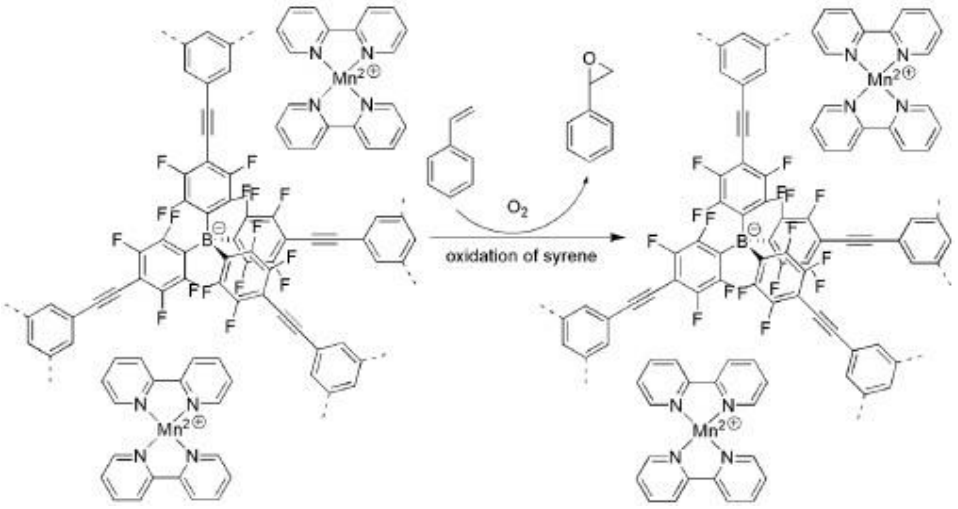

Figure 24. Immobilization of $[Mn(bpy)_2]^{2+}$ in an anionic borate network and its catalysis of styrene oxidation. This figure has been reproduced with permission from reference no 43b.

CMPs also show excellent photocatalytic activity for various organic transformations. Vilela *et al.* reported photolytic singlet oxygen generation in thiadiazole CMPs and studied transformation of α-terpinene to ascaridole.[44a] Han *et al.* recently reported detailed studies on similar photolytic singlet oxygen generation using porphyrinic CMPs.[44b] Zhang *et al.* reported oxidative coupling of benzyl amines under visible light conditions using photoactive CMPs.[44c] Cooper *et al.* reported CMPs derived from rosebengal dye building blocks for heterogeneous photocatalytic aza-Henry reaction with good activity over 10 cycles.[44d]

Conversion of solar energy into useful chemical energy is well noticed in plants through photosynthesis. Artificial light-harvesting antennas connected to molecular water oxidation centers have been evolved to produce energy from sunlight.[45] TiO_2 is a

prominently studied semiconducting photocatalyst for proton reduction or H_2 generation.[45] Other photo-catalysts such as graphitic carbon nitrides, triazine frameworks and covalent organic frameworks or metal-organic frameworks have also been studied with/without the aid of Pt co-catalyst under UV illumination conditions.[46] In contrast, the synthetic control available in CMPs facilitate precise tuning of band gap properties which in turn affect the photocatalytic properties. Recently, Cooper *et al.*

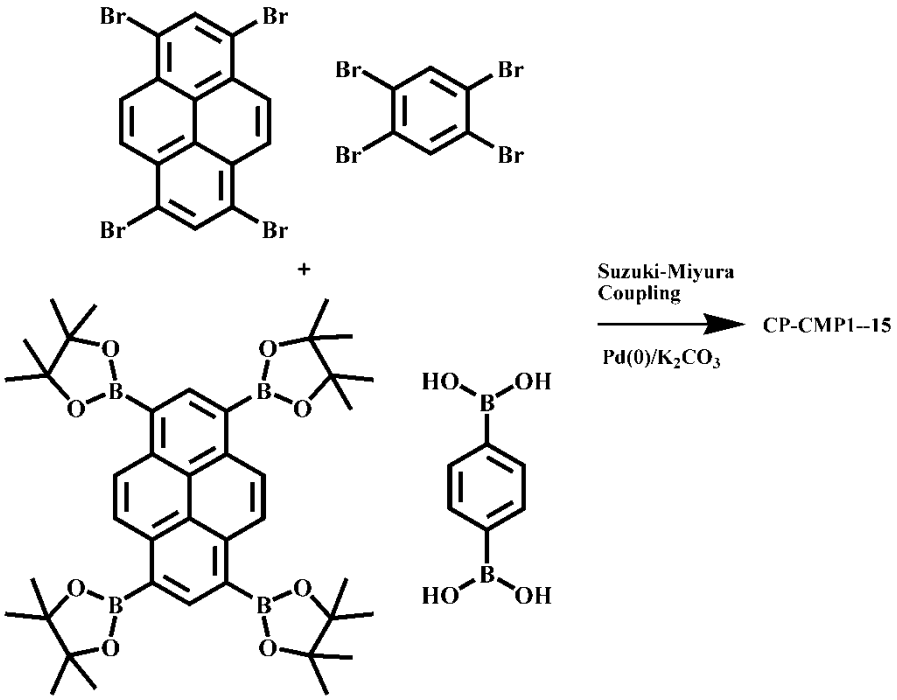

Figure 25. Synthesis of various conjugated microporous copolymer photocatalysts.

reported a systematic control over optical band gap using copolymerization technique in pyrene CMPs for photocatalytic H_2 evolution under visible light conditions without any metal co-catalyst (Figure 25).[47] A series of CMPs (CP-CMP1-15) showing gradual red-shift in the onset optical absorption were prepared from 1,4-benzenediboronic acid, pyrene 1,3,6,8-tetraboronic pinacol ester, 1,2,4,5-tetrabromobenzene and 1,3,6,8-tetrabromopyrene. Emission of CP-CMP found to show a drastic red-shift from 445 nm to 588 nm with increasing content of the pyrene in the CMP. Interestingly, CP-CMP solution having diethylamine as sacrificial donor without any metal co-catalyst showed significant evolution of H_2 on irradiation with visible light (420 nm) and rate of H_2 evolution is observed to increase with decrease in the band gap for CP-CMP1 to CP-CMP10. CP-CMP 10 with an optical gap of 2.33 eV is observed to show highest (100 μmol for 6 hours) among all CMPs. Interestingly, all polymers were found to be highly robust and showed active H_2 evolution even after 100 hours of photoirradiation.

1.5 Scope of the work

Synthesizing nanoMOFs is not new and development of new methods to attain diverse morphologies is already in acceleration. Bottom up approach and use of external modulating agents have been key to assemble nanoNMOFs. Nonetheless, simple and straightforward methods to get desired MOF nanostrucutres using ligand design approach and their light-harvesting properties are unexplored. Targeted imaging using NMOFs by external doping of luminescent lanthanides has been studied and covalent integration of donor-acceptor chromophores in NMOF are reported for light-harvesting applications. However NMOF showing bimodal imaging properties without any external modification or doping is not achieved. Hence a serious amount of work has to be done in this direction. Some of the NMOFs reported in this thesis address such problems using a predesigned high quantum yield π-conjugated linker. Ligand directed dynamic and soft assemblies of MOF with various morphologies are explored and their light-harvesting properties are studied. Self-assembled luminescent NMOF based on paramagnetic inorganic components is explored for bimodal imaging applications. Luminescent materials based on conventional chromophores are well explored for light-harvesting, sensing and for colour tunability applications. However, the problem of aggregation caused quenching (ACQ) in conventional chromophores is limiting issue. Organic assemblies using high quantum yield AIE chromophores are well explored, however fabrication of easy processable and highly luminescent inorganic-organic AIE hybrids are relatively less explored. This thesis partly deals with such AIE hybrid materials using predesigned AIE chromophores for colour tunable emission including white light. Stronger C-C covalent linkages in porous organic polymers like CMPs provides high hydrolytic stability and has been an alternative and superior to MOFs in achieving gas separation or capture from industrial streams or in heterogeneous catalysis under extreme conditions. High surface areas, modifiable porosity are achieved in CMPs. Variety of CMPs with strong luminescence properties are studied for light-harvesting and sensing applications. Understanding important photophysical properties such as intramolecular charger transfer and energy transfer is crucial in designing novel luminescent materials for optoelectronics and photocatalysis. This thesis partly demonstrates study of such complex charge transfer and energy transfer properties in donor-acceptor CMPs and their precise band gap engineering. Also, charge transfer properties in CMPs are explored for

reversible and selective molecular sensing and capture application under aqueous conditions.

1.6 Outlook

Prospect of processable nanoscale luminescent porous materials are huge. Synthetic diversity, ease of functionalization and modularity make them extremely useful materials for versatile applications. There have been several advances in synthesis of metal-organic nanomaterials or NMOFs and their potential applications in gas storage, imaging, drug delivery and sensing. Luminescent NMOFs are still at infancy stage and have great promise as biomedical imaging agents, sensing and light-harvesting platforms owing to their structural and chemical diversity. Modification of ligand can lead to several NMOF morphologies with varied applications. Taking advantage of tunable nature of NMOFs, combining both optical imaging and MRI imaging in same NMOF system should greatly facilitate development of multimodal imaging agents. AIE luminophores are functional materials with brilliant and practically useful solid state emission than in solution state. The beneficial effects of AIE chromophores showed exponential growth in the field of luminescent materials. AIE chromophores are highly emissive in solid state and potential in electroluminescent devices. Hybridization of these AIEgens can lead to improved thermal and mechanical stability along with their high photostability. CMPs are unique class of porous organic polymers combining porosity and π-conjugation. The diversity of organic building blocks, flexible molecular design and various synthetic methods made them extremely useful in variety of applications. CMPs showing excellent exciton migration and inherent porosity have been platform for sensing and light-harvesting applications. CMP thin films or devices are still at the beginning state and have great promise as portable sensing devices or in organic photovoltaics. In this thesis dynamic nature of MOF hybrid assemblies is used to prepare various nanomorphologies and their luminescence properties have been exploited for light-harvesting and bimodal imaging applications. Also, hybridization of AIE chromophores using inorganic components has been exploited for fabrication of processable and colour tunable AIE hybrids including white light emitting hydrogels. In addition to these, synthesis of CMPs and their band gap engineering by controlling the important photophysical properties such as charge transfer and energy transfer between donor-acceptor moieties have been explored. Also, photophysical properties of CMPs are detailed and their molecular sensing applications under aqueous conditions are studied.

1.5 References

[1] a) C. Perego, R. Millini, *Chem. Soc. Rev.* **2013**, *42*, 3956-3976; b) M. E. Davis, *Nature* **2002**, *417*, 813; c) A. G. Slater, A. I. Cooper, *Science* **2015**, *348*, 6238; d) Y. Ma, W. Tong, H. Zhou, S. L. Suib, *Microporous Mesoporous Mater.* **2000**, *37*, 243; e) H. D. Gesser, P. C. Goswami, *Chem. Rev.* **1989**, *89*, 765; f) Y. Li, Z.-Y. Fu, B.-L. Su, *Adv. Funct. Mater.* **2012**, *22*, 4634.

[2] a) J. V. Smith, *Chem. Rev.* **1988**, *88*, 149; b) A. Primo, H. Garcia, *Chem. Soc. Rev.* **2014**, *43*, 7548; c) X. Meng, F.-S. Xiao, *Chem. Rev.* **2014**, *114*, 1521; d) W. J. Roth, P. Nachtigall, R. E. Morris, J. Čejka, *Chem. Rev.* **2014**, *114*, 4807; e) A. Corma, *Chem. Rev.* **1995**, *95*, 559; f) J. Perez-Ramirez, C. H. Christensen, K. Egeblad, C. H. Christensen, J. C. Groen, *Chem. Soc. Rev.* **2008**, *37*, 2530; g) L. Chuenchom, R. Kraehnert, B. M. Smarsly, *Soft Matter* **2012**, *8*, 10801; h) S. De, A. M. Balu, J. C. van der Waal, R. Luque, *ChemCatChem* **2015**, *7*, 1608; i) L. Zhang, X. Yang, F. Zhang, G. Long, T. Zhang, K. Leng, Y. Zhang, Y. Huang, Y. Ma, M. Zhang, Y. Chen, *J. Am. Chem. Soc.* **2013**, *135*, 5921.

[3] a) S. Furukawa, J. Reboul, S. Diring, K. Sumida, S. Kitagawa, *Chem. Soc. Rev.* **2014**, *43*, 5700; b) P. Falcaro, R. Ricco, C. M. Doherty, K. Liang, A. J. Hill, M. J. Styles, *Chem. Soc. Rev.* **2014**, *43*, 5513; c) V. Stavila, A. A. Talin, M. D. Allendorf, *Chem. Soc. Rev.* **2014**, *43*, 5994; d) Y. Zhang, S. N. Riduan, *Chem. Soc. Rev.* **2012**, *41*, 2083; e) W. Lu, D. Yuan, D. Zhao, C. I. Schilling, O. Plietzsch, T. Muller, S. Bräse, J. Guenther, J. Blümel, R. Krishna, Z. Li, H.-C. Zhou, *Chem. Mater.* **2010**, *22*, 5964; f) S.-i. Noro, D. Tanaka, H. Sakamoto, S. Shimomura, S. Kitagawa, S. Takeda, K. Uemura, H. Kita, T. Akutagawa, T. Nakamura, *Chem. Mater.* **2009**, *21*, 3346; g) P. Kanoo, G. Mostafa, R. Matsuda, S. Kitagawa, T. K. Maji, *Chem. Commun.* **2011**, *47*, 8106; h) R. Haldar, R. Matsuda, S. Kitagawa, S. J. George, T. K. Maji, *Angew. Chem.* **2014**, *126*, 11966; i) P. Kanoo, A. C. Ghosh, S. T. Cyriac, T. K. Maji, *Chem. Eur. J.* **2012**, *18*, 237; j) S. Mohapatra, B. Rajeswaran, A. Chakraborty, A. Sundaresan, T. K. Maji, *Chem. Mater.* **2013**, *25*, 1673; k) K. Jayaramulu, P. Kanoo, S. J. George, T. K. Maji, *Chem. Commun.* **2010**, *46*, 7906.

[4] D. J. Transchemontangne, J. L. Mendoza-Cortés, M. O'Keeffe, O. M. Yaghi, *Chem. Soc. Rev.* **2009**, *38*, 1257.

[5] a) O. M. Yaghi, H. Li, *J. Am. Chem. Soc.* **1996**, *118*, 295; b) T. R. Whitfield, X. Wang, L. Liu, A. J. Jacobson, *Solid State Sci.* **2005**, *7*, 1096.

[6] a) R. Yang, L. Li, Y. Xiong, J. Li, H. Zhou, C. Su, *Chem. Asian J.* **2010**, *5*, 2358; b) J. Cheng, S. Zheng, G. Yang, *Inorg. Chem.* **2007**, *46*, 10261; c) M. Higuchi, K. Nakamura, S. Horike, Y. Hijikata, N. Yanai, T. Fukushima, J. Kim, K. Kato, M. Takata, D. Watanaba, S. Oshima, S. Kitagawa, *Angew. Chem. Int. Ed.* **2012**, *51*, 8369; d) O. Z. Yesxilel, G. Günay, C. Darcan, M. S. Soylu, S. Keskind, S. W. Ng, *CrystEngComm.* **2012**, *14*, 2817; e) T. K. Maji, S. Pal, K. L Gurunatha, A. Govindaraj, C. N. R. Rao, *Dalton Trans.* **2009**, 4426.

[7] a) J. L. C. Rowsell,O. M. Yaghi, *Microporous Mesoporous Mater.* **2004**, *73*, 3; b) W. Lu, Z. Wei, Z.-Y. Gu, T.-F. Liu, J. Park, J. Park, J. Tian, M. Zhang, Q. Zhang, T. Gentle Iii, M. Bosch, H.-C. Zhou, *Chem. Soc. Rev.* **2014**, *43*, 5561; c) A. G. Wong-Foy, A. J. Matzger, O. M. Yaghi, *J. Am. Chem. Soc.* **2006**, *128*, 3494; d) M. Eddaoudi, J. Kim, N. Rosi, D. Vodak, J. Wachter, M. O'Keeffe, O. M. Yaghi, *Science* **2002**, *295*, 469.

[8] a) G. Ferey, C. Mellot-Draznieks, C. Serre, F. Millange, J. Dutour, S. Surble, I. Margiolaki, *Science* **2005**, *309*, 2040; b) G. Ferey, *Chem. Soc. Rev.* **2008**, *37*, 191; c) F. Millange, C. Serre, G. Ferey, *Chem. Commun.* **2002**, 822; d) C. Serre, F. Millange, C. Thouvenot, M. Noguès, G. Marsolier, D. Louër, G. Férey, *J. Am. Chem. Soc.* **2002**, *124*, 13519.

[9] K. S. Park, Z. Ni, A. P. Côté, J. Y. Choi, R. Huang, F. J. Uribe-Romo, H. K. Chae, M. O'Keeffe, O. M. Yaghi, *Proc. Natl. Acad. Sci.* U. S. A. **2006**, *103*, 10186.

[10] a) O. K. Farha, I. Eryazici, N. C. Jeong, B. G. Hauser, C. E. Wilmer, A. A. Sarjeant, Q. Snurr, S. T. Nguyen, A. Ö. Yazaydın, J. T. Hupp, *J. Am. Chem. Soc*. **2012**, *134*, 15016; b) H. K. Chae, D. Y. Siberio-Perez, J. Kim, Y. Go, M. Eddaoudi, A. J. Matzger, M. O'Keeffe, O. M. Yaghi, *Nature* **2004**, *427*, 523; c) G. Férey, C. Mellot-Draznieks, C. Serre, F. Millange, J. Dutour, S. Surble, I. Margiolaki, *Science.* **2005**, *309*, 2040; d) K. Koh, A. G. Wong-Foy, A. J. Matzger, *J. Am. Chem. Soc*. **2009**, *131*, 4184; e) H. Furukawa, N. Ko, Y. B. Go, N. Aratani, S. B. Choi, E. Choi, A. O. Yazaydin, R. Q. Snurr, M. O'Keeffe, J. Kim, O. M. Yaghi, *Science* **2010**, *329*, 424.

[11] a) A. Carne, C. Carbonell, I. Imaz, D. Maspoch, *Chem. Soc. Rev.* **2011**, *40*, 291; b) J. Della Rocca, D. Liu, W. Lin, *Acc. Chem. Res.* **2011**, *44*, 957.

[12] a) S. Vaucher, M. Li, S. Mann, *Angew. Chem. Int. Ed.* **2000**, *39*, 1793; b) K. M. L. Taylor, W. J. Rieter, W. Lin, *J. Am. Chem. Soc.* **2008**, *130*, 14358; c) A. Carné-Sánchez, I. Imaz, M. Cano-Sarabia, D. Maspoch, *Nat. Chem.* **2013**, *5*, 203.

[13] a) T. Tsuruoka, S. Furukawa, Y. Takashima, K. Yoshida, S. Isoda, S. Kitagawa, *Angew. Chem. Int. Ed.* **2009**, *48*, 4739; b) A. Umemura, S. Diring, S. Furukawa, H. Uehara, T. Tsuruoka, S. Kitagawa, *J. Am. Chem. Soc.* **2011**, *133*, 15506; c) H. Guo, Y. Zhu, S. Wang, S. Su, L. Zhou, H. Zhang, *Chem. Mater.* **2012**, *24*, 444; d) P. Horcajada, T. Chalati, C. Serre, B. Gillet, C. Sebrie, T. Baati, J. F. Eubank, D. Heurtaux, P. Clayette, C. Kreuz, J.-S. Chang, Y. K. Hwang, V. Marsaud, P.-N. Bories, L. Cynober, S. Gil, G. Ferey, P. Couvreur, R. Gref, *Nat. Mater.* **2010**, *9*, 172; e) Z. Ni, R. I. Masel, *J. Am. Chem. Soc.* **2006**, *128*, 12394; f) W.-J. Son, J. Kim, J. Kim, W.-S. Ahn, *Chem. Commun.* **2008**, 6336; g) X. Sun, S. Dong, E. Wang, *J. Am. Chem. Soc.* **2005**, *127*, 13102; h) M. Oh, C. A. Mirkin, *Nature* **2005**, *438*, 651.

[14] a) H. Lee, L. J. Kepley, H. G. Hong, T. E. Mallouk, *J. Am. Chem. Soc*. **1988**, *110*, 618; b) B. Liu, O. Shekhah, H. K. Arslan, J. Liu, C. Wöll, R. A. Fischer, *Angew. Chem. Int. Ed.* **2012**, *51*, 807; c) O. Shekhah, H. Wang, M. Paradinas, C. Ocal, B. Schupbach, A. Terfort, D. Zacher, R. A. Fischer, C. Woll, *Nat. Mater.* **2009**, *8*, 481; d) Y.-S. Li, F.-Y. Liang, H. Bux, A. Feldhoff, W.-S. Yang, J. Caro, *Angew. Chem. Int. Ed.* **2010**, *49*, 548.

[15] a) O. K. Farha, A. Ö. Yaza -ydın, I. Eryazici, C. D. Malliakas, B. G. Hauser, M. G. Kanatzidis, S. T. Nguyen, R. Q. Snurr, J. T. Hupp, *Nat. Chem*. **2010**, *2*, 944; b) X.-S. Wang, S. Ma, P. M. Forster, D. Yuan, J. Eckert, J. J. Lopez, B. J. Murphy, J. B. Parise, H.-C. Zhou, *Angew. Chem. Int. Ed*. **2008**, *47*, 7263; c) A. G. Wong-Foy, A. J. Matzger, O. M. Yaghi, *J. Am. Chem. Soc*. **2006**, *128*, 3494; d) P. Nugent, Y. Belmabkhout, S. D. Burd, A. J. Cairns, R. Luebke, K. Forrest, T. Pham, S. Ma, B. Space, L. Wojtas, M. Eddaoudi, M. J. Zaworotko, *Nature* **2013**, *495*, 80.

[16] a) L. Alaerts, E. Séguin, H. Poelman, F. Thibault-Starzyk, P. A. Jacobs, D. De Vos, *Chem.–Eur. J.* **2006**, *12*, 7353; b) S. Hasegawa, S. Horike, R. Matsuda, S. Furukawa, K. Mochizuki, Y. Kinoshita, S. Kitagawa, *J. Am. Chem. Soc*. **2007**, *129*, 2607.

[17] a) N. Sikdar, A. Hazra, T. K. Maji, *Inorg. Chem.* **2014**, *53*, 5993; b) D. Tanaka, A. Henke, K. Albrecht, M. Moeller, K. Nakagawa, S. Kitagawa, J. Groll, *Nat. Chem.* **2010**, *2*, 410; c) W. Cho, H. J. Lee, M. Oh, *J. Am. Chem. Soc.* **2008**, *130*, 16943.

[18] a) S. Mohapatra, S. Adhikari, H. Riju, T. K. Maji, *Inorg. Chem.* **2012**, *51*, 4891; b) B. Chen, Y. Yang, F. Zapata, G. Lin, G. Qian, E. B. Lobkovsky, *Adv. Mater.* **2007**, *19*, 1693.

[19] a) Y. Takashima, V. M. Martinez, S. Furukawa, M. Kondo, S. Shimomura, H. Uehara, M. Nakahama, K. Sugimoto, S. Kitagawa, *Nat. Commun.* **2011**, *2*, 168; b) K. Jayaramulu, P. Kanoo, S. J. George, T. K. Maji, *Chem. Commun*. **2010**, *46*, 7906.

[20] a) G. D. Scholes, G. R. Fleming, A. Olaya-Castro, R. van Grondelle, *Nat. Chem.* **2011**, *3*, 763; b) G. Calzaferri, K. Lutkouskaya, *Photochem. Photobiol. Sci.* **2008**, *7*, 879; c) M. Kozaki, A. Uetomo, S. Suzuki, K. Okada, *Org. Lett.* **2008**, *10*, 4477; d) C. Devadoss, P. Bharathi, J. S. Moore, *J. Am. Chem. Soc.* **1996**, *118*, 9635; e) T. Shu, J. Wu, M. Lu, L. Chen, T. Yi, F. Li, C. Huang, *J. Mater. Chem.* **2008**, *18*, 886; f) K. V. Rao, K. K. R. Datta, M. Eswaramoorthy, S. J. George, *Chem. Eur. J.* **2012**, *18*, 2184.

[21] a) C. N. Fleming, K. A. Maxwell, J. M. DeSimone, T. J. Meyer, J. M. Papanikolas, *J. Am. Chem. Soc.* **2001**, *123*, 10336; b) H.-J. Son, S. Jin, S. Patwardhan, S. J. Wezenberg, N. C. Jeong, M. So, C. E. Wilmer, A. A. Sarjeant, G. C. Schatz, R. Q. Snurr, O. K. Farha, G. P. Wiederrecht, J. T. Hupp, *J. Am. Chem. Soc.* **2013**, *135*, 862.

[22] a) C. Y. Lee, O. K. Farha, B. J. Hong, A. A. Sarjeant, S. T. Nguyen, J. T. Hupp, *J. Am. Chem. Soc.* **2011**, *133*, 15858; b) S. Jin, H. Son, O. K. Farha, G. P. Wiederrecht, J. T. Hupp, *J. Am. Chem. Soc*. **2013**, *135*, 955; c) H.-J. Son, S. Jin, S. Patwardhan, S. J. Wezenberg, N. C. Jeong, M. So, C. E. Wilmer, A. A. Sarjeant, G. C. Schatz, R. Q. Snurr, O. K. Farha, G. P. Wiederrecht, J. T. Hupp, *J. Am. Chem. Soc.* **2013**, *135*, 862.

[23] a) C. A. Kent, D. Liu, L. Ma, J. M. Papanikolas, T. J. Meyer, W. Lin, *J. Am. Chem. Soc*. **2011**, *133*, 12940; b) X. Zhang, M. A. Ballem, Z.-J. Hu, P. Bergman, K. Uvdal, *Angew. Chem. Int. Ed.* **2011**, *50*, 5729; c) X. Zhang, M. A. Ballem, M. Ahrén, A. Suska, P. Bergman, K. Uvdal, *J. Am. Chem. Soc.* **2010**, *132*, 10391.

[24] a) W. J. Rieter, K. M. Pott, K. M. L. Taylor, W. Lin, *J. Am. Chem. Soc.* **2008**, *130*, 11584; b) K. M. L. Taylor-Pashow, J. D. Rocca, Z. Xie, S. Tran, W. Lin, *J. Am. Chem. Soc.* **2009**, *131*, 14261; c) P. Horcajada, T. Chalati, C. Serre, B. Gillet, C. Sebrie, T. Baati, J. F. Eubank, D. Heurtaux, P. Clayette, C. Kreuz, J.-S. Chang, Y. K. Hwang, V. Marsaud, P.-N. Bories, L. Cynober, S. Gil, G. Ferey, P. Couvreur, R. Gref, *Nat. Mater*. **2010**, *9*, 172.

[25] a) W. J. Rieter, K. M. L. Taylor, H. An, W. Lin, W. Lin, *J. Am. Chem. Soc.* **2006**, *128*, 9024; b) K. M. L. Taylor, A. Jin, W. Lin, *Angew. Chem. Int. Ed.* **2008**, *47*, 7722.

[26] a) V. Valtchev, L. Tosheva, *Chem. Rev.* **2013**, *113*, 6734; b) W. J. Roth, P. Nachtigall, R. E. Morris, J. Čejka, *Chem. Rev.* **2014**, *114*, 4807; (c) T. Sun, K. Seff, *Chem. Rev.* **1994**, *94*, 857; d) X. Meng,F.-S. Xiao, *Chem. Rev.* **2014**, *114*, 1521; e) P. Yang, S. Gai, J. Lin, *Chem. Soc. Rev.* **2012**, *41*, 3679; f) J. R. Long, O. M. Yaghi, *Chem. Soc. Rev.* **2009**, *38*, 1213; g) A. U. Czaja, N. Trukhan, U. Muller, *Chem. Soc. Rev.* **2009**, *38*, 1284; h) S. L. James, *Chem. Soc. Rev.* **2003**, *32*, 276; i) J.-R. Li, R. J. Kuppler, H.-C. Zhou, *Chem. Soc. Rev.* **2009**, *38*, 1477; j) M. Meilikhov, K. Yusenko, D. Esken, S. Turner, G. Van Tendeloo, R. A. Fischer, *Eur. J. Inorg. Chem.* **2010**, 3701; k) M. Mueller, A. Devaux, C.-H. Yang, L. De Cola, R. A. Fischer, *Photochem. Photobiol. Sci.* **2010**, *9*, 846; l) D. Tanaka, A. Henke, K. Albrecht, M. Moeller, K. Nakagawa, S. Kitagawa, J. Groll, *Nat. Chem.* **2010**, *2*, 410;

[27] a) N. Fontanals, R. M. Marce, F. Borrull, P. Cormack, *Polym. Chem.* **2015**, *6*, 7231; b) M.-L. Chen, Y.-L. Liu, X.-W. Xing, X. Zhou, Y.-Q. Feng, B.-F. Yuan, *Chem. Eur. J.* **2013**, *19*, 1035; c) J. Zhang, Z.-A. Qiao, S. M. Mahurin, X. Jiang, S.-H. Chai, H. Lu, K. Nelson, S. Dai, *Angew. Chem. Int. Ed.* **2015**, *54*, 4582; d) Y. Luo, B. Li, W. Wang, K. Wu, B. Tan, *Adv. Mater.* **2012**, *24*, 5703; e) J. Urban, F. Svec, J. M. J. Fréchet, *J. Chromatogr. A* **2010**, *1217*, 8212.

[28] a) A. Thomas, *Angew. Chem. Int. Ed.* **2010**, *49*, 8328; b) T. A. Makal, J.-R. Li, W. Lu, H.-C. Zhou, *Chem. Soc. Rev.* **2012**, *41*, 7761; b) A. Modak, M. Nandi, J. Mondal, A. Bhaumik,

Chem. Commun. **2012**, *48*, 248; c) X. Zou, H. Ren, G. Zhu, *Chem. Commun.* **2013**, *49*, 3925; d) X. Zhu, C. Tian, T. Jin, J. Wang, S. M. Mahurin, W. Mei, Y. Xiong, J. Hu, X. Feng, H. Liu, S. Dai, *Chem. Commun.* **2014**, *50*, 15055; e) Y. Zhao, X. Liu, Y. Han, *RSC Adv.* **2015**, *5*, 30310; f) P. Kaur, J. T. Hupp, S. T. Nguyen, *ACS Catal.* **2011**, *1*, 819; f) Y. Zhang, S. N. Riduan, *Chem. Soc. Rev.* **2012**, *41*, 2083; g) S. Chakraborty,Y. J. Colon,R. Q. Snurr,S. T. Nguyen, *Chem. Sci.* **2015**, *6*, 384; h) A. Trewin,A. I. Cooper, *Angew. Chem. Int. Ed.* **2010**, *49*, 1533.

[29] a)Y. Xu, S. Jin, H. Xu, A. Nagai, D. Jiang, *Chem. Soc. Rev.* **2013**, *42*, 8012; b) A. I. Cooper, *Adv. Mater.* **2009**, *21*, 1291; c) J.-X. Jiang, F. Su, A. Trewin, C. D. Wood, H. Niu, J. T. A. Jones, Y. Z. Khimyak, A. I. Cooper, *J. Am. Chem. Soc.* **2008**, *130*, 7710; d) Q. Liu, Z. Tang, M. Wu, Z. Zhou, *Polym. Int.* **2014**, *63*, 381; e) N. B. McKeown, B. Gahnem, K. J. Msayib, P. M. Budd, C. E. Tattershall, K. Mahmood, S. Tan, D. Book, H. W. Langmi, A. Walton, *Angew. Chem. Int. Ed.* **2006**, *45*, 1804.

[30] a) N. B. McKeown, P. M. Budd, *Chem. Soc. Rev.* **2006**, *35*, 675; b) N. B. McKeown, P. M. Budd, *Macromolecules* **2010**, *43*, 5163; c) A. Del Regno, A. Gonciaruk, L. Leay, M. Carta, M. Croad, R. Malpass-Evans, N. B. McKeown, F. R. Siperstein, *Ind. Eng. Chem. Res.* **2013**, *52*, 16939; d) N. Du, G. P. Robertson, I. Pinnau, M. D. Guiver, *Macromolecules* **2010**, *43*, 8580; e) N. Du, H. B. Park, G. P. Robertson, M. M. Dal-Cin, T. Visser, L. Scoles, M. D. Guiver, *Nat. Mater.* **2011**, *10*, 372.

[31] a) H. A. Patel, S. Hyun Je, J. Park, D. P. Chen, Y. Jung, C. T. Yavuz, A. Coskun, *Nat. Commun.* **2013**, *4*, 1357; b) H. A. Patel, F. Karadas, A. Canlier, J. Park, E. Deniz, Y. Jung, M. Atilhan, C. T. Yavuz, *J. Mater. Chem.* **2012**, *22*, 8431; c) Z. Xiang, X. Zhou, C. Zhou, S. Zhong, X. He, C. Qin, D. Cao, *J. Mater. Chem.* **2012**, *22*, 22663; d) J. Byun, S.-H. Je, H. A. Patel, A. Coskun, C. T. Yavuz, *J. Mater. Chem. A* **2014**, *2*, 12507.

[32] P. Katekomol, J. Roeser, M. Bojdys, J. Weber, A. Thomas, *Chem. Mater.* **2013**, *25*, 1542; b) X. Jiang, P. Wang, J. Zhao, *J. Mater. Chem. A* **2015**, *3*, 7750; c) S. Hug, M. B. Mesch, H. Oh, N. Popp, M. Hirscher, J. Senker, B. V. Lotsch, *J. Mater. Chem. A* **2014**, *2*, 5928; d) P. Kuhn, M. Antonietti, A. Thomas, *Angew. Chem. Int. Ed.* **2008**, *47*, 3450; e) K. Kamiya, R. Kamai, K. Hashimoto, S. Nakanishi, *Nat. Commun.* **2014**, *5*, 5040; f) J. Liu, E. Zong, H. Fu, S. Zheng, Z. Xu, D. Zhu, *J. Colloid Interface Sci.* **2012**, *372*, 99.

[33] a) A. P. Côté, A. I. Benin, N. W. Ockwig, M. O'Keeffe, A. J. Matzger, O. M. Yaghi, *Science* **2005**, *310*, 1166; b) Q. Fang, Z. Zhuang, S. Gu, R. B. Kaspar, J. Zheng, J. Wang, S. Qiu, Y. Yan, *Nat. Commun.* **2014**, *5*, 4503; c) H. Xu, D. Jiang, *Nat. Chem.* **2014**, *6*, 564; d) B. Yang, J. Björk, H. Lin, X. Zhang, H. Zhang, Y. Li, J. Fan, Q. Li, L. Chi, *J. Am. Chem. Soc.* **2015**, *137*, 4904; e) A. I. Cooper, *CrystEngComm* **2013**, *15*, 1483; f) X. Feng, X. Ding, D. Jiang, *Chem. Soc. Rev.* **2012**, *41*, 6010; g) S.-Y. Ding, W. Wang, *Chem. Soc. Rev.* **2013**, *42*, 548; h)Y.-B. Zhang, J. Su, H. Furukawa, Y. Yun, F. Gándara, A. Duong, X. Zou, O. M. Yaghi, *J. Am. Chem. Soc.* **2013**, *135*, 16336.

[34] J.-X. Jiang, F. Su, A. Trewin, C. D. Wood, N. L. Campbell, H. Niu, C. Dickinson, A. Y. Ganin, M. J. Rosseinsky, Y. Z. Khimyak, A. I. Cooper, *Angew. Chem.* **2007**, *119*, 8728.

[35] a) J.-X. Jiang, F. Su, A. Trewin, C. D. Wood, H. Niu, J. T. A. Jones, Y. Z. Khimyak, A. I. Cooper, *J. Am. Chem. Soc.* **2008**, *130*, 7710; b) Q. Chen, D.-P. Liu, J.-H. Zhu, B.-H. Han, *Macromolecules* **2014**, *47*, 5926; c) J.-X. Jiang, A. Trewin, F. Su, C. D. Wood, H. Niu, J. T. A. Jones, Y. Z. Khimyak, A. I. Cooper, *Macromolecules* **2009**, *42*, 2658; d) R. Dawson, A. Laybourn, Y. Z. Khimyak, D. J. Adams, A. I. Cooper, *Macromolecules* **2010**, *43*, 8524; e) X. Wang, Y. Zhao, L. Wei, C. Zhang, J.-X. Jiang, *J. Mater. Chem. A* **2015**, *3*, 21185.

[36] a) C. D. Wood, B. Tan, A. Trewin, H. Niu, D. Bradshaw, M. J. Rosseinsky, Y. Z. Khimyak, N. L. Campbell, R. Kirk, E. Stöckel, A. I. Cooper, *Chem. Mater.* **2007**, *19*, 2034; b) A. Li, R.-F. Lu, Y. Wang, X. Wang, K.-L. Han, W.-Q. Deng, *Angew. Chem. Int. Ed.* **2010**, *49*, 3330; c) C. D. Wood, B. Tan, A. Trewin, F. Su, M. J. Rosseinsky, D. Bradshaw, Y. Sun, L. Zhou, A. I. Cooper, *Adv. Mater.* **2008**, *20*, 1916; d) D. Yuan, W. Lu, D. Zhao, H.-C. Zhou, *Adv. Mater.* **2011**, *23*, 3723.

[37] a) R. Dawson, D. J. Adams, A. I. Cooper, *Chem. Sci.* **2011**, *2*, 1173; b) K. V. Rao, S. Mohapatra, C. Kulkarni, T. K. Maji, S. J. George, *J. Mater. Chem.* **2011**, *21*, 12958.

[38] a) S. Qiao, W. Huang, Z. Du, X. Chen, F.-K. Shieh, R. Yang, *New J. Chem.* **2015**, *39*, 136; b) Y. Xie, T.-T. Wang, X.-H. Liu, K. Zou, W.-Q. Deng, *Nat. Commun.* **2013**, *4*, 1960; c) X. Liu, Y. Xu, Z. Guo, A. Nagai, D. Jiang, *Chem. Commun.* **2013**, *49*, 3233.

[39] G. Cheng,T. Hasell,A. Trewin,D. J. Adams,A. I. Cooper, *Angew. Chem. Int. Ed.* **2012**, *51*, 12727.

[40] a) Y. Xu, L. Chen, Z. Guo, A. Nagai, D. Jiang, *J. Am. Chem. Soc.* **2011**, *133*, 17622; b) H. Bildirir, J. P. Paraknowitsch, A. Thomas, *Chem. Eur. J.* **2014**, *20*, 9543; c) X. Liu, Y. Zhang, H. Li, A. Sigen, H. Xia, Y. Mu, *RSC Adv.* **2013**, *3*, 21267; d) J.-X. Jiang, A. Trewin, D. J. Adams, A. I. Cooper, *Chem. Sci.* **2011**, *2*, 1777.

[41] a) Y. Xu, A. Nagai, D. Jiang, *Chem. Commun.* **2013**, *49*, 1591; b) Q. Chen, J.-X. Wang, F. Yang, D. Zhou, N. Bian, X.-J. Zhang, C.-G. Yan, B.-H. Han, *J. Mater. Chem.* **2011**, *21*, 13554; c) J. Brandt, J. Schmidt, A. Thomas, J. D. Epping, J. Weber, *Polym. Chem.* **2011**, *2*, 1950; d) X. Liu, Y. Xu, D. Jiang, *J. Am. Chem. Soc.* **2012**, *134*, 8738.

[42] a) C. Gu, N. Huang, J. Gao, F. Xu, Y. Xu, D. Jiang, *Angew. Chem. Int. Ed.* **2014**, *53*, 4850; b) Y. Zhang, S. A,Y. Zou, X. Luo, Z. Li, H. Xia, X. Liu, Y. Mu, *J. Mater. Chem. A* **2014**, *2*, 13422; c) L. Xiang, Y. Zhu, S. Gu, D. Chen, X. Fu, Y. Zhang, G. Yu, C. Pan, Y. Hu, *Macromol. Rapid Commun.* **2015**, *36*, 1566; d) L. Chen, Y. Honsho, S. Seki, D. Jiang, *J. Am. Chem. Soc.* **2010**, *132*, 6742; e) C. Gu, N. Huang, F. Xu, J. Gao, D. Jiang, *Sci. Rep.* **2015**, *5*, 8867.

[43] a) J.-X. Jiang, C. Wang, A. Laybourn, T. Hasell, R. Clowes, Y. Z. Khimyak, J. Xiao, S. J. Higgins, D. J. Adams, A. I. Cooper, *Angew. Chem. Int. Ed.* **2011**, *50*, 1072; b) S. Fischer, J. Schmidt, P. Strauch, A. Thomas, *Angew. Chem. Int. Ed.* **2013**, *52*, 12174.

[44] a) K. Zhang, D. Kopetzki, P. H. Seeberger, M. Antonietti, F. Vilela, *Angew. Chem. Int. Ed.* **2013**, *52*, 1432; b) X. Ding, B.-H. Han, *Angew. Chem. Int. Ed.* **2015**, *54*, 6536; c) Z. J. Wang, S. Ghasimi, K. Landfester, K. A. I. Zhang, *Adv. Mater.* **2015**, DOI: 10.1002/adma.201502735; d) J.-X. Jiang, Y. Li, X. Wu, J. Xiao, D. J. Adams, A. I. Cooper, *Macromolecules* **2013**, *46*, 8779.

[45] a) G. D. Scholes, G. R. Fleming, A. Olaya-Castro, R. van Grondelle, *Nat. Chem.* **2011**, *3*, 763; b) N. Aratani, D. Kim, A. Osuka, *Acc. Chem. Res.* **2009**, *42*, 1922; c) Y. Ma, X. Wang, Y. Jia, X. Chen, H. Han, C. Li, *Chem. Rev.* **2014**, *114*, 9987; d) Y. K. Kho, A. Iwase, W. Y. Teoh, L. Mädler, A. Kudo, R. Amal, *J. Phys. Chem. C* **2010**, *114*, 2821; (e) R. Li, Y. Weng, X. Zhou, X. Wang, Y. Mi, R. Chong, H. Han, C. Li, *Energy Environ. Sci.* **2015**, *8*, 2377.

[46] a) F. Yang, M. Lublow, S. Orthmann, C. Merschjann, T. Tyborski, M. Rusu, S. Kubala, A. Thomas, R. Arrigo, M. Hävecker, T. Schedel-Niedrig, *ChemSusChem* **2012**, *5*, 1227; b) X.-H. Li, J. Zhang, X. Chen, A. Fischer, A. Thomas, M. Antonietti, X. Wang, *Chem. Mater.* **2011**, *23*, 4344; c) D. Hollmann, M. Karnahl, S. Tschierlei, K. Kailasam, M. Schneider, J. Radnik, K. Grabow, U. Bentrup, H. Junge, M. Beller, S. Lochbrunner, A. Thomas, A. Brückner, *Chem. Mater.* **2014**, *26*, 1727; d) V. W.-h. Lau, M. B. Mesch, V. Duppel, V.

Blum, J. Senker, B. V. Lotsch, *J. Am. Chem. Soc.* **2015**, *137*, 1064; e) K. Kailasam, J. Schmidt, H. Bildirir, G. Zhang, S. Blechert, X. Wang, A. Thomas, *Macromol. Rapid Commun.* **2013**, *34*, 1008; f) K. Schwinghammer, S. Hug, M. B. Mesch, J. Senker, B. V. Lotsch, *Energy Environ. Sci.* **2015**, *8*, 3345; g) V. S. Vyas, F. Haase, L. Stegbauer, G. Savasci, F. Podjaski, C. Ochsenfeld, B. V. Lotsch, *Nat. Commun.* **2015**, *6*, 8508.

[47] R. S. Sprick, J.-X. Jiang, B. Bonillo, S. Ren, T. Ratvijitvech, P. Guiglion, M. A. Zwijnenburg, D. J. Adams, A. I. Cooper, *J. Am. Chem. Soc.* **2015**, *137*, 3265.

Chapter 2A

MOF Nanovesicles and Toroids: Self-Assembled Porous Soft-hybrids for Light Harvesting

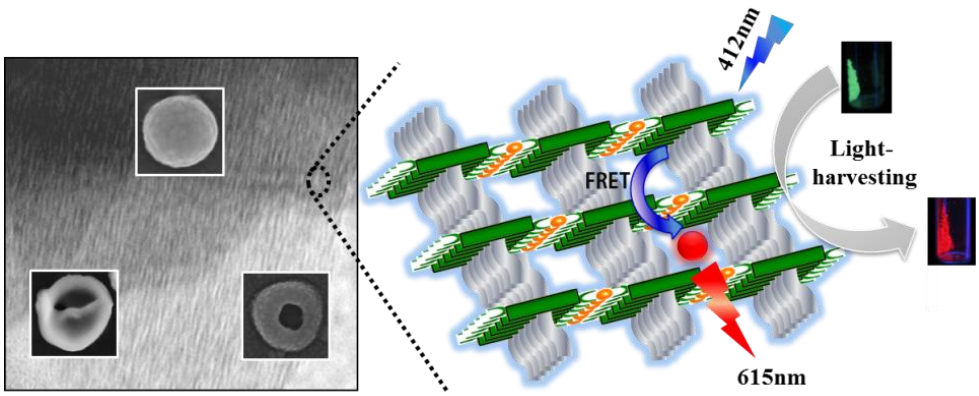

Summary

This chapter reports synthesis and characterization of metal-organic vesicular and toroid nanostructures of {Zn(OPE)·$2H_2O$} (**1**) obtained by coordination-directed self-assembly of oligo-(*p*-phenyleneethynylene)dicarboxylic acid (OPEA) as a linker with $Zn(OAc)_2$ by controlling the reaction parameters. Self-assembled nanostructures are characterized by powder X-ray diffraction, field emission scanning electron microscopy (FESEM), transmission electron microscopy (TEM), and adsorption study. The amphiphilic nature of the coordination-polymer with long alkyl chains renders different soft vesicular and toroidal nanostructures. The permanent porosity of the framework is established by gas adsorption study. Highly luminescent 3D porous framework is exploited for Förster's resonance energy transfer (FRET) by encapsulation of a suitable cationic dye (DSMP) which shows efficient funneling of excitation energy. These results demonstrate that dynamic and soft nature of the MOF, resulting in unprecedented vesicular and toroidal nanostructures with efficient light harvesting applications.

V. M. Suresh, S. J. George, T. K. Maji, *Adv. Funct. Mater.* **2013**, *23*, 5585. ***(This work has been highlighted on the Back Cover Page of the journal and Hot Article)***

2A.1 Introduction

Metal-organic frameworks (MOFs), an interesting class of inorganic-organic hybrid porous materials,[1] showed promising applications in different fields including gas storage, separation, catalysis, sensors and drug delivery.[2] Multi-functional luminescent MOFs with a chromophoric linker combined with permanent porosity are gaining attention,[3] and are attractive candidates for optoelectronics too.[4] However, the solution processability of these hybrid frameworks is one of the critical features to be addressed for the advancement of this field. In this context, nanoscale MOFs (NMOFs), are an exciting class of tunable and modular soft-hybrids with unprecedented processable nature.[5] These soft luminescent porous hybrids would show guest dependent emission either via energy-transfer or through the formation of intermolecular complexes such as excimer or exciplex and, hence, are striking materials for sensor or energy-transfer applications.[6] Recently, light-harvesting organic-inorganic hybrids have gathered immense attention as transparent luminescent materials.[7] Although, various organic assemblies have been well-studied for light-harvesting applications,[8] they often exhibit fluorescence quenching due to intermolecular interactions, either in the self-assembled state or on solid-substrates. In this context, the nanoscale periodicity of the inorganic components in the hybrid design would help for the spatial organization of organic donor and acceptor chromophores, thereby minimizing the inter-chromophoric interactions to enhance the luminescence quantum yield. With this objective, several elegant designs based on zeolites,[9] ordered mesoporous organosilica (PMO),[10] and clay composites [11] have been reported as efficient light-harvesting hybrids. We envision that the design of supramolecular MOF framework with fluorescent organic linkers will result in luminescent inorganic-organic soft-hybrids with dynamic feature of being able to change their structure according to the external stimuli. The dynamic nature of the framework would provide a pathway for modulating their nanostructure morphology and for the guest encapsulation.[12] Moreover, these self-assembled soft-hybrids would act as efficient light-harvesting scaffolds for non-covalently entrapped dye molecules and will have processable features for luminescent device applications. With this objective, we have carried out the coordination-assisted self-assembly of oligo-(*p*-phenyleneethynylene) dicarboxylic acid (OPEA), with solubilizing side chains. Although OPE derivatives are well studied from organic assembly point of view for optoelectronic functions,[13] their coordination assisted self-assembly have not yet been studied. Crystalline NMOFs of

different morphologies like sphere, cube, rod, hollow sphere have been reported.[14] However, the nano-architectures with vesicular or toroidal morphologies are yet to be realized in metal-organic framework systems. This chapter report synthesis and characterization of unprecedented MOF nanostructures, such as vesicles and toroids, achieved by the coordination-assisted self-assembly of OPEA with Zn^{II} metal ion. These porous soft-hybrids can funnel the excitation energy to appropriate acceptor molecule, and hence acts as an efficient light harvesting antenna.

2A.2 Experimental section

2A.2.1 Materials

Tetrakis(triphenylphosphine)palladium(0), copper iodide (CuI) and $Zn(OAc)_2 \cdot 2H_2O$ were purchased from Sigma-Aldrich Chemical Co. Required solvents were dried prior to use. Oligo-(*p*-phenyleneethynylene)dicarboxylic acid (OPEA) is synthesized according to the literature procedures.[15]

2A.2.2 Physical measurements

The elemental analyses were carried out using a Thermo Scientific Flash 2000 CHN analyzer. Infrared spectral studies were done by making samples with KBr pellets using Bruker FT-IR spectrometer. Thermal stability of the coordination polymer is analysed using Mettler Toledo TGA 850 instrument under inert atmosphere in the temperature range of 30-800 °C at the heating rate of 3 °C per min. Powder X-ray diffraction studies in different state of the samples were recorded on a Bruker D8 discover instrument using Cu-Kα radiation. Morphological studies have been carried out using Lica-S440I field emission scanning electron microscope (FESEM) by placing samples on a silicon wafer under high vacuum with an accelerating voltage of 10 kV. Transmission electron microscopy (TEM) analysis has been performed using JEOL JEM-3010 with an accelerating voltage at 300 kV. For this analysis NMOF dispersed in ethanol by sonication before drop casting on a carbon-coated copper grid. Porosity measurements were carried out using QUNATACHROME QUADRASORD-SI analyser at 77 K for N_2 and 195 K for CO_2. Fluorescence studies were accomplished using Perkin Elmer Ls 55 Luminescence spectrometer. ^{1}H NMR is recorded on a Bruker AV-400 spectrometer with chemical shifts reported as ppm (in DCl with TMS as internal standard).

2A.2.3 Synthesis of {Zn(OPE)·2H$_2$O} (1)

$Zn(OAc)_2 \cdot 2H_2O$ (1eq) is dissolved in 5 mL THF and then drop-wise added to a

THF solution of OPE (1eq) under continuous stirring. The white colloids start forming within few minutes, and reaction was continued for further 6 h at room temperature. These white colloids were centrifuged, thoroughly washed with THF, and dried under vacuum for 6 h. Similar reactions have been performed for different time scale like 24, 32, 36 and 42 h. The resultant products were characterized by different techniques. Yield: 54%. Elemental analysis for $ZnC_{40}H_{48}O_8$. Calculated: C, 66.5; H, 6.69. Found: C, 64.4; H, 6.7. FTIR in KBr (cm^{-1}): 3441(br), 2925(sh), 2854(sh), 2208(w), 1602(vs), 1531(w), 1411(vs), 1280(w), 1216(sh), 1162(s), 1018(br), 862(w), 781(s).

2A.2.4 Preparation of {Zn(OPE)-DSMP} (2)

The desolvated ZnOPE (10 mg) was taken in 3 mL of dry THF and then *trans*-4-[4-(dimethylamino)styryl]-1-methylpyridinium iodide (DSMP) dye in dichloromethane (DCM) (2 mol %) is added. The resulting reaction mixture is stirred for 24 hours at room temperature. It was centrifuged and washed with DCM, THF several times and dried under vacuum at room temperature. The product was characterized by PXRD and ^{1}H-NMR.

2A.3 Results and discussion

2A.3.1 Structural characterization

The coordination polymer is prepared by mixing $Zn(OAc)_2{\cdot}2H_2O$ (1 mM) and OPEA (1 mM) in tetrahydrofuran (THF) (5 mL) solution at room temperature. Coordination of Zn^{II} ions to the carboxylate groups of the ligand is evident from the instantaneous formation of white colloids. The reaction is further continued for 6 h to yield a neutral coordination polymer with a molecular formula of $\{Zn(OPE){\cdot}2H_2O\}$ (**1**),

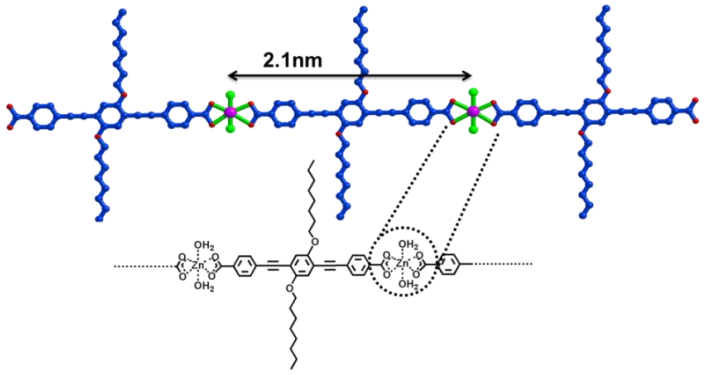

Scheme 1. Self-assembled 1D coordination chain of $\{Zn(OPE)(H_2O)_2\}$ (**1**), below: showing the coordination environment around Zn(II) and the chromophoric linker OPE.

calculated through elemental analysis, in which the OPE and metal ions are assembled in a 1:1 alternate fashion (Scheme 1). The presence of the metal ions in the coordination polymer is further confirmed by energy dispersive X-ray analysis (EDAX) (Figure 1). Fourier transform IR spectroscopy (FT-IR) shows strong peaks at 1602 cm^{-1} and 1411 cm^{-1}, characteristic of the carboxylate stretching frequency (Figure 2a), and $\Delta \approx 191$ cm^{-1} suggesting the bidentate coordination to Zn^{II} metal ions, as shown in Scheme 1. Interestingly, gas adsorption studies of **1** provided insights into the three dimensional (3D) self-organization of the coordination polymer **1** into a supramolecular porous

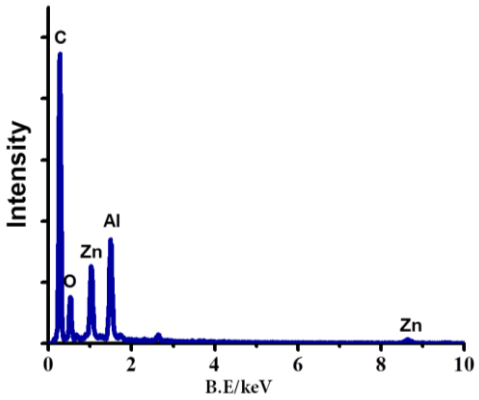

Figure 1. EDAX analysis of the {Zn(OPE)(H_2O)$_2$} (**1**) nanocolloids obtained after 6 hrs.

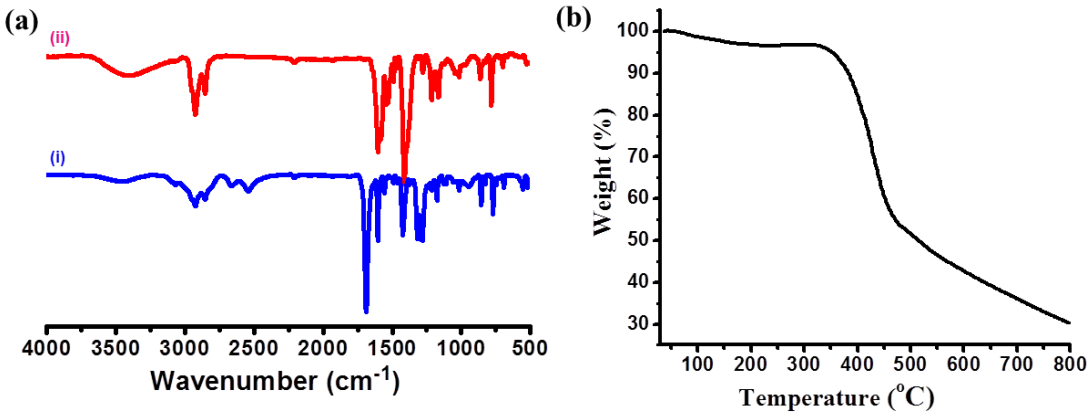

Figure 2. (a) FT-IR spectra of OPEA ligand (blue) and **1** (red), (b) TGA of **1** in the temperature range of 30-800 °C with a heating rate of 3 °C/min.

framework structure. Thermogravimetric analysis (TGA) of **1** (Figure 2b) shows an initial weight loss of 3.3% at 110 °C corresponding to the loss of coordinated water molecules, and the resulting desolvated framework is stable up to 350 °C. Hence, compound **1** was desolvated at 110 °C, before performing the adsorption measurements of N_2 (at 77 K) and CO_2 (at 195 K). Gas adsorption of the N_2 (kinetic diameter = 3.46 Å) at 77 K shows a

typical type II profile (Figure 3a) and the pore size distribution (NLDFT method) suggest the presence of both micro and meso pores (Figure 3b). Furthermore, CO_2 adsorption measurement of **1** shows a sharp uptake of CO_2 at low pressure regions, with a typical type I profile, unveiling the microporous nature of the framework (Figure 3c). The amount of the CO_2 uptake at the end point is found to be 48.6 mLg^{-1} suggesting 1.34 CO_2 molecules per formula unit and the corresponding Langmuir surface area is calculated to be 273 m^2g^{-1}. Powder X-ray diffraction (PXRD) measurements of **1** provided structural insights into the self-assembled framework. The PXRD pattern (Figure 3d) of **1** shows several peaks corresponding to the *d*-spacings of 21.01 Å, 12.52 Å and 4 Å. The intense low angle peak with a *d*-spacing of 21 Å is in agreement with the repeating distance between the two metal centers in the 1D coordination polymer chains (Scheme 1). The stacking of these 1D polymeric chains through π-π interactions is further evident from the presence of a diffraction peak with *d*-spacing value of 4 Å. We envisage that the presence of hydrophobic interactions arising from the alkyl chains leads to the three-dimensionally extended supramolecular framework, in which the π-stacked planes of the coordination polymer chains are connected via interdigitated alkyl chains. This is supported by the

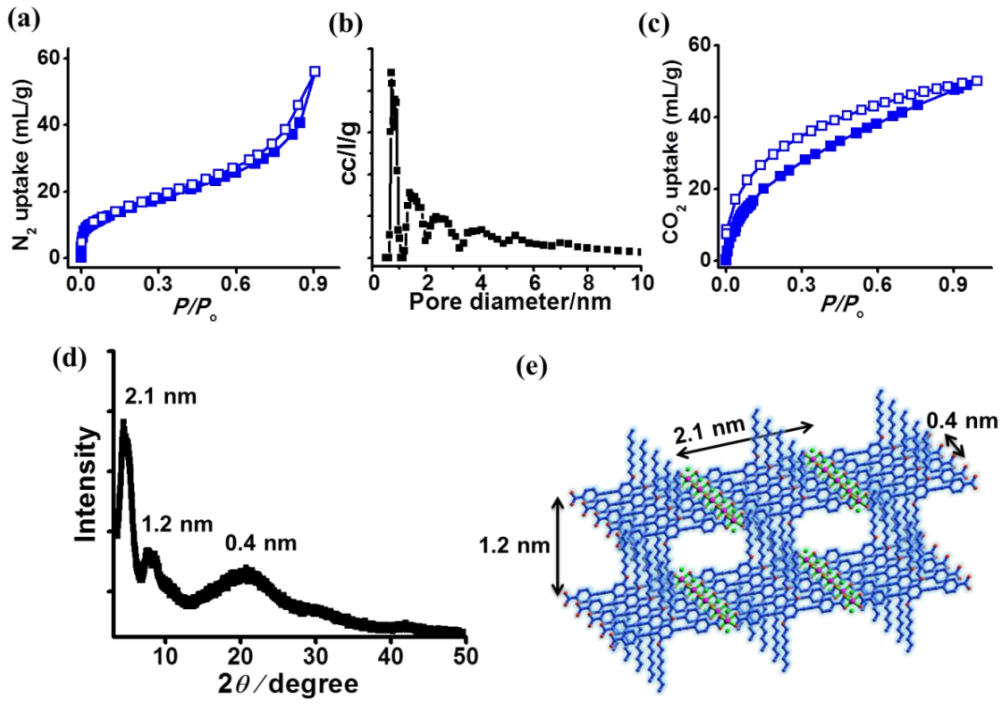

Figure 3. (a) N_2 (at 77 K), (b) CO_2 (at 195 K) adsorption isotherms for desolvated compound **1** and (c) pore-size distribution of **1** based on NLDFT method calculated from N_2 adsorption isotherm at 77 K. (d) PXRD pattern of **1**, and (e) schematic representation of the 3D supramolecular organization of **1** proposed based on the PXRD data.

presence of the peak at 7.73° corresponding to a *d*-spacing value of 1.2 nm, suggesting that alkyl chains are indeed interdigitated. A proposed model of this supramolecular framework structure is schematically shown in Figure 3e. Interestingly, the micropore dimensions calculated from the adsorption measurements (≈13 Å) is in agreement with the proposed interdigitated 3D structure. The mesoporosity observed in the N_2 adsorption measurements can be attributed to the inter-particle separation. The self-assembled structure of **1** was further investigated using various microscopic techniques (field emission scanning electron microscope (FESEM) and transmission electron microscope (TEM)). FESEM and TEM analyses of **1** showed clusters of small flaky particles having dimensions of 0.8-2 μm (Figures 4a-d). Interestingly, high-resolution TEM analysis at the edges of this particle showed a highly ordered structure, as evident from the regularly spaced dark lines with an interspacing distance of 0.8-1.1 nm (Figures 4e-h). The close agreement between the periodic spacing with that of the PXRD data suggests that, the dark lines corresponds to the π-stacked polymer chains, whereas the bright regions are filled with interdigitated alkyl chains of successive 2D sheets. We envisage that 1D coordination chains would exhibit an amphiphilic nature because of the presence of nonpolar flexible side chains and polar carboxylate groups attached to Zn^{II} ions. It is well known that the morphology of amphiphilic molecules can be controlled with structural modifications and thereby changing the polar-nonpolar ratio.[16] This provides an opportu-

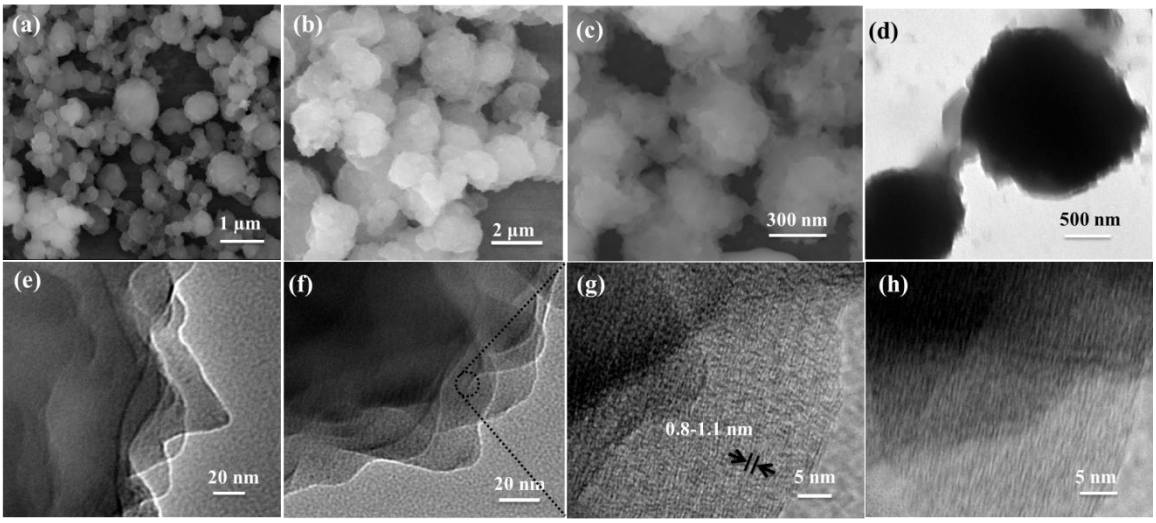

Figure 4. (a), (b) and (c) FESEM images of **1** obtained after 6 h reaction time showing the clusters of flaky particles. (d) TEM image of a clustered spherical particle and (e), (f) edges of the cluster. (g), (h) High resolution TEM image of **1** showing structural ordering of 1D coordination chains to a higher dimensional supramolecular organization through the interdigitation of alkyl chains.

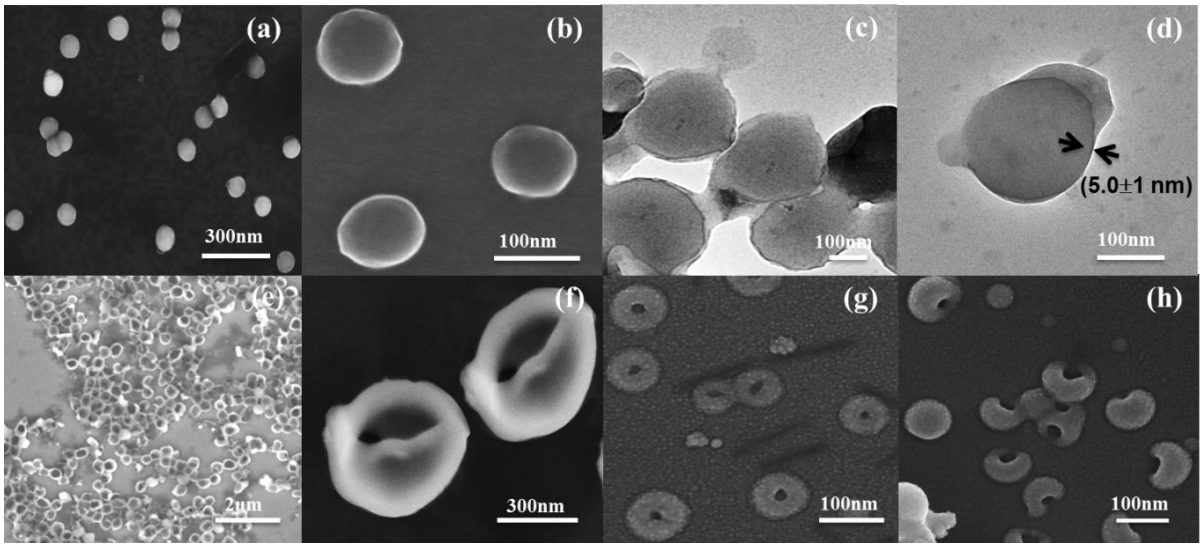

Figure 5. MOF Nanostructures: (a), (b) FESEM images of nanovesicles of **1**. (c) TEM images of nanovesicles. (d) TEM of nanovesicles at higher magnification showing light core and thick shell of thickness 5.0 ± 1 nm. FESEM images of (e) nanobowls, (f) open nanobowls, (g) toroids, and (h) hemispherical shapes.

-nity to modulate the nanostructure morphology of these hybrid assemblies in polar solvents by varying the reaction parameters, which would result in coordination-polymeric chains with different lengths. Furthermore, the noncovalent nature of the present framework would render dynamic nature to these hybrid assemblies to facilitate structural re-organization. In order to validate this proposal, we have varied the reaction time from 6 h to 24 h and analyzed the morphology at periodic intervals. Remarkably, hybrid flaky-nanoparticles transformed into spherical vesicular structures of 100-300 nm diameter upon continuing the reaction for 24 h, as evident from the FESEM analyses (Figures 5a, b). The formation of nanovesicles is further evident from the TEM analysis, which clearly showed the presence of spherical assemblies with dark shell and bright core (Figures 5c). Since the alkyl regions of these hybrid assemblies are more soluble in the reaction solvent THF, we believe that these nanostructures are inverse vesicles with alkyl chains projected to the exterior, as shown in the schematic representation (Figure 6). Detailed TEM analysis revealed a thickness of 5 ± 1 nm for the dark regions, which suggests that vesicular walls consists of 5 to 6 interdigitated layers of π-stacked polymeric chains (Figure 5d). In this context, thin films of layered MOF nanostructures have been recently documented for selective permeability and gas sensing applications.[17] Interestingly, further reaction up to 32-34 h, resulted in bowl, toroidal, and hemispherical shaped nanostructures of 100-300 nm in diameter, as evident from the FESEM (Figures

5e-h), TEM and AFM images (Figure 7). PXRD analyses showed that these nanostructures retains the same framework structure of the initial flaky particles (Figure 8), suggesting that changes in the length (degree of polymerization) and amphiphilic nature of coordination polymer chains drive the formation of these unprecedented hybrid nanostructures. To the best of our knowledge, this is the first report of MOF nanovesicles (or toroids).

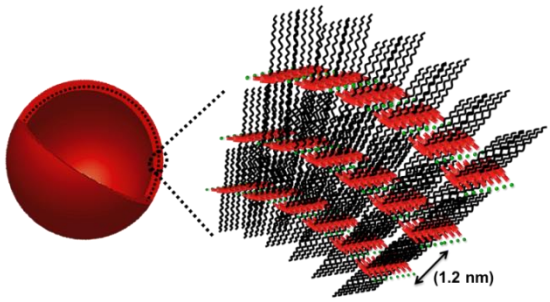

Figure 6. Schematic illustration of the proposed molecular organization of **1** in multi-layered inverse vesicles.

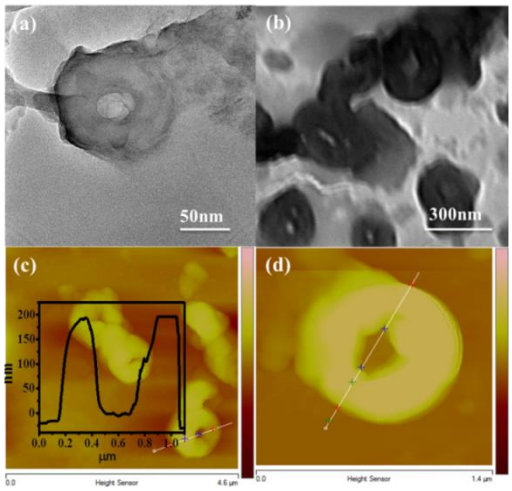

Figure 7. (a), (b) TEM images of toroids obtained after 32 hrs. (c), (d) corresponding AFM images of toroids. (Inset shows the height profile of toroids).

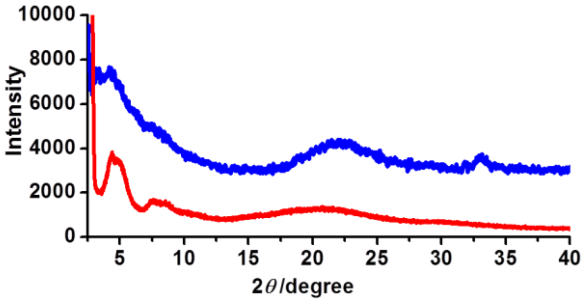

Figure 8. Comparison of PXRD patterns of **1** in different states, red: as synthesized **1** obtained after 6 hrs; blue: as synthesized nanovesicles of **1** obtained after 24 hrs.

2A.3.2 Photophysical studies and light-harvesting

Flaky nanostructures of **1**, obtained after 6 h exhibits green fluorescence with a maximum at 462 nm upon excitation at 412 nm (Figure 9a). The permanent porosity and intense luminescence behaviour of **1** prompted us to explore the Förster Resonance Energy Transfer (FRET) from OPE linkers to non-covalently encapsulated acceptor dye molecules. In the present study a cationic dye, *trans*-4-[4-(dimethylamino)styryl]-1-methylpyridinium iodide (DSMP) has been chosen as the excitation energy acceptor (λ_{max} = 480 nm, λ_{em}= 615 nm), because of good spectral overlap between its absorption with the emission of **1** (Figure 9b). Room temperature mixing of the DSMP (2 mol %) with activated compound **1** in dry THF for 24 h resulted in the formation of a stable, mixed nanocolloids, {Zn(OPE)-DSMP}(**2**). The mixed hybrids were separated by centrifugation

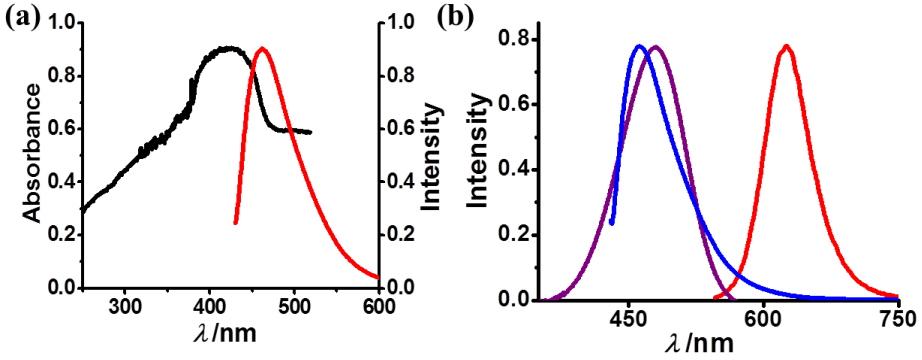

Figure 9. (a) Absorption (black) and emission spectrum (blue) of **1** in solid state. (b) Normalized absorption (violet) and emission spectrum (red) of DSMP in solution and emission spectrum of **1** (blue) in solid state.

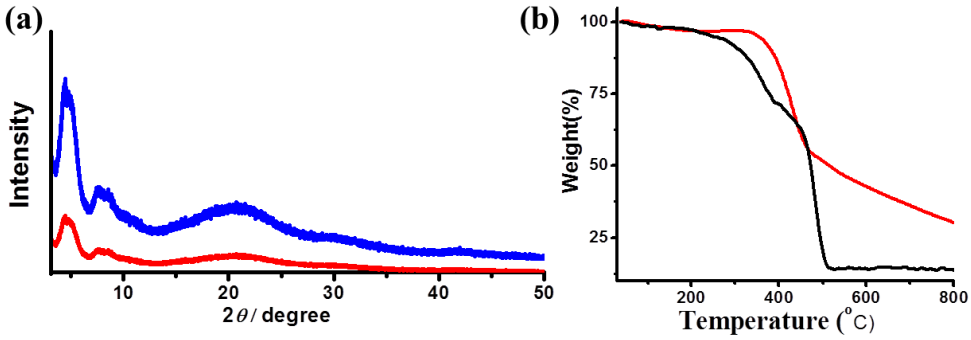

Figure 10. (a) PXRD patterns of **1** (blue) and DSMP encapsulated hybrid {Zn(OPE)-DSMP} **(2)** (red). (b) TGA of **1**(red) and {Zn(OPE)-DSMP} **(2)** (black) at heating rate of 3 °C/min.

and dried under vacuum at room temperature. Similar PXRD patterns of **2** with that of **1** reveal that there are no structural changes in the framework upon guest encapsulation of

the dye molecules (Figure 10a). Furthermore, the TGA analysis of **2** displays an additional step at 310 °C suggesting the presence of DSMP in the framework (Figure 10b). The inclusion of DSMP into the coordination network is further confirmed by ^{1}H NMR (Figure 11). ^{1}H NMR of **2** by disintegrating in DCl shows the presence of 0.04 DSMP molecules per formula unit of the framework. We believe that cationic DSMP dyes are located in the relatively polar regions of the MOF created by the carboxylate

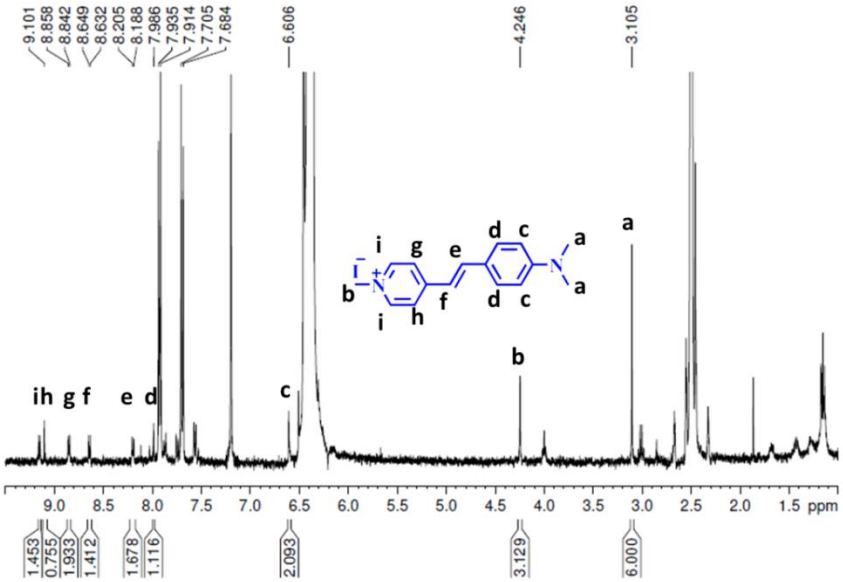

Figure 11. ^{1}H NMR spectra of {Zn(OPE)-DSMP} **(2)** dissolute in DCl with dmso-d^{6} solvent. Inset showing DSMP with highlighting corresponding peaks in the NMR spectra.

groups of OPE, chelating the Zn^{II} metal ion in the coordination chain (Scheme 1). When the dye loaded mixed hybrids, **2** is selectively excited at 412 nm, the framework emission at 462 nm is completely quenched, whereas a strong DSMP emission appeared at 625 nm. This indicates an efficient excitation energy transfer from the framework to the encapsulated dye molecules (Figure 12a). This resonance energy transfer is further supported by the excitation spectrum of **2** collected at the DSMP emission (625 nm), which showed a maximum at 425 nm clearly suggesting the contribution of OPE linkers to the observed emission (Figure 12b). In addition, the direct excitation of DSMP molecules in **2** at 480 nm shows less intensity compared to the indirect excitation at 412 nm, clearly indicating a light-harvesting process through FRET mechanism. Fluorescence decay profiles of the framework loaded with 0.5 mol% of DSMP monitored at the OPE emission (462 nm) showed shortening (2.3 ns) of life-time compared to that of pure framework **1** (5.9 ns), providing further proof for energy transfer. In addition, life time of

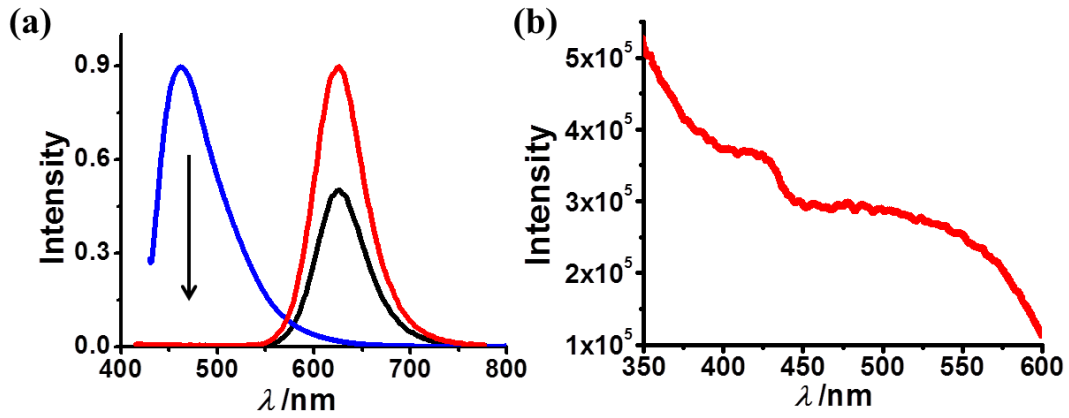

Figure 12. (a) Normalized emission spectra of **1** excited at 412 nm (blue), {Zn(OPE)-DSMP}**(2)** excited at 412 nm (red) and at 480 nm (black, indirect excitation). (b) Excitation spectrum of {Zn(OPE)-DSMP} **(2)** collected at 625nm.

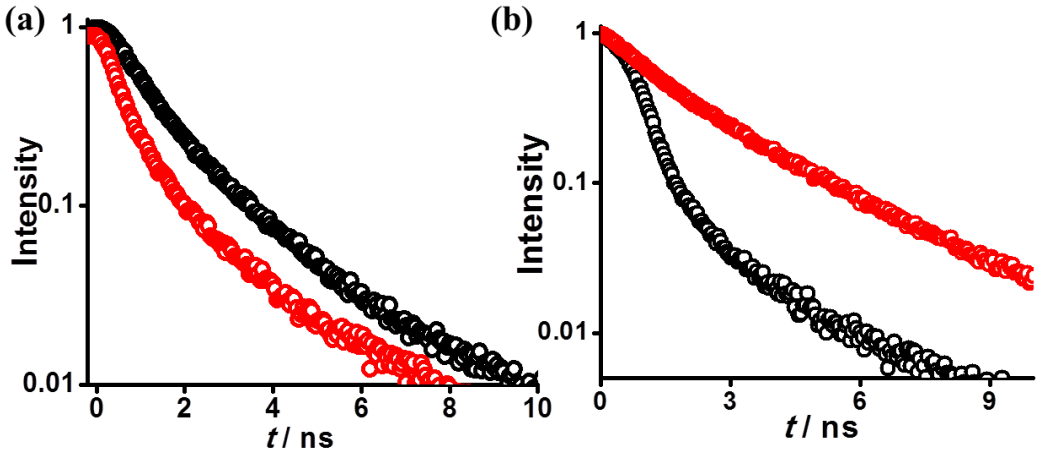

Figure 13. Life time decay profiles. (a) For **1** (black) and **1** loaded with 0.5 mol% of the DSMP (red) detected at 463 nm. (b) For {Zn(OPE)-DSMP} **(2)** (red) and DSMP (black) detected at 625 nm. Excitation wavelength is 405 nm in all cases.

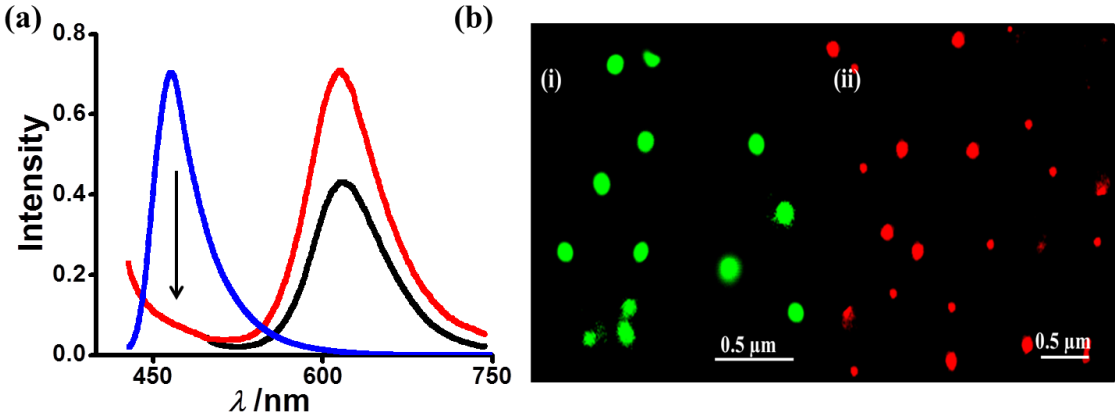

Figure 14. (a) Normalized emission spectra of nanovesicles of **1** (blue), and DSMP included nanovesicles excited at 412 nm (red) and 480 nm (black).Confocal microscopy images of (b) (i) nanovesicles of **1**, and (ii) DSMP incorporated nanovesicles of **2**.

DSMP encapsulated in **2** monitored at 625 nm is longer (5.1 ns) than free DSMP molecules (2.9 ns) (Figure 13). Motivated by these observations, we further extended energy transfer studies to the vesicular hybrid nanostructures of **1** by loading DSMP dye (2 mol %). Fluorescence measurements of these mixed hybrid vesicles have also shown a very efficient energy transfer as shown in Figure 14a. This is further evident form confocal fluorescence microscopic images of the hybrid vesicles (Figure 14b) which showed green and red emission, respectively.

2A.4 Conclusion

The results presented here illustrate a novel strategy to prepare unprecedented nanoscale MOF morphologies like vesicles, toroids, and bowls by controlling the coordination interactions between metal (Zn^{II}) and linker (OPEA) during the self-assembly process. The inherent porous nature of the MOF system with soft modular nanoscale morphologies would enhance dynamicity for guest uptake. The porosity of these MOF nanostructures has been further exploited for the spatial organization of acceptor molecules, which resulted in an efficient excitation energy transfer from the luminescent framework to the dye molecules in their pores. The functionalities of porous metal-organic vesicular structures can be extended as a low density capsule for controlled release of drugs or dyes, and as a microreactor for catalysis.

2A.5 References

[1] a) S. Kitagawa, R. Kitaura, S. Noro, *Angew. Chem. Int. Ed.* **2004**, *43*, 2334; b) S. L. James, *Chem. Soc. Rev.* **2003**, *32*, 276; c) G. Ferey, *Dalton Trans*. **2009**, 4400; d) J. J. I. V. Perry, J. A. Perman, M. J. Zaworotko, *Chem. Soc. Rev.* **2009**, *38*, 1400; e) H. –L. Jiang, Q. Xu, *Chem. Commun*. **2011**, *47*, 3351; f) S. T. Meek, J. A. Greathouse, M. D. Allendorf, *Adv. Mater.* **2011**, *23*, 249; g) C. Janiak, *Dalton Trans.* **2003**, 2781; h) C. N. Rao, S. Natarajan, R. Vaidhyanathan, *Angew. Chem. Int. Ed.* **2004**, *43*, 1466; i) T. K. Maji, S. Kitagawa, *Pure. Appl. Chem.* **2007**, *79*, 2155; j) O. M. Yaghi, M. O'Keeffe, N. W. Ockwig, H. K. Chae, M. Eddaoudi, J. Kim, *Nature*, **2003**, *423*, 705.

[2] a) N. L. Rosi, J. Eckert, M. Eddaoudi, D. T. Vodak, J. Kim, M. O'Keeffe, O. M. Yaghi, *Science* **2003**, *300*, 1127; b) S. Mohapatra, K. P. S. S. Hembram, U. Waghmare, T. K. Maji, *Chem. Mater.* **2009**, *21*, 5406; c) P. Kanoo, A. C. Ghosh, S. T. Cyriac, T. K. Maji, *Chem. Eur. J.* **2012**, *18*, 237; d) N. Nijem, H. Wu, P. Canepa, A. Marti, K. J. Jr. Balkus, T. Thonhauser, J. Li, Y. J. Chabal, *J. Am. Chem.Soc.* **2012**, *134*, 15201; e) S. Ma, H. –C. Zhou, *Chem. Commun.* **2010**, *46*, 44; f) K. Sumida, D. L. Rogow, J. A. Mason, T. M. McDonald, E. D. Bloch, Z. R. Herm, T. -H. Bae, J. R. Long, *Chem. Rev.* **2012**, *112*, 724; g) J. Lee, O. K. Farha, J. Roberts, K. A. Scheidt, S. T. Nguyen, J. T. Hupp, *Chem. Soc. Rev.* **2009**, *38*, 1450; h) B. Chen, L. Wang, Y. Xiao, F. R. Fronczek, M. Xue, Y. Cui, G. Qian, *Angew. Chem. Int. Ed.* **2009**, *48*, 500; i) P. Horcajada, C. Serre, G. Maurin, N. A.

Ramsahye, F. Balas, M. Vallet-Regi, M. Sebban, F. Taulelle, G. Ferey, *J. Am. Chem. Soc.* **2008**, *130*, 6774.

[3] a) C. Y. Lee, O. K. Farha, B. J. Hong, A. A. Sarjeant, S. T. Nguyen, J. T. Hupp, *J. Am. Chem. Soc.* **2011**, *133*, 15858; b) K. Jayaramulu, P. Kanoo, S. J. George, T. K. Maji, *Chem. Commun.* **2010**, *46*, 7906; c) C. A. Bauer, T. V. Timofeeva, T. B. Settersten, B. D. Patterson, V. H. Liu, B. A. Simmons, M. D. Allendorf, *J. Am. Chem. Soc.* **2007**, *129*, 7136; d) K. C. Stylianou, R. Heck, S. Y. Chong, J. Bacsa, J. T. A. Jones, Y. Z. Khimyak, D. Bradshaw, M. J. Rosseinsky, *J. Am. Chem. Soc.* **2010**, *132*, 4119.

[4] a)Y. Takashima, V. Martinez Martinez, S. Furukawa, M. Kondo, S. Shimomura, H. Uehara, M. Nakahama, K. Sugimoto, S. Kitagawa, *Nat. Commun.* **2011**, *2*, 168; b) H. Khajavi, J. Gascon, J. M. Schins, L. D. A. Siebbeles, F. Kapteijn, *J. Phy. Chem. C* **2011**, *115*, 12487; c) W. B. Lin, Z. Y. Wang, L. Ma, *J. Am. Chem. Soc.* **1999**, *121*, 11249; d) O. R. Evans, R. Xiong, Z. Wang, G. K. Wong, W. Lin, *Angew. Chem. Int. Ed.* **1999**, *38*, 536; e) M. Mueller, A. Devaux, C. -H. Yang, L. De Cola, R. A. Fischer, *Photochem. & Photobio. Sci.* **2010**, *9*, 846.

[5] a) J. Della Rocca, D. Liu, W. Lin, *Acc. Chem. Res.* **2011**, *44*, 957; b) A. Carne, C. Carbonell, I. Imaz, D. Maspoch, *Chem. Soc. Rev.* **2011**, *40*, 291; c) B. Liu, O. Shekhah, H. K. Arslan, J. Liu, C. Woell, R. A. Fischer, *Angew. Chem. Int. Ed.* **2012**, *51*, 807; d) W. J. Rieter, K. M. Pott, K. M. L. Taylor, W. Lin, *J. Am. Chem. Soc.* **2008**, *130*, 11584; e) K. Otsubo, T. Haraguchi, O. Sakata, A. Fujiwara, H. Kitagawa, *J. Am. Chem. Soc.* **2012**, *134*, 9605; f) I. Imaz, J. Hernando, D. Ruiz-Molina, D. Maspoch, *Angew. Chem. Int. Ed.* **2009**, *48*, 2325.

[6] a) X. Zhang, M. A. Ballem, M. Ahren, A. Suska, P. Bergman, K. Uvdal, *J. Am. Chem. Soc.* **2010**, *132*, 10391; b) C. A. Kent, D. Liu, L. Ma, J. M. Papanikolas, T. J. Meyer, W. Lin, *J. Am. Chem. Soc.*, **2011**, *133*, 12940; c) X. Zhang, M. A. Ballem, Z. -J. Hu, P. Bergman, K. Uvdal, *Angew. Chem. Int. Ed.* **2011**, *50*, 5728; d) H. Xu, F. Liu, Y. Cui, B. Chen, G. Qian, *Chem. Commun.***2011**, *47*, 3153; e) X. Zhang, Z. -K. Chen, K. P. Loh, *J. Am. Chem. Soc.* **2009**, *131*, 7210.

[7] a) K. V. Rao, K. K. R. Datta, M. Eswaramoorthy, S. J. George, *Chem. Eur. J.* **2012**, *18*, 2184; b) R. Haldar, K. V. Rao, S. J. George, T. K. Maji, *Chem. Eur. J.* **2012**, *18*, 5848.

[8] a) T. Nakashima, N. Kimizuka, *Adv. Mater.* **2002**, *14*, 1113; b) A. Ajayaghosh, S. J. George, V. K. Praveen, *Angew. Chem. Int. Ed.* **2003**, *42*, 332; c) K. Sugiyasu, N. Fujita, S. Shinkai, *Angew. Chem. Int. Ed.* **2004**, *43*, 1229; d) S. J. George, A. Ajayaghosh, P. Jonkheijm, A. Schenning, E. W. Meijer, *Angew. Chem. Int. Ed.* **2004**, *43*, 3422; e) A. Ajayaghosh, V. K. Praveen, C. Vijayakumar, *Chem. Soc. Rev.* **2008**, *37*, 109; f) C. Devadoss, P. Bharathi, J. S. Moore, *J. Am. Chem. Soc.* **1996**, *118*, 9635; g) N. Aratani, D. Kim, A. Osuka, *Acc. Chem. Res.* **2009**, *42*, 1922; h) R. A. Haycock, A. Yartsev, U. Michelsen, V. Sundstrom, C. A. Hunter, *Angew. Chem. Int. Ed.* **2000**, *39*, 3616; i) M. S. Choi, T. Yamazaki, I. Yamazaki, T. Aida, *Angew. Chem. Int. Ed.* **2004**, *43*, 150; j) Y. Ishida, T. Shimada, D. Masui, H. Tachibana, H. Inoue, S. Takagi, *J. Am. Chem. Soc.* **2011**, *133*, 14280.

[9] a) G. Calzaferri, S. Huber, H. Maas, C. Minkowski, *Angew. Chem. Int. Ed.* **2003**, *42*, 3732; b) G. Calzaferri, K. Lutkouskaya, *Photochem. Photobiol. Sci.* **2008**, *7*, 879; c) T. Q. Nguyen, J. Wu, S. H. Tolbert, B. J. Schwartz, *Adv. Mater.* **2001**, *13*, 609.

[10] a) N. Mizoshita, Y. Goto, T. Tani, S. Inagaki, *Adv. Mater.* **2009**, *21*, 4798; b) S. Inagaki, O. Ohtani, Y. Goto, K. Okamoto, M. Ikai, K.-i. Yamanaka, T. Tani, T. Okada, *Angew. Chem. Int. Ed.* **2009**, *48*, 4042; c) T. Q. Nguyen, J. J. Wu, V. Doan, B. J. Schwartz, S. H. Tolbert,

Science **2000**, *288*, 652; d) Y. Maegawa, N. Mizoshita, T. Tani, S. Inagaki, *J. Mater. Chem.* **2010**, *20*, 4399.

[11] a) K. V. Rao, K. K. R. Datta, M. Eswaramoorthy, S. J. George, *Angew. Chem. Int. Ed.* **2011**, *50*, 1179; b) K. V. Rao, K. K. R. Datta, M. Eswaramoorthy, S. J. George, *Adv. Mater.* **2013**, *25*, 1713.

[12] a) S. Horike, S. Shimomura, S. Kitagawa, *Nat. Chem.* **2009**, *1*, 695; b) S. Shimomura, S. Kitagawa, *J. Mater. Chem.* **2011**, *21*, 5537.

[13] a) K. Becker, P. G. Lagoudakis, G. Gaefke, S. Hoeger, J. M. Lupton, *Angew. Chem. Int. Ed.* **2007**, *46*, 3450; b) P. V. James, P. K. Sudeep, C. H. Suresh, K. G. Thomas, *J. Phys. Chem. A* **2006**, *110*, 4329; c) G. Duvanel, J. Grilj, A. Schuwey, A. Gossauer, E. Vauthey, *Photochem. Photobiol. Sci.* **2007**, *6*, 956.

[14] E. A. Fluegel, A. Ranft, F. Haase, B. V. Lotsch, *J. Mater. Chem.* **2012**, *22*, 10119.

[15] a) Q. Li, A. V. Rukavishnikov, P. A. Petukhov, T. O. Zaikova, C. S. Jin, J. F. W. Keana, *J. Org. Chem.* **2003**, *68*, 4862; b) A. Mangalum, R. J. Gilliard Jr., J. M. Hanley, A. M. Parker, R. C. Smith, *Org. Bio. Chem.* **2010**, *8*, 5620.

[16] a) M. Masuda, V. Vill, T. Shimizu, *J. Am. Chem. Soc.* **2000**, *122*, 12327; b) R. Iwaura, T. Iizawa, H. Minamikawa, M. Ohnishi-Kameyama, T. Shimizu, *Small* **2010**, *6*, 1131.

[17] a) R. Makiura, S. Motoyama, Y. Umemura, H. Yamanaka, O. Sakata, H. Kitagawa, *Nat. Mater.* **2010**, *9*, 565; b) R. Ameloot, F. Vermoortele, W. Vanhove, M. B. J. Roeffaers, B. F. Sels, D. E. De Vos, *Nat. Chem.* **2011**, *3*, 382.

Chapter 2B

Oligo(*p*-phenyleneethynylene)-Derived Porous Luminescent Nanoscale Coordination Polymer of Gd^{III}: Bimodal Imaging and Nitroaromatic Sensing

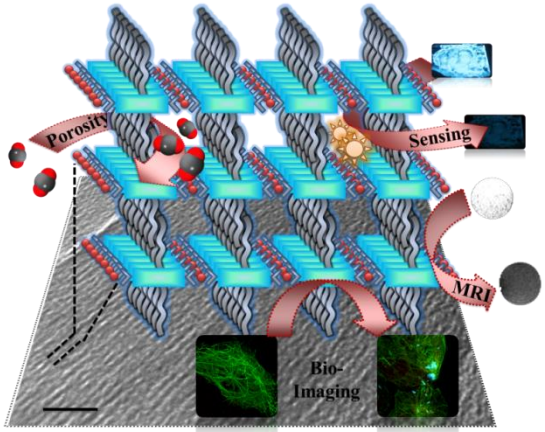

Luminescent Nanoscale Porous Coordination Polymer

Summary

This chapter reports synthesis of highly luminescent nanoscale metal-organic framework, {[Gd(OPE)(NO_3)(H_2O)$_2$]·H_2O} (**NMOF-1**), (OPE = Oligo-(*p*-phenyleneethyny lene)dicarboxylate) by the coordination-driven self-assembly of oligo-(*p*-phenylene ethynylene)dicarboxylic acid and Gd^{III} in polar solvent. This nanostructure has been characterized by FESEM, TEM, powder X-ray diffraction, and adsorption study. Interdigitation between 1D coordination polymers through alkyl chains results in a porous supramolecular 3D extended structure. **NMOF-1** shows permanent microporosity as revealed by type-I CO_2 uptake profile. FESEM and TEM studies of **NMOF-1** reveal nanorod like morphology with square-type cross section having dimensions of 50-100 nm in width and 0.5 - 0.8 μm length. High magnification TEM images show presence of uniform dark lines having an interspacing distance of 0.9-1.1 nm suggesting long range structural ordering present in **NMOF-1** with. Physiological stability and strong luminescence features of **NMOF-1** have been exploited for bio-imaging based on internalization into mammalian cultured cell lines HEK 293T and H1299. Magnetic resonance imaging (MRI) studies suggest that **NMOF-1** could act as a potential negative (*T2*) contrast agent. These results demonstrate that hybridization of a paramagnetic metal center and luminescent linker in a nanoscale metal-organic framework culminates in a functional hybrid material with potential bimodal imaging and sensing applications.

V. M. Suresh, S. Chatterjee, R. Modak, V. Tiwari, A. B. Patel, T. K. Kundu, T. K. Maji, *J. Phys. Chem. C* **2014**, *118*, 12241.

2B.1 Introduction

Porous coordination polymers (PCPs) or metal-organic frameworks (MOFs)[1] are a class of crystalline materials constructed by the self-assembly of metal ions and polydentate organic linkers with wide range of modular pore size and surface area and have been extensively studied for applications in gas storage,[2] separation,[3] sensing,[4] drug delivery,[5] optical properties[6] and catalysis.[7] The recent upsurge in synthesis of PCPs stems from their functional behavior with a set of well-defined properties such as magnetism and porosity, photoluminescence and magnetism, conductivity and luminescence, and luminescence and porosity in a single framework system.[8] The pre-synthetic design strategies like judicious choice of building blocks and suitable reaction conditions can address the challenges of synthesizing such functional hybrid materials. For example Veciana *et al.* reported highly porous magnetic framework $\{Cu_3(PTMTC)_2(py)_6(CH_3CH_2OH)_2(H_2O)\}$ using polychlorinated triphenylmethyl radical functionalized with three carboxylic acids (PTMTC) as a bridging linker that reveals guest responsive change in magnetic properties.[9]

In this context, design and synthesis of luminescent porous metal-organic frameworks with suitable chromophoric linkers and metal ions and their potential applications in different fields is yet to be properly explored. Particularly the hydrolytic instability or bulk crystalline phase of most of the MOFs limits their applications in biomedical and biological fields.[10] Therefore, luminescent nanoscale metal-organic frameworks (NMOFs) with uniform size and morphologies[11] are highly promising in designing functional nanomaterials for multimodal imaging and drug delivery applications based on their easy internalization into cells.[12] Nanoscale dimensions of these inherent microporous materials would enhance solution processability that would help in fabrication of thin film devices and sensors.[13] Recently, Lin *et al.* reported BODIPY grafted Fe^{III}-carboxylate $[Fe_3(\mu_3\text{-}O)Cl(H_2O)_2(NH_2\text{-}BDC)_3]$ nanoparticles as delivery vehicles and optical imaging agents.[14] They have also reported nanorods of $\{Gd(BDC)_{1.5}(H_2O)_2\}$ for magnetic resonance imaging (MRI) with high relaxivity and further doping with Tb^{3+} and Eu^{3+} of the Gd-nanorods multimodal imaging application was realized.[15] However, NMOFs based on a MRI active metal ion and a highly luminescent organic linker is yet to be explored and such hybrid material would offer unique class of multifunctional material for potential applications in multimodal imaging, drug delivery and sensing. With this objective we envision the design and synthesis of

functional hybrid nanostructures based on a luminescent π-conjugated linker and Gd^{III} paramagnetic metal center. In our design, we have self-assembled oligo-(*p*-phenyleneethynylene)dicarboxylic acid (OPEA) with soluble alkyl chains on both ends and Gd^{III} metal ion into a new luminescent nanoscale MOF, $\{[Gd(OPE)(NO_3)(H_2O)_2]\cdot H_2O\}$ (**NMOF-1**). This **NMOF-1** is characterized by several spectroscopic and microscopic techniques and has been studied for properties like bimodal imaging based on a luminescent OPEA linker and MRI active Gd^{III} metal ion.

2B.2 Experimental section

2B.2.1 Materials

Tetrakis(triphenylphosphine)palladium(0), copper iodide (CuI) and $Gd(NO_3)_3.6H_2O$ were purchased from Sigma-Aldrich Chemical Co. Oligo-(*p*-phenyleneethynylene)dicarboxylic acid (OPEA) is synthesized using literature procedures.[16] Required solvents were dried prior to use.

2B.2.2 Physical measurements

Elemental analysis was carried out using Thermo Scientific Flash 2000 CHN analyzer. Infrared spectral studies were done by making samples with KBr pellets using Bruker FT-IR spectrometer. Thermal stability of coordination polymer was analyzed using Mettler Toledo TGA 850 instrument under inert atmosphere in the temperature range of 30-800 °C at a heating rate of 5 °C per min. Powder X-ray diffraction studies of the samples were recorded on a Bruker D8 discover instrument using Cu-Kα radiation. Morphological studies have been carried out using Lica-S440I field emission scanning electron microscope (FESEM) by placing samples on a silicon wafer under high vacuum with an accelerating voltage of 10 kV. Transmission electron microscopy (TEM) analysis has been performed using JEOL JEM-3010 with an accelerating voltage at 300 kV. For this analysis **NMOF-1** is dispersed in ethanol by sonication before drop casting on a carbon-coated copper grid. Porosity measurements were carried out using QUNATACHROME QUADRASORD-SI analyser at 77 K for N_2 and 195 K for CO_2. Fluorescence studies were accomplished using Perkin Elmer Ls 55 Luminescence spectrometer. ^{1}H-NMR is recorded on a Bruker AV-400 spectrometer with chemical shifts reported as ppm.

2B.2.3 MRI imaging studies

T1 and T2 measurements were carried out at 25 °C using a vertical wide bore (89 mm) 14.1 T magnet interfaced with Avance II Microimager (Bruker Biospin, Germany) equipped with 60 mm actively shielded gradient. Nanorods were dispersed in 0.5% agarose at different concentration and placed into a 0.7 mL microfuge tube. Axial images of the microfuge tube filled with nanorod disperse in agarose were acquired for the relaxation time measurements. The typical parameters used for T1 measurements are: echo time (TE) = 7 ms; repetition time (TR) = varies from 250 ms to 15000 ms; slice thickness = 0.5 mm; field of view: 15 mm × 15 mm; matrix size = 64 × 64. The T1 value was determined by fitting the function $S_{TR} = S_{TR(\infty)}(1 - \exp(-TR/T1))$ to the signal intensity versus repetition time graph, where $S_{TR(\infty)}$ represents MR intensity at infinite repetition time. The parameters used for the T2 measurements were: TR = 10000 ms and TE varying between 10 and 320 ms. All other parameters used were same as that of the T1 measurements. The T2 value was obtained by fitting the function $S_{TE} = S_{TE(0)} \exp(-TE/T2)$ to the signal intensity versus echo time graph, where $S_{TE(0)}$ represents MR intensity with zero echo time. The longitudinal (r_1) and transverse relaxivity (r_2) of the nanorods were calculated from the slope of R1(1/T1)/R2(1/T2) versus concentration graph.

2B.2.4 Cell culture and Immunofluorescence in cell line

HEK293T and H1299 cells were grown in presence of Dulbecco modified Eagle medium (DMEM) supplemented with 10% fetal bovine serum at 37 °C in a 5% CO_2 incubator.

Immunofluorescence with confocal microscopy was performed as described elsewhere.[17] Briefly, HEK293T or H1299 cells were grown on poly-L-lysine coated coverslips at 37 °C in a 5% CO_2 incubator to 30-50% confluency and 40 μg of **NMOF-1** was added. After the indicated time points, the coverslips containing adhered cells were washed with 1X phosphate buffer saline (PBS) fixed using 4% paraformaldehyde followed by permeabilization with Triton-X 100. Nonspecific antigens were blocked with FBS**,** and appropriate dilution of antitubulin primary antibody was added. The secondary antibody was fluorescently tagged and was used with appropriate dilution. Washes with buffer were performed after each step. Images were taken with Carl Zeiss LSM 510 META laser scanning confocal microscope.

2B.2.5 Synthesis of {[Gd(OPE)(NO_3)(H_2O)$_2$]·H_2O}, (NMOF-1)

$Gd(NO_3)_3·6H_2O$ (1eq, 14 mg) was dissolved in 5 mL of dimethylformamide (DMF) and added drop wise to OPEA (1 eq, 25 mg) solution in DMF at 140 °C and stirred for 30 minutes. The reaction mixture was cooled to room temperature and then a mixture of ethanol/water (1:1) was added that resulted in a colloid formation. These colloids were centrifuged and thoroughly washed with ethanol and dried under vacuum for 6 h. The resultant products were characterized by different techniques. Yield: 54%. Elemental analysis for $GdC_{40}H_{50}NO_{12.}$ Calcd: C, 53.7; H, 5.6; N, 1.5. Found: C, 54.2; H, 5.6; N, 1.6. FTIR in KBr (cm^{-1}): 3357(br), 2925(sh), 2854(sh), 2670(w), 2543(w), 2208(w), 1689(vs), 1602(s), 1531(m), 1417(s), 1382(vs), 1282(m), 1216(w), 1178(w), 1018(w), 862(w), 773(w).

2B.3 Results and discussion

2B.3.1 Structural characterization

Oligo(*p*-phenyleneethynylene)dicarboxylic acid with octyloxy (C8) chains on both sides is synthesized through the Sonogashira coupling strategy and characterized by ^{1}H NMR (Figure 1). DMF solution of $Gd(NO_3)_3·6H_2O$ (1eq) is added to OPEA (1eq) ligand and heated at 140 °C for 30 min and then cooled to room temperature. Slow addition of EtOH/H_2O (1:1) to the reaction mixture at room temperature results in a colloidal solution. These colloids were collected by centrifugation, washed with ethanol and dried under vacuum at room temperature for 6 h. The compound is further

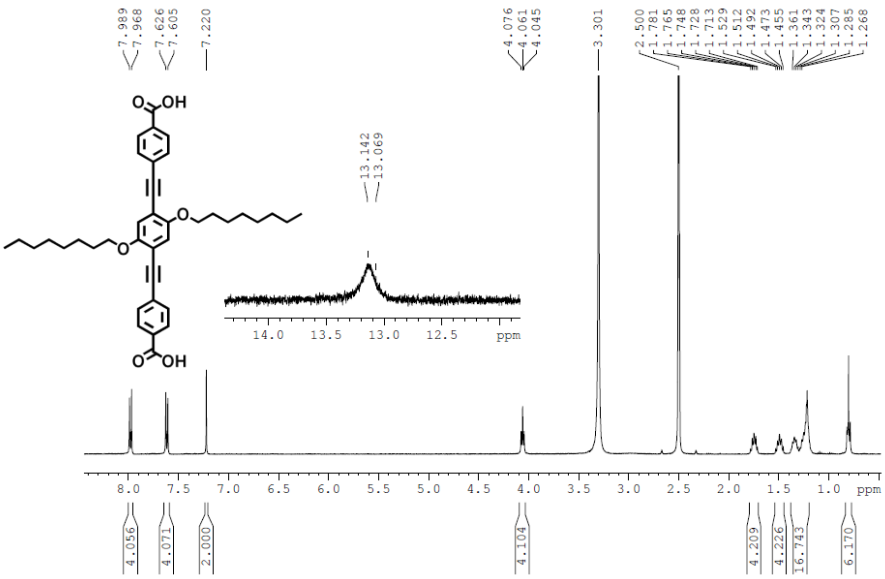

Figure 1. ^{1}H NMR spectra of OPEA in dmso-d^6.

characterized by elemental analysis, Fourier transform infrared spectroscopy (FTIR), powder X-ray diffraction (PXRD), thermogravimetric analysis (TGA), field-emission scanning electron microscopy (FESEM), transmission electron microscopy (TEM) and adsorption measurements. The presence of Gd^{III} in colloids is supported by energy dispersive X-ray analysis (EDAX) (Figure 2a), and elemental analysis suggests a molecular formula of $\{[Gd(OPE)(NO_3)(H_2O)_2]\cdot H_2O\}$, (**NMOF-1**) for as-synthesized compound. FTIR of **NMOF-1** shows strong bands at 1687 cm^{-1} and 1525 cm^{-1} characteristic of ν_s(COO) and ν_{as}(COO) of OPE linker bound to Gd^{III} center (Figure 2b).

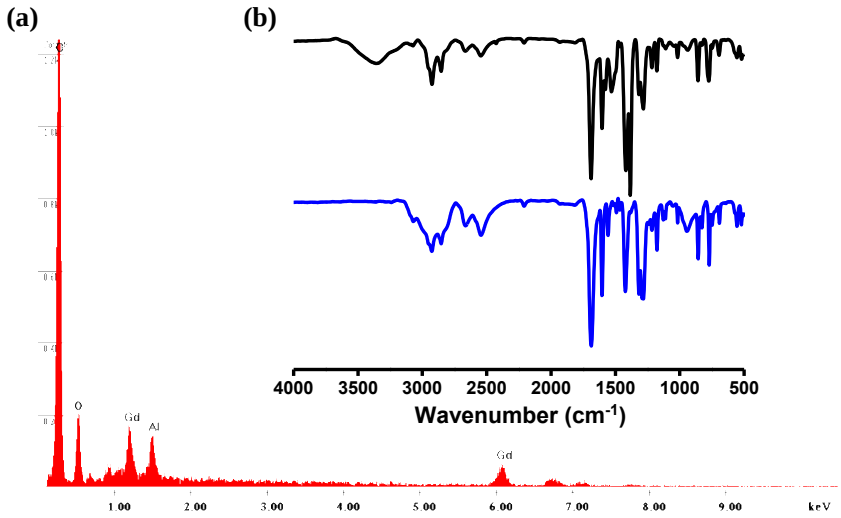

Figure 2. (a) Energy dispersive X-ray analysis (EDAX) of **NMOF-1**. (b) FTIR spectra of OPEA (blue) and **NMOF-1** (black).

The presence of a strong signal at 1385 cm^{-1} corresponds to the ν(NO) of nitrate ion indicates its coordination to Gd^{III} center. In addition, the remaining coordination sites in Gd^{III} could be fulfilled by the water molecules (Figure 3a) which is supported by the broad band centered at 3560-3212 cm^{-1}. TGA analysis shows intial weight loss (6% equal to three water molecules) in the range of 65 - 150 °C corresponds to loss of guest as well as coordinated water molecules (Figure 3b), and further heating results no weight loss till 350 °C suggesting that dehydrated compound is highly stable. Therefore, **NMOF-1** is activated at 150 °C before doing N_2 (77 K) and CO_2 (195 K) gas adsorption measurements. It is worth mentioning that **NMOF-1** is crystalline in nature, and PXRD pattern of dehydrated **NMOF-1** show no changes compared to assynthesized compound suggesting stability of framework on removal of guest molecules (Figure 4a). Adsorption of N_2 (kinetic diameter = 3.64 Å) at 77 K shows a typical type-II profile suggesting

NMOF-1 is nonporous with respect to N_2 (Figure 4b). Interestingly, CO_2 adsorption shows sharp uptake in the low-pressure region with typical type-I profile indicating the microporous nature of **NMOF-1** with pore size < 2nm. The amount of the CO_2 uptake at the end point is found to be 52 mL/g (Figure 4b, Inset) corresponds to 2.1 CO_2 molecules per formula unit, and the Langmuir surface area is calculated to be 293 $m^2 g^{-1}$.

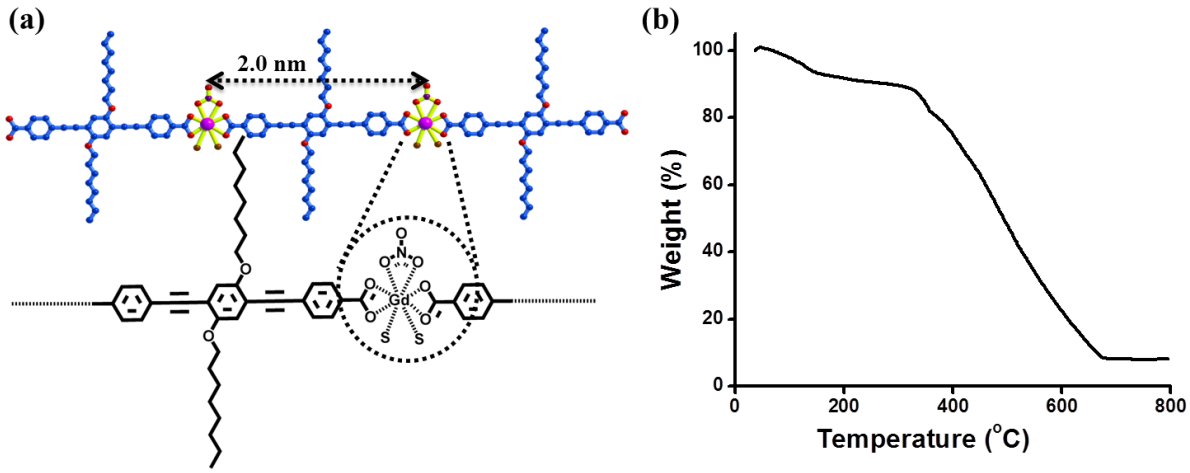

Figure 3. (a) Schematic representation showing coordination environment of Gd^{III} ion in **NCP-1**. (b) TGA of **NMOF-1** in the temperature range of 30-800 °C with a heating rate of 5 °C/min.

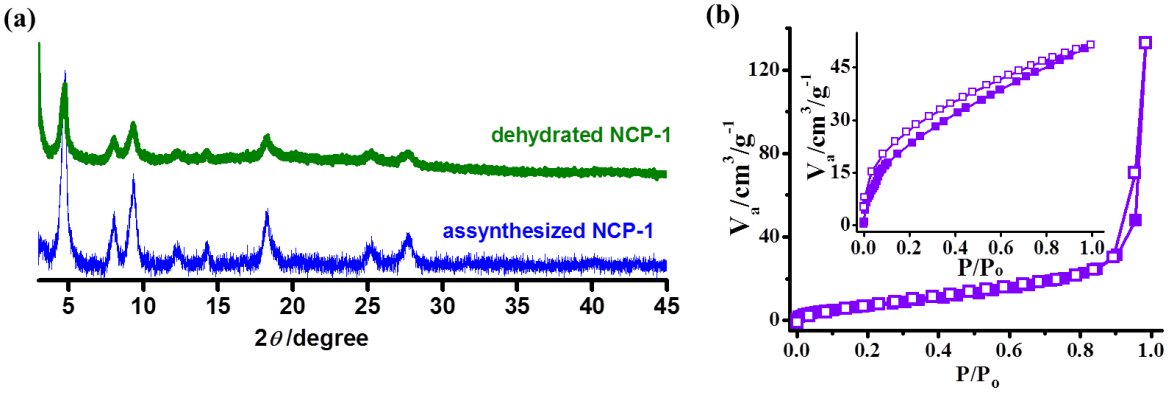

Figure 4. (a) PXRD patterns of assynthesized **NMOF-1** (blue) and dehydrated **NMOF-1** (green) showing the stability of compound on removal of guest molecules. (b) Adsorption isotherms of **NMOF-1**, N_2 at 77 K and inset shows CO_2 adsorption at 195 K.

Crystallization of OPEA and $Gd(NO_3)_3 \cdot 6H_2O$ through several methods has failed, so a possible structure is arrived from studies like PXRD, adsorption and TEM as described in the literature.[18] The experimental powder diffraction pattern (Figure 5a), has been evaluated using CRYSFIRE powder indexing system using Taup (TP) program, and the results were listed in Table 1 with unit cell parameters, *hkl* values for different planes. Diffraction pattern suggest orthorhombic phase for **NMOF-1**, where a = 7.74927 Å,

Table1. Unit-cell parameters of NMOF-1[a]

h	*k*	*l*	2θ	*D*(exptl)	*D*(calcd)	max. dev.
0	0	1	4.7417	18.52920	18.6211	0.0493
0	1	0	8.1134	10.94396	10.8885	0.0830
0	1	1	9.4014	9.44214	9.3995	0.0961
1	0	1	12.3617	7.18812	7.1544	0.0126
0	0	3	14.2577	6.23676	6.2070	0.0145
1	0	3	18.2981	4.84529	4.8445	0.0185
0	1	5	25.2535	3.52004	3.5238	0.0252
1	1	5	27.7894	3.20829	3.2077	0.0275

[a]V = 1571.22 (Å^3). Phase = Orthorhombic. Parameters: a = 7.74927 Å, b = 10.888 Å , c = 18.6211 Å; α = 90°, β = 90° and γ = 90°

b = 10.8886 Å and c = 18.6211 Å and insignificant deviations in d-values suggest that the calculated values fitted well with experimental data. Diffraction peak in the low angle region at 4.7° with d-spacing 18.6 Å corresponds to (001) plane and can be assigned to the repetition of metal centers separated by OPE linker and formation of a 1D coordination chain (Figure 5b). Now, these 1D chains can undergo interdigitation through octlyoxy (C8) side chains based on H-bonding interactions between alkyl CH and alkoxy oxygen and hydrophobic interactions to form a 2D structure, which is supported by the diffraction peak at 2θ value of 8° (d = 10.8 Å) and is assigned to (010) plane. Interdigitation of long chain alkoxy chains of *p*-phenyleneethynylenes is known to

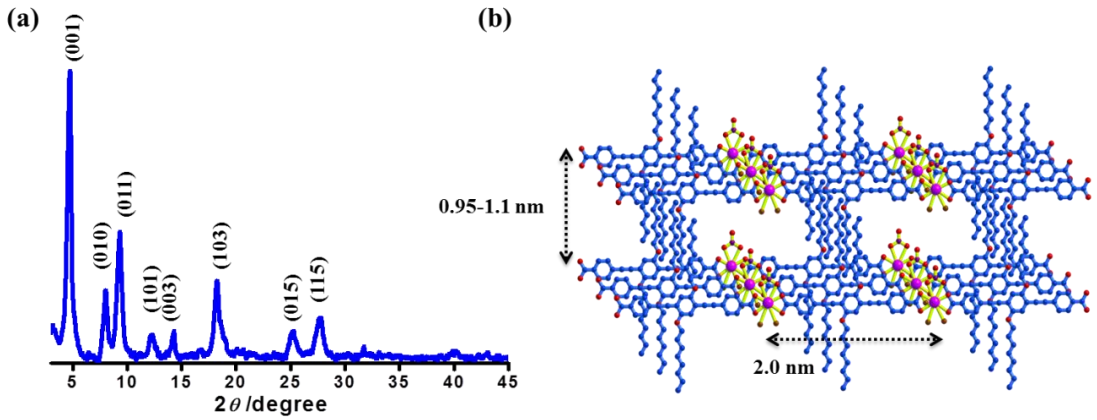

Figure 5. (a) PXRD pattern of **NMOF-1** and (b) proposed model structure of 3D interdigitated porous structure of **NMOF-1**.

form through hydrogen bonding between alkyl CH and alkoxy oxygen and is documented in literature.[19] We believe that these types of H-bonding interactions along with

hydrophobic interactions helped to form extended interdigitated structure. These 2D network could preferably pack through weak π-π interactions of the OPE core as supported by the diffraction peak at 27.7° with *d*-spacing of 3.6 Å and forms a 3D extended supramolecular porous structure. A proposed model of **NMOF-1** developed from the above results is shown in Figure 5b.

2B.3.2 SEM and TEM studies

NMOF-1 is further studied by electron microscopy techniques (FESEM and TEM). As shown in Figures 6a and b, **NMOF-1** exhibit nanorod type morphology with square type of cross section. Most of the nanorods show width ranges from 50 to100 nm with 0.5 - 0.8 μm length as shown in particle size distribution diagram (Figure 6c). TEM

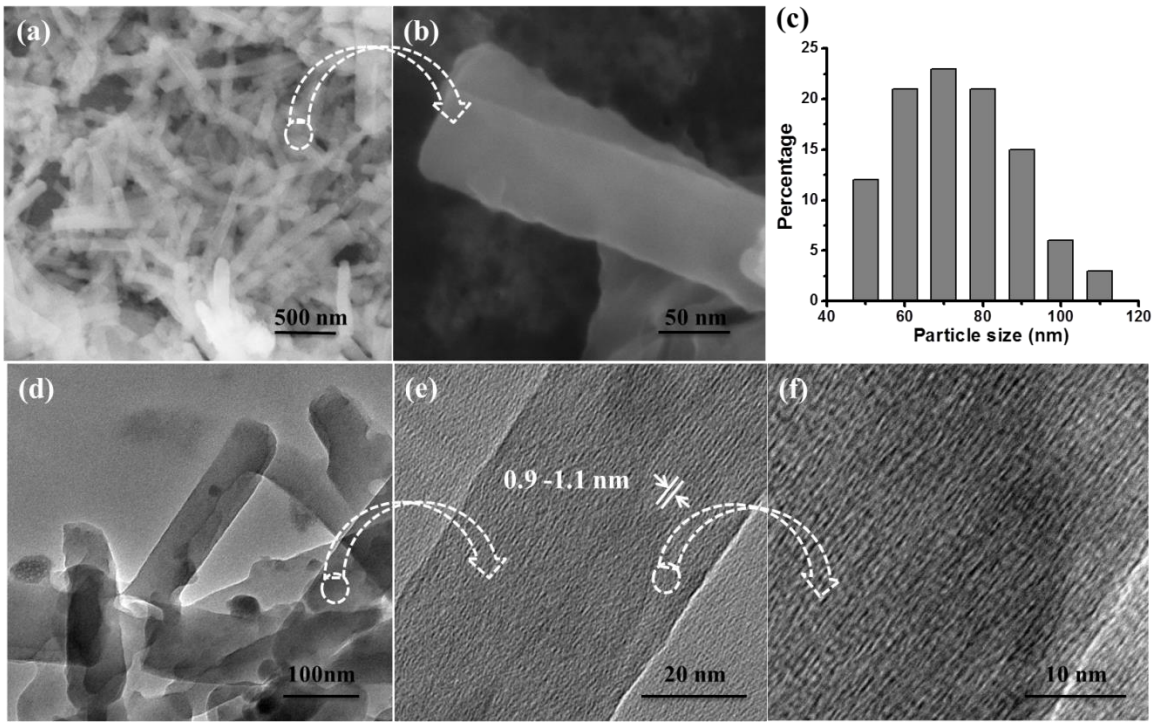

Figure 6. Electron microscope images of **NMOF-1**: (a), (b) FESEM images at different magnifications and (c) particle size distribution diagram. TEM images (d) at low magnification and (e), (f) at high magnification showing dark and bright regions indicating the ordering present in **NMOF-1**.

studies also reveal well-defined rodlike morophology (Figure 6d) which is likely the result of preferred arrangment of several 1D coordination chains in polar solvent. Interestingly, TEM of these nanorods at higher magnification shows clear ordering present in **NMOF-1** with equally distant dark lines throughout the nanorod (Figure 6e, f). Interspacing measured between two successive dark lines is found to be 0.95-1.1 nm, which is in well agreement with the *d*-spacing (1.08 nm) calculated from PXRD pattern.

These observations unequavocally suggest the interdigitation of 1D coordination chains. Furthermore, microporous nature of **NMOF-1** obtained from type-I CO_2 profile can be correlated with the porosity created due to the interdigitaion of alkyl chains in **NMOF-1**. Therefore the hydrophobic and H-bonding interactions between alkyl chains in polar solvents drive the formation of a 3D interdigitated supramolecular microporous structure.

2B.3.3 Photoluminescent properties of NMOF-1: Bimodal imaging

Oligo-(*p*-phenyleneethynylene)dicarboxylic acid (OPEA) with alkyl chains on both side show high solubility in polar solvents like tetrahydrofuran, ethanol, *N, N*′-dimethylformamide (DMF), dimethylsulfoxide (DMSO). Ethanolic solution of OPEA shows strong blue emission (λ_{em} = 440 nm) when excited at 330 nm (Figure 7a) and strong cyan emission at 473 nm (Figure 7b) in solid state when excited at 390 nm. On the other hand, **NMOF-1** forms stable colloid in DMF and no precipitation is observed for several months suggesting the significant solution processibility of **NMOF-1** colloids. Similar to OPEA, ethanol dispersion of **NMOF-1** showed strong linker based blue emission (λ_{em} = 445 nm) on excitation at 330 nm and intense cyan emission (λ_{em} = 463 nm, λ_{ex} = 390 nm) in solid state (Figure 8). Strong emission features of porous **NMOF-1** prompted us to study the internalization of these nanostructures into mammalian cells for bioimaging applications. Before doing optical imaging studies, **NMOF-1** is tested for its hydrolytic stability under physiological conditions. Incubation of nanorods of **NMOF-1** in PBS buffer for 12 h shows no considerable changes in emission properties (λ_{em} = 453 nm, λ_{ex} = 390 nm, only OPEA in PBS emit at 473 nm on 390 nm excitation) suggesting

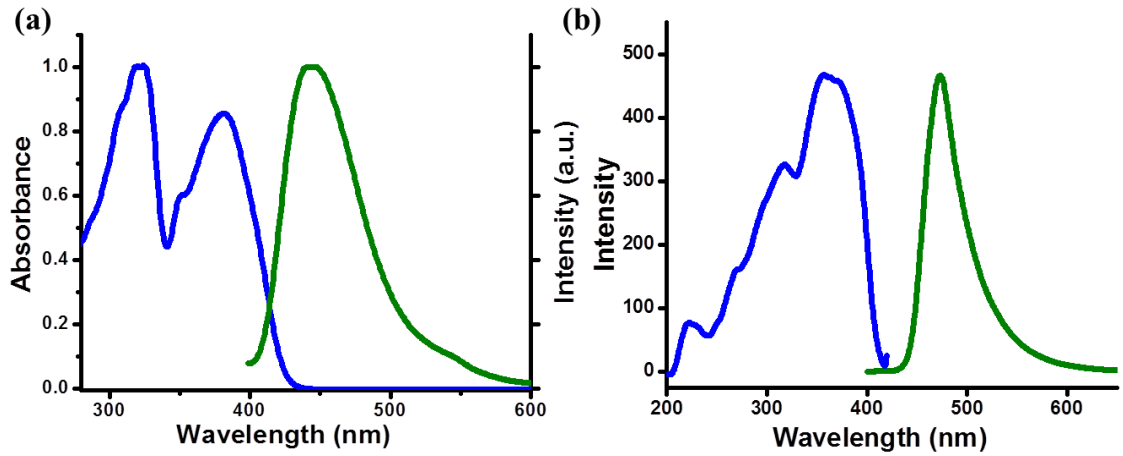

Figure 7. (a) Absorbance (blue) and fluorescence spectrum (green) of OPEA ligand in ethanol. (b) Excitation (blue) and fluorescence spectrum (green) of OPEA in solid state.

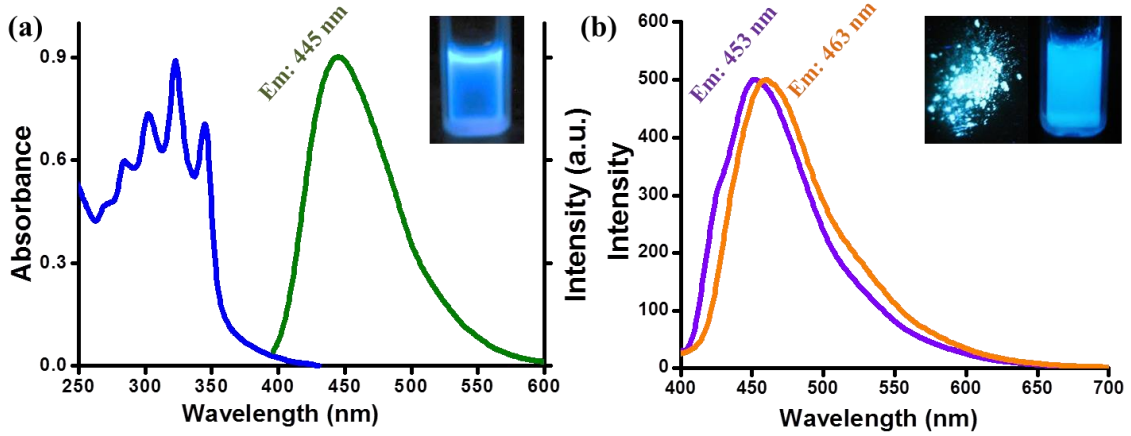

Figure 8. (a) Absorbance (blue) and fluorescence spectrum (green) of **NMOF-1** dispersed in ethanol. (b) Fluorescence spectrum of **NMOF-1** in PBS buffer (violet) and solid state (orange). Inset; Images of **NMOF-1** in ethanol (left), solid state and PBS dispersion (right) under UV light, respectively.

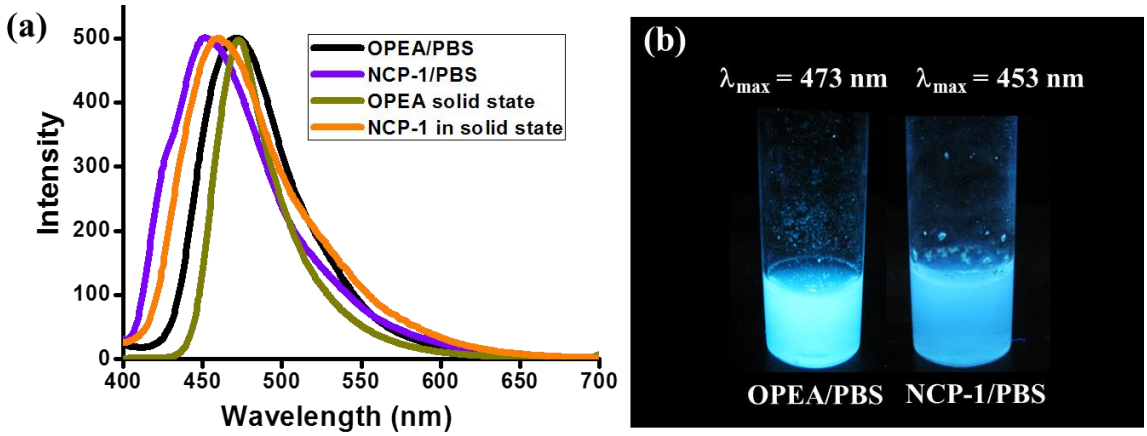

Figure 9. (a) Fluorescence spectra; OPEA in solid state (dark yellow), OPEA in PBS (black), **NCP-1** in solid state (orange) and **NMOF-1** in PBS buffer (violet). Excitation wavelength is 390 nm in all cases. (b) Images of OPEA and **NMOF-1** dispersed in PBS buffer under UV light.

the stability of NCPs in physiological conditions (Figure 9). Further, the stability of NCPs is studied using X-ray diffraction measurements. Figure 10a shows the diffraction pattern of NCPs incubated in PBS compared with assynthesized NCPs, all the diffraction peaks characteristic of **NMOF-1** is retained in the PBS incubated **NMOF-1** suggesting its stability under physiological conditions. Further, EDAX analysis of decant obtained from PBS incubated **NMOF-1** show no leaching of Gd^{III} ion into the PBS solution (Figure 10b). Further, ICP analysis of decant from **NMOF-1**/PBS showed nearly 0.3 ppm which is very feeble amount of Gd^{III} ion present in the solution, indicating no significant decomposition of **NMOF-1** in PBS. In order to study the cell permeability of **NMOF-1**,

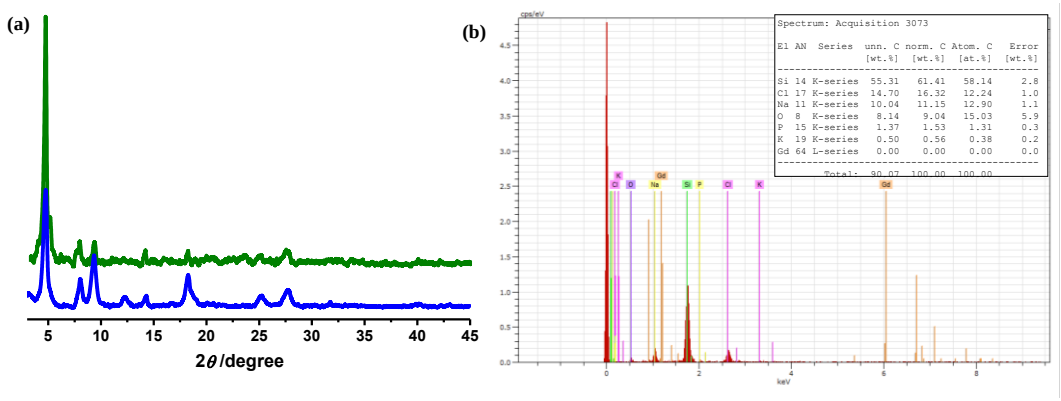

Figure 10. (a) Powder X-ray diffraction pattern of assynthesized **NMOF-1** (blue) and **NMOF-1** incubated in PBS (green). (b) EDAX analysis of decant obtained from **NMOF-1** incubated in PBS showing no leaching of Gd^{III} ions into the solution and stability of **NMOF-1** under physiological conditions.

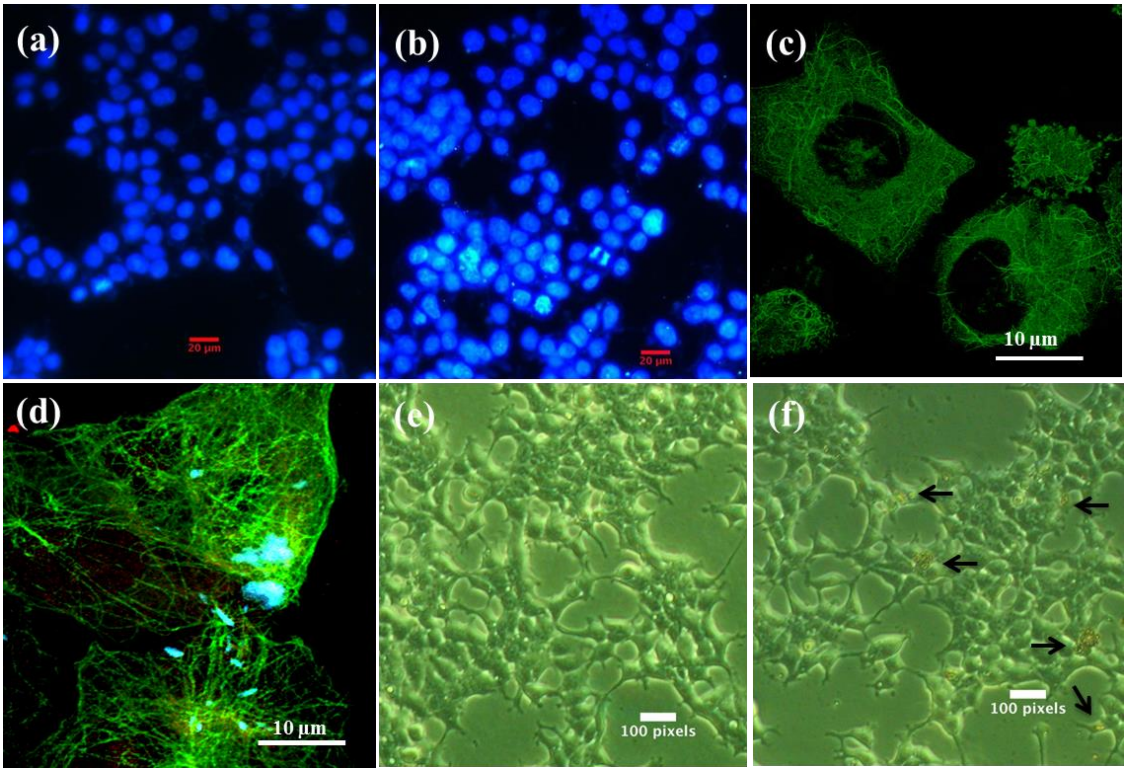

Figure 11. Fluorescence microscope images of HEK 293T cells (a) before and (b) after treating with nanoparticles of **NMOF-1** showing its nontoxicity. Blue colour represents nucleus (DAPI staining) and the cyan colour represents **NMOF-1**. (c), (d) Confocal microscope images of H1299 cells before and after treating with nanoparticles of **NMOF-1** respectively. Green colour represents cell cytoskeleton (tubulin staining), and the cyan colour represents **NMOF-1**. Inverted microscopic images of H1299 cells (e) before and (f) after treatment with **NMOF-1**. Arrows indicate the nanoparticles.

we selected human embryonic kidney cell line HEK 293T and human nonsmall cell lung carcinoma cell line H1299. The cells were grown upto 30-50% confluency for the cell

membrane permeabilization study. **NMOF-1** (40 µg) suspended in buffer was added to cells adhered on a 30 mm dish HEK and incubated for 12 h. By virtue of its self-fluorescence, we studied the distribution of **NMOF-1** in the above-mentioned cell lines. Surprisingly, we observed appreciable distribution of **NMOF-1** throughout 293T cells evidenced through confocal imaging (Figures 11a, b). Immunofluorescence using antitubulin antibody also suggested the internalization of **NMOF-1** within the cytoplasm of H1299 cells further strengthening its potential to cross cell membranes (Figures 11c, d). It is expected that the nanorods enter the cell line longitudinally due to their nanoscale dimension of width (50-100 nm). Interestingly, no floating or dead cells were observed even after 24 h of treatment signifying non-toxic effect of **NMOF-1** upon cellular internalization (Figures 11e, f). These results suggest that high stability, less toxic nanostructures of **NMOF-1** can be satisfactorily internalized into cells for bio-imaging applications under physiological conditions.

Magnetic resonance imaging (MRI) is an immensely valuable noninvasive technique used in diagnostic clinical imaging to obtain temporal information with significantly improved resolution. Changes in the longitudinal (T1) and transverse (T2) relaxations of water protons from different tissues alter the signal intensities in MR imaging. Administration of contrast agent changes the signal intensity by decreasing relaxation rate of mobile water protons in tissue. Nanocarriers containing contrast agents like Gd^{III}-chelates has been used for MR imaging applications.[20] The well-defined nanorod-like morphology, presence of large number of periodically aligned Gd^{III} ions, high biological stability, excellent cell permeability and luminescence imaging properties of **NMOF-1** could mark it as a potential bimodal MRI/optical imaging probe. To check the efficiency of **NMOF-1** as a contrast agent, T1 and T2 relaxation times were measured using a vertical wide bore (89 mm) 14.1 T NMR Microimager at 25 °C. In a typical experiment, aqueous suspension of **NMOF-1** in 0.5% agarose is tested for longitudinal and transverse relaxation times with different concentration of NCP particles (0.0, 0.6, and 1.5 mM). Relaxivities r_1 (0.3 s^{-1}/ mM) and r_2 (27.9 s^{-1}per /mM) were measured by plotting 1/T1 and 1/T2 respectively against concentration of **NMOF-1** (Figures 12a, b). The relaxivities ratio r_2/r_1 is found to be higher (95) than reported Prussian blue nanoparticles and comparable to iron oxide nanoparticles.[21] High r_2/r_1 ratio value clearly indicates that **NMOF-1** has high potential as a T2 contrast agent, and recently Gd-containing gels and complexes have been demonstrated as negative contrast agents (T2

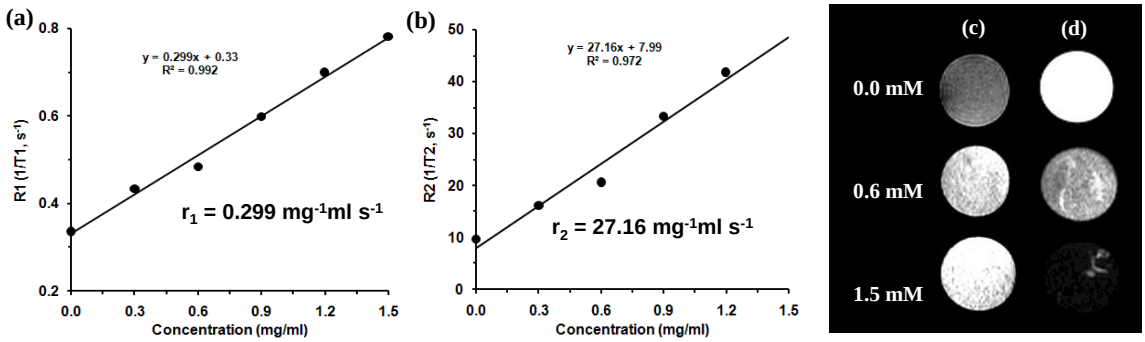

Figure 12. Variation of (a) R1 and (b) R2 of water with increasing concentration of nanorods of **NMOF-1**. The slope of the line represents the corresponding relaxivity. (c) T1- and (d) T2-weighted MR images of microfuge containing **NMOF-1** in 0.5% agarose.

contrast agents).[22] Figure 12c shows T1 and T2-weighted MR images of agarose gel containing different concentrations of **NMOF-1** as compared to control (agarose gel). In T1-weighted MR imaging, the intensity of the image increases with the concentration of contrast materials while MR intensity decreases in T2-weighted image. These results can be explained on the basis of hydrophobicity of **NMOF-1**. As shown in Figure 5b, Gd^{III} ion with coordinated water molecules are aligned in the hydrophobic pore surface derived from the interdigitation of the alkyl chains. T1 contrast agents require immediate contact with water molecules to accelerate T1 relaxation through spin-lattice interaction. However, hydrophobicity at the pore window of **NMOF-1** restricts outer water molecules to enter pore channels and interact with Gd^{III} ion which results in low longitudinal relaxivity (r_1). However, transverse (T2) relaxation (spin-spin) of coordinated water molecules is greatly shortened due to their strong interaction with Gd^{III} centre resulting in high transverse relaxivity (r_2).

2B.4 Conclusions

In conclusion, a new porous nanoscale metal-organic framework based on Gd^{III} metal ion and luminescent OPE-dicarboxylic acid has been successfully synthesized. Elegant design of OPEA with long alky chains on both ends results in interdigitation of 1D coordination chains assembled with Gd^{III} and OPEA result in a supramolecular 3D porous structure in polar solvent. CO_2 adsorption isotherms, electron microscopy images, and diffraction measurements validate proposed interdigitated structure with permanent microporosity and long range structural ordering of NCPs. Significant hydrolytic stability, low toxicity and self-luminescence features of **NMOF-1** have been successfully explored for cell internalization and optical imaging applications. Further, the presence of a large

number of Gd^{III} centers in **NMOF-1** resulted enhanced transverse relaxivity of water and showed to be potential negative contrast agent (T2 contrast agent). To the best of our knowledge, luminescent NCPs having permanent microporosity have never been reported for multimodal imaging applications.

2B.5 References

[1] a) H. -C. Zhou, J. R. Long, O. M. Yaghi, *Chem. Rev.* **2012**, *112*, 673; b) S. Kitagawa, R. Kitaura, S. Noro, *Angew. Chem. Int. Ed.* **2004**, *43*, 2334; c) J. J. I. V. Perry, J. A. Perman, M. J. Zaworotko, *Chem. Soc. Rev.* **2009**, *38*, 1400; d) S. L. James, *Chem. Soc. Rev.* **2003**, *32*, 276; e) Z. Wang, S. M. Cohen, *Chem. Soc. Rev.* **2009**, *38*, 1315; f) W. Morris, C. J. Doonan, H. Furukawa, R. Banerjee, O. M. Yaghi, *J. Am. Chem. Soc.* **2008**, *130*, 12626; g) B. Liu, M. Ma, D. Zacher, A. Betard, K. Yusenko, N. Metzler-Nolte, C. Woell, R. A. Fischer, *J. Am. Chem. Soc.* **2011**, *133*, 1734.

[2] a) K. Sumida, D. L. Rogow, J. A. Mason, T. M. McDonald, E. D. Bloch, Z. R. Herm, T.-H. Bae, J. R. Long, *Chem. Rev.* **2012**, *112*, 724; b) S. Ma, H.-C. Zhou, *Chem. Commun.* **2010**, *46*, 44; c) L. J. Murray, M. Dinca, J. R. Long, *Chem. Soc. Rev.* **2009**, *38*, 1294; d) J. Liu, P. K. Thallapally, B. P. McGrail, D. R. Brown, J. Liu, *Chem. Soc. Rev.* **2012**, *41*, 2308; e) R. Vaidhyanathan, S. S. Iremonger, G. K. H. Shimizu, P. G. Boyd, S. Alavi, T. K. Woo, *Angew. Chem. Int. Ed.* **2012**, *51*, 1826; f) P. Kanoo, G. Mostafa, R. Matsuda, S. Kitagawa, T. K. Maji, *Chem. Commun.* **2011**, *47*, 8106.

[3] a) J. -R. Li, R. J. Kuppler, H.-C. Zhou, *Chem. Soc. Rev.* **2009**, *38*, 1477; b) H. B. T. Jeazet, C. Staudt, C. Janiak, *Dalton Trans.* **2012**, *41*, 14003; c) J. -R. Li, Y. Ma, M. C. McCarthy, J. Sculley, J. Yu, H. -K. Jeong, P. B. Balbuena, H. –C. Zhou, *Coord. Chem. Rev.* **2011**, *255*, 1791; d) T. -H. Bae, J. S. Lee, W. Qiu, W. J. Koros, C. W. Jones, S. Nair, *Angew. Chem. Int. Ed.* **2010**, *49*, 9863; e) S. Xiong, Y. He, R. Krishna, B. Chen, Z. Wang, *Cryst. Growth Des.* **2013**, *13*, 2670.

[4] a) M. D. Allendorf, R. J. T. Houk, L. Andruszkiewicz, A. A. Talin, J. Pikarsky, A. Choudhury, K. A. Gall, P. J. Hesketh, *J. Am. Chem. Soc.* **2008**, *130*, 14404; b) L. Chen, K. Tan, Y.-Q. Lan, S.-L. Li, K.-Z. Shao, Z.-M. Su, *Chem. Commun.* **2012**, *48*, 5919; c) B. Chen, L. Wang, Y. Xiao, F. R. Fronczek, M. Xue, Y. Cui, G. Qian, *Angew. Chem. Int. Ed.* **2009**, *48*, 500.

[5] a) P. Horcajada, C. Serre, G. Maurin, N. A. Ramsahye, F. Balas, M. Vallet-Regi, M. Sebban, F. Taulelle, G. Ferey, *J. Am. Chem. Soc.* **2008**, *130*, 6774; b) A. C. McKinlay, R. E. Morris, P. Horcajada, G. Ferey, R. Gref, P. Couvreur, C. Serre, *Angew. Chem. Int. Ed.* **2010**, *49*, 6260; c) R. C. Huxford, J. Della Rocca, W. Lin, *Curr. Opin. Chem. Biol.* **2010**, *14*, 262; d) P. Horcajada, R. Gref, T. Baati, P. K. Allan, G. Maurin, P. Couvreur, G. Ferey, R. E. Morris, C. Serre, *Chem. Rev.* **2012**, *112*, 1232.

[6] a) B. D. Chandler, D. T. Cramb, G. K. H. Shimizu, *J. Am. Chem. Soc.* **2006**, *128*, 10403; b) V. M. Suresh, S. J. George, T. K. Maji, *Adv. Funct. Mater.* **2013**, *23*, 5585; c) Y. Takashima, V. Martinez Martinez, S. Furukawa, M. Kondo, S. Shimomura, H. Uehara, M. Nakahama, K. Sugimoto, S. Kitagawa, *Nat. Commun.* **2011**, *2*, 168.

[7] a) P. K. Thallapally, C. A. Fernandez, R. K. Motkuri, S. K. Nune, J. Liu, C. H. F. Peden, *Dalton Trans.* **2010**, *39*, 1692; b) J. Lee, O. K. Farha, J. Roberts, K. A. Scheidt, S. T. Nguyen, J. T. Hupp, *Chem. Soc. Rev.* **2009**, *38*, 1450; c) L. Ma, C. Abney, W. Lin, *Chem.*

Soc. Rev. **2009**, *38*, 1248; d) F. Song, C. Wang, J. M. Falkowski, L. Ma, W. Lin, *J. Am. Chem. Soc.* **2010**, *132*, 15390.

[8] a) B. Chen, S. Xiang, G. Qian, *Acc. Chem. Res.* **2010**, *43*, 1115; b) T. Uemura, N. Yanai, S. Kitagawa, *Chem. Soc. Rev.* **2009**, *38*, 1228; c) L. Wen, L. Zhou, B. Zhang, X. Meng, H. Qu, D. Li, *J. Mater. Chem.* **2012**, *22*, 22603; d) S. M. F. Vilela, D. Ananias, A. C. Gomes, A. A. Valente, L. D. Carlos, J. A. S. Cavaleiro, J. Rocha, J. P. C. Tome, F. A. Almeida Paz, *J. Mater. Chem.* **2012**, *22*, 18354; e) S. Mohapatra, B. Rajeswaran, A. Chakraborty, A. Sundaresan, T. K. Maji, *Chem. Mater.* **2013**, *25*, 1673; f) A. Hazra, P. Kanoo, T. K. Maji, *Chem. Commun.* **2011**, *47*, 538; g) K. Jayaramulu, P. Kanoo, S. J. George, T. K. Maji, *Chem. Commun.* **2010**, *46*, 7906; h) P. Kanoo, A. C. Ghosh, S. T. Cyriac, T. K. Maji, *Chem. Eur. J.* **2012**, *18*, 237; i) Z. Guo, R. Cao, X. Wang, H. Li, W. Yuan, G. Wang, H. Wu, J. Li, *J. Am. Chem. Soc.* **2009**, *131*, 6894.

[9] D. Maspoch, D. Ruiz-Molina, K. Wurst, N. Domingo, M. Cavallini, F. Biscarini, J. Tejada, C. Rovira, J. Veciana, *Nat. Mater.* **2003**, *2*, 190.

[10] M. D. Allendorf, C. A. Bauer, R. K. Bhakta, R. J. T. Houk, *Chem. Soc. Rev.* **2009**, *38*, 1330.

[11] a) A. Umemura, S. Diring, S. Furukawa, H. Uehara, T. Tsuruoka, S. Kitagawa, *J. Am. Chem. Soc.* **2011**, *133*, 15506; b) H. Xu, F. Liu, Y. Cui, B. Chen, G. Qian, *Chem. Commun.* **2011**, *47*, 3153.

[12] a) J. Della Rocca, D. Liu, W. Lin, *Acc. Chem. Res.* **2011**, *44*, 957; b) A. Carne, C. Carbonell, I. Imaz, D. Maspoch, *Chem. Soc. Rev.* **2011**, *40*, 291; c) I. Imaz, J. Hernando, D. Ruiz-Molina, D. Maspoch, *Angew. Chem. Int. Ed.* **2009**, *48*, 2325; d) R. Nishiyabu, N. Hashimoto, T. Cho, K. Watanabe, T. Yasunaga, A. Endo, K. Kaneko, T. Niidome, M. Murata, C. Adachi, Y. Katayama, M. Hashizume, N. Kimizuka, *J. Am. Chem. Soc.* **2009**, *131*, 2151; e) K. E. deKrafft, W. S. Boyle, L. M. Burk, O. Z. Zhou, W. Lin, *J. Mater. Chem.* **2012**, *22*, 18139.

[13] a) W. J. Rieter, K. M. L. Taylor, W. Lin, *J. Am. Chem. Soc.* **2007**, *129*, 9852; b) P. Horcajada, T. Chalati, C. Serre, B. Gillet, C. Sebrie, T. Baati, J. F. Eubank, D. Heurtaux, P. Clayette, C. Kreuz, J.-S. Chang, Y. K. Hwang, V. Marsaud, P.-N. Bories, L. Cynober, S. Gil, G. Ferey, P. Couvreur, R. Gref, *Nat. Mater.* **2010**, *9*, 172; c) K. Otsubo, T. Haraguchi, O. Sakata, A. Fujiwara, H. Kitagawa, *J. Am. Chem. Soc.* **2012**, *134*, 9605; d) W. J. Rieter, K. M. Pott, K. M. L. Taylor, W. Lin, *J. Am. Chem. Soc.* **2008**, *130*, 11584; e) K. M. L. Taylor, W. J. Rieter, W. Lin, *J. Am. Chem. Soc.* **2008**, *130*, 14358; f) O. Shekhah, K. Hirai, H. Wang, H. Uehara, M. Kondo, S. Diring, D. Zacher, R. A. Fischer, O. Sakata, S. Kitagawa, S. Furukawa, C. Woll, *Dalton Trans.* **2011**, *40*, 4954; g) B. Liu, O. Shekhah, H. K. Arslan, J. Liu, C. Woll, R. A. Fischer, *Angew. Chem. Int. Ed.* **2012**, *51*, 807; h) D. Bradshaw, A. Garai, J. Huo, *Chem. Soc. Rev.* **2012**, *41*, 2344.

[14] K. M. L. Taylor-Pashow, J. Della Rocca, Z. Xie, S. Tran, W. Lin, *J. Am. Chem. Soc.* **2009**, *131*, 14261.

[15] K. M. L. Taylor, A. Jin, W. Lin, *Angew. Chem. Int. Ed.* **2008**, *47*, 7722.

[16] a) Q. Li, A. V. Rukavishnikov, P. A. Petukhov, T. O. Zaikova, C. S. Jin, J. F. W. Keana, *J. Org. Chem.* **2003**, *68*, 4862; b) A. Mangalum, R. J. Gilliard Jr., J. M. Hanley, A. M. Parker, R. C. Smith, *Org. Bio. Chem.* **2010**, *8*, 5620.

[17] S. Chatterjee, P. Mizar, R. Cassel, R. Neidl, B. R. Selvi, D. V. Mohankrishna, B. M. Vedamurthy, A. Schneider, O. Bousiges, C. Mathis, *J. Neurosci.* **2013**, *33*, 10698.

[18] a) A. Dutta, J. Mondal, A. K. Patra, A. Bhaumik, *Chem. Eur. J.* **2012**, *18*, 13372; b) H. Wei, B. Li, Y. Du, S. Dong, E. Wang, *Chem. Mater.* **2007**, *19*, 2987; c) E. Noh, S. Park, S.

Kang, J. Y. Lee, J. H. Jung, *Chem. Eur. J.* **2013**, *19*, 2620; d) J. H. Lee, S. Kang, J. Y. Lee, J. Jaworski, J. H. Jung, *Chem. Eur. J.* **2013**, *19*, 16665.

[19] K. Yoosaf, A. R. Ramesh, J. George, C. H. Suresh, K. G. Thomas, *J. Phys. Chem. C* **2009**, *113*, 11836.

[20] E. Battistini, E. Gianolio, R. Gref, P. Couvreur, S. Fuzerova, M. Othman, S. Aime, B. Badet, P. Durand, *Chem. Eur. J.* **2008**, *14*, 45511.

[21] a) P. Chaturbedy, S. Chatterjee, R. B. Selvi, A. Bhat, M. K. Kavitha, V. Tiwari, A. B. Patel, T. K. Kundu, T. K. Maji, M. Eswaramoothy, *J. Mater. Chem. B* **2013**, *1*, 939; b) J. Qin, S. Laurent, Y. S. Jo, A. Roch, M. Mikhaylova, Z. M. Bhujwalla, R. N. Muller, M. Muhammed, *Adv. Mater.* **2007**, *19*, 1874.

[22] a) C. Richard, B.-T. Doan, J.-C. Beloeil, M. Bessodes, E. Toth, D. Scherman, *Nano Lett.* **2008**, *8*, 232; b) C.-K. Lim, A. Singh, J. Heo, D. Kim, K. E. Lee, H. Jeon, J. Koh, I.-C. Kwon, S. Kim, *Biomaterials* **2013**, *34*, 6846; c) M. F. Casula, P. Floris, C. Innocenti, A. Lascialfari, M. Marinone, M. Corti, R. A. Sperling, W. J. Parak, C. Sangregorio, *Chem. Mater.* **2010**, *22*, 1739.

Chapter 3A

Framework Induced Emission and Bang Gap Engineering in Donor-Acceptor Conjugated Microporous Polymers

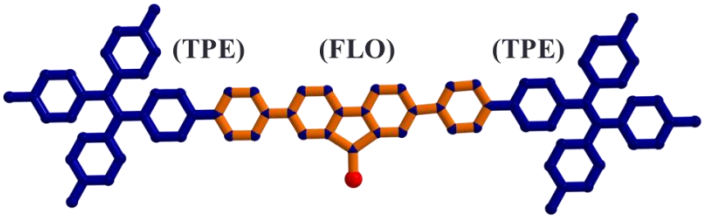

(Donor-Acceptor Conjugated Microporous Polymer)

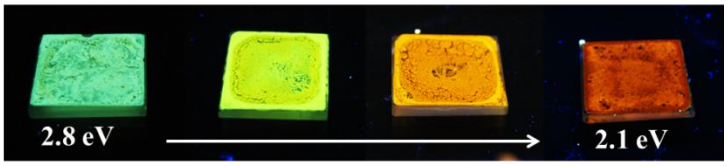

Summary

Band gap engineering in donor-acceptor conjugated microporous polymers (CMPs) is a potential way to increase the solar energy harvesting property of polymers. This chapter demonstrates, framework induced emission (FIE) in tetraphenylethene (TPE) based CMPs and utilization of FIE for precise band gap tuning in donor-acceptor CMPs where the TPE acts as donor and fluorenone (F) acts as acceptor. **TPE-CMP-1** is constructed from tetrakis(4-bromophenyl)ethene and 4,4′-diethynylbiphenyl while **TPE-CMP-F's** (**TPE-CMP-1**, **TPE-CMP-F0**, **TPE-CMP-F1**, **TPE-CMP-F2** and **TPE-CMP-F3**) have been prepared by replacing the linker with fluorenone (0.0, 0.1, 0.5 and 2 eq w.r.t TPE) through C-C coupling reaction. **TPE-CMP-1** adsorbs N_2 at 77 K (surface area = 854 m^2g^{-1}) while **TPE-CMP-F's** are nonporous to N_2. **TPE-CMP-F's** showed type-I CO_2 uptake profile at 195 K. **TPE-CMP-1** and **TPE-CMP-F0** showed strong FIE at 550 and 524 nm. All fluorenone containing polymers **TPE-CMP-F1, 2, and 3** showed strong intramolecular charge transfer (ICT) absorption band at 480 nm and emission in the range of 540-580 nm. Increasing the fluorenone in the polymer reduces the band gap and is finely tuned from 2.8 eV to 2.1 eV. **TPE-CMP-F's** (except $F_{0.0}$CMP) also showed excitation energy transfer from TPE to fluorenone as evident from life time analysis.

V. M. Suresh, S. Bonakala, S. Roy, S. Balasubramanian, T. K. Maji, *J. Phys. Chem. C* **2014**, *118*, 24369.

V. M. Suresh, A. De, S. J. George, T. K. Maji, **Manuscript under preparation**

3A.1 Introduction

Tetraphenylethene (TPE) is known for its typical aggregation-induced emission (AIE) behaviour due to restricted rotation of phenyl rings in concentrated solutions/solid state[1] and it has been shown to have potential applications in organic light emitting diodes,[2a] field effect transistors (FET)[2b] and sensors.[2c] In a recent study, Dinca *et al.* demonstrated turn-on luminescence in a MOF with TPE tetracarboxylate linker, where the phenyl rotations of TPE were restricted by metal coordination.[3a,b] On the other hand, Jiang *et al.* showed integration of TPE into a conjugated microporous polymer result in strong emission to the polymer where the strong framework forces through C-C covalent bonds restrict the phenyl rotation.[3c,d] Microporous organic polymers, [4] especially conjugated microporous polymers (CMPs) resembling conjugated polymer counterparts in their optical behaviour, have been of great interest in organic light emitting diodes, organic electronics, light-harvesting, polymer solar cells, photocatalysis, sensing and gas storage.[5] In order to achieve these luminescence derived applications in CMPs fine control over their absorbance/emission or band gap is crucial. Improving the visible light absorption capacity of these CMPs by reducing the band gap is one of the efficient approaches to increase their performance in photovoltaic devices or for photochemical water splitting reactions.[6a,b] Recently, Cooper *et al.* reported such tunable band gap in pyrene based CMPs by using copolymerization strategy.[6c] Design and synthesis of donor-acceptor polymers with visible light photon absorbing ability based on intramolecular charge transfer is of paramount importance for tuning the band gap.[7] Such band gap engineering in CMPs can also give rise to tunable emission for optoelectronic applications.[7] In contrast to linear conjugated polymers where the inter-chain π-π interactions between chromophore segments in aggregates lead to annihilation of excitation energy, CMPs with three-dimensional polymeric network structures possesses spatially separated chromophoric chains and show efficient exciton migration along the polymer chain motifs owing to electronic communication through conjugated backbone.[3c] The aspects of extended π-conjugation and choice of suitable chromophoric monomers can lead to semiconducting porous polymer networks with unique electronic properties.[8a] Recently, Jiang *et al.* reported the efficient exciton migration in a tetraphenylethene based CMP and a polyphenylene CMP for excitation energy transfer applications.[8b,c] Here in we intend to do a systematic study of band gap tuning in donor(tetraphenylethene)-acceptor(fluorenone) CMP by changing the donor-acceptor

concentration in the polymers. Fluorenone has been well studied as strong acceptor and its charge transfer properties are reported in linear conjugated polymers.[9] We, envision the donor-acceptor CMP containing TPE and fluorenone could show efficient charge transfer properties thereby the band gap can be reduced by controlling the strength of the CT character in the polymer.[9] Initially the FIE of TPE-CMP is tested by synthesizing CMP using a rigid spacer, 4,4′-diethynylbiphenyl, then the donor-acceptor polymer of TPE and fluorenone are synthesized. By changing the equivalents of fluorenone content during the polymerization reaction, a series of polymers with different emission properties were synthesized thereby the band gap is finely tuned.

3A.2 Experimental section

3A.2.1 Materials

Tetrakis(triphenylphosphine)palladium(0), bis(triphenylphosphine)palladium(II)di chloride and cuprous iodide (CuI), tetraphenylethene, 2,7-dibromo-9-fluorenone, 4,4′-diiodobiphenyl were purchased from Sigma-Aldrich Chemical Co. Required solvents were dried prior to use.

3A.2.2 Physical measurements

Elemental analysis was carried out using Thermo Scientific Flash 2000 CHN analyzer. Infrared spectral studies were done by making samples with KBr pellets using Bruker FT-IR spectrometer. Thermal stability was analyzed using Mettler Toledo TGA 850 instrument under inert atmosphere in the temperature range of 30-800 °C at a heating rate of 5 °C/min. Powder X-ray diffraction studies of the samples were recorded on a Bruker D8 discover instrument using Cu Kα radiation. Morphological studies have been carried out using Lica-S440I field emission scanning electron microscope (FESEM) by placing samples on a silicon wafer under high vacuum with an accelerating voltage of 10 kV. Transmission electron microscopy (TEM) analysis has been performed using JEOL JEM-3010 with an accelerating voltage at 300 kV. For this analysis **TPE-CMP-1** is dispersed in ethanol by sonication before drop casting on a carbon-coated copper grid. Porosity measurements were carried out using QUNATACHROME QUADRASORD-SI analyser at 77 K for N_2 and 195 K for CO_2. Fluorescence studies were accomplished using Perkin Elmer Ls 55 Luminescence spectrometer. Solid state ^{13}C cross-polarization magic angle spinning (CP/MAS) NMR spectra were measured on a varian infinity plus 300WB spectrometer at a MAS rate of 5 kHz and a CP contact time of 1.4 ms. ^{1}H NMR is

recorded on a Bruker AV-400 spectrometer with chemical shifts reported as ppm.

3A.2.3 Synthesis of tetrakis(4-bromophenyl)ethene

Tetraphenylethene (0.77 mmol, 500 mg) is dissolved in dry dichloromethane (DCM) (20 mL) and cooled to 0 °C followed by addition of Br_2 (1.54 mmol, 0.04 mL). Reaction mixture is stirred at room temperature for 15 hrs, the excess Br_2 is quenched by adding aq. $N_2S_2O_4$(Hypo). Mixture is extracted with DCM and concentrated under reduced pressure. The crude product is purified by column chromatography by eluting with hexane. White solid, Yield: 80%.

3A.2.4 Synthesis of 2,7-biphenyl-9H-fluoren-9-one

2,7-dibromo-9H-fluoren-9-one (1.47 mmol, 500 mg) and phenylboronic acid (2.9 mmol, 361 mg) is dissolved in dry THF (10 mL) and degassed/purged with N_2. To this, $Pd(PPh_3)_4$ (0.03 mmol, 33mg) is added followed by aq. K_2CO_3. The reaction mixture is refluxed for 24 hrs and cooled to room temperature. The mixture is added to water and extracted with DCM and filtered over Na_2SO_4. The solution is concentrated under reduced pressure to result in crystalline yellow solid. Yield, 60 %.

3A.2.5 Synthesis of TPE-CMP-1

The Sonogashira-Hagihara coupling reaction of 1,1,2,2-tetrakis(4-bromophenyl)ethene and 4,4′-diethynylbiphenyl in *N*,*N*′-dimethylformamide(DMF) resulted in conjugated microporous polymer **TPE-CMP-1**. In a typical synthesis, a mixture of 1,1,2,2-tetrakis(4-bromophenyl)ethene (0.15 mmol) and 4,4′-diethynylbiphenyl (0.3 mmol) is dissolved in 3 mL dry DMF and 1.5 mL anhydrous triethylamine, and the mixture was degassed by four freeze-thaw pump cycles and purged with N_2. To this, $Pd(PPh_3)_4$ (0.03 mmol) and CuI (0.06 mmol) was added under continuous N_2 flow. The reaction mixture was refluxed for 48 h and cooled to room temperature. The yellow precipitates were collected through filtration and washed with methanol. Final purification was done using Soxhlet extraction to remove traces of catalysts with tetrahydrofuran (THF) and methanol for 24 h. Yield: 60%. Anal. Calcd for $C_{86}H_{48}$: C 95.8, H 4.1. Found: C 90.61, H 4.1 (0.3-0.6 mol% Pd is found from EDAX analysis).

3A.2.6 Synthesis of TPE-CMP-F0

In a typical synthesis, a mixture of tetrakis(4-bromophenyl)ethene (0.15 mmol), 1,4-benzenediboronic acid (0.3 mmol) and 4,4′-dibromobiphenyl (0.3 mmol) were taken in a Schlenk tube and dissolved in dry DMF. The reaction mixture is allowed for Freeze-

Thaw pump cycles and purged with N_2 continuously. To the mixture $Pd(PPh_3)_4$ (0.0105 mmol, 12 mg) is added under N_2 flow. To the mixture aq. K_2CO_3 is added and refluxed for 24 hrs under N_2 atmosphere. Precipitates were collected by filtration and washed with ethanol and THF several times. Final purification was done using Soxhelet extraction with THF and methanol for 48 hrs. EDAX: C, 96; Pd, 0.31.

3A.2.7 Synthesis of TPE-CMP-F1

Similar reaction procedure of **TPE-CMP-F0** is followed except 2,7-dibromo-9H-fluoren-9-one (0.1 eq, 0.015 mmol) is used instead of 4,4′-dibromobiphenyl. Soxhelet purified with THF and methanol for 48 hrs each. EDAX: C, 91; O, 0.88; Pd, 0.31.

3A.2.8 Synthesis of TPE-CMP-F2

Similar reaction procedure of **TPE-CMP-F0** is followed except 2,7-dibromo-9H-fluoren-9-one (0.5 eq, 0.075 mmol) is used. Soxhelet purified with THF and methanol for 48 hrs each. EDAX: C, 89; O, 1.6; Pd, 0.33.

3A.2.9 Synthesis of TPE-CMP-F3

Similar reaction procedure of **TPE-CMP-F0** is followed except 2,7-dibromo-9H-fluoren-9-one (2 eq, 0.3 mmol) is used. Soxhelet purified with THF and methanol for 48 hrs each. EDAX: C, 81; O, 14; Pd, 0.92.

3A.3 Results and discussion

3A.3.1 Structural characterization and morphology

Metal catalyzed C-C coupling has been a versatile route for the construction of several high surface area CMPs.[5a] Sonogashira coupling of tetrakis(4-bromophenyl)ethene and 4,4′-diethynylbiphenyl in DMF under reflux conditions yields a 3D polymeric network, **TPE-CMP-1** and **TPE-CMP-F's** are prepared via Suzuki-Miyura coupling strategy as described in experimental section(Figure 1). Fourier transform infrared spectrum (FT-IR) of **TPE-CMP-1** shows bands at 2206 and 1635 cm^{-1} corresponding to C≡C and C=C stretching vibrations (Figure 2a), thereby confirming the incorporation of TPE and linker in **1**. The peaks at 1652 cm^{-1}, 3436 cm^{-1} in case of **TPE-CMP-F0** are assigned to the C=C and aromatic C-H stretching vibrations (Figure 2b). All the other polymers (**TPE-CMP-F1, TPE-CMP-F2** & **TPE-CMP-F3**) showed strong band at 1713 cm^{-1} corresponding to the carbonyl of the fluorenone suggesting its incorporation in the polymers (Figure 2b). Solid-state ^{13}C/CP-MAS NMR of **TPE-CMP-**

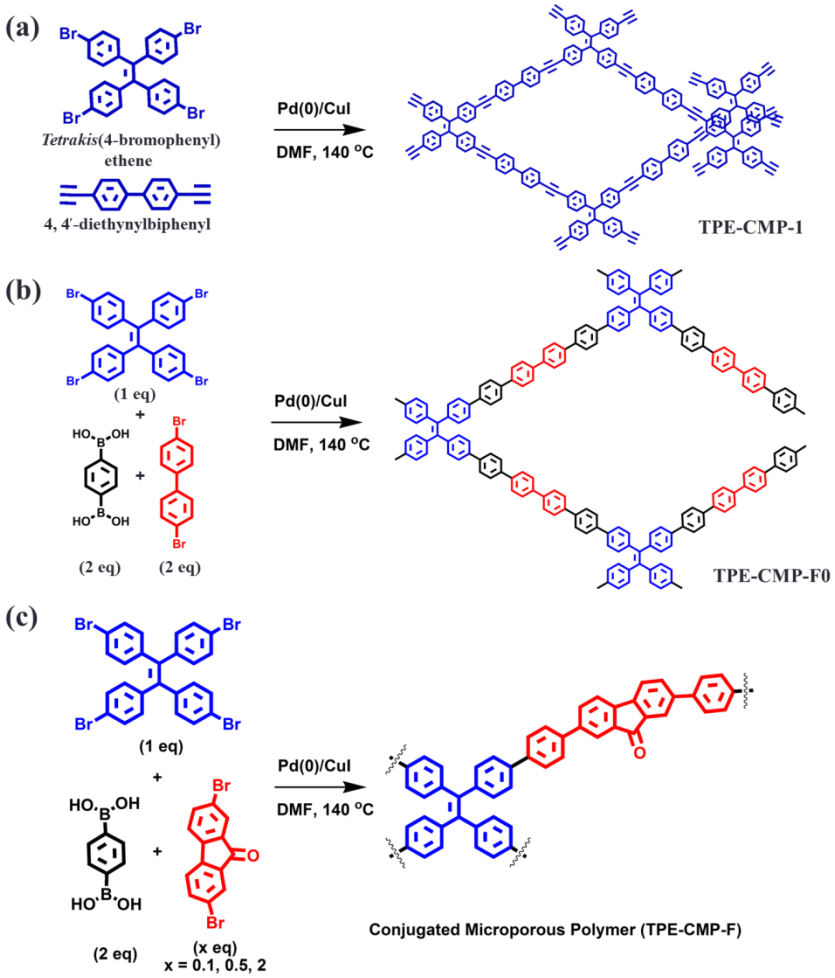

Figure 1. Representation of synthetic scheme of (a) **TPE-CMP-1**using Sonogashira coupling and (b) **TPE-CMP-F0**, (c) **TPE-CMP-F1-3** using Suzuki-Miyura coupling.

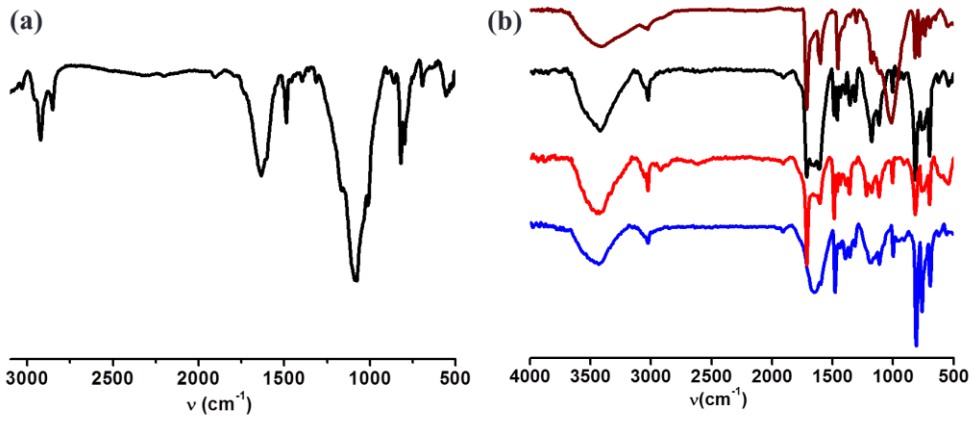

Figure 2. Fourier Transform infrared (FTIR) spectrum of (a) **TPE-CMP-1** and (b) **TPE-CMP-F0** (blue), **TPE-CMP-F1** (red), **TPE-CMP-F2** (black) **and TPE-CMP-F3** (wine red).

1 shows a signal at 91 ppm due to C≡C of the linker, while the peaks in the range 120-150 ppm corresponds to aromatic carbons of TPE and diethynylbiphenyl linker (Figure 3a). Whereas, **TPE-CMP-F's** show peaks in the range of 120-140 ppm assigned to the

aromatic 'C' of the phenyls of both TPE and fluorenone and a peak at 193 cm^{-1} is observed in **TPE-CMP-F1, TPE-CMP-F2** and **TPE-CMP-F3** which is assigned to the carbonyl 'C' of the fluorenone moiety (Figure 3b) . It is worthy to mention, the peak intensity increases with increasing the fluorenone content in the polymer. Powder X-ray

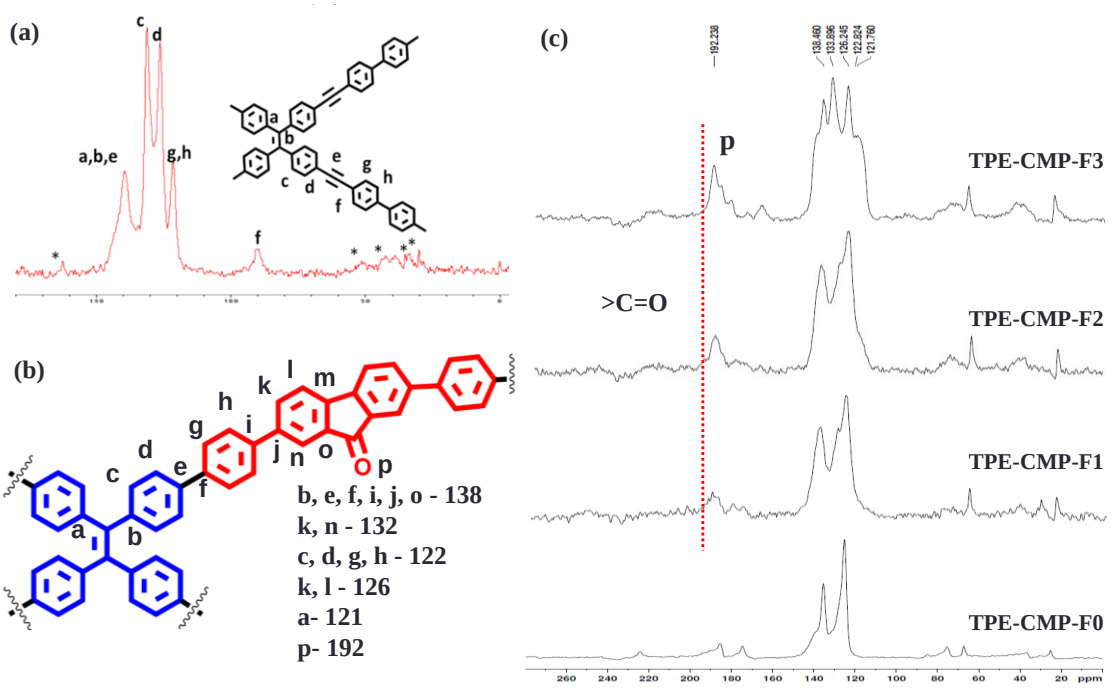

Figure 3. ^{13}C-CP/MAS solid state NMR spectra of (a) **TPE-CMP-1** and (c) **TPE-CMP-F0-3**. (b) Schematic of **TPE-CMP-F's**.

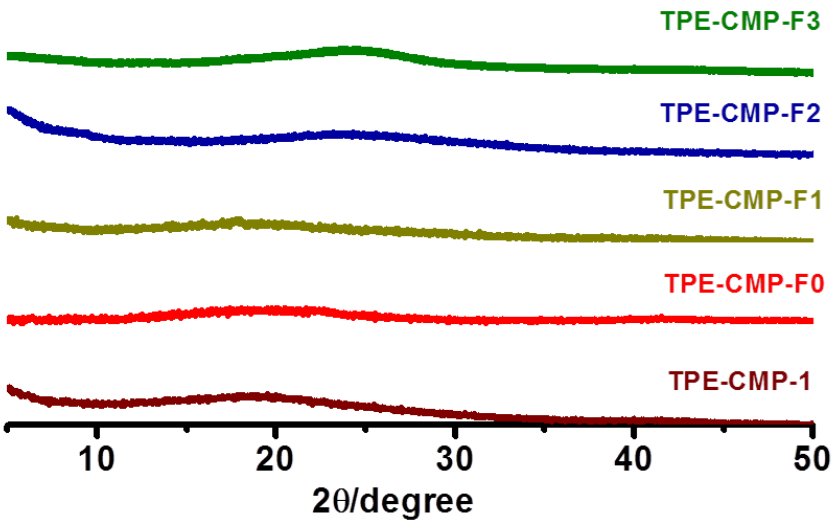

Figure 4. PXRD of all the polymers **TPE-CMP-1** (wine), **TPE-CMP-F0** (red), **TPE-CMP-F1** (light yellow), **TPE-CMP-F2** (blue) and **TPE-CMP-F3** (green).

diffraction (PXRD) measurements revealed all the polymers are amorphous in nature (Figure 4), indicating the absence of a long-range order in the structure, which suggests that the polymerization reaction is likely to be a kinetically controlled. Field emission scanning electron microscopy (FESEM) shows formation of spherical particles linked together with an average size of 300-500 nm for all the polymers (Figure 5). The energy-

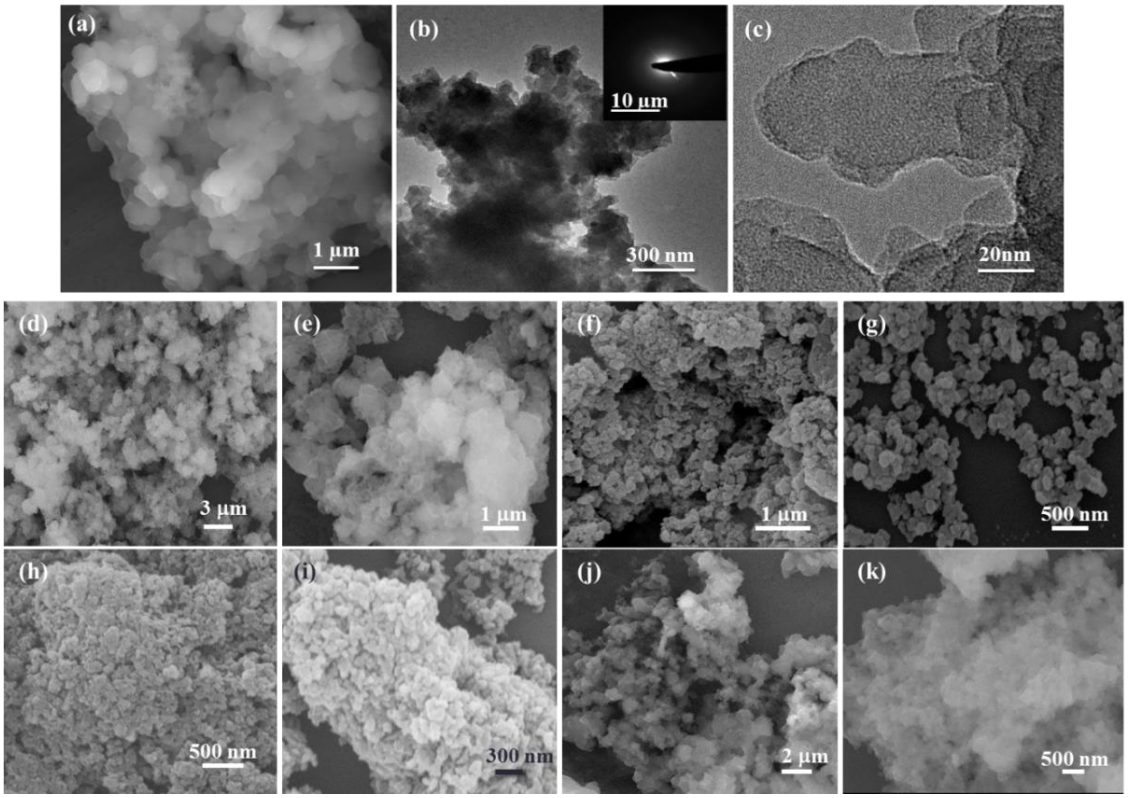

Figure 5. (a) SEM, (b), (c) TEM images of **TPE-CMP-1** (Inset: ED pattern). SEM image of (d), (e) **TPE-CMP-F0**; (f), (g) **TPE-CMP-F1**; (h), (i) **TPE-CMP-F2** and (j), (k) **TPE-CMP-F3**.

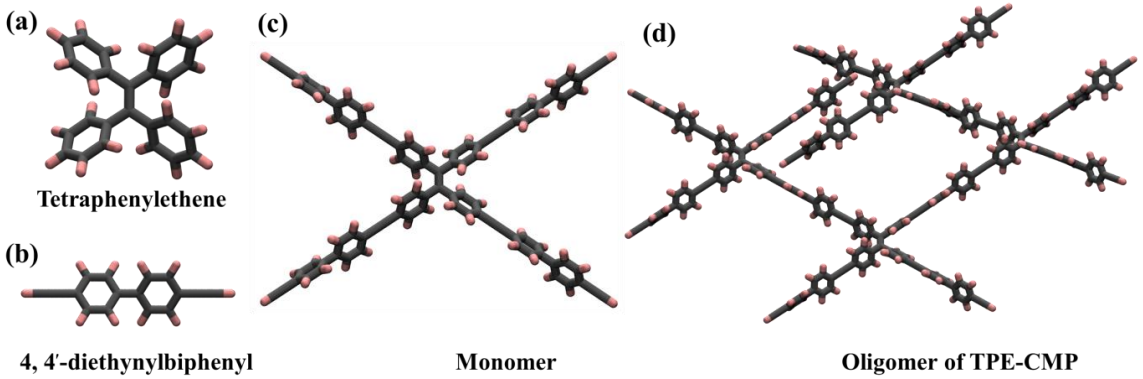

Figure 6. Optimized molecular groups constituting the polymer, **TPE-CMP-1**; (a) tetraphenylethene, (b) 4,4′-diethynylbiphenyl, (c) monomer constituted by these groups and (d) geometry of an oligomer unit of **TPE-CMP-1**. Colour scheme: C-grey and H-Pink.

minimized configuration of oligomer unit of **TPE-CMP-1** shows a propeller-like noncoplanar geometry of the four phenyl groups oriented with respect to the central ethene group; these are further extended through 4,4′-diethynylbiphenyl units in four different directions (Figure 6). Hence, the resulting structure can be visualized as an extended three-dimensional polymer.

3A.3.2 Thermal stability and porosity

Thermogravimetric analysis (TGA) of **TPE-CMP-1** suggests no apparent weight loss up to 300 °C, and further heating results in steady weight loss (up to 70%) (Figure 7a). All the **TPE-CMP-F's** observed to have high thermal stability as suggested by thermogravemetric analysis (TGA) (Figure 7b). TGA of **TPE-CMP-F0** showed no appreciable weight loss till 350 °C, on further heating a continuous weight loss of nearly 50% is observed till 800 °C, on the other hand, **TPE-CMP-F1, TPE-CMP-F2** and **TPE-CMP-F3** show no appreciable weight loss upto 600 °C, and on further heating 10-20% weight loss is observed. These results suggest that the incorporation of fluorenone moiety into the polymer chain leads to an increase of thermal stability of the polymer. All the samples were activated at 160 °C under vacuum prior to gas adsorption measurements. Adsorption measurement of N_2 for **TPE- CMP-1** at 77 K up to a pressure of 1 atm shows steep uptake at low pressures signifying the microporous nature of **TPE-CMP-1** (Figure 8a), and the final uptake is observed to be 471 mL/g. Application of the Brunauer–Emmet–Teller (BET) model on the N_2 isotherm yielded a surface area of 854 m^2/g and corresponding Langmuir surface area is 1256 m^2/g. Also, a nonlocal density functional theory (NL-DFT) was fitted to the N_2 adsorption isotherm to estimate the pore volume

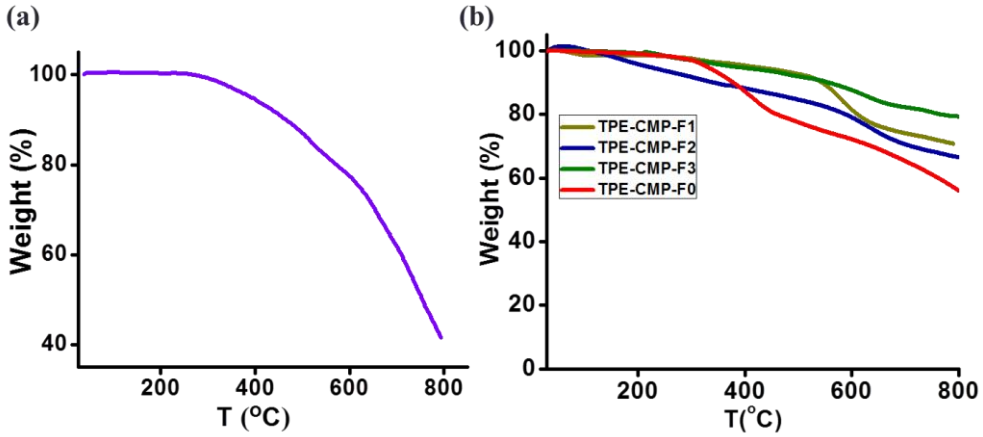

Figure 7. TGA profiles of (a) **TPE-CMP-1** and (b) **TPE-CMP-F's** in the range of 30-800 °C at 5 °C/min.

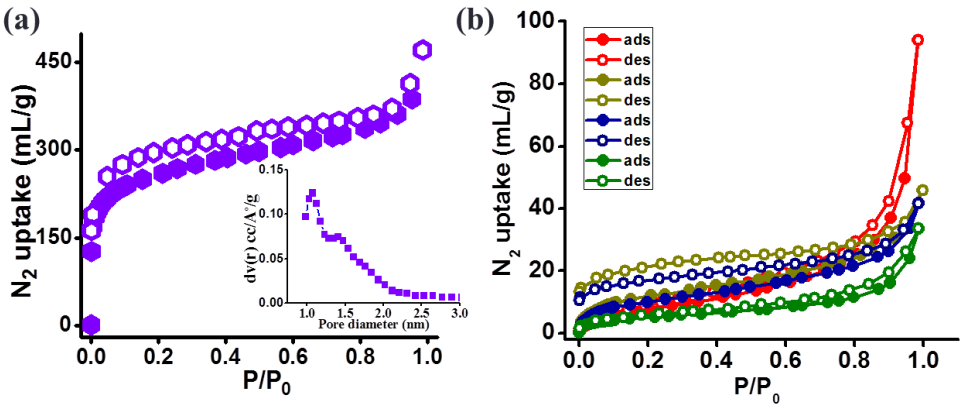

Figure 8. (a) N_2 adsorption isotherms of **TPE-CMP-1** and (b) **TPE-CMP-F's** at 77 K. Inset of (a): Pore size distribution of **TPE-CMP-1**.

and pore size distribution of **TPE-CMP-1**. The average pore size was found to be 1.08 nm, reiterating the microporous nature of the framework (Figure 8a; Inset), and the pore volume is estimated to be about 0.57 cm^3/g. Whereas, N_2 adsorption measurements of all **TPE-CMP-F's** at 77 K showed only type-II uptake profile thereby suggesting their non-porous nature to N_2 and surface adsorption (Figure 8b). It is to be noted that the relative

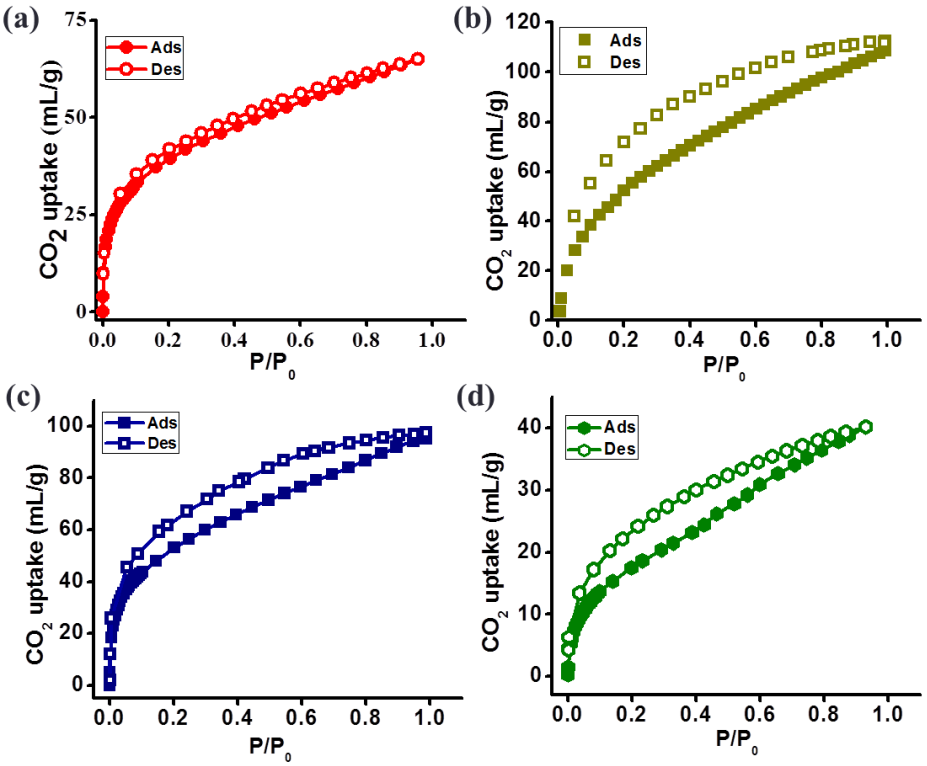

Figure 9. CO_2 adsorption isotherms of **TPE-CMP-F's** at 195 K: (a) **TPE-CMP-F0**, (b) **TPE-CMP-F1**, (c) **TPE-CMP-F2** and (d) **TPE-CMP-F3**.

uptake amount is observed to be decreasing on moving from **TPE-CMP-F0** to **TPE-CMP-F3**, this is attributed to the pore blockage due to increase in degree of

interpenetration with increase in the fluorenone concentration due to the increase in length of the connecting linker. In contrast, CO_2 adsorption measurements at 195 K showed appreciable CO_2 uptake in the low pressure region with type-I uptake profile suggesting microporous (< 2 nm) nature of all **TPE-CMP-F's** and the final amount is observed to be 65 mL (**TPE-CMP-F0**), 109 mL (**TPE-CMP-F1**), and 98 mL (**TPE-CMP-F2**) and 40 mL (**TPE-CMP-F3**) (Figure 9). This selective uptake of CO_2 compared to N_2 is driven by the interactions between polar carbonyl group decorated on the pore surface of the polymer and CO_2; however the uptake decreases with increase in fluorenone concentration in polymer due to interpenetration which ultimately decreases accessible pores. These results clearly suggest that it is possible to tune the pore size and surface area of the **TPE-CMP-F's** by controlling the amount of fluorenone within the polymer. Langmuir surface areas are calculated to be 366 m^2/g, 612 m^2/g, 537 m^2/g and 226 m^2/g.

3A.3.3 Photophysical studies

1,1,2,2-Tetrakis(4-bromophenyl)ethene shows strong blue emission with λ_{max} = 445 nm in the solid state due to AIE phenomenon (Figure 10a, b) and is weakly emissive in dilute solutions due to fast dynamics of phenyl rings. On the other hand, **TPE-CMP-1** exhibits strong greenish- yellow emission in both solution dispersed and solid state with a maximum at 550 nm when excited at 390 nm (Figure 10a, c). AIE is essentially driven by the molecular interactions between TPE cores in aggregated state,[1a] and the approach of

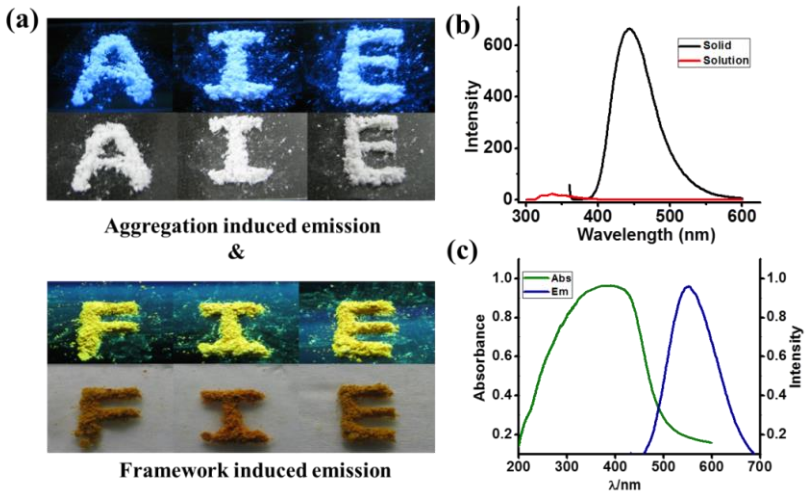

Figure 10. (a) Top: Images of tetrakis(4-bromophenyl)ethene and Bottom: Images of **TPE-CMP-1** under UV light and day light. (b) Emission spectrum of tetrakis(4-bromophenyl)ethene in solution (red) and in solid state (black). (c) Normalized absorption (green) and emission spectrum (blue) of **TPE-CMP-1**.

TPE molecules through aggregation is essential; however, the three-dimensional structure of **TPE-CMP-1** leaves no possibility for the close approach of two TPE units in the polymer. Hence, we anticipate that the fluorescence turn-on of **TPE-CMP-1**in the polymeric state likely occurs due to the restricted rotation of phenyls of TPE integrated in the network. Red shifted emission of **TPE-CMP-1** can be attributed to the increase in the extent of π-orbital overlap of TPE in the polymer structure.

Prior to the study of **TPE-CMP-F's** photophysical properties, emission property of TPE and biphenylfluorenone in monomeric state is studied. TPE immobilized in poly(ethylene glycol)-*block*-poly(propylene glycol)-*block*-poly(ethylene glycol) matrix showed moderate emission at 438 nm (λ_{ex} = 350 nm) due to phenyl rotation restriction while biphenylfluorenone in dichloromethane emits at 396 nm (540 nm in solid state) (Figure 11). Polymer **TPE-CMP-F0** showed similar behaviour as that of **TPE-CMP-1**; it showed a single broad absorption (Figure 12a, black) band with maximum at 310 nm

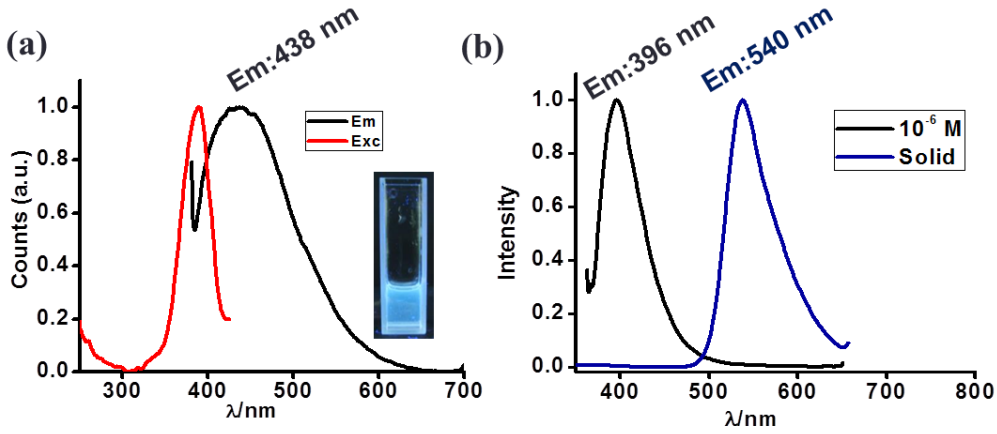

Figure 11. Emission spectrum of (a) TPE in a polymer matrix (Red: Excitation spectrum) and (b) biphenylfluorenone in dilute solution (10^{-6} M) (black) and solid state (blue).

(π-π^* transition of TPE) and emit at 525 nm (due to restricted rotation of phenyls) (Figure 12b, black). On the other hand, absorbance spectra of **TPE-CMP-F1**, **TPE-CMP-F2** and **TPE-CMP-F3** showed a broad band around 350 nm (π-π^* transition) along with an additional band in the visible region at 480 nm which is likely related to the intramolecular charge transfer (ICT) transition from TPE to fluorenone segment in the polymer.[9a] It is to be noted that the intensity of 480 nm band is observed to increase with increasing the amount of fluorenone concentration in polymer (Figure 12a). **TPE-CMP-F's** showed emission at 540 (**TPE-CMP-F1**), 560 (**TPE-CMP-F2**), and 580 nm (**TPE-CMP-F3**) on excitation at 350 nm and are attributed to the ICT emission. All polymers showed

an additional emission band at 425 nm which is assigned to TPE segment in the polymer (Figure 12b, c). The red shift in long wavelength emission band clearly suggests the stabilization of ICT state on moving from **TPE-CMP-F1** to **TPE-CMP-F3**. ICT emission in **TPE-CMP-F's** is further evident from solvent dependent emission spectra (Figure 13a), in a nonpolar solvent like hexane the relative intensity of 580 nm band is observed to be

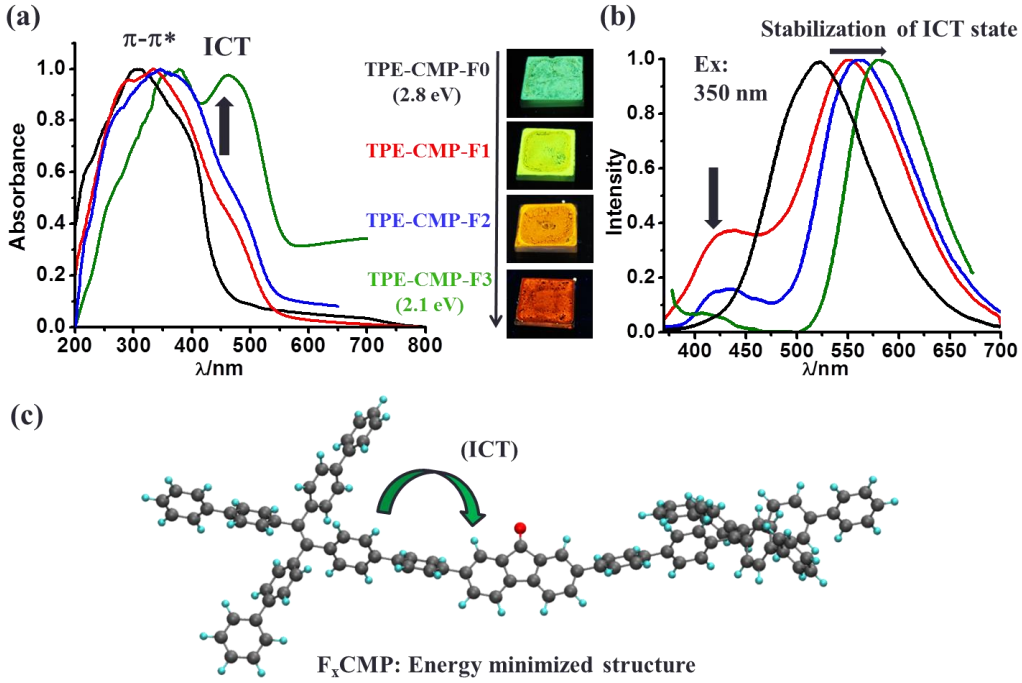

Figure 12. Solid state (a) absorption and (b) emission spectra of **TPE-CMP-F0** (black), **TPE-CMP-F1** (red), **TPE-CMP-F2** (blue) and **TPE-CMP-F3** (green). (c) Energy minimized structure of the **TPE-CMP-F's** fragment showing ICT.

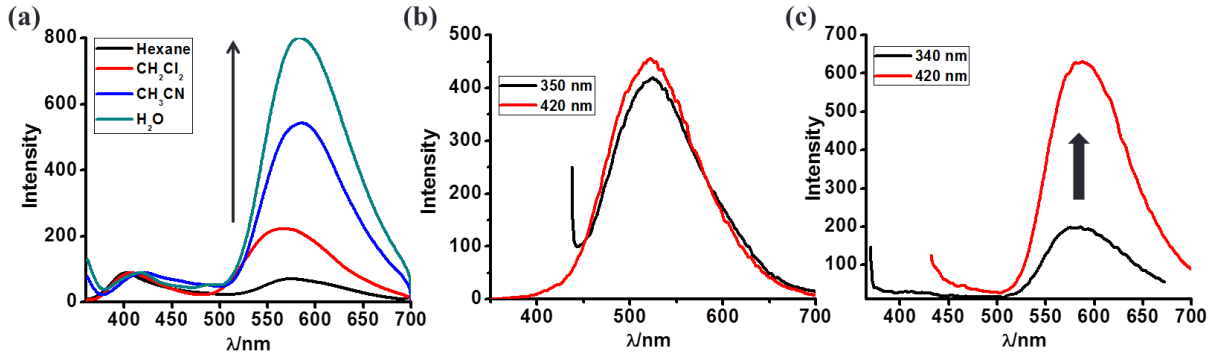

Figure 13. (a) Emissions spectra of **TPE-CMP-F3** in different solvents showing emission intensity changes of 580 nm band. Emission spectra of (b) **TPE-CMP-F0** and (c) **TPE-CMP-F3** at 350 nm (black) and 420 nm (red) excitation wavelength.

weak, however with changing the solvent to CH_2Cl_2 the emission intensity at 580 nm increases and in a highly polar solvent like H_2O the emission intensity is observed to

higher. This strong dependence of emission at 580 nm on polarity of the solvent clearly suggests the ICT character of the excited state and its stabilization in a highly polar solvent. ICT emission in **TPE-CMP-F3** is further supported by excitation dependent emission spectra (Figure 13b, c), when **TPE-CMP-F3** is excited at 420 nm (ICT absorption is stronger) emission intensity at 580 nm is observed to be higher compared to 340 nm excitation (CT absorption is weak). In contrast, **TPE-CMP-F0s** showed no such excitation dependent emission intensity changes. These results clearly suggest that the long wavelength emission in **TPE-CMP-F's** is indeed associated with intramolecular charge transfer.

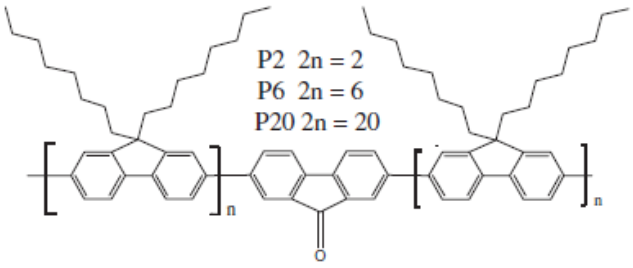

Figure 14. Structure of polyfluorene containing fluorenone moiety. This figure has been reproduced with permission from reference no. 9b.

It is well-known in literature, fluorenone when connected to aromatic system like fluorine show inter-chain energy transfer properties.[9a] Huang *et al*. reported such energy transfer phenomena in linear conjugated polymers (Figure 14), where the polyfluorene containing fluorenone (P20/PF) in thin film state observed to inter-chain energy transfer from PF segment to fluorenone. We expect such energy transfer from TPE to fluorenone segment in **TPE-CMP-F** polymers. As seen from the **TPE-CMP-F's** emission spectra, even at lower concentrations of fluorenone (0.1, 0.5 eq) the emission quenching at 425 nm band is relatively stronger (Figure 12b) suggesting that the emission quenching at 425 nm is not only because of the ICT but also there is contribution from excitation energy transfer from TPE to fluorenone moiety. To further study this we have collected emission spectrum of **TPE-CMP-F3** by exciting at wavelength where there is no CT absorption *i.e.* 260 nm (Figure 15a, b). Surprisingly, even at this excitation a strong emission at 580 nm corresponding to fluorenone moiety is observed which is clearly suggesting the emission at 580 nm is due an indirect excitation energy transfer from TPE to the fluorenone segment in the polymer. In order to further support this, excitation spectra were collected at three different wavelengths (650, 600 and 550 nm). As seen in Figure 15c, the

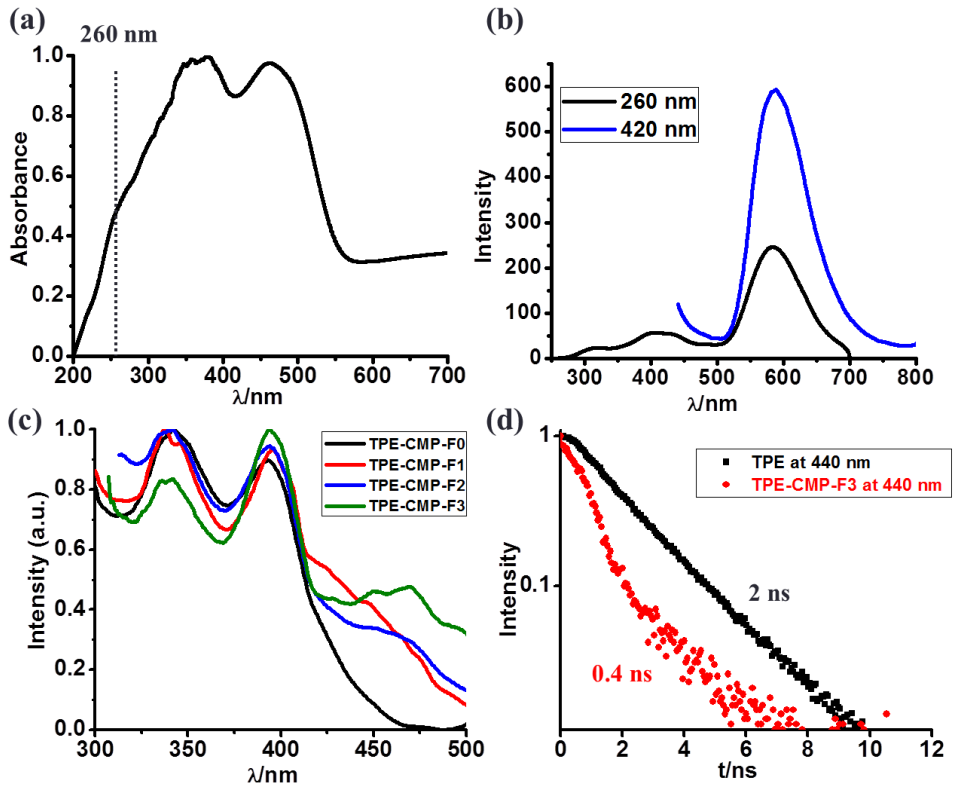

Figure 15. (a) Absorption and (b) emission spectrum (Exc: 260 nm, black and 420 nm, blue) for **TPE-CMP-F3**. (c) Excitation spectra of **TPE-CMP-F's** collected at emission maxima. (d) Fluorescence decay profiles of **TPE-CMP-F3** and TPE in solid state collected at 440 nm.

excitation spectra not only showed the bands corresponding to CT (470 nm) but also due to the TPE segment at 350 nm. These results clearly suggest that the low energy emission at 580 nm is not only due to ICT but also due to the excitation energy transfer from TPE to the fluorenone segment. Energy transfer between TPE-fluorenone is further supported by time-resolved fluorescence life time measurements, life time of TPE donor in **TPE-CMP-F3** collected at 450 nm is found to be 0.4 ns which is shorter than pure TPE donor (2 ns) further proving transfer of excitation energy from TPE to the fluorenone moiety in the polymer (Figure 15d). With increase of equivalents of fluorenone (0.1 to 2 eq) the emission quenching at 425 nm increases due to increase in efficiency of energy transfer. Thus the above results suggest that the emission at 540-580 nm in **TPE-CMP-F's** (0.1 to 2eq) is governed by both ICT and energy transfer. The band gap values calculated from absorbance spectra are observed to be 2.8 eV for **TPE-CMP-F0** which is reduced to value of 2.1 eV for **TPE-CMP-F3**. So a fine tuning of the band gap is achieved by changing the acceptor concentration in the fluorenone polymers. All these polymers are

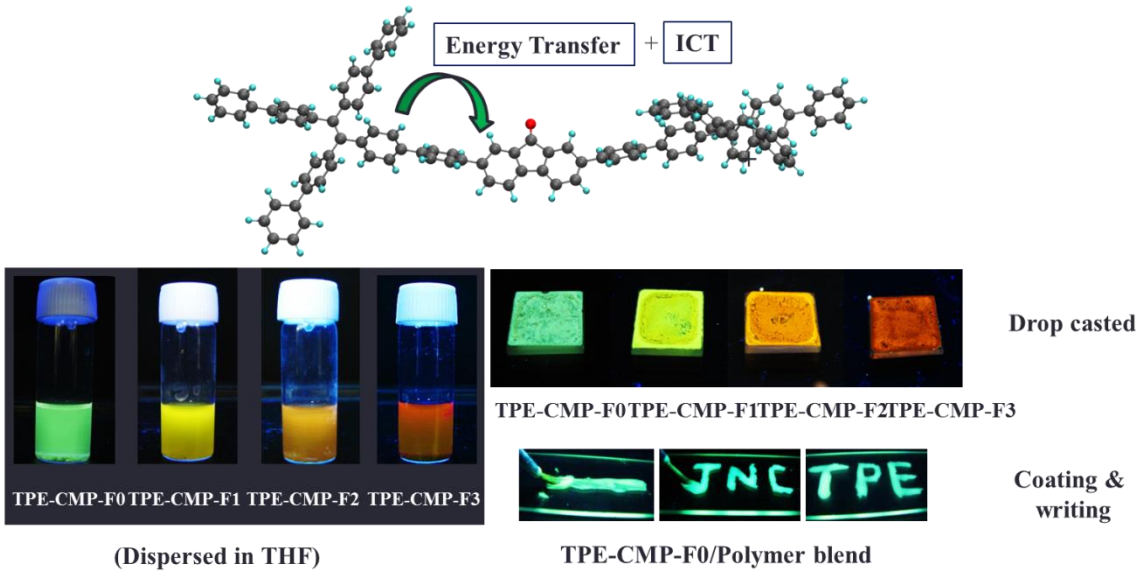

Figure 16. Images of **TPE-CMP-F's** dispersed in THF, drop casted on solid glass substrate under UV light. Images of **TPE-CMP-F0** mixed with poly(ethylene glycol)-*block*-poly(propylene glycol)-*block*-poly(ethylene glycol) under UV light: Writing and coating.

highly dispersible in THF and are drop casted onto solid substrates. Mixing these **TPE-CMP-F's** with poly(ethylene glycol)-*block*-poly(propylene glycol)-*block*-poly(ethylene glycol) improve the processability without changing their emission behaviour (Figure 16).

3A.4 Conclusion

In conclusion, we have demonstrated a new series of tetraphenylethene (TPE) based π-conjugated microporous polymers have been synthesized and thoroughly characterized. Pendant functional groups decorating the pore surface minimized the effective pore size accessible for gas molecules and resulted in tunable pore size, selective CO_2 capture. Framework induced restriction of phenyl rotation of TPE segment resulted strong luminescence. The ability of fluorenone acceptor segment in the polymer showed a combination of energy transfer and intramolecular charge transfer between TPE-fluorenone in the polymer. By controlling donor-acceptor ratio, the efficiency of energy transfer is tuned which resulted in tunable emission colour ranging from green to red. This approach of using energy transfer for tuning the emission colour in CMPs would provide new strategies in fabricating highly efficient light emitting CMPs with no excitation energy annihilation and find applications in light emitting diodes and photovoltaics.

3A.5 References

[1] a)Y. Hong, J. W. Y. Lam, B. Z. Tang, *Chem. Soc. Rev.* **2011**, *40*, 5361; b) W. Z. Yuan, Y. Tan, Y. Gong, P. Lu, J. W. Y. Lam, X. Y. Shen, C. Feng, H. H. Y. Sung, Y. Lu, I. D. Williams, J. Z. Sun, Y. Zhang, B. Z. Tang, *Adv. Mater.* **2013**, *25*, 2837; c) W.-H. Yu, C. Chen, P. Hu, B.-Q. Wang, C. Redshaw, K.-Q. Zhao, *RSC Adv.* **2013**, *3*, 14099.

[2] a) W. Z. Yuan, P. Lu, S. Chen, J. W. Y. Lam, Z. Wang, Y. Liu, H. S. Kwok, Y. Ma, B. Z. Tang, *Adv. Mater.* **2010**, *22*, 2159; b) M. P. Aldred, G.-F. Zhang, C. Li, G. Chen, T. Chen, M.-Q. Zhu, *J. Mater. Chem. C* **2013**, *1*, 6709; c) H. Tong, Y. Hong, Y. Dong, M. Haeussler, J. W. Y. Lam, Z. Li, Z. Guo, Z. Guo, B. Z. Tang, *Chem. Commun.* **2006**, 3705.

[3] a) N. B. Shustova, B. D. McCarthy, M. Dincă, *J. Am. Chem. Soc.* **2011**, *133*, 20126; b) N. B. Shustova, T.-C. Ong, A. F. Cozzolino, V. K. Michaelis, R. G. Griffin, M. Dincă, *J. Am. Chem. Soc.* **2012**, *134*, 15061; c) Y. Xu, L. Chen, Z. Guo, A. Nagai, D. Jiang, *J. Am. Chem. Soc.* **2011**, *133*, 17622; d) Q. Chen, J.-X. Wang, F. Yang, D. Zhou, N. Bian, X.-J. Zhang, C.-G. Yan, B.-H. Han, *J. Mater. Chem.* **2011**, *21*, 13554.

[4] a) K. Kailasam, J. Schmidt, H. Bildirir, G. Zhang, S. Blechert, X. Wang, A. Thomas, *Macromol. Rapid Commun.* **2013**, *34*, 1008; b) S. Hug, M. B. Mesch, H. Oh, N. Popp, M. Hirscher, J. Senker, B. V. Lotsch, *J. Mater. Chem. A* **2014**, *2*, 5928; c) J. Byun, S.-H. Je, H. A. Patel, A. Coskun, C. T. Yavuz, *J. Mater. Chem. A* **2014**, *2*, 12507; d) K. Schwinghammer, S. Hug, M. B. Mesch, J. Senker, B. V. Lotsch, *Energy Environ. Sci.* **2015**, *8*, 3345; e) P. Katekomol, J. Roeser, M. Bojdys, J. Weber, A. Thomas, *Chem. Mater.* **2013**, *25*, 1542; f) Y. Zhang, S. N. Riduan, *Chem. Soc. Rev.* **2012**, *41*, 2083.

[5] a) Y. Xu, S. Jin, H. Xu, A. Nagai, D. Jiang, *Chem. Soc. Rev.* **2013**, *42*, 8012; b) X. Liu, Y. Zhang, H. Li, A. Sigen, H. Xia, Y. Mu, *RSC Adv.* **2013**, *3*, 21267; c) J.-X. Jiang, Y. Li, X. Wu, J. Xiao, D. J. Adams, A. I. Cooper, *Macromolecules* **2013**, *46*, 8779; d) X. Liu, Y. Xu, D. Jiang, *J. Am. Chem. Soc.* **2012**, *134*, 8738; e) H. Bildirir, J. P. Paraknowitsch, A. Thomas, *Chem. Eur. J.* **2014**, *20*, 9543.

[6] a) J.-X. Jiang, A. Trewin, D. J. Adams, A. I. Cooper, *Chem. Sci.* **2011**, *2*, 1777; b) L. Chen, Y. Honsho, S. Seki, D. Jiang, *J. Am. Chem. Soc.* **2010**, *132*, 6742; c) R. S. Sprick, J.-X. Jiang, B. Bonillo, S. Ren, T. Ratvijitvech, P. Guiglion, M. A. Zwijnenburg, D. J. Adams, A. I. Cooper, *J. Am. Chem. Soc.* **2015**, *137*, 3265.

[7] a) J. Subbiah, K. R. Choudhury, S. Ellinger, J. R. Reynolds, F. So, *IEEE J. Sel. Top. Quantum Electron.* **2010**, *16*, 1792; b) K. Zhang, B. Tieke, J. C. Forgie, F. Vilela, P. J. Skabara, *Macromolecules* **2012**, *45*, 743; c) X. Ma, X. Mao, S. Zhang, X. Huang, Y. Cheng, C. Zhu, *Poly. Chem.* **2013**, *4*, 520; d) P. M. Beaujuge, S. Ellinger, J. R. Reynolds, *Nat. Mater.* **2008**, *7*, 795.

[8] a) J.-X. Jiang, F. Su, A. Trewin, C. D. Wood, H. Niu, J. T. A. Jones, Y. Z. Khimyak, A. I. Cooper, *J. Am. Chem. Soc.* **2008**, *130*, 7710; b) X. Liu, Y. Xu, D. Jiang, *J. Am. Chem. Soc.* **2012**, *134*, 8738; c) L. Chen, Y. Honsho, S. Seki, D. Jiang, *J. Am. Chem. Soc.* **2010**, *132*, 6742.

[9] a) M. Shigeta, M. Morita, G.-i. Konishi, *Molecules* **2012**, *17*, 4452; b) B. He, J. Li, Z. Bo, Y. Huang, *Polym. J.* **2007**, *39*, 1345; c) S. Shekhar, E. Aharon, N. Tian, F. Galbrecht, U. Scherf, E. Holder, G. L. Frey, *Chemphyschem* **2009**, *10*, 576; d) A. P. Kulkarni, X. Kong, S. A. Jenekhe, *Macromolecules* **2006**, *39*, 8699.

Chapter 3B

Highly Processable Self-assembled White-Light Emitting Nanoscale Metal-Organic Soft Hybrids

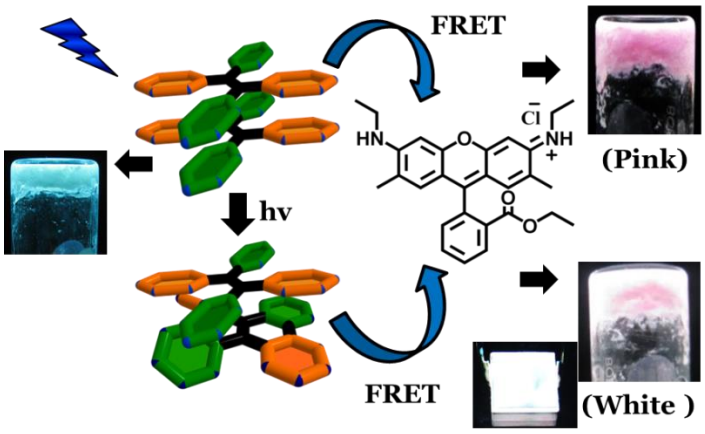

Summary

In this chapter highly processable white light emitting hydrogel of metal-organic cube (MOC) and tetraphenylethene (TPE) derivatives is demonstrated. Supramolecular self-assembly of anionic metal-organic cube $[Ga_8(ImDC)_{12}][Me_2NH_2]_{12}\cdot 24H_2O$ and cationic chromophoric TPE derivative resulted in stable hybrid hydrogel. Self-assembled hybrids showed nanocube like morphology and the MOC structure is retained in the hybrid as evident from PXRD. Hybrid gel showed strong cyan emission due to aggregation induced emission from the TPE derivative. Further hybrid gel has been used as a platform to immobilize another cationic dye, rhodamine 6G (Rh6G) for tuning the emission colour by partial energy transfer through FRET mechanism. Hybrid gel with 0.08 % loading of Rh6G exhibits strong pink emission with CIE coordinates of (0.30, 0.28), which on photoirradiation for about 5 min resulted pure white light emission. Such light induced change in emission colour is realized by transforming definite percentage of TPE derivative to phenanthrene derivative which is non-emissive in aggregated state thus modulating cyan and orange emission to pure dichromatic white light emission with CIE coordinates of (0.33, 0.32). White light emitting hybrids are easily painted on flexible substrates and are highly transparent. Writing and coating on glass substrates is also demonstrated.

V. M. Suresh, P. Sutar, A. De, T. K. Maji, ***manuscript under preparation***

3B.1 Introduction

Highly processable white light emitting materials have received immense interest for applications in lighting and flexible displays.[1] Many organic polymer or supramolecular chromophoric assemblies have been extensively studied for the generation of white light emission owing to low cost, fine structural control, optical output, processibility and flexibility for device preparation, over purely inorganic systems.[2] By controlling the energy transfer based on appropriate molecular design of donor-acceptor chromophores, several white light emitting assemblies like gels,[3] nanofibers,[4] polymers,[2a-c] vesicles,[5] micelles,[6] nanoparticles[7] *etc.* have been reported. However, retaining pure white light emission after device fabrication has been a challenging issue as solvent drying leads to aggregation of aromatic chromophoric segments which may pose inter-chromophoric interactions thereby alteration in white light emission or quantum efficiency. Thus fluorescence quenching of organic chromophoric assemblies in aggregated state (known as aggregation caused quenching, ACQ) restrict the real world technological application of these light emitters.[8] Hybridization of organic chromophores with inorganic components has shown to be an alternative strategy to avoid the inter-chromophoric interactions.[9] Spatial organization and confinement of well-separated organic chromophores in porous materials like zeolites and ordered mesoporous silica were shown to achieve efficient energy transfer. While, periodic organization of organic chromophores through metal ion coordination in extended framework structures also called metal-organic frameworks (MOFs) has shown to provide well-separated chromophores and studied for efficient energy transfer applications.[10] Although these hybrids are efficient and robust, poor solution processibility limits their applications for device fabrication. Recently, Uvdal *et al.* and our group have shown light-harvesting nanoscale MOFs as soft hybrid materials encompassing both solution processibility and hybrid properties.[11] George *et al.* showed co-assembly of donor-acceptor chromophores with clay for preparation of white light emitting hybrid gels. [12] However, pure white-light emitting soft-hybrid gels based on metal-organic systems are yet to be documented. Another facile strategy to avoid ACQ effect is use of aggregation induced emission (AIE) active chromophores for the fabrication of white light emitting materials. Chromophores showing enhanced emission in aggregated state are highly potential and are alternative to the conventional organic chromophores for the fabrication of solid state lighting devices.[13] Tetraphenylethene

(TPE) belongs to such class of chromophores known to show aggregation induced emission (AIE) as non-planar nature of TPE chromophores completely restrict intermolecular π-π stacking thereby reduce quenching in aggregated state (ACQ effect), and therefore excellent candidates for the fabrication of highly efficient solid state white light emitting materials.[13] Several TPE based organic assemblies have been studied for applications in electroluminescent (EL) devices, organic field effect transistors (OFET), organic light emitting devices (OLED), sensing *etc*.[14] TPE systems show high quantum yields in solid state, and can act as donor scaffolds showing efficient excitation energy transfer to acceptor moieties. Recently, Chen *et al.* reported organogels of TPE, spiropyran and perylenediimide derivatives for multi-colour tunable emission by controlling the energy transfer between donor-acceptors.[15]

Here in we envisage combining both hybridization and AIE phenomena into a single system to fabricate solution processable soft hybrids, based on self-assembly of water soluble anionic metal-organic cube (MOC) (of Ga^{III}) with cationic TPE derivative. The ionic assembly forms stable hydrogel with cyan emission based on strong AIE

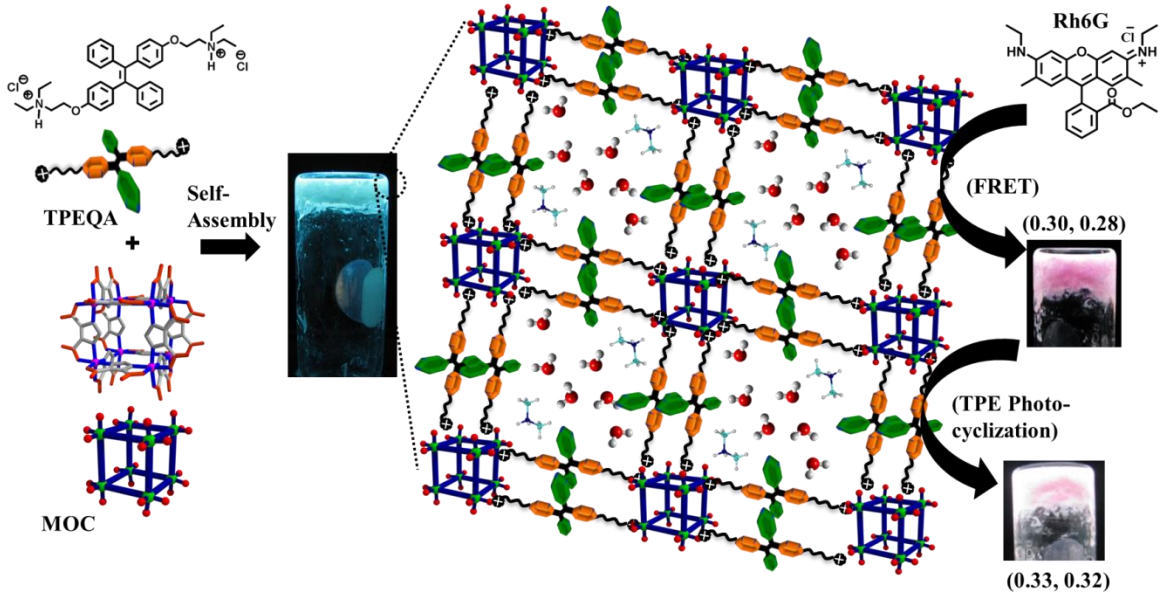

Scheme 1. Schematic showing the self-assembly of MOC and TPEQA to form hydrogel and immobilization of Rh6G acceptor into gel to tune the emission colour and also white light emission through photocyclization of TPEQA.

emission of TPE derivative (Scheme 1). Further this hybrid has been used as a donor scaffold for tunable emission by non-covalent immobilization of rhodamine 6G (Rh6G) which acts as an acceptor. Photocyclization property of TPE in hybrid has been exploited to attain white light emission with ideal Commission Internationale de L'Eclairage (CIE)

co-ordinates of (0.33, 0.32). These hybrids are demonstrated to be highly solution processable by coating on flexible substrates and by writing or drop casting on glass surface.

3B.2 Experimental section

3B.2.1 Materials

$Ga(NO_3)_3 \cdot 6H_2O$, 4,5-imidazoledicarboxylic acid, $TiCl_4$, Zn-dust, 4-hydroxybenzoquinone, 1,2-dibromoethane were purchased from Sigma-Aldrich Chemical Co. Required solvents were dried prior to use. Diethylamine, THF, K_2CO_3, acetone were purchased from Spectrochem Chemical Co. 1,2-bis[4-(4-bromoethoxy)phenyl]-1,2-tetraphenylethene was synthesized according to literature procedure.[16]

3B.2.2 Physical measurements

Infrared spectral studies were done by making samples with KBr pellets using Bruker FT-IR spectrometer. Thermal stability of the metal-organic cube is analysed using Mettler Toledo TGA 850 instrument under N_2 atmosphere in the temperature range of 30-800 °C at the heating rate of 3 °C per min. Powder X-ray diffraction studies in different state of the samples were recorded on a Bruker D8 discover instrument using Cu-Kα radiation. Morphological studies have been carried out using Lica-S440I field emission scanning electron microscope (FESEM) by placing samples on a silicon wafer under high vacuum with an accelerating voltage of 10 kV. Transmission electron microscopy (TEM) analysis has been performed using JEOL JEM-3010 with an accelerating voltage of 300 kV. For this analysis MOC-TPEQA hybrid dispersed in ethanol by sonication before drop casting on a carbon-coated copper grid. Fluorescence studies were accomplished using Perkin Elmer Ls 55 Luminescence spectrometer. ^{1}H NMR is recorded on a Bruker AV-400 spectrometer with chemical shifts reported as ppm (in DCl with TMS as internal standard). The solid state fluorescence quantum yield of MOC-TPEQA hybrid was determined by using integrating sphere, an absolute quantum yield measurement and calculated by Horiba Jobin Yvon instrument. Lifetime measurements were carried out on an EPL-405 ps pulsed diode laser (Edinburgh instrument) used as the excitation source (λ_{ex}= 370 nm).

3B.2.3 Synthesis of the metal-organic cube, $[Ga_8(ImDC)_{12}][Me_2NH_2]_{12} \cdot 24H_2O$ (1)

4,5-H_3ImDC (0.5 mmol), $Ga(NO_3)_3.6H_2O$ (0.5 mmol), 10 mL DMF and 15 μL NEt_3 were mixed in a 20 mL Teflon container which is kept in a stainless steel lined autoclave and the reaction mixture was then heated at 120 °C for 24 hours and left to cool down to room temperature. The product was collected by filtration and washed repeatedly by methanol and dried in air. The air dried powder was dissolved in 5 ml water and kept for crystallization. Within 4 days colourless, block shaped crystals were obtained. The as-synthesized compound was formulated as $[Ga_8(ImDC)_{12}][Me_2NH_2]_{12}.24H_2O$. Selected IR data (KBr, cm^{-1}): 3447 (b), 3086 (m), 2775 (m), 1676 (s), 1473 (s), 1363 (s), 1100 (s), 857 (m), 660 (m), 550 (m). Anal. Calcd for $C_{60}H_{12}Ga_8N_{24}O_{48}$: C, 30.15; H, 0.50; N, 14.07. Found: C, 30.14; H, 0.55; N, 14.76. The phase purity of the powder sample was checked by comparing PXRD of the bulk powder sample with the simulated data from single crystal.

3B.2.4 Synthesis of 1,2-bis{4-[4-(*N,N*-diethylammonium)ethoxy]phenyl} -1,2-tetraphenylethene dibromide hydrochloride (TPEQA)

1,2-bis[4-(4-bromoethoxy)phenyl]-1,2-tetraphenylethene (1 eq, 100 mg) was dissolved in acetonitrile in a round bottom flask followed by addition of diethylamine (5 eq, 90 μL) and K_2CO_3 (5 eq, 118. 8 mg) and the reaction mixture was refluxed for 6 hrs. Excess water is added to the reaction mixture and extracted with ethyl acetate and concentrated under reduced pressure. A brown liquid is obtained. This brown liquid is dissolved in methanol and stirred with 1.6 N HCl (in methanol) for 15 min. Solvents were evaporated under reduced pressured to obtain compound as brown liquid. Yield: 75 %. ^{1}H-NMR (400 MHz, DMSO-d^6) 10.5 (br, H, NH) 7.1 (m, 4H, CH) 6.8 (m, 3H, CH) 6.7 (m, 2H, CH) 4.2 (m, 2H, OCH_2) 3.4 (d, 2H, CH_2) 3.1 (s, 4H, NCH_2) 1.2 (t, 6H, CH_3).

3B.3 Results and discussion

3B.3.1 Structural description of metal-organic cube (MOC)

Solvothermal reaction of $Ga(NO_3)_3.6H_2O$, 4,5-imidazoledicarboxylic acid (ImDC) and triethylamine (Et_3N) in *N*,*N*′-dimethylformamide (DMF) at 120 ^oC affords a pale yellow powder, aqueous solution of which on slow evaporation results block shape crystals of compound **1**. Single-crystal X-ray diffraction studies reveal that **1** crystallizes in the trigonal *R-3* space group. The asymmetric unit of **1** consists of one anionic cube $[Ga_8(ImDC)_{12}]^{12-}$, 12 $Me_2NH_2^+$ (dimethyl ammonium, DMA) cations and guest water molecules. The DMA cations are formed *in-situ* from DMF under solvothermal

condition.[17] Two crystallographically independent Ga^{3+} (Ga1 and Ga2) ions are coordinated to three nitrogen atoms (N1, N3, N4 for Ga1 and N2, N2', N2'' for Ga2) and three oxygen atoms (O1, O5, O8 for Ga1 and O2, O2', O2'' for Ga2) from three different $ImDC^{3-}$ ligands and adapt facial octahedral geometry. Each anionic cube consists of eight Ga^{3+} ions at the vertices and twelve triply deprotonated $ImDC^{3-}$ *exo*-ligand at the edges. Each $ImDC^{3-}$ ligand chelated to two individual Ga^{3+} centres in a bridging bis(bidentate)

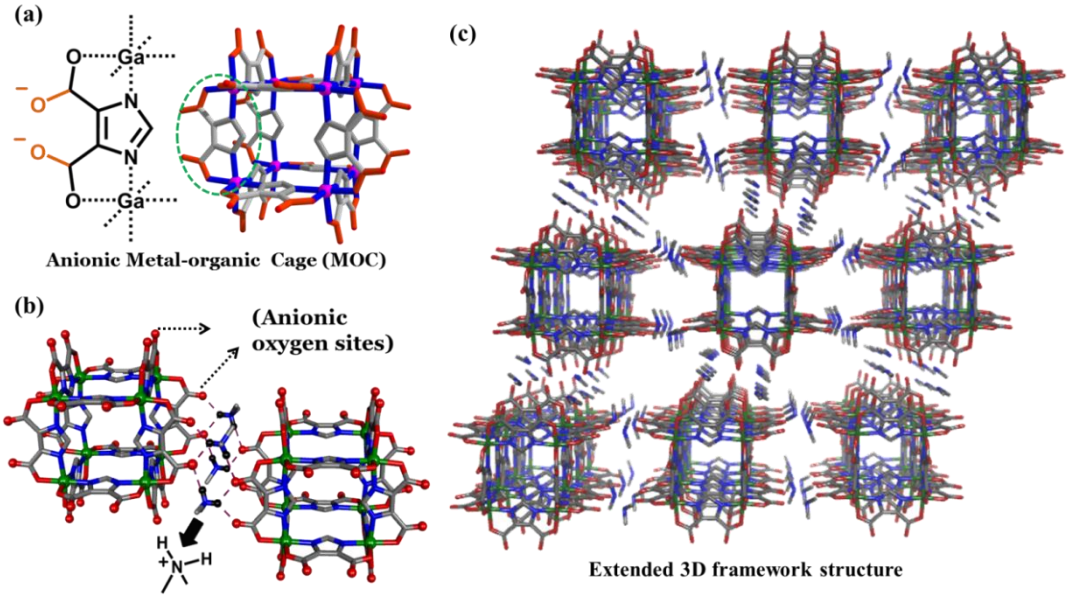

Figure 1. (a) Structure of anionic MOC and schematic representation of anionic carboxylate ions of ImDC. (b) Interaction of DMA cations with MOCs through intermolecular H-bonding. (c) Single crystal structure of extended framework of MOC in solid state.

fashion through imidazole nitrogen and carboxylate oxygen (N1, O1 or N2, O2) or (N3, O5 or N4, O8) atoms, while other two oxygen (O3, O4) or (O6, O7) atoms remain free. One cube has 24 peripheral non-coordinated oxygen atoms which generate -12 negative charges. This negative charge is neutralized by twelve DMA cations which surround the anionic cube. Ga-Ga distances along the edges of the cube lie in the range of 6.232Å-6.244 Å and Ga-Ga-Ga angles are in between 90.11°- 89.89°, indicating cube-like structure. Two crystallographically independent DMA cations (N5 and N7) play important role in packing of anionic cubes. Both DMA cations bridges two adjacent $[Ga_8(ImDC)_{12}]^{12-}$ cubes through charge assisted N-H···O hydrogen bonding interactions (2.012 Å) (Figure 1). Each cube is connecting six neighbouring cubes by 24 DMA cations (4 DMA cations between two cubes) through intermolecular hydrogen bonding (Figure 1) and their periodic arrangement results in an open framework exhibiting two alternative

3D channels with approximate window size of (8.14 × 5.95 $Å^2$) and (7.66 × 0.49 $Å^2$) respectively (in both case considering the van der Waals radii). The solvent accessible volume of **1** is estimated to be 48.2% of the unit cell volume (obtained using the PLATON software). Thermogravimetric analysis (TGA) of as-synthesized **1** shows an initial weight-loss of 13% at 110 ºC corresponding to 24 guest water molecules, on further heating beyond 200 ºC framework decomposes.

3B.3.2 MOC-TPEQA hybrid gel formation

TPEQA is rationally designed in order to mimic the DMA cations and can extend the MOCs by H-bonding and electrostatic interaction like DMA cations. Cationic nature of TPEQA provides an electrostatic interaction with MOC and terminal N-H groups connected through flexible ethoxy chains offers H-bonding with negatively charged carboxylate oxygen atoms of the MOC (Figure 2a, b). It a recent observation from our group, addition of NH_4^+, a mimic of DMA to the MOC solution is found to form transparent hydrogel.[18] We envisage that cationic 'NH' terminals of TPEQA molecules on both sides would resemble the NH_4^+ in forming the self-assembled hydrogel where the MOCs are interconnected by TPEQA molecules. Also, the hydrophobic aromatic core of TPE is expected to provide balance between hydrophilic and hydrophobic interactions.

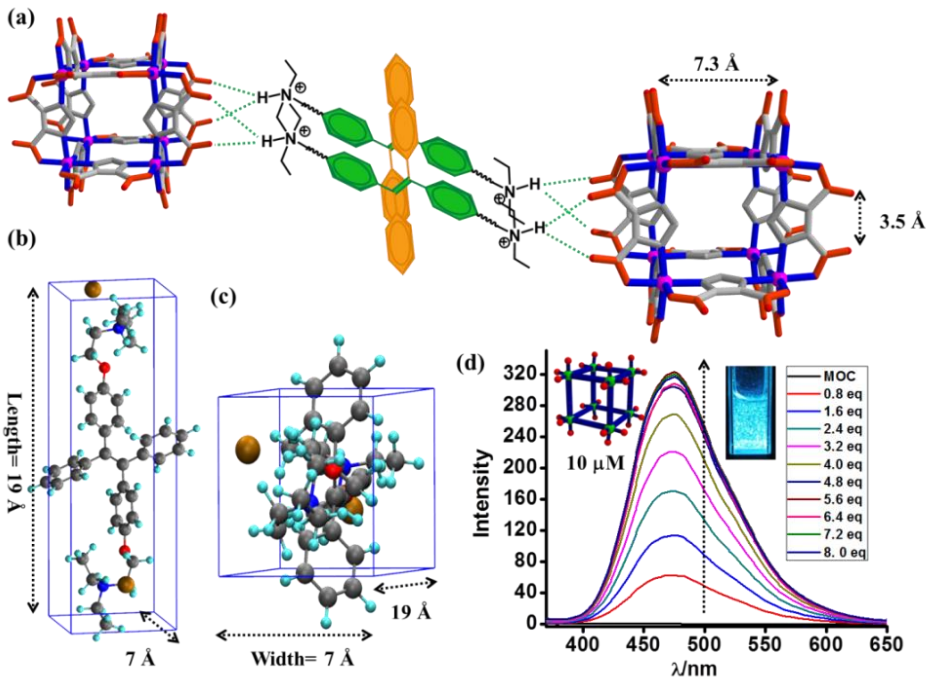

Figure 2. (a) Schematic presentation of possible interaction of TPEQA with MOCs. (b) Molecular dimensions of TPEQA. (d) Changes in emission spectra of MOC solution on addition of equivalents of TPEQA.

Interaction between MOC and TPEQA is indeed evident from titration experiments; Aq. MOC (10 μM) did not show any emission upon excitation at 350 nm, on addition of 0.8 eq of aq. TPEQA a band at 474 nm is observed (Figure 2c). The emission intensity gradually increases with increasing the equivalents of TPEQA and saturated after 6.4 eq of TPEQA. This reveals a definite interaction of MOC with TPEQA possibly through H-bonding and electrostatic interaction. Binding isotherms reveal the emission saturates at 6

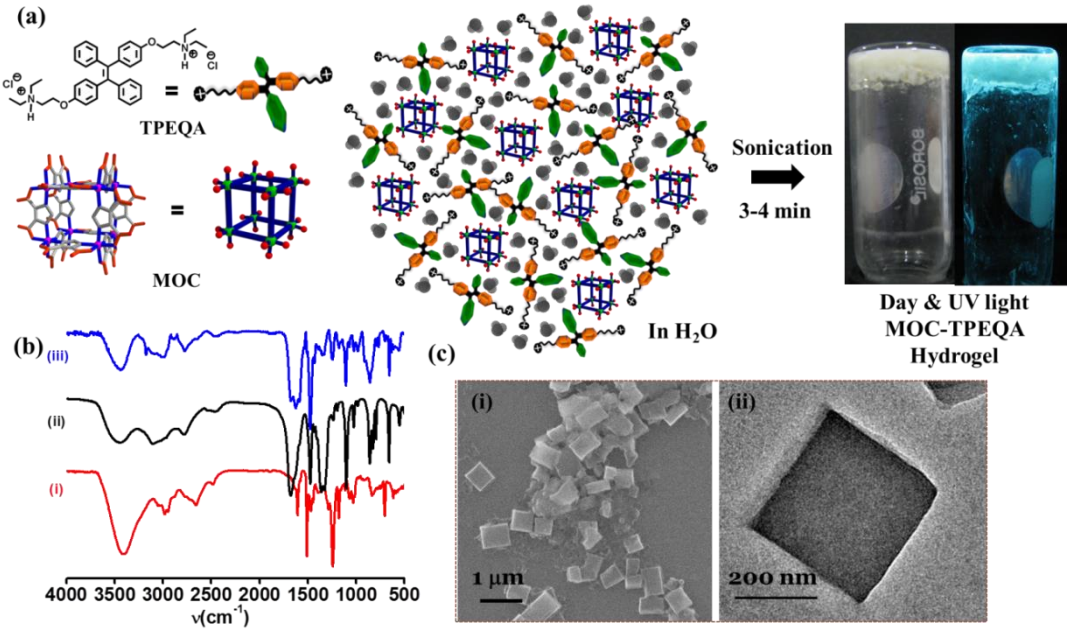

Figure 3. (a) Schematic showing the MOC-TPEQA gel formation in water. (b) FTIR spectra of TPEQA (i), MOC (ii) and MOC-TPEQA (iii). (c) Morphology of MOC-TPEQA hybrids (i) SEM and (ii) TEM.

eq of TPEQA; as shown in Figure 2 each TPEQA interacts with two carboxylate oxygen's and shared between two MOCs. Each TPEQA contains two 'NH' termini i.e. 6 eq of TPEQA is equals to 6 molecules of TPEQA per each MOC. It is to be noted that the emission at 474 nm is originated from TPEQA due to AIE phenomena. As seen in Figure 3, clear formation of MOC-TPEQA aggregates were observed during the titration. Room temperature mixing of aq. MOC (12 mM) and aq. TPEQA (8.3 mM) followed by sonication leads to formation of stable gel as evident from inversion test method (Figure 3a). FTIR of hybrid xerogel showed all peaks characteristic of MOC as well as TPEQA thereby suggesting their presence in hybrid gel (Figure 3b). SEM showed cubic particles for MOC-TPEQA hybrid with dimensions of 500-800 nm and is further supported by TEM measurements (Figure 3c). All the diffraction peaks characteristic of MOC are retained in the MOC- TPEQA hybrid clearly suggesting its stability on gelation (Figure

4a). From the above results a proposed self-assembly of MOC-TPEQA hybrid is proposed as shown in Figure 4b, initially MOC dissolved in water interacts with TPEQA through H-bonding interaction in all directions at an average of 12 molecules of TPEQA per MOC and forms smaller aggregates. Now these MOC-TPEQA aggregates are further connected by other MOCs and extend to form a three dimensional network like structure where the water and DMA cations are filled within the pores of the network to form a stable gel.

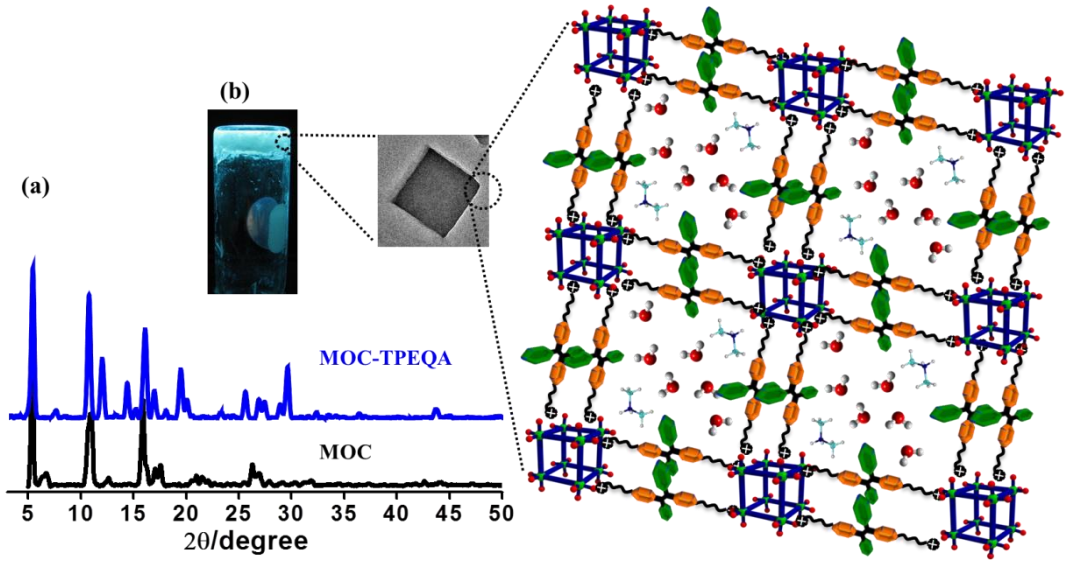

Figure 4. (a) Powder X-ray diffraction of MOC (black), MOC-TPEQA hybrid (blue). (b) Proposed self-assembly of MOC-TPEQA hybrid forming hydrogel with cube like morphology. Notice the water and DMA cations are entrapped within the gel network.

3B.3.3 Energy transfer and white light emission

MOC-TPEQA hybrid showed strong AIE emission at 474 nm upon excitation at 350 nm due to TPEQA (Figure 5a) with a CIE coordinates of (0.19 0.25). We envision such luminescent hybrid gel can act as a donor scaffold for potential light-harvesting application. The periodic arrangement of MOC and TPEQA in the gel network offers easy immobilization of cationic acceptor dye molecules thereby the interaction between donor-acceptor moieties results in partial energy transfer and show colour tunable emission including white light. We have chosen rhodamine 6G (Rh6G) as an acceptor which shows good partial spectral overlap between its absorption, and emission spectrum of MOC-TPEQA hybrid (Figure 5a). Mixing of MOC (12 mM), TPEQA (8.3 mM) and 0.02 mol% of Rh6G under sonication triggers instant co-assembly and forms higher order assemblies containing Rh6G. Excitation of $Rh6G_{0.02\%}$MOC-TPEQA at 350 nm showed a

decrease in emission at 474 nm and a band due to Rh6G appears at 560 nm due to excitation energy transfer between donor and acceptor in the hybrid gel (Figure 5b). The emission at 474 nm decreases gradually and a simultaneous increase in emission at 580 nm is observed with increasing the Rh6G loading from (0.02-0.08 %). While the emission colour changes from cyan to pink (Figure 5c-e). As shown in Figure 6c co-assembly of 0.08 mol% Rh6G results in pink emitting hydrogel with CIE coordinates of (0.31, 0.27). This clearly suggests that the emission of these soft-hybrids can be easily tuned from cyan to pink by simple co-assembly of acceptor molecules (Figure 5d). It is anticipated, both

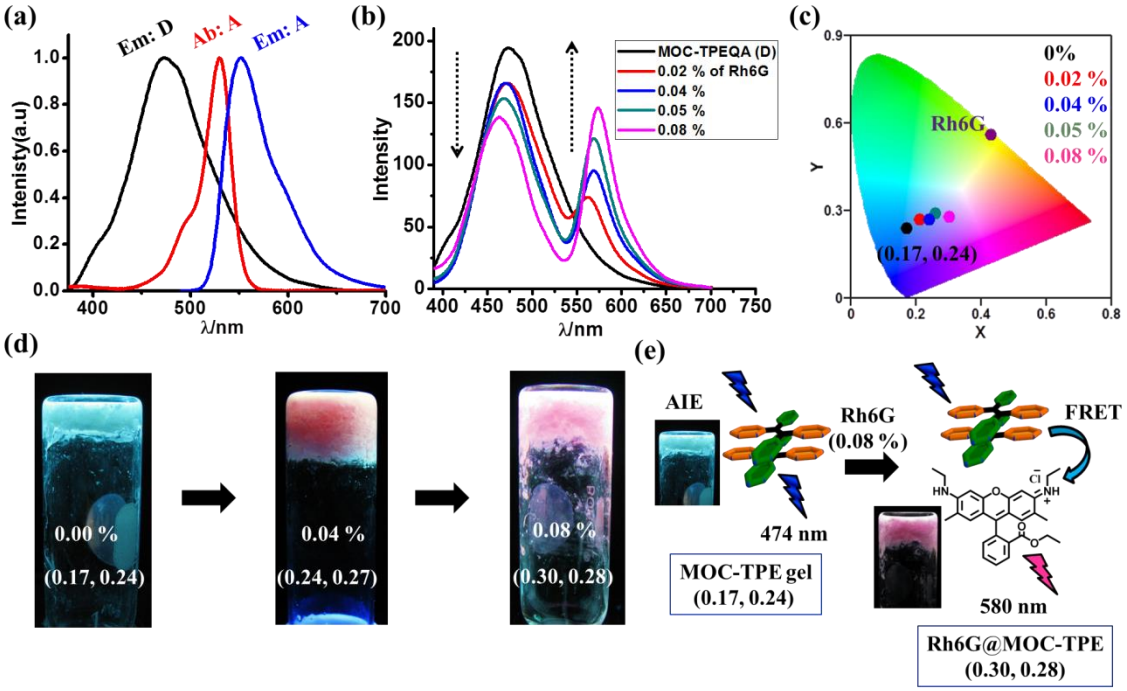

Figure 5. (a) Emission spectrum of MOC-TPEQA (black), absorption (red) and emission spectrum of Rh6G (blue). (b) Emission spectra of MOC-TPEQA loaded with different amounts of Rh6G (arrows indicate changes), (c) corresponding 1931 CIE diagram. (d) Images of hybrid hydrogels with various loading of Rh6G under UV lamp. (e) Schematic showing energy transfer pathway in Rh6G loaded MOC-TPEQA hybrids: Images of MOC-TPEQA and $Rh6G_{0.08\%}$@MOC-TPEQA hydrogel under UV lamp and corresponding CIE coordinates.

cationic molecules assembled through the cube by electrostatic and H-bonding interaction and their close proximity in hybrid gel results in efficient energy transfer from donor to acceptor through Förster resonance energy transfer (FRET) mechanism. On further increasing the loading of Rh6G to 1% results in only viscous liquid even after 24 hrs and did not show energy transfer may be due to inadequate co-assembly of donor-acceptors. On the other hand, increasing donor concentration also did not show gel formation or

energy transfer. In a dichromatic approach the colour balance between donor-acceptor is essential to achieve white light emission. In order to further adjust the emission at 580 nm of dye loaded mixed hybrids, photocyclization property of TPE is utilized. TPE is well known to undergo photocyclization to diphenylphenanthrene (DPP) on photo irradiation (Figure 6a).[16]

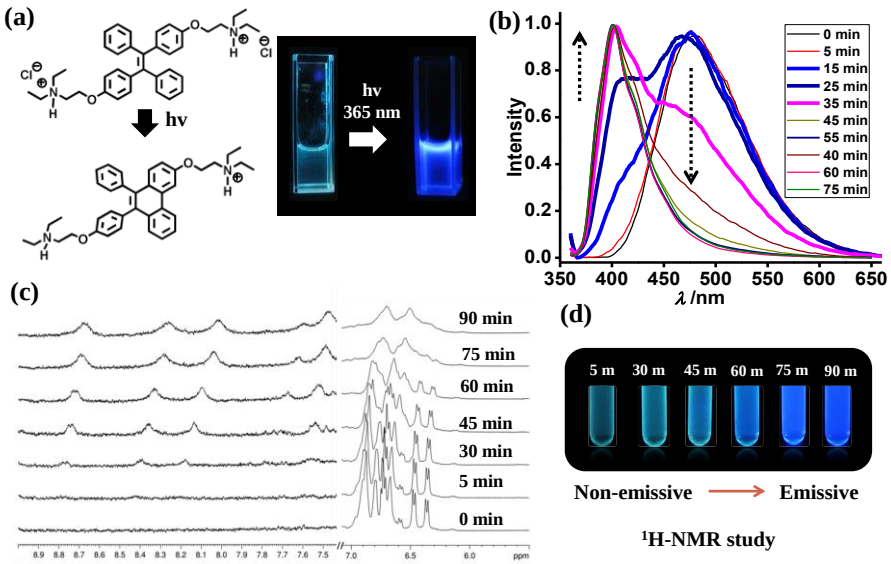

Figure 6. (a) Schematic showing the photocyclization of pure TPEQA to DPPQA on photoirradiation. (b) Time dependant changes in emission spectra (normalized) of TPEQA in water on irradiation with 365 nm light. (c) Changes in ^{1}H-NMR (D_2O) spectra at different intervals of photoirradiation and (d) corresponding images of TPEQA in NMR tube under UV lamp.

DPP shows strong blue emission in dilute solution while the emission quenches in concentrated or solid aggregated state (Aggregation caused quenching, ACQ effect). Prior to the photoirradiation study of $Rh6G_{0.08\%}$MOC-TPEQA, we have initially tested photocyclization of pure TPEQA dissolved in water (D_2O in case of NMR) and MOC-TPEQA hydrogel using emission spectra and ^{1}H-NMR. TPEQA molecule dissolved in water showed weak emission at 470 nm (Figure 6a, b), however on photoirradiation for 15 min a weak shoulder at 410 nm corresponding to the DPPQA is observed and its intensity gradually increases with increasing irradiation time. At or more than 45 min the emission at 470 nm nearly faded and only emission at 410 nm is observed. It is to be noted, emission colour of the solution completely changes from weakly emissive to highly blue emissive. These results are consistent with literature reports,[16] and clearly suggests the photocyclization of TPEQA to DPPQA in solution. This is also supported by ^{1}H-NMR study of pure TPEQA in D_2O at different intervals of time (Figure 6c, d), peaks

in the range of 7-9 ppm are assigned to the DPPQA aromatic protons. Photocyclization of TPEQA in aggregated state *i.e.* MOC-TPEQA hybrid hydrogel is also studied, MOC-TPEQA gel coated on glass substrate showed strong AIE emission at 474 nm (Figure 7a, red) due to TPEQA, however after photoirradiation for 20 min with 365 nm light source the emission completely quenched (Figure 7a, black) which also clear from images under UV lamp before and after photoirradiation (Figure 7a). This quenching is attributed to the ACQ effect in aggregated state of DPPQA formed after photoirradiation. Interestingly, on dissolving these aggregates in water a strong blue emission at 410 nm (Figure 7b, red) is observed indicating the presence of molecularly dissolved DPPQA units in solution.

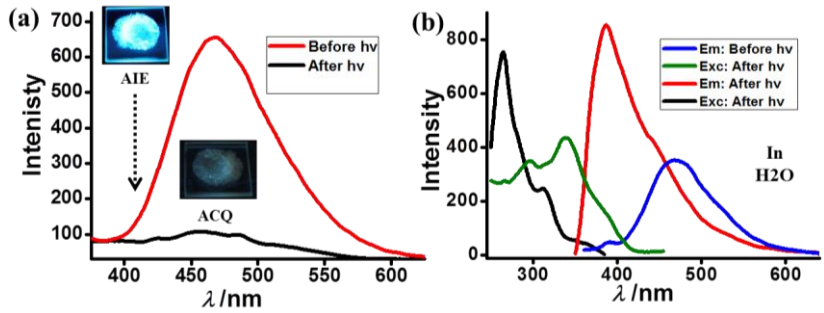

Figure 7. (a) Emission quenching of MOC-TPEQA hybrid coated on glass substrate on photoirradiation with 365 nm light source. (b) Emission and excitation spectra of MOC-TPEQA (blue, black) and MOC-DPP (red, green) hybrids dispersed in water before and after photoirradiation.

Now we envisioned controlled irradiation of dye loaded MOC-TPEQA hybrid gel could lead to the formation of DPPQA in Rh6G@MOC-TPEQA hydrogel where the DPPQA molecules would be in aggregated state (Figure 8a). Aggregated DPPQA molecules cause emission quenching at 474 nm due to ACQ phenomena. Indeed, photoirradiation of $Rh6G_{0.08\%}$@MOC-TPEQA for 5 min results in partial quenching of 474 nm band along with slight broadening. Interestingly, the emission colour of the gel changes pink to white under UV lamp and the CIE coordinates are found to be (0.33, 0.32) which is suggesting a pure white light emission from the hybrid gel (Figure 8b-d). Partial quenching of emission at 474 nm is attributed to the ACQ effect of DPPQA formed on photoirradiation. Formation of DPPQA in hybrid is evident from HRMS spectra, obtained on dissolving the hybrids in water (Figure 9). It is expected to be nearly 8 % of the TPEQA molecules are converted to DPPQA on photoirradiation for 5 min. The energy transfer in white light emitting hybrids is further evident from direct excitation of the Rh6G at 530 nm which showed less emission intensity compared to the indirect

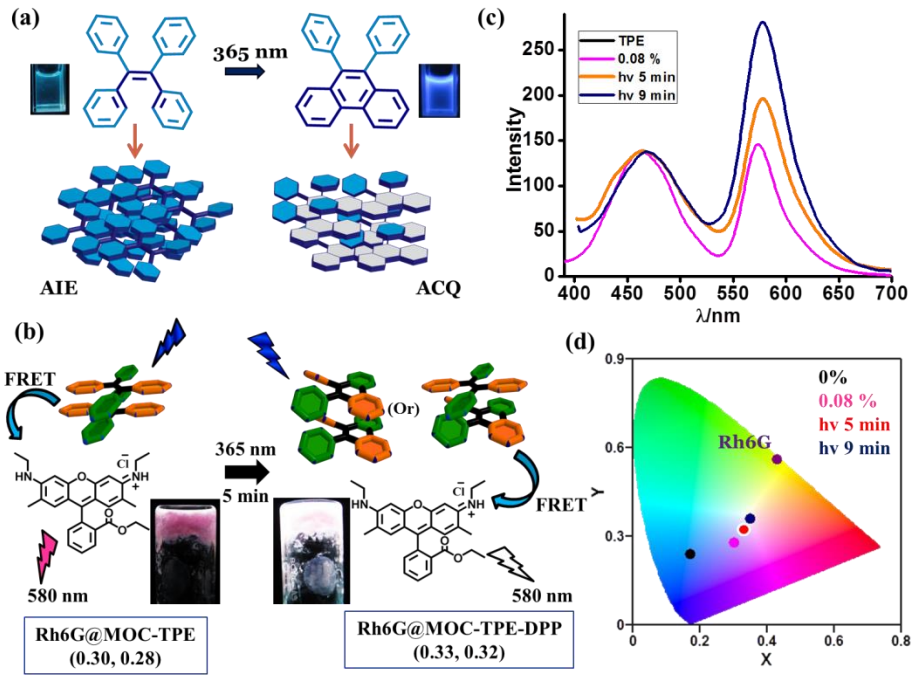

Figure 8. (a) Schematic showing photocyclization of TPE to DPP on photoirradiation. (b) Change of pink hydrogel to white light emitting gel on irradiation with 365 nm light source for 5 min and (c) corresponding emission spectra. (d) 1931 CIE diagram of MOC-TPEQA hybrid (black), pink emitting gel (pink), white light emitting gel (red), orange hydrogel formed after 9 min irradiation (navy blue) and pure Rh6G (wine).

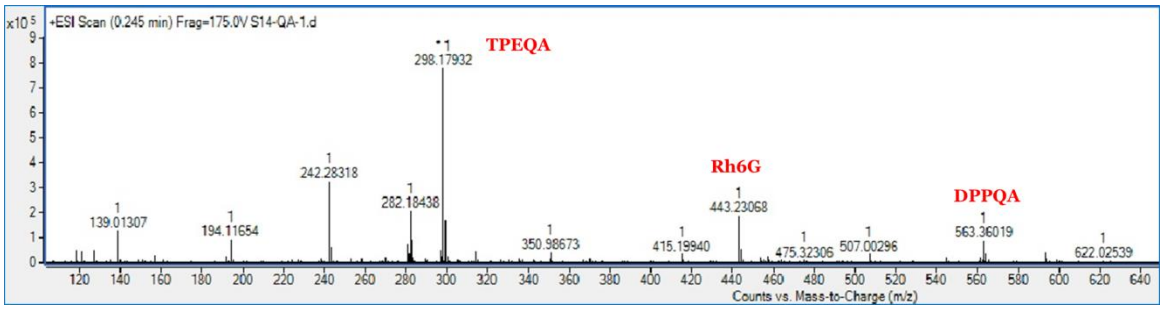

Figure 9. HRMS spectrum of white light emitting hybrids dissolved in water showing individual components of the gel and conversion of TPEQA to DPPQA on photoirradiation.

excitation at 350 nm (Figure 10a), clearly suggesting efficient light-harvesting process in hybrid gel through Försters mechanism. Energy transfer in white light emitting hydrogel is further evident from excitation spectrum collected at Rh6G emission (580 nm), which showed maximum at 350 nm clearly suggesting the contribution of TPEQA to the observed emission (Figure 10b). Fluorescence decay profiles of white light emitting gel monitored at TPEQA emission (470 nm) shows shorter life time value (1.5 ns) than MOC-TPEQA hybrid gel (4.5 ns) clearly indicating excitation energy transfer from TPEQA to Rh6G in the hybrid gel (Figure 10c).

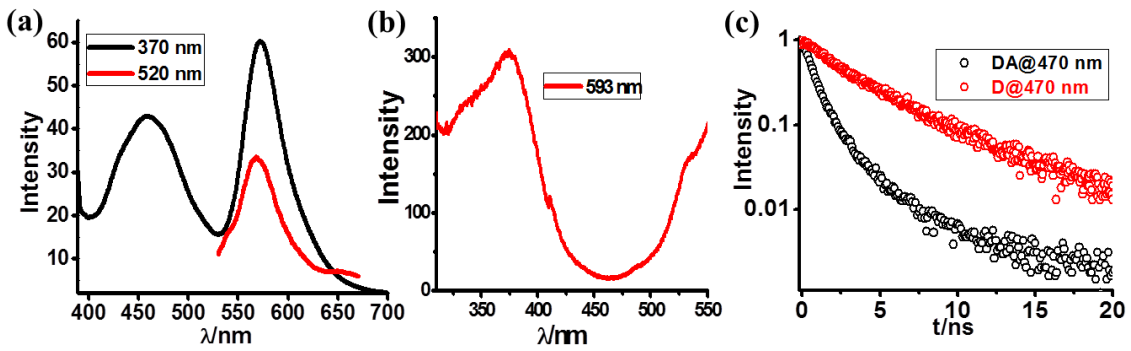

Figure 10. (a) Emission spectra of white light emitting hydrogel excited at 370 (black, indirect) and 520 nm (red, direct). (b) Excitation spectrum of white light emitting gel collected at 593 nm. (c) Fluorescence decay profiles of MOC-TPEQA hybrid (red) and white light emitting gel (black) collected at 470 nm.

3B.3.4 Processibility

Substrate transferability of these white light emitting materials is prime importance for device fabrication and real time applications. These soft-hybrids are transformed to viscous liquid by simple shaking. Extreme softness and environmentally benign solvents used in the co-assembly prompted us to study the large area coating of these white light emitting gels. It could be used to write or paint on any substrate, it is

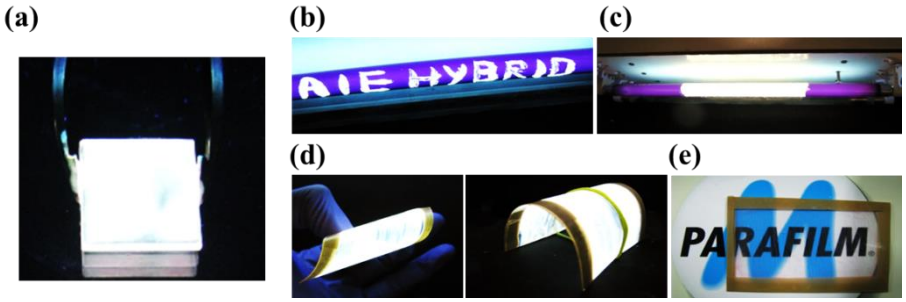

Figure 11. Substrate transferability of white light emitting gel: (a) coated on glass substrate, (b) writing and (c) painting on UV lamp. (d) White light emitting hybrids coated on plastic substrate (5× 3 cm) and (e) its day light image showing its transparency.

demonstrated in Figure 11a, b, c, where the white light emitting gels are partially painted on a commercially available UV lamp, on switching the electric power uncoated portion showed remains blue while coated part emits strong white light uniformly. On the other hand, the writing "AIE hybrid" showed strong white colour from the letters. As seen in Figure 11d, white light emitting gel is painted on flexible plastic substrates showed strong white emission under UV lamp and no significant difference is observed for the substrate under visible light even after coating, clearly suggesting its high transparent behaviour (Figure 11e). White light emission is retained even on bending the flexible substrate.

3B.4 Conclusions

In conclusion, a novel class of white light emitting soft hybrid materials have been demonstrated. Supramolecular self-assembly of anionic metal-organic cubes with cationic TPE chromophores resulted strongly luminescent hydrogel due to AIE phenomena. MOC-TPEQA hybrids co-assembled with rhodamine 6G molecules provided colour tunable soft-hybrids by fine controlling of energy transfer. Photomodulation of pink emitting hybrid hydrogel resulted strongly white light emitting soft hybrid material with a CIE coordinates of (0.33, 0.32). White light emitting hybrids showed high solution processibility and are painted on any flexible substrates. They are easy to write and coat on any substrate. These white light emitting soft hybrids derived from AIE chromophores provides a platform for the fabrication of white light emitting devices with high quantum efficiency and other optoelectronic applications.

3B.5 References

[1] a) B. W. D'Andrade, S. R. Forrest, *Adv. Mater.* **2004**, *16*, 1585; b) K. T. Kamtekar, A. P. Monkman, M. R. Bryce, *Adv. Mater.* **2010**, *22*, 572; c) S. Mukherjee, P. Thilagar, *Dyes and Pigments* **2014**, *110*, 2; d) L. Chen, C.-C. Lin, C.-W. Yeh, R.-S. Liu, *Materials* **2010**, *3*, 2172; e) H. J. Bolink, E. Coronado, M. Sessolo, *Chem. Mater.* **2009**, *21*, 439.

[2] a) J. Huang, G. Li, E. Wu, Q. Xu, Y. Yang, *Adv. Mater.* **2006**, *18*, 114; b) J. Huang, W.-J. Hou, J.-H. Li, G. Li, Y. Yang, *Appl. Phys. Lett.* **2006**, *89*, 133509; c) C. Tang, X.-D. Liu, F. Liu, X.-L. Wang, H. Xu, W. Huang, *Macromol. Chem. Phys.* **2013**, *214*, 314; d) J. Kido, M. Kimura, K. Nagai, *Science* **1995**, *267*, 1332; e) R. Abbel, C. Grenier, M. J. Pouderoijen, J. W. Stouwdam, P. E. L. G. Leclère, R. P. Sijbesma, E. W. Meijer, A. P. H. J. Schenning, *J. Am. Chem. Soc.* **2009**, *131*, 833; f) D. K. Maiti, R. Bhattacharjee, A. Datta, A. Banerjee, *J. Phys. Chem. C* **2013**, *117*, 23178; g) R. Abbel, R. van der Weegen, W. Pisula, M. Surin, P. Leclere, R. Lazzaroni, E. W. Meijer, A. P. H. J. Schenning, *Chem. Eur. J.* **2009**, *15*, 9737; h) C. Vijayakumar, V. K. Praveen, A. Ajayaghosh, *Adv. Mater.* **2009**, *21*, 2059; i) Tsujimura T. OLED display fundamentals and applications (Wiley series in display technology). Wiley-VCH; 2012.

[3] a) V. K. Praveen, C. Ranjith, N. Armaroli, *Angew. Chem. Int. Ed.* **2014**, *53*, 365; b) A. Ajayaghosh, V. K. Praveen, C. Vijayakumar, S. J. George, *Angew. Chem. Int. Ed.* **2007**, *46*, 6260; c) S. Roy, A. K. Katiyar, S. P. Mondal, S. K. Ray, K. Biradha, *ACS Appl. Mater. Interfaces* **2014**, *6*, 11493; d) P. Bairi, B. Roy, P. Chakraborty, A. K. Nandi, *ACS Appl. Mater. Interfaces* **2013**, *5*, 5478; e) X. Cao, Y. Wu, K. Liu, X. Yu, B. Wu, H. Wu, Z. Gong, T. Yi, *J. Mater. Chem.* **2012**, *22*, 2650.

[4] a) C. Giansante, G. Raffy, C. Schäfer, H. Rahma, M.-T. Kao, A. G. L. Olive, A. Del Guerzo, *J. Am. Chem. Soc.* **2011**, *133*, 316; b) C. Giansante, C. Schäfer, G. Raffy, A. Del Guerzo, *J. Phys. Chem. C* **2012**, *116*, 21706.

[5] a)N. Sakai, S. Matile, *Nat. Chem.* **2009**, *1*, 599; b) N. Liu, C.-G. Qi, Y. Wang, D.-F. Liu, J. Yin, Y.-Y. Zhu, Z.-Q. Wu, *Macromolecules* **2013**, *46*, 7753; c) X. Zhang, S. Rehm, M. M. Safont-Sempere, F. Würthner, *Nat. Chem.* **2009**, *1*, 623; d) R. Wang, J. Peng, F. Qiu, Y. Yang, Z. Xie, *Chem. Commun.* **2009**, 6723.

[6] a) X. Zhang, D. Gorl, F. Wurthner, *Chem. Commun.* **2013**, *49*, 8178; b) A. Ozawa, A. Shimizu, R. Nishiyabu, Y. Kubo, *Chem. Commun.* **2015**, *51*, 118.
[7] C. Vijayakumar, K. Sugiyasu, M. Takeuchi, *Chem. Sci.* **2011**, *2*, 291.
[8] J. Mei, Y. Hong, J. W. Y. Lam, A. Qin, Y. Tang, B. Z. Tang, *Adv. Mater.* **2014**, *26*, 5429.
[9] a) C. Y. Lee, O. K. Farha, B. J. Hong, A. A. Sarjeant, S. T. Nguyen, J. T. Hupp, *J. Am. Chem. Soc.* **2011**, *133*, 15858; b) M. E. Foster, J. D. Azoulay, B. M. Wong, M. D. Allendorf, *Chem. Sci.* **2014**, *5*, 2081.
[10] a) H.-J. Son, S. Jin, S. Patwardhan, S. J. Wezenberg, N. C. Jeong, M. So, C. E. Wilmer, A. A. Sarjeant, G. C. Schatz, R. Q. Snurr, O. K. Farha, G. P. Wiederrecht, J. T. Hupp, *J. Am. Chem. Soc.* **2013**, *135*, 862; b) C. A. Kent, B. P. Mehl, L. Ma, J. M. Papanikolas, T. J. Meyer, W. Lin, *J. Am. Chem. Soc.* **2010**, *132*, 12767; c) G. Calzaferri, S. Huber, H. Maas, C. Minkowski, *Angew. Chem. Int. Ed.* **2003**, *42*, 3732; d) T. Q. Nguyen, J. Wu, S. H. Tolbert, B. J. Schwartz, *Adv. Mater.* **2001**, *13*, 609; e) N. Mizoshita, Y. Goto, T. Tani, S. Inagaki, *Adv. Mater.* **2009**, *21*, 4798.
[11] a) X. Zhang, M. A. Ballem, Z.-J. Hu, P. Bergman, K. Uvdal, *Angew. Chem. Int. Ed.* **2011**, *50*, 5728; b) X. Zhang, M. A. Ballem, M. Ahren, A. Suska, P. Bergman, K. Uvdal, *J. Am. Chem. Soc.* **2010**, *132*, 10391; c) V. M. Suresh, S. J. George, T. K. Maji, *Adv. Funct. Mater.* **2013**, *23*, 5585.
[12] K. V. Rao, K. K. R. Datta, M. Eswaramoorthy, S. J. George, *Adv. Mater.* **2013**, *25*, 1713.
[13] Y. Hong, J. W. Y. Lam, B. Z. Tang, *Chem. Soc. Rev.* **2011**, *40*, 5361.
[14] a) W. Z. Yuan, Y. Tan, Y. Gong, P. Lu, J. W. Y. Lam, X. Y. Shen, C. Feng, H. H. Y. Sung, Y. Lu, I. D. Williams, J. Z. Sun, Y. Zhang, B. Z. Tang, *Adv. Mater.* **2013**, *25*, 2837; b) W. Z. Yuan, P. Lu, S. Chen, J. W. Y. Lam, Z. Wang, Y. Liu, H. S. Kwok, Y. Ma, B. Z. Tang, *Adv. Mater.* **2010**, *22*, 2159; c) H. Tong, Y. Hong, Y. Dong, M. Haeussler, J. W. Y. Lam, Z. Li, Z. Guo, Z. Guo, B. Z. Tang, *Chem. Commun.* **2006**, 3705; d) M. P. Aldred, G.-F. Zhang, C. Li, G. Chen, T. Chen, M.-Q. Zhu, *J. Mater. Chem. C* **2013**, *1*, 6709; e) N. B. Shustova, T.-C. Ong, A. F. Cozzolino, V. K. Michaelis, R. G. Griffin, M. Dinca, *J. Am. Chem. Soc.* **2012**, *134*, 15061.
[15] Q. Chen, D. Zhang, G. Zhang, X. Yang, Y. Feng, Q. Fan, D. Zhu, *Adv. Funct. Mater.* **2010**, *20*, 3244.
[16] B.-P. Jiang, D.-S. Guo, Y.-C. Liu, K.-P. Wang, Y. Liu, *Acs Nano* **2014**, *8*, 1609.
[17] D. T. Genna, A. G. Wong-Foy, A. J. Matzger, M. S. Sanford, *J. Am. Chem. Soc.* **2013**, *135*, 10586.
[18] P. Sutar, V. M. Suresh, T. K. Maji, (manuscript under preparation).

Chapter 3C

High aspect ratio, processable coordination polymer gel nanotubes based on an AIE-active LMWG with tunable emission

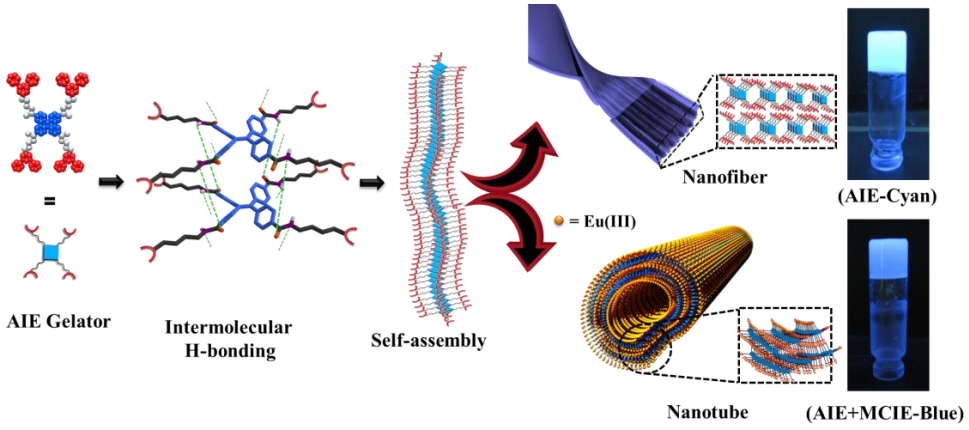

Summary

This chapter reports design and synthesis of an aggregation induced emission (AIE) active tetraphenylethene (TPE) based low molecular weight gelator (LMWG) which displays tunable emission in solid and gel state. LMWG self-assembles to form 1D nanofibers by H-bonding between amide functional groups. LMWG acts as a four connected linker to form a coordination polymer gel (CPG) with Eu^{III} by chelating terpyridine moiety. Dramatic morphology transformation from nanofibers to nanotubes is realized upon metal ion coordination. CPG shows enhanced mechanical stability along with tunable emission properties.

V. M. Suresh, A. De, T. K. Maji, *Chem. Commun.* **2015**, *51*, 14678

3C.1 Introduction

Self-assembly of π-conjugated low molecular weight gelators (LMWGs) having hydrophobic and hydrophilic segments through non-covalent interactions has been an attractive strategy in designing artificial nanostructures such as fibres, vesicles, rings, ribbons and tubes.[1] Particularly, one dimensional (1D) fibrillar or tubular morphologies of self-assembled π-conjugated chromophores are important for optoelectronic applications, as they provide feasible pathway for efficient energy migration or charge transport, and several such systems based on organic LMWGs have been well documented.[2] However, aggregation caused luminescence quenching (ACQ) in π-stacked chromophoric organic assemblies and their thermal/mechanical stability have been limiting issues for practical applications in organic light emitting diodes and luminescent sensors. The discovery of aggregation induced emission (AIE) phenomena of tetraphenylethene (TPE) in solid aggregates has provided an opportunity to overcome the ACQ effect.[3] The restricted rotation of phenyl rings through intermolecular Ph···H and Ph···Ph stacking interactions between TPE molecules in aggregated state dramatically enhances the emission and quantum yields compared to solutions and offer potential applications in biological sensors, organic light emitting diodes (OLEDs) and field effect transistors (FETs).[4] Nevertheless, the restricted rotation of phenyl moieties in TPE which populate the radiative states and increase the emission intensity have also been achieved either by integrating the TPE into a metal-organic framework (MOFs) structure through metal ion coordination known as matrix coordination induced emission (MCIE) or into conjugated microporous polymers (CMPs) by covalent linkage known as framework induced emission (FIE).[5] Despite its integration in 3D porous frameworks, complete restriction of phenyl ring rotation is not achieved due to a very low energy barrier of phenyl rotation,[6] which causes partial quenching of fluorescence of the framework. Therefore, we envision to design a new amide functionalized LMWG based on a TPE derivative (AIE active) with terminal terpyridine (TPY) units which would self-assemble via intermolecular H-bonding (Scheme 1) and metal coordination to form a three dimensional coordination polymer gel, where both AIE and MCIE phenomena can be observed. Thus soft CPG with enhanced and tunable emission can be realized.[7] In contrast to metal-organic gels derived from discrete metal complexes,[8] coordination polymer gels (CPGs) based on polydentate π-conjugated LMWGs are superior due to their long range structural ordering of the chromophores based on nanoscale periodicity

of inorganic components. In addition, CPGs possess high thermal/mechanical stability and show functions related to metal-ions such as magnetism, luminescence and catalytic activity can be comprehended.[9] Furthermore, the metal ligand bonds are amenable to reaction parameters thereby modular nanoscale materials with versatile morphologies can be perceived.[10] Here in, we aim to study the effect of metal-coordination on the secondary structure of self-assembly thus nanomorphologies and their luminescence properties arising from the combination of AIE and MCIE phenomena of tetrakis(4-carboxyphenylethene)acid tetrakis-{[3-([2,2′:6,2″]terpyridine-4′-ylamino)-propyl]-amide} (**L**) in corresponding gel state.

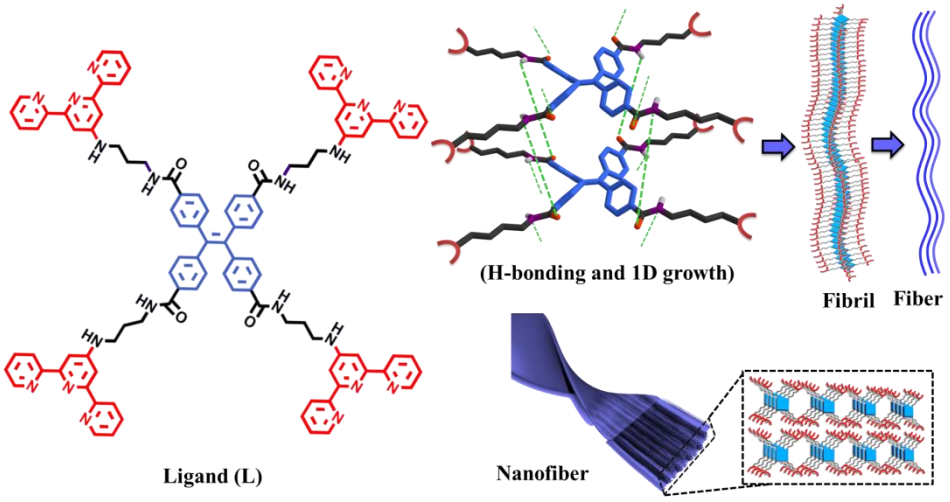

Scheme 1. Schematic representation of self-assembly of **L** through H-bonding between amide groups and formation of 1D nanostructure.

3C.2 Experimental section

3C.2.1 Materials

Tetraphenylethene, 1,3-diaminopropane, 4′-chloro-2,2′:6′,2″-terpyridine, trichloroisocyanuric acid (TCIC) and triphenylphosphine (PPh_3) are purchased from Sigma-Aldrich chemical Co. Ltd. Required solvents are pre-dried using standard literature procedures. UV-Vis experiments are carried out with spectroscopic grade solvents purchased from Spectrochem Ltd.

3C.2.2 Physical measurements

^{1}H NMR spectrum is recorded on a Bruker AV-400 spectrometer with chemical shifts recorded as ppm and all spectra are calibrated against TMS. UV-Vis spectra are recorded in a Perkin-Elmer lambda 900 spectrometer. Fluorescence measurements are accomplished using Perkin Elmer Ls 55 Luminescence spectrometer. Fourier transform

infrared (FTIR) spectra are recorded by making samples with KBr pellets using Bruker FT-IR spectrometer. Rheological measurements are performed using a Physica interfacial rheology system (IRS). Powder X-ray diffraction measurements are carried out on a Bruker D8 discover instrument using Cu-Kα radiation. Elemental analyses are carried out using a Thermo Scientific Flash 2000 CHN analyzer. Morphology studies are done using Lica-S440I field emission scanning electron microscopy (FESEM) by placing samples on silicon wafer under vacuum with an accelerating voltage of 10 kV. Transmission electron microscopy (TEM) studies are done on JOEL JEM-3010 with accelerating voltage of 300 kV. For this analysis the xerogels are dispersed in ethanol and then drop casted on a carbon coated copper grid. The solid state fluorescence quantum yield of **L** solid powder and **L** xerogel is determined by using integrating sphere, an absolute quantum yield measurement and calculated by Horiba Jobin Yvon. Lifetime measurements are carried out on an EPL-405 ps pulsed diode laser (Edinburgh instrument) used as the excitation source (λ_{ex}= 405 nm).

3C.2.3 Synthesis of ligand (L)

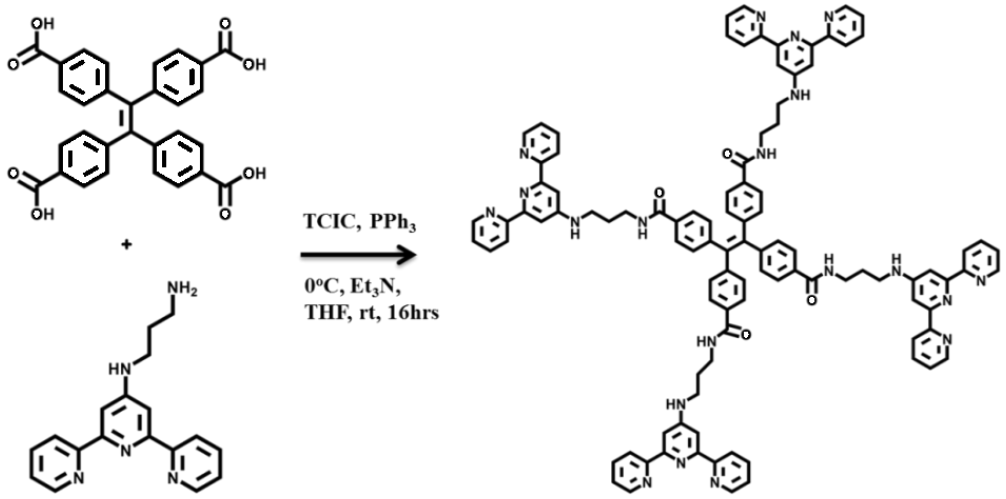

Figure 1. Synthetic scheme of **L** using amide coupling strategy.

Tetrkis(4-carboxy)tetraphenylethene and 2,2′;6′,2″-terpyridin-4′-yl-propane-1,3-diamine are synthesized by the reported procedures (Figure 1),[1] tetrkis(4-carboxy)tetraphenylethene (1 eq) is dissolved in tetrahydrofuran (THF) and cooled to 0 °C followed by addition of trichloroisocyanuric acid (TCIC) (4.2 eq) and triphenylphosphine (PPh_3) (4.2 eq) is added portion wise. The reaction mixture is stirred for 30 minutes at 0 °C under inert atmosphere. To the reaction mixture, a solution of 2,2′;6′,2″-terpyridin-4′-yl-propane-1,3-diamine (4 eq) and Et_3N in THF are added under

continuous stirring at 0 °C for 15 min and stirred at room temperature for 16 hrs. Precipitate is collected by filtration and washed several times with chloroform and acetone to get **L** in 60 % yield. **L** is dried under vacuum for 6 hrs at room temperature and analysed (Figure 2) with ^{1}H-NMR and HRMS. Elemental analysis Calcd. for **L** ($C_{102}H_{88}N_{20}O_4$): C, 72.3; H, 5.47; N, 16.54. Found: C, 72.16; H, 5.91; N, 16.28. HRMS (+ESI): *m/z* calculated for $C_{102}H_{88}N_{20}O_4$: 1657.9217, found: 1658.72339 $[M+H]^+$.

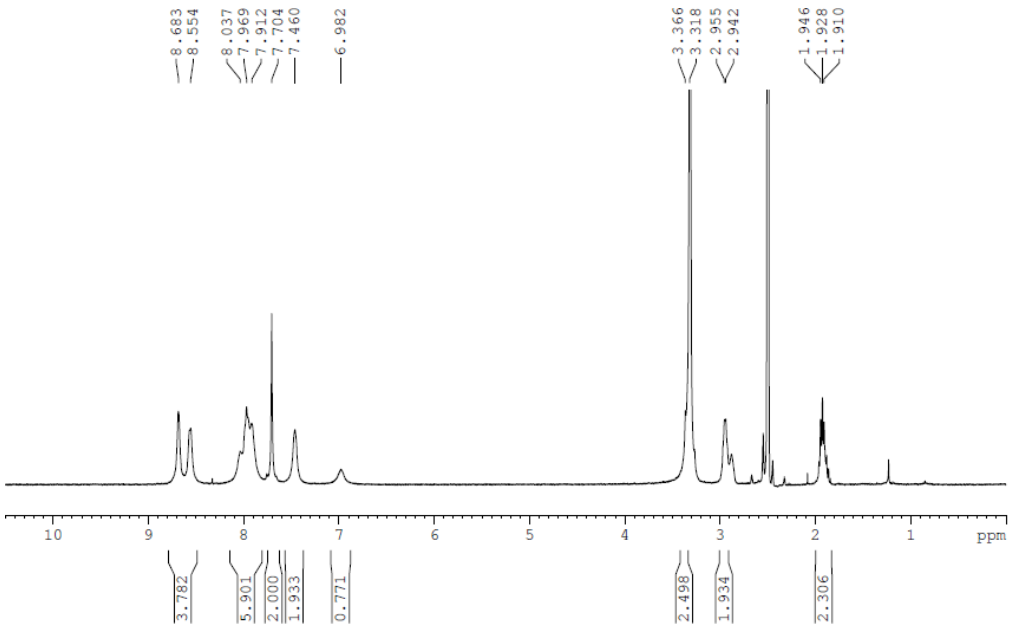

Figure 2. ^{1}H-NMR spectrum of **L** in dmso-d^6 solvent.

3C.2.4 Titration of L with Eu(III) ion in methanol

Figure 3 shows changes in absorbance spectra of **L** (3×10^{-5} M), on incremental addition of 10 μL of Eu(III) solution (10^{-3} M) which is equivalent to 0.3 eq of Eu(III) ion. The absorbance maxima at 280 nm is shifted bathochromically with a concomitant increase in the band centered at 320 nm suggesting clear binding of metal ion with ligand as observed in literature reports.[1c] The results of the titration are plotted along with Jobs plot which indeed suggest a 1:2 (L/Eu) complex formation (Figure 3). The emission spectrum of **L** in solution is shown in Figure 3. Excitation of **L** at 280 nm shows weak fluorescence centered at 410 nm assigned to TPY unit of **L** and no emission bands corresponding to Eu(III) are observed on incremental addition of Eu(III) solution. Slight changes in shift in emission at 410 nm may be attributed to the conformational changes in TPY on metal ion binding. It is worth mentioning that no TPE centered emission is observed may be due to the non-radiative decay of TPE emission at dilutions.

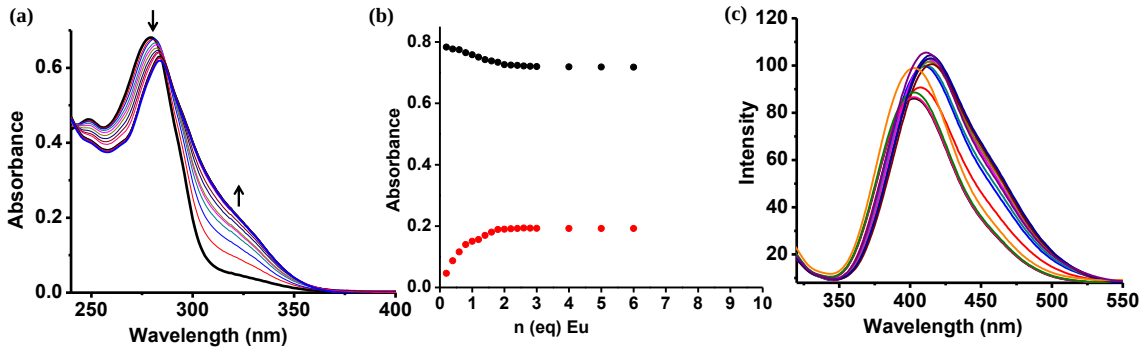

Figure 3. Changes in (a) absorption spectra of **L** (3×10^{-5} M) in methanol upon titrating with equivalents of $Eu(NO_3)_3{\cdot}6H_2O$ at 298 K and (b) binding isotherms for UV/Vis absorption spectra (black:280 nm and red:320 nm). (c) Changes in emission spectra on addition of incremental amounts of $Eu(NO_3)_3{\cdot}6H_2O$. Arrows indicate the changes in absorption spectrum on addition of amounts of Eu(III) ion to the **L** solution.

3C.2.5 Synthesis of L gel

7×10^{-3} M ligand solution in 1:2 $CHCl_3$/THF mixture is heated at 90 ºC for few minutes to dissolve which on cooling results in immediate opaque gel formation. Gel is observed to be stable upon inversion. Selected IR data of xerogel (KBr, cm^{-1}): 3399 (b), 3228 (w), 2946-2822 (m), 1632 (m), 1464 (s), 1301 (m), 1166 (m), 1023 (m), 806 (m). CHN analysis: Calculated values for $(C_{102}H_{88}N_{20}O_4)(C_4H_8O)_2$: C;73.29, H; 5.82, N; 15.55. Found: C; 72.57, H; 5.87, N; 15.39. Predicted formula: [**L**·2THF·0.5H_2O]

3C.2.6 Synthesis of CPG

Solution of **L** (7×10^{-3} M) in $CHCl_3$/THF (1:2) is mixed with solution of $Eu(NO_3)_3.6H_2O$ (1.4×10^{-2} M) in THF and heated at 90 ºC for few minutes. Formation of viscous liquid is observed initially which on cooling to room temperature yields a stable opaque gel. Selected IR data for xerogel (KBr, cm^{-1}): 3379 (b), 3211 (w), 2963-2829 (m), 1629 (m), 1461 (s), 1382 (m), 1172 (w), 1108 (w), 1016 (w), 801 (m). CHN analysis: Found: C, 53.51; H, 4.35; N, 14.98. Predicted formula: [Eu_2**L**·6(NO_3)·2THF].

3C.3 Results and discussion

3C.3.1 Structure and AIE property of L

LMWG, **L** has been synthesized by amide coupling reaction. FTIR of **L** show bands at 1643 cm^{-1} and 3420 cm^{-1} corresponding to ν(>C=O) and ν(N-H) stretching vibrations confirming the formation of an amide bond (Figure 4). Absorbance spectra of **L** in the solid state (Figure 5a) showed two major bands at 280 nm and 350 nm corresponding to π-π* transition of TPY and TPE groups, respectively (Figure 5b and 5c)

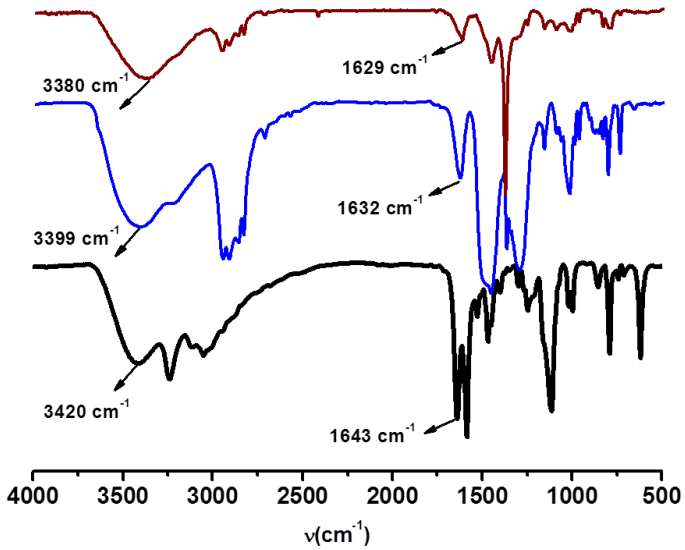

Figure 4. FTIR spectra of ligand powder (black), **L** xerogel (blue) and CPG (wine).

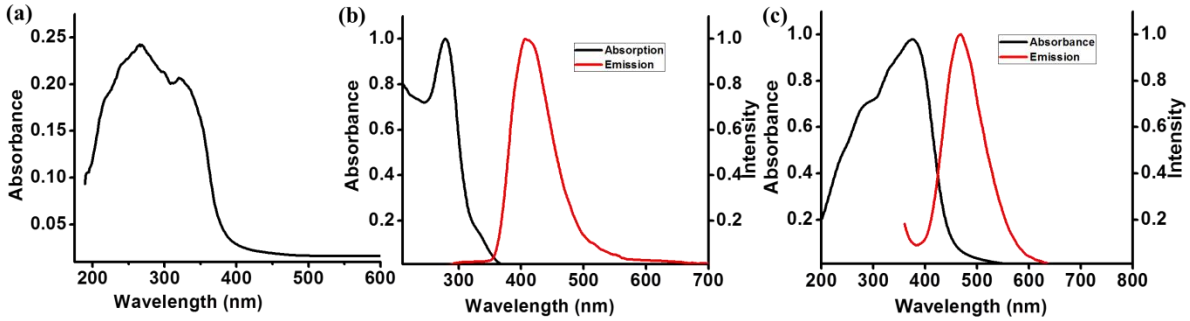

Figure 5. (a) Absorption spectrum of **L** in solid state, (b) absorbance (black) and emission (red) spectra of TPY in methanol, (c) absorbance (black) and emission (red) spectra of tetrkis(4-carboxy)tetraphenylethene in solid state.

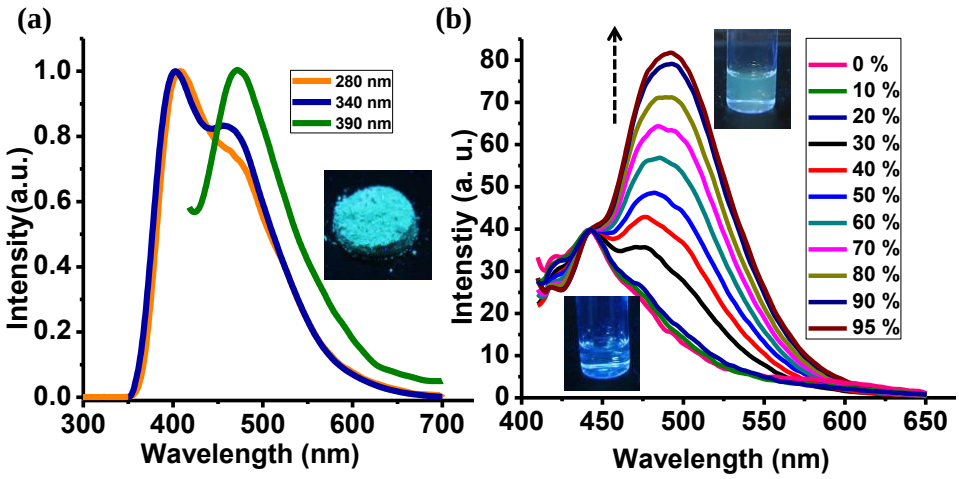

Figure 6. Aggregation induced emission behaviour of **L** in solid state: (a) Emission of **L** in solid state at different excitation wavelengths (inset: Image of **L** solid powder under UV light). (b) Gradual changes in emission spectra of **L** (10^{-3} M) in methanol on increasing the volume fraction of H_2O from 0-95 % (Normalized at 440 nm).

suggesting the presence of two individual chromophoric units in **L**.[5a,9g] Excitation at 280 nm showed the main emission at 410 nm ascribed to the TPY core while excitation at 390 nm showed the main emission at 480 nm originating from the TPE core of **L** due to the AIE phenomena operating in solid state (Figure 6a).[3a] Dilute solution of **L** in different solvents showed emission at 410 nm and only weak emission at 480 nm due to fast phenyl rotations of the TPE segment (Figure 7). To further study the AIE of **L**, emission studies are carried out in a binary mixture of MeOH/H_2O. Dilute solution of **L** (10^{-3} M) upon excitation at 380 nm showed very weak emission at 480 nm in pure methanol (0 % H_2O). However, upon increasing the H_2O content from 0-95 % by volume fraction, gradual enhancement in emission intensity at 480 nm is observed (Figure 6b). This emission enhancement at 480 nm is ascribed to the formation of **L** aggregates on addition of H_2O. These results are explained on the basis of AIE effect of TPE core of **L**. In dilute solutions (10^{-3} M); the phenyl ring rotations of TPE segment are exclusively significant which opens up the non-radiative decay channels thereby quenching the emission from TPE core. However, upon addition of H_2O, aggregation of **L** occurs where the Ph···Ph or Ph···H intermolecular interactions greatly reduce the phenyl rotation of TPE and open up radiative channels resulting in enhanced emission.

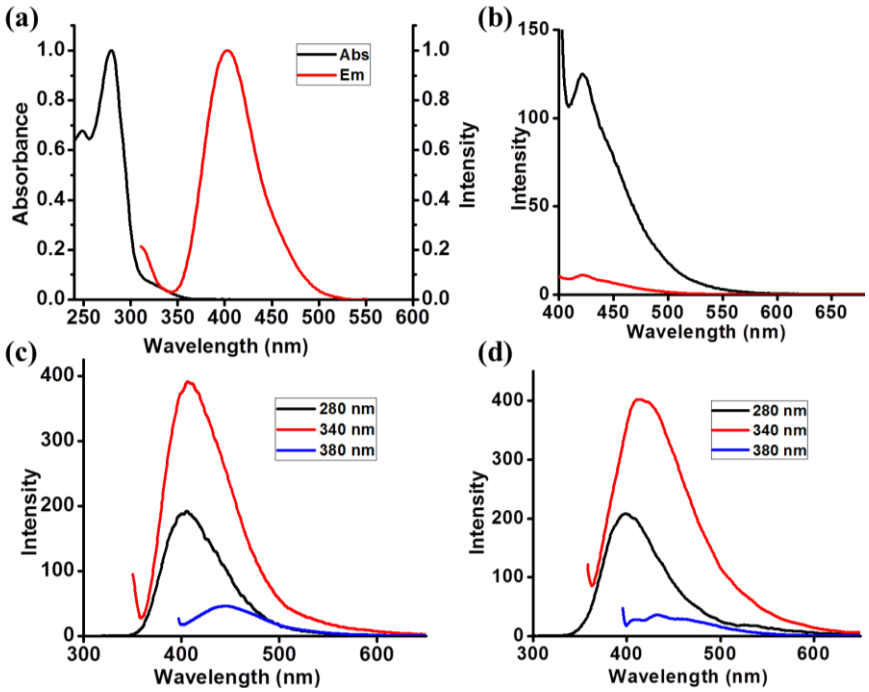

Figure 7. (a) UV/Vis absorption (black), emission spectrum excited at 280 nm (red), (b) 350 nm (black) and 390 nm (red) of methanol solution of **L** (3×10^{-5} M) at 298 K showing no TPE based emission. Emission spectra of **L** (3×10^{-5} M) at different excitation wavelengths (c) in DMF and (d) EtOH.

3C.3.2 Synthesis and characterization of L gel and CPG

Heating and cooling of **L** (7×10^{-3} M) in $CHCl_3$/THF (1:2) mixture results in the formation of a stable gel and is confirmed by inversion test method (Figure 8a). As shown in Scheme 1, it is expected that **L** self-assembles through intermolecular H-bonding interaction between amide functional groups and forms 1D nanostructure. FTIR of **L** xerogel shows bands at 1632 cm^{-1} and 3399 cm^{-1} corresponding to ν(>C=O) and ν(N-H) stretching vibrations, respectively, which are shifted to lower regions in comparison to assynthesized ligand suggesting the presence of intermolecular H-bonding (Figure 4). On the other hand, field emission scanning electron microscopy (FESEM) images of the **L** xerogel shows formation of micrometer long nanofibers of diameter 90-100 nm along with coiled nanostructures or rings with varied diameters (Figure 8b, Inset). Furthermore, transmission electron microscopy (TEM) shows formation of nanofibers and coiled

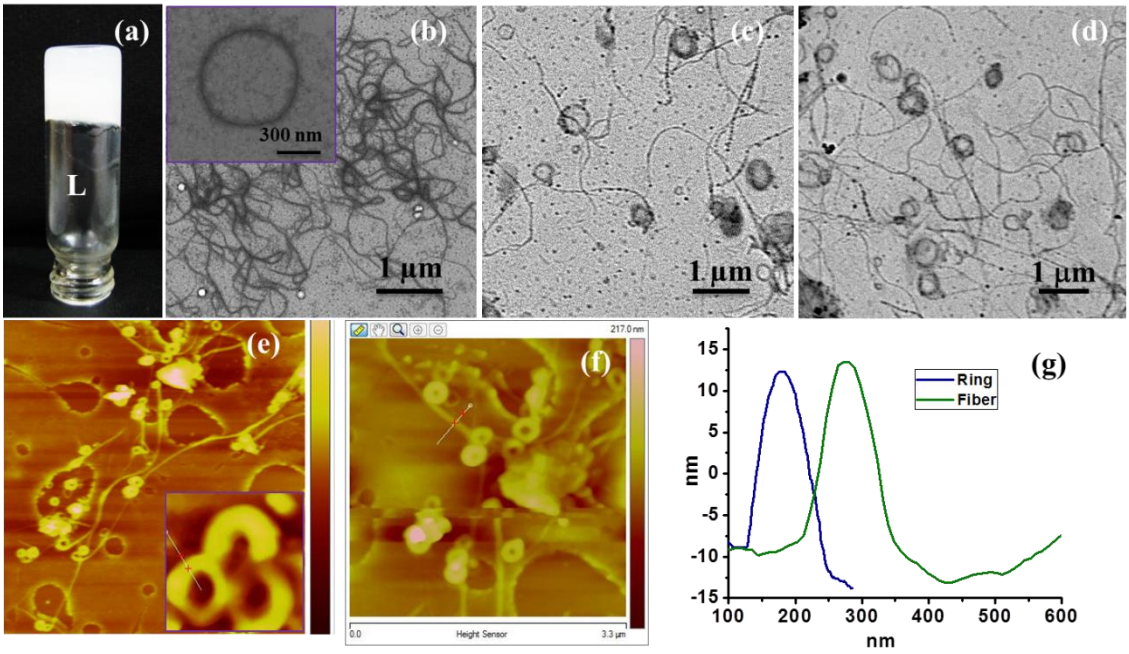

Figure 8. (a) Day light image of **L** gel, (b) FESEM image of **L** gel fibres (Inset: Single nanoring of **L** gel), (c), (d) TEM image showing presence of nanofibers and coiling of nanofibers toward ring formation in **L** gel and (e), (f) AFM images of nanorings and nanofibers of **L** gel and (g) corresponding height profiles.

nanostructures (Figure 8c and 8d) of dimensions consistent with SEM. AFM cross-sectional analysis (Figure 8e and 8f) of **L** xerogel shows nanofibers and coiled nanostructures of diameter 100±10 nm, and the corresponding height of the fibres is found to be 21±1 nm (Figure 8g). The packing in the gel is further supported by X-ray

diffraction (XRD) measurements of the **L** xerogel; a diffraction peak at 21.7° with a *d*-spacing value of 4.0 Å suggests weak π-π interactions between TPE cores of **L**.[12a]

L/$Eu(NO_3)_3 \cdot 6H_2O$, (1:2 eq.) in $CHCl_3$/THF (1:2) results in turbid solution which upon further heating and cooling leads to immediate gel formation (see Experimental details), which is confirmed by an inversion test method (Figure 9a). The presence of Eu(III) ions in the CPG is confirmed by energy dispersive X-ray analysis (EDAX) (Figure 10). The presence of intermolecular H-bonding in CPG is evident from FTIR studies. Furthermore, a strong peak at 1382 cm^{-1} corresponds to *ν*(N-O) stretching vibration, indicating the presence of coordinated nitrate ions in CPG (Figure 4). FESEM of xerogel shows 1D nanostructures of micron length with diameter of 160-200 nm (Figure 9b). While, TEM at high magnification shows formation of high aspect ratio nanotubes with uniformly spaced dark lines separated by a bright core. The wall thickness is observed to be 80-100 nm with several micron lengths (Figure 9c-e). The height of the nanotubes calculated from the AFM cross-sectional analysis is found to be 40±2 nm (Figure 9f, Inset).

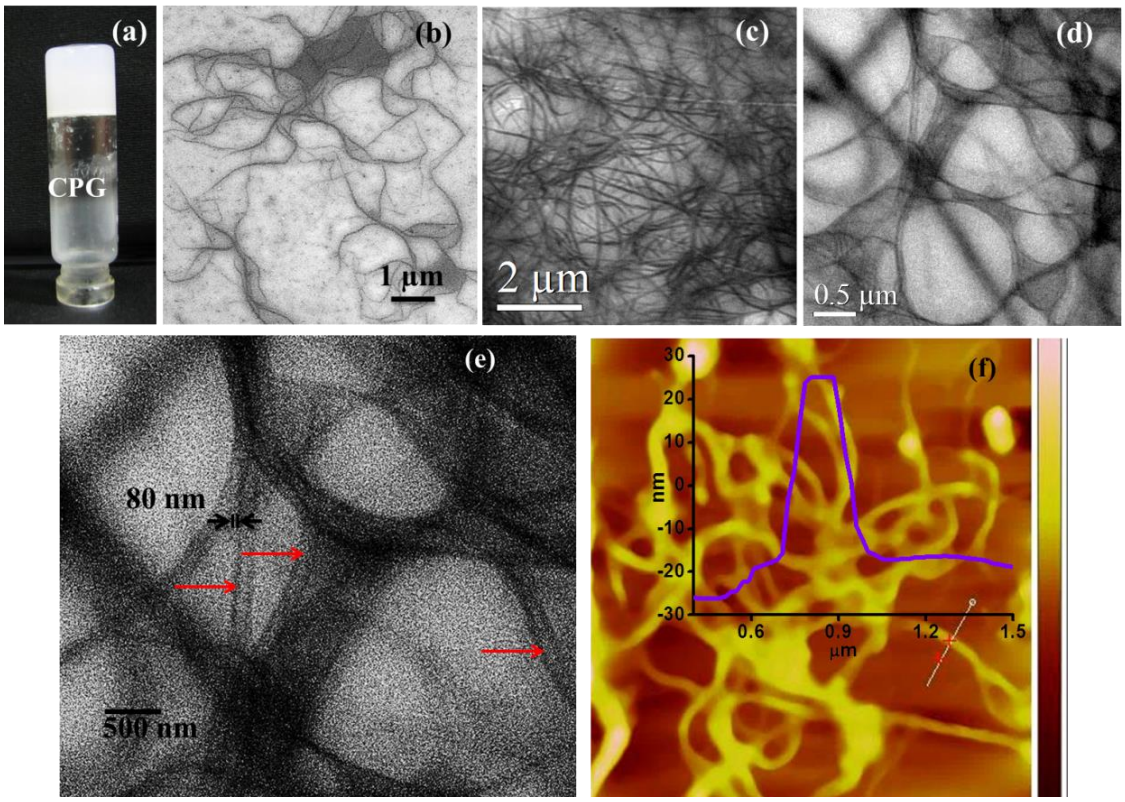

Figure 9. (a) Day light image of CPG, (b) FESEM image, (c), (d), (e) TEM images showing the nanotubular structures of CPG and (f) AFM image of nanotubes and corresponding height profile (Inset).

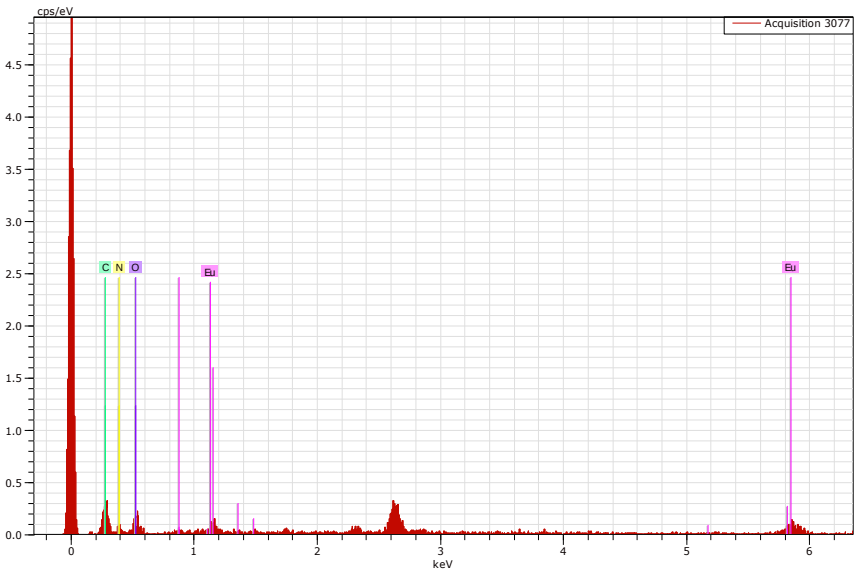

Figure 10. EDAX of CPG showing the presence of Eu(III) ion.

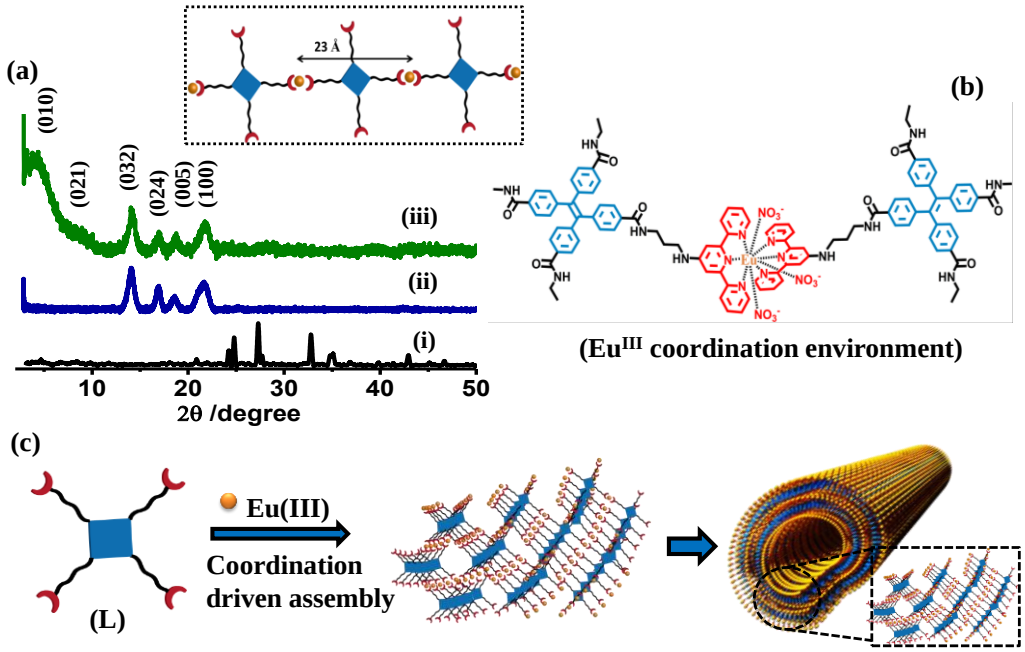

Figure 11. (a) PXRD at different state: Solid ligand powder (i), **L** xerogel (ii), and CPG (iii), (Inset: Distance between two Eu(III) centers in CPG). (b) Probable coordination environment around the Eu(III) center showing the orthogonal orientation of TPY units in CPG. (c) Schematic showing the proposed self-assembly of CPG to form nanotubular structure.

Structural ordering by metal ion binding is further evident by XRD measurements. Interestingly, diffraction pattern of CPG at higher angle is observed to be comparable with **L** gel, suggesting similarity in the primary structure of the self-assembled gels.

However, an additional diffraction peak at 4.0° (*d*-spacing: 21.9 Å) is observed in case of CPG, and this *d*-spacing value closely matches with the calculated distance between two Eu(III) centers bridged by **L** (Figure 11a). Indexing the diffraction pattern of CPG (Fig. 2i) using a CRYSFIRE powder indexing system using the Taup (TP) program (Table 1) suggest an orthorhombic phase for CPG, where a = 4.08574 Å, b = 22.3266 Å, c = 23.6498 Å and V= 2157.35 (Å^3). A low angle diffraction peak at 4.0° is assigned to the (010) plane, the corresponding periodicity of which along the metal centers (Figure 11a, Inset) and the peak at 21.7° (d = 4 Å) correlate to the molecular stacking of TPE units.[12a] Based on the preceding results, a proposed model for self-assembly of CPG is envisaged (Figure 11b, c). Initially, **L** self-assembles through intermolecular H-bonding of amide groups and forms 1D nanostructure leaving free TPY moieties on the surface which are bridged by the metal ions and extend the self-assembly into an infinite 3D coordination polymeric structure. It is believed that the TPY units around Eu(III) ions arrange themselves into an orthogonal orientation in order to reduce steric repulsion and results in bending of nanostructures to form nanotubular morphology. To investigate the effect of

Table 1. Unit cell parameters of CPG[a], Indexed using CRYSFIRE powder indexing system using Taup (TP) program[13]

h	*k*	*l*	2*θ*	*D*(exptl)	*D*(cald)	max. dev.
0	1	0	4.0277	21.92022	22.32656	.417E-04
0	2	1	8.8255	10.01158	10.09515	.907E-04
0	3	2	14.0302	6.30717	6.29857	.143E-03
0	2	4	16.9468	5.22768	5.22488	.172E-03
0	0	5	18.7555	4.72743	4.72996	.190E-03
1	0	0	21.7445	4.08388	4.08574	.218E-03
1	4	2	28.0661	28.0661	3.17574	.277E-03
1	3	8	39.4929	2.27995	2.27989	.374E-03

[a]V= 2157.35 (Å^3). Phase = orthorhombic. Parameters : a = 4.08574 Å, b = 22.3266 Å, c = 23.6498 Å ; α = 90°, β = 90°, and γ = 90°.

metal ion binding on mechanical properties, we have performed oscillatory strain sweep measurements on organogel and CPG at a frequency of 1 rad s^{-1}. As seen in Figure 12, the storage modulus (G′) for both the gels is larger than the loss modulus (G″) for $\gamma < 5$ % thereby suggesting elastic nature of the gels. For both gels G′>G″ at smaller strains and with increasing strain G′ decreases with a simultaneous rise in G″ indicating the transition of gels from a viscoelastic solid to a viscoelastic liquid region. Interestingly, we observed

that G′ of CPG is at least an order of magnitude larger than G′ of the **L** gel suggesting enhanced rigidity of CPG over the **L** gel. The higher rigidity of CPG can be visualized from an interconnected 3D network like structure present in CPG due to metal-coordination.

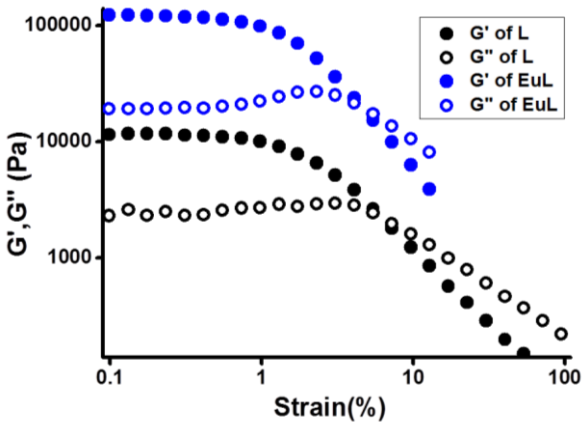

Figure 12. Oscillatory strain measurements of **L** gel (black) and CPG or Eu**L** (blue), filled and open circles indicate storage and loss modulus respectively.

3C.3.3 Photophysical properties of L gel and CPG

The **L** xerogel shows a broad absorption band (Figure 13a) with λ_{max} = 340 nm, while the CPG shows 10 nm blue shifted absorption band with λ_{max} = 330 nm, this blue shift in the absorbance spectra of CPG can be attributed to the decrease in the planarization of TPE moiety or more twisting of phenyl moieties of TPE upon metal coordination in contrast to **L** xerogel. The **L** gel shows strong cyan emission when excited at 340 nm with maxima at 460 nm, while CPG shows strong blue emission with maxima at 435 nm (λ_{ex} = 330 nm) with a significant hypsochromic shift of 25 nm with respect to the **L** gel (Figure 13b and 13c). In general, the enhanced emission intensity of AIE chromophores is dependent on the extent of aggregation, and emission maxima strongly depend on the extent of planarization or conjugation of TPE phenyls in aggregated state. When **L** self-assembles through H-bonding the rotation of phenyls is greatly inhibited due to effective Ph···Ph interactions between the stacked TPE units of **L** which results in the opening of radiative decay pathways and thus AIE is realized. On the other hand, when Eu(III) binds to **L** in case of CPG, the emission properties can be attributed to the combined effect of MCIE and AIE. Also, the three dimensional coordination polymer networks like structure of CPG where the two TPY units position orthogonally decreases effective close packing of **L** TPE units leading to decreased

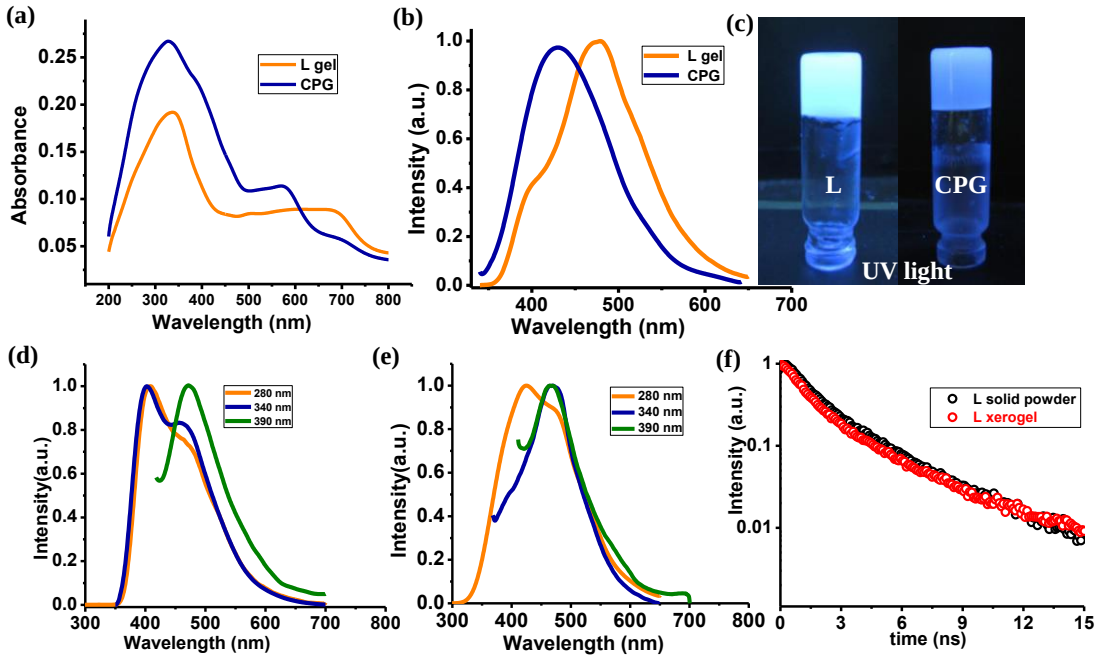

Figure 13. (a) Absorption, (b) emission spectra of **L** xerogel (green) and CPG xerogel (blue) and (c) corresponding images under UV light. (d) Emission spectra at different excitation wavelengths (280, 340 and 390 nm) for **L** solid powder and (e) **L** xerogel. (f) Time resolved fluorescence life-time of **L** solid powder (black) and **L** xerogel (red).

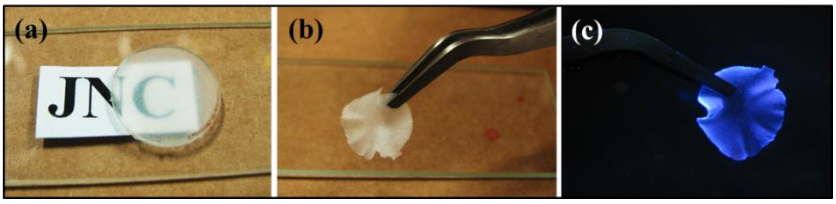

Figure 14. Formation of transparent and stable films of CPG showing its easy processability and stability. (a-c) Images of CPG under day and UV light.

planarization of TPE phenyls in CPG in comparison to **L** gel. Thus metal coordination of **L** decreases planarization and results in blue emission for CPG.[12b] Resembling **L** solid powder, excitation of **L** gel at 280 nm showed two bands at 420 nm corresponding to TPY and 460 nm corresponding to TPE (Figure 13d and 13e). Excitation at 340 and 390 nm showed the main emission at 460 nm corresponding to the TPE segment similar to **L** solid powder. Time resolved fluorescence life times showed life time of 0.9 (τ_1), 3.1 ns (τ_2) and 0.8(τ_1), 3.2 ns(τ_2) for **L** solid powder and **L** gel, respectively, and the corresponding quantum yields are found to be 4.3 % and 2.6 % upon excitation at 380 nm respectively (Figure 13f). Solution processibility is key for several practical applications or device fabrication of these gels. In spite of their rigidity, CPG gel can be easily transferred onto solid substrates with gentle shaking. Figure 14a-c shows the quartz glass

substrate cast with CPG which forms transparent films on drying. The emission property of this film CPG remains intact. This clearly indicates that these hybrid nano-assemblies are highly processable which is of paramount importance for large area coating.

3C.4 Conclusion

In conclusion, the preceding results show the design and synthesis of a new coordination polymer gel based on a TPE gelator and Eu(III) ion. Metal coordination provided structural control and transforms the morphology from 1D nanofiber to nanotubes with high mechanical stability. The combined effect of AIE and metal-coordination leads to enhanced and tunable emission in self-assembled gel state. CPGs are highly solution processable and made into transparent films. This new approach of combining AIE and MCIE would provide alternative route for fabrication of luminescent soft functional hybrid materials for solid state lighting and related applications.

3C.5 References

[1] a) J. W. Steed, *Chem. Soc. Rev.* **2010**, *39*, 3686; b) A. Ajayaghosh, V. K. Praveen, *Acc. Chem. Res.* **2007**, *40*, 644; c) L. C. Palmer, S. I. Stupp, *Acc. Chem. Res.* **2008**, *41*, 1674; d) T. Shimizu, M. Masuda, H. Minamikawa, *Chem. Rev.* **2005**, *105*, 1401; e) J. P. Hill, W. S. Jin, A. Kosaka, T. Fukushima, H. Ichihara, T. Shimomura, K. Ito, T. Hashizume, N. Ishii, T. Aida, *Science* **2004**, *304*, 1481; f) D. Goerl, X. Zhang, F. Würthner, *Angew. Chem. Int. Ed.* **2012**, *51*, 6328; g) F. J. M. Hoeben, P. Jonkheijm, E. W. Meijer, A. P. H. J. Schenning, *Chem. Rev.* **2005**, *105*, 1491.

[2] a) A. Schenning, E. W. Meijer, *Chem. Commun.* **2005**, 3245; b) A. Ajayaghosh, V. K. Praveen, C. Vijayakumar, *Chem. Soc. Rev.* **2008**, *37*, 109; c) T. Sendai, S. Biswas, T. Aida, *J. Am. Chem. Soc.* **2013**, *135*, 11509; d) C. Vijayakumar, V. K. Praveen, A. Ajayaghosh, *Adv. Mater.* **2009**, *21*, 2059; e) T. Kato, N. Mizoshita, K. Kishimoto, *Angew. Chem. Int. Ed.* **2006**, *45*, 38; f) P. A. Korevaar, T. F. A. de Greef, E. W. Meijer, *Chem. Mater.* **2014**, *26*, 576; g) W. Y. Yang, E. Lee, M. Lee, *J. Am. Chem. Soc.* **2006**, *128*, 3484.

[3] a) Y. Hong, J. W. Y. Lam, B. Z. Tang, *Chem. Soc. Rev.* **2011**, *40*, 5361; b) P. -I. Shih, C. -Y. Chuang, C. -H. Chien, E. W. -G. Diau, C. -F. Shu, *Adv. Funct. Mater.* **2007**, *17*, 3141; c) Q. Chen, D. Zhang, G. Zhang, X. Yang, Y. Feng, Q. Fan, D. Zhu, *Adv. Funct. Mater.* **2010**, *20*, 3244.

[4] a) W. Z. Yuan, P. Lu, S. Chen, J. W. Y. Lam, Z. Wang, Y. Liu, H. S. Kwok, Y. Ma, B. Z. Tang, *Adv. Mater.* **2010**, *22*, 2159; b) J. Y. Kim, T. Yasuda, Y. S. Yang, C. Adachi, *Adv. Mater.* **2013**, *25*, 2666; c) Y. Liu, C. Deng, L. Tang, A. Qin, R. Hu, J. Z. Sun, B. Z. Tang, *J. Am. Chem. Soc.* **2010**, *133*, 660.

[5] a) N. B. Shustova, B. D. McCarthy, M. Dinca, *J. Am. Chem. Soc.* **2011**, *133*, 20126; b) V. M. Suresh, S. Bonakala, S. Roy, S. Balasubramanian, T. K. Maji, *J. Phys. Chem. C* **2014**, *118*, 24369.

[6] S. L. Gould, D. Tranchemontagne, O. M. Yaghi, M. A. Garcia-Garibay, *J. Am. Chem. Soc.* **2008**, *130*, 3246.

[7] a) A. Y. -Y. Tam, V. W. -W. Yam, *Chem. Soc. Rev.* **2013**, *42*, 1540; b) L. Wang, Y. Liu, Z. Shen, T. Wang, M. Liu, *Chem. Commun.* **2014**, *50*, 15874; c) H. J. Kim, W. C. Zin, M. Lee, *J. Am. Chem. Soc.* **2004**, *126*, 7009; d) C. Li, K. Deng, Z. Tang, L. Jiang, *J. Am. Chem. Soc.* **2010**, *132*, 8202; e) P. Byrne, G. O. Lloyd, L. Applegarth, K. M. Anderson, N. Clarke, J. W. Steed, *New J. Chem.* **2010**, *34*, 2261; f) J. Zhang, X. Wang, L. He, L. Chen, C. -Y. Su, S. L. James, *New J. Chem.* **2009**, *33*, 1070.

[8] a) Y. Pan, Y. Gao, J. Shi, L. Wang, B. Xu, *J. Mater. Chem.* **2011**, *21*, 6804; b) Y. Li, A. Y. -Y. Tam, K. M. -C. Wong, W. Li, L. Wu, V. W. -W. Yam, *Chem. Eur. J.* **2011**, *17*, 8048.

[9] a) M. -O. M. Piepenbrock, G. O. Lloyd, N. Clarke, J. W. Steed, *Chem. Rev.* **2010**, *110*, 1960; b) P. Sutar, V. M. Suresh, T. K. Maji, *Chem. Commun.* **2015**, *51*, 9876; c) O. Roubeau, A. Colin, W. Schmitt, R. Clerac, *Angew. Chem. Int. Ed.* **2004**, *43*, 3283; d) M. -O. M. Piepenbrock, N. Clarke, J. W. Steed, *Soft Matter* **2011**, *7*, 2412; e) Q. Liu, Y. Wang, W. Li, L. Wu, *Langmuir* **2007**, *23*, 8217; f) O. Kotova, R. Daly, C. M. G. dos Santos, M. Boese, P. E. Kruger, J. J. Boland, T. Gunnlaugsson, *Angew. Chem. Int. Ed.* **2012**, *51*, 7208; g) Y. Zhang, B. Zhang, Y. Kuang, Y. Gao, J. Shi, X. X. Zhang, B. Xu, *J. Am. Chem. Soc.* **2013**, *135*, 5008; h) J. B. Beck, S. J. Rowan, *J. Am. Chem. Soc.* **2003**, *125*, 13922; i) P. K. Vemula, G. John, *Chem. Commun.* **2006**, 2218.

[10] a) V. M. Suresh, S. J. George, T. K. Maji, *Adv. Funct. Mater.* **2013**, *23*, 5585; b) V. M. Suresh, S. Chatterjee, R. Modak, V. Tiwari, A. B. Patel, T. K. Kundu, T. K. Maji, *J. Phys. Chem. C* **2014**, *118*, 12241.

[11] a) N. B. Shustova, B. D. McCarthy, M. Dinca, *J. Am. Chem. Soc.* **2011**, *133*, 20126; b) O. Kotova, R. Daly, C. M. G. dos Santos, M. Boese, P. E. Kruger, J. J. Boland, T. Gunnlaugsson, *Angew. Chem. Int. Ed.* **2012**, *51*, 7208; c) R. D. Rodrigues, I. M. A. Barros, E. L. S. Lima, *Tetrahedron Lett.* **2005**, *46*, 5945.

[12] a) W.-H. Yu, C. Chen, P. Hu, B.-Q. Wang, C. Redshaw, K.-Q. Zhao, *RSC Adv.* **2013**, *3*, 14099; b) W. Z. Yuan, F. Mahtab, Y. Gong, Z.-Q. Yu, P. Lu, Y. Tang, J. W. Y. Lam, C. Zhu, B. Z. Tang, *J. Mater. Chem.* **2012**, *22*, 10472.

[13] D. Taupin, *J. Appl. Cryst.* **1973**, *6*, 380.

Chapter 4

Highly Luminescent Microporous Organic Polymer with Lewis acidic 'Boron' Sites on the Pore Surface: Ratiometric Sensing and Capture of F^- Ions

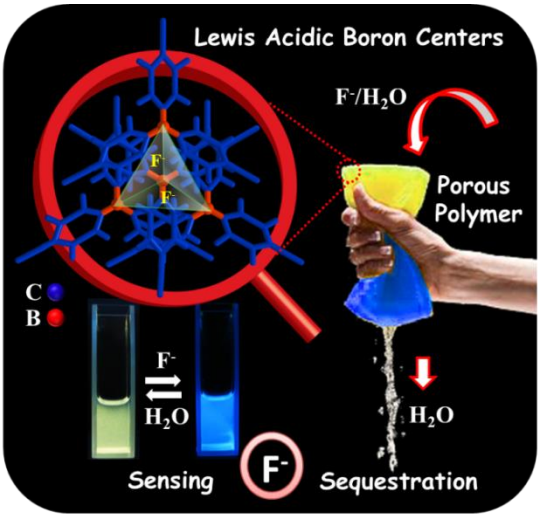

Summary

Reversible and selective capture/detection of F^- ion in water is highly important as excess intake leads to adverse effects on human health. Highly robust Lewis acidic luminescent porous organic materials have potential for efficient sequestration and detection of F^- ions. This chapter reports rational design and synthesis of a boron-based, Lewis acidic microporous organic polymer (**BMOP**) derived from tris(4-bromo-2,3,5,6-tetramethylphenyl)boron nodes diethynylbiphenyl linker with a pore size of 1.08 nm for selective turn-on sensing and capture of F^- ion in aqueous medium. The presence of a vacant p_π orbital on boron center of **BMOP** results intramolecular charge transfer (ICT) from the linker to boron. **BMOP** shows selective turn-on blue emission for F^- ions in aqueous mixtures with a detection limit of 2.6 μM. Strong B-F interactions facilitate rapid sequestration of F^- by BMOP. ICT emission of BMOP can be reversibly regenerated by addition of excess water, and the polymer can be reused for several times.

V. M. Suresh, A. Bandyopadhyay, S. Roy, S. K. Pati, T. K. Maji, *Chem. Eur. J.* **2015**, *21*, 1079. ***A patent has been filed for this work (Patent No: 1871/CHE/2015)***

4.1 Introduction

Reversible and selective detection/capture of excess F^- ion is important due to its impact on human health and the environment.[1,2] The World Health Organization recommends F^- contents in drinking water of less than 1.5 ppm, and overexposure is known to cause dental fluorosis, osteoporosis, and other serious health problems.[1] Although several methods for the detection and sequestration of F^- ions have appeared, less selectivity, poor recyclability, leaching, and weak or no analytical signal output demand development of new materials that would show both selective and reversible readout fluorescence signals and sequestration of F^- ions.[3] Recently, small-molecule sensors having vacant Lewis acidic centers have been studied for colorimetric and fluorimetric sensing of small anions such as F^- in organic solvents.[4] However, they often suffer from very low density of active sites and vulnerability to micro environmental conditions such as solvent, and the counter ion-pairing effect limits real-time monitoring of F^-.[5] On the other hand, metal complexes and small organic molecular sensors for F^- detection in solvents such as H_2O, THF, DMF have been reported, but they suffer from poor reversibility, low recyclability, or difficult y in regeneration.[6] Reversibility and easy recyclability are necessary for the commercialization and industrial application of a sensor. In this context, the confined nanospaces enclosed by a high density of F^- binding sites with fluorescence read-out signalling ability of solid porous materials [7] are potential for rapid and selective detection of F^- ions. The insoluble nature of porous solid materials facilitates heterogeneous-phase detection of F^- ions and allows easy recovery of the sensor material from aqueous solutions. Sensors based on inorganic-organic hybrid systems such as metal-organic frameworks (MOFs) have been reported, but their poor hydrolytic stability and limited regenerability due to disintegration of framework on F^- binding limits their application.[8] In this respect, porous organic polymer solid adsorbents[9] such as conjugated microporous polymers (CMPs), pioneered by Cooper *et al.*, [10] have great potential for selective sensing and capture of F^- ions, owing to their strong fluorescence signalling ability and pronounced chemical/thermal and hydrolytic stability due to strong covalent linkages between their building blocks. Synthetic diversity and the availability of large number of organic struts provides functionalized pore surfaces for desired applications.[11] In addition, the ability to host various guests in the confined environment of nanopores offers guest-responsive modulation of optical and electronic properties and can be exploited for sensing applications.[12] Among the CMPs,[13] heteroatom-containing

conjugated porous polymers in which electron-donor atoms such as N are replaced by electron-deficient B centers have potential for the detection of F^- ions. Conjugation through the vacant p_π orbital on boron results in characteristic photophysical and electronic properties in the polymer. Therefore such a polymer would have a potential as a nonlinear optical material, as an electroluminescent and charge transporter in organic light-emitting diodes (OLEDs).[14] Herein, we report the rational design and synthesis of a boron microporous organic polymer (BMOP) containing methyl-protected triarylborane as node and diethynylbiphenyl as linker for selective and turn-on fluorescent sensing and sequestration of F^- ions with excellent recyclability from aqueous solution. High-density Lewis acidic B centers throughout the polymer facilitate selective and rapid detection of small anions, which would significantly obstruct intramolecular charge transfer (ICT) from the diethynylbiphenyl linker to empty p_π orbital of boron. The ICT emission changes to intense blue emission on binding of F^- ion to the boron center at levels as low as 0.2 ppm in aqueous binary mixtures. Furthermore, strong covalent linkages in the polymer provide high hydrolytic stability and easy regeneration of the sensor on addition of an excess of water.

4.2 Experimental section

4.2.1 Materials

Tetrakis(triphenylphosphine)palladium(0), bis(triphenylphosphine)palladium(II) dichloride and copper iodide (CuI) are purchased from Sigma-Aldrich Chemical Co. Required solvents are dried prior to use.

4.2.2 Physical measurements

Elemental analysis is carried out using Thermo Scientific Flash 2000 CHN analyzer. Infrared spectral studies are done by making samples with KBr pellets using Bruker FT-IR spectrometer. Thermal stability is analyzed using Mettler Toledo TGA 850 instrument under inert atmosphere in the temperature range of 30-800 °C at a heating rate of 5 °C/min. Powder X-ray diffraction studies of the samples are recorded on a Bruker D8 discover instrument using Cu-Kα radiation. Morphological studies have been carried out using Lica-S440I scanning electron microscope (SEM) by placing samples on a silicon wafer under high vacuum with an accelerating voltage of 10 kV. Transmission electron microscopy (TEM) analysis has been performed using JEOL JEM-3010 with an accelerating voltage at 300 kV. For this analysis **BMOP** is dispersed in ethanol by

sonication before drop casting on a carbon-coated copper grid. Porosity measurements are carried out using QUNATACHROME QUADRASORD-SI analyzer at 77 K for N_2 and 195 K for CO_2. Fluorescence studies are accomplished using PerkinElmer Ls 55 Luminescence spectrometer. Solid state ^{13}C cross-polarization magnetic angle spinning (CP/MAS) NMR spectrum is measured on a varian infinity plus 300WB spectrometer at a MAS rate of 5 kHz and a CP contact time of 1.4 ms. ^{1}H-NMR is recorded on a Bruker AV-400 spectrometer with chemical shifts reported as ppm.

4.2.3 Computational details

Energy optimization of all structures and electronic property calculations have been carried out using Gaussian 09 DFT software.[15] We have used the hybrid B3LYP (Becke exchange with Lee, Yang, and Parr correlation) functional[16-18] combined with 6-31+G(d) basis set for all the calculations. Optical properties have been calculated using the time dependent density functional theory (TD-DFT) method as implemented in the Gaussian 09 package with hybrid B3LYP exchange-correlation functional and with the basis set 6-31+g(d). It has been already found that B3LYP/6-31+g(d) calculations are very accurate to predict the low energy excited states.[19-20] TD-DFT calculations are performed for some molecules in gas phase as well as in water or dichloromethane medium, using polarizable continuum model (PCM) to include the solvent effect.[21]

The excited state geometries for the linkers are optimized using the TD-DFT method and the emission spectra are calculated using the optimized first excited state (S_1) geometry of the linker and the extended linker. All the calculated absorption spectra in this work have been calculated for the first 12 singlet excited states and all the calculated emission spectra are for the first 6 low lying singlet excited states.

4.2.4 Synthesis of 1,4-dibromo-2,3,5,6-tetramethylbenzene

2,3,5,6-tetramethylbenzene (2 g, 14.9 mmol) is dissolved in dry dichloromethane (10 mL) and cooled to 0° C. Then, Br_2 (14.9 mmol, 0.7 mL) is added dropwise at 0° C under continuous stirring and N_2 atmosphere. The reaction mixture brought to room temperature and stirred for further 10 hrs. The excess Br_2 is quenched with sodium thiosulphate and extracted with dichloromethane, and purified by column chromatography with hexane as eluent. Yield: 70 %

4.2.5 Synthesis of tris(4-bromo-2,3,5,6-tetramethylphenyl)boron

1,4-dibromo-2,3,5,6-tetramethylbenzene (1g, 3.42 mmol) is dissolved in dry diethyl ether and pentane solution of *n*-BuLi (2.5 M, 3.4 mmol, 1.4 mL) is added at -78°

C under inert atmosphere. Reaction mixture is allowed to warm to 0° C and stirred for 20 min, and then $BF_3.Et_2O$ (1.1 mmol, 0.14 mL) is added dropwise at -78° C. The reaction mixture is warmed to room temperature and then stirred for further 16 hrs. An excess amount of water is added to the reaction mixture resulting in a white precipitate. The precipitate is collected by filtration and the filtrate is extracted with ether and then dried over sodium sulfate. The solid is washed with ether and methanol to obtain pure product. Analyzed using ^{1}H-NMR spectra (Figure 1a). Yield: 65 %

4.2.6 Synthesis of 4, 4′-diethynylbiphenyl

4,4′-diiodobiphenyl (2g, 4.92 mmol) and Et_3N (40 mL) are dissolved in THF, degassed and purged with Ar gas. Then, $PdCl_2(PPh_3)_2$ (0.24 mmol, 140 mg), CuI (0.24 mmol, 38 mg) and trimethylsilylacetylene (19.7 mmol, 2.8 mL) are added under inert atmosphere. The reaction mixture is degassed/purged with Ar and stirred for 10 hrs at room temperature. Then the reaction mixture is filtered and washed with ether and hexane several times, and then the filtrate is dried under reduced pressure. Mixture is purified by column chromatography. 4,4′-bis(trimethylsilylpropynyl)biphenyl (1g, 2.89 mmol) is dissolved in methanol/dichloromethane mixture (1:1, 50 mL) and K_2CO_3 (1.6 g, 11.5 mmol) is added and stirred for 6 hrs at room temperature. Reaction mixture is added to water to dissolve unreacted K_2CO_3 and extracted with dichloromethane. The DCM solution is dried under reduced pressure to result in pale yellow powder. Analyzed using ^{1}H-NMR spectra (Figure 1b). Yield: 80%

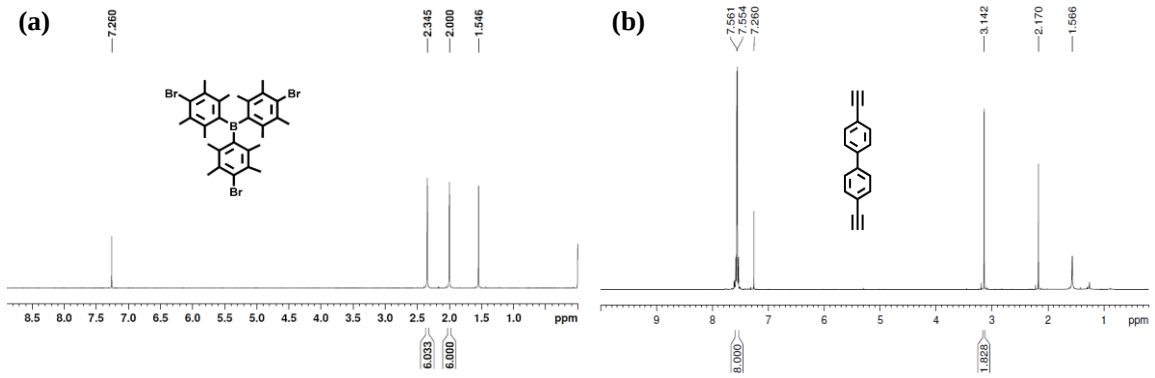

Figure 1. ^{1}H-NMR spectrum of (a) tris(4-bromo-2,3,5,6-tetramethylphenyl)boron and (b) 4,4′-diethynylbiphenyl in $CDCl_3$.

4.2.7 Synthesis of BMOP

Tris(4-bromo-2,3,5,6-tetramethylphenyl)boron (120 mg, 0.18 mmol) and 4,4′-diethynylbiphenyl (60 mg, 0.29 mmol) are dissolved in dry DMF (5 mL), Et_3N (1.5 mL),

degassed and Ar purged. To the reaction mixture $Pd(PPh_3)_4$ (36 mg, 0.03 mmol) and CuI (12 mg, 0.063 mmol) is added under Ar atmosphere followed by refluxing at 140 °C for 24 hrs. The precipitate formed is filtered and washed several times with THF and ethanol. Further purification is done using Soxhelet extraction with THF and MeOH for 24 hrs each. Yield: 60%. Anal. Calcd. for $C_{76}H_{63}B$: C 92.6, H 6.3; Found: C 84.69, H 4.1 (0.3-0.5 mol% of Pd(0) is found from EDAX analysis).

4.3 Results and discussion

4.3.1 Synthesis and characterization

BMOP is synthesized by Pd^0/CuI-catalyzed Sonogashira C-C coupling between tris(4-bromo-2,3,5,6-tetramethylphenyl)boron node and 4,4′-diethynylbiphenyl linker as shown in Figure 2. The FTIR spectrum of **BMOP** show bands at 980, 1600 and 2100 cm^{-1}

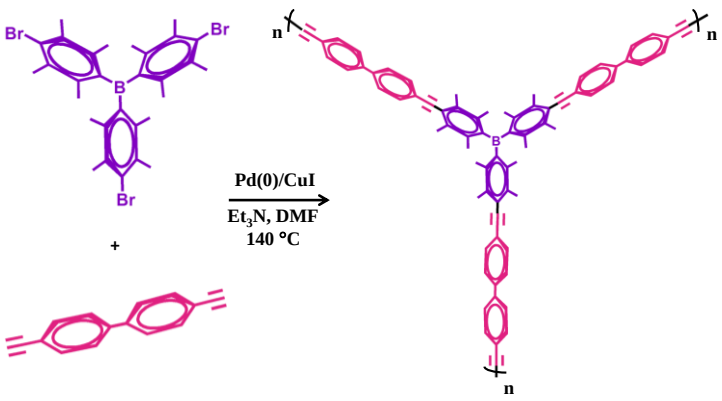

Figure 2. Synthesis of **BMOP** using Sonogashira C-C coupling reaction between tris(4-bromo-2,3,5,6-tetramethylphenyl)boron and diethynylbiphenyl.

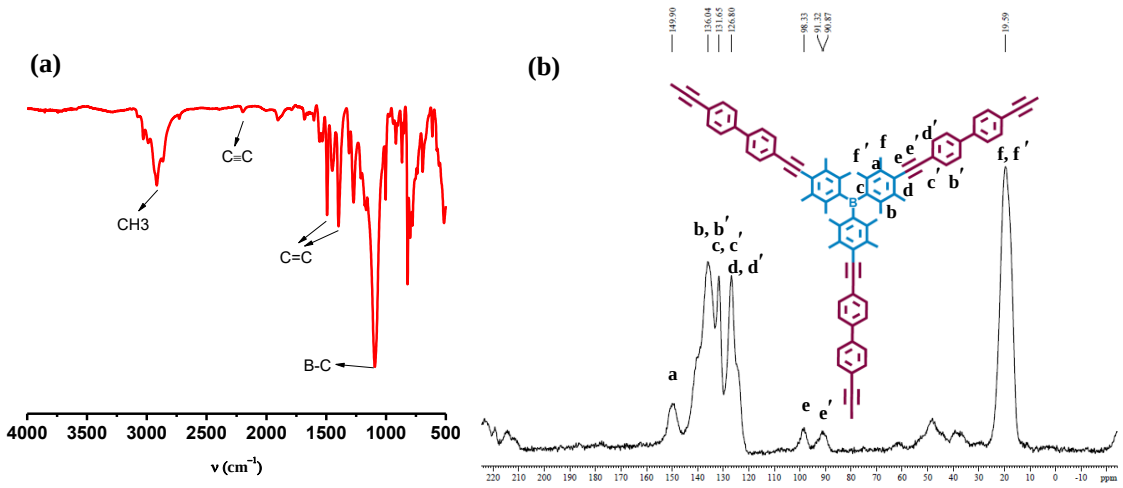

Figure 3. (a) FT-IR spectrum of **BMOP** and (b) ^{13}C-CP/MAS solid state NMR spectrum of **BMOP** confirming the linkage of node and linker through C-C bond.

corresponding to the C-B, C=C, and C≡C stretching vibrations, respectively [12a, 22] (Figure 3a), confirmed the presence of both node and linker moieties in the polymer. Furthermore, the solid-state ^{13}C CP/MAS NMR spectrum (Figure 3b) shows a moderate signal at 90 ppm assigned to C of the C≡C bond, suggests bonding of the triarylborane node and 4, 4′-diethynylbiphenyl linker. Other peaks ranging from 120-150 ppm can be assigned to the aromatic C atoms of phenyl rings,[12a, 23] and the peak at 19 ppm to aliphatic methyl substituents of the phenyl rings.[6a, 24] The presence of boron in **BMOP** is confirmed by X-ray photoelectron spectroscopy (XPS). XPS (Figure 4a) shows a B1s peak centered at 189.90 eV and a Br3$p_{3/2}$ peak at 184.45 eV suggesting the presence of boron and free terminal bromine of the triarylborane node in **BMOP**.[25] Powder XRD measurements showed a broad peak at 20° indicating amorphous nature of **BMOP** (Figure 4b).

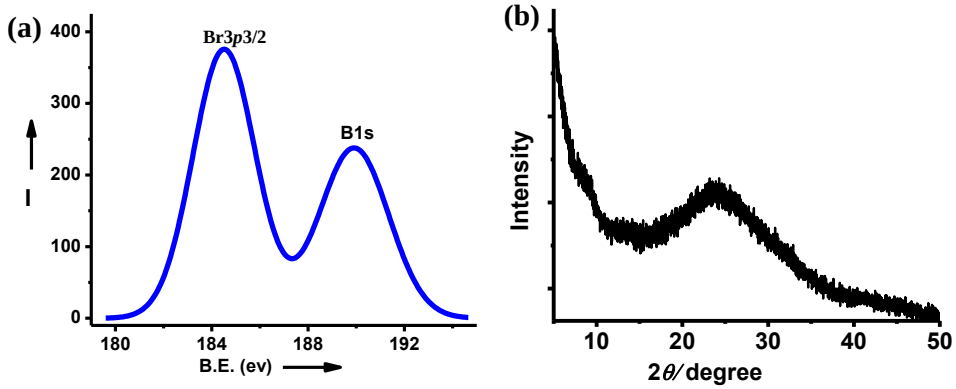

Figure 4. (a) XPS transitions for Br3$p_{3/2}$ and B1*s* in **BMOP** and (b) powder X-ray diffraction pattern of **BMOP** in the range of 5-50° collected using Cu Kα radiation.

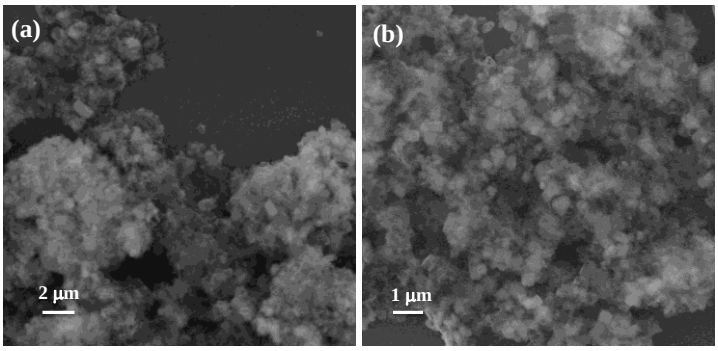

Figure 5. (a), (b) SEM images of **BMOP** at different magnifications showing the clustered spherical particles.

SEM images showed formation of clustered spherical particles of size varying from 100 to 300 nm (Figure 5). TEM images also revealed the presence of clustered

particles (Figure 6a) and, presence of micropores in the particle are observed at higher magnification, the (Figure 6b). Thermogravimetric analysis of **BMOP** showed no

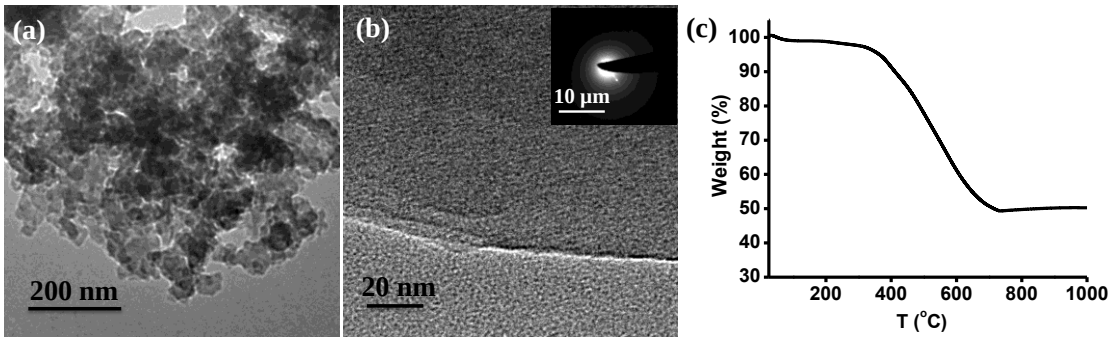

Figure 6. (a) TEM image of **BMOP** showing the clustered spherical particles and (b) micropores at higher magnifications (Inset: ED pattern). (c) TGA profile of **BMOP** in the range of 25-1000 °C with a heating rate of 5 °C/min under N_2 atmosphere.

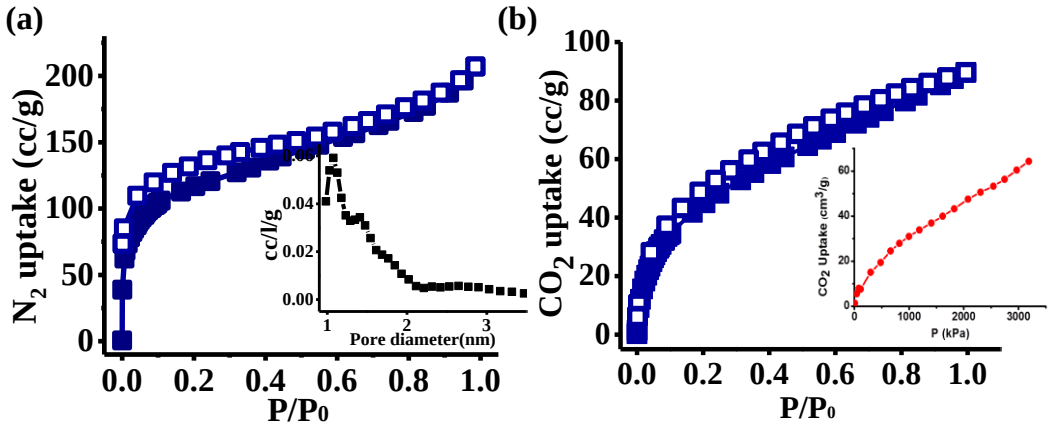

Figure 7. (a) Adsorption isotherms of **BMOP**; N_2 adsorption at 77 K (Inset: Pore size distribution diagram) and (b) CO_2 adsorption profile at 195 K (Inset: CO_2 adsorption isotherm of **BMOP** at 273 K).

appreciable weight loss up to 280 °C, and further heating resulted in steady weight loss (50 %) up to 720 °C (Figure 6c), and constant mass is observed up to 1000 °C. N_2 adsorption measurements at 77 K showed type I adsorption profile with an appreciable uptake in the lower pressure range, and the final uptake is 207 mL/g (Figure 7a). Application of the Brunauer–Emmet–Teller (BET) model to the N_2 isotherm in the range of P/P_0 = 0.01-0.3 yielded a surface area of 390 m^2/g. A non-local density functional theory (NL-DFT) model fitted to the N_2 adsorption isotherm gave an average pore size of 1.08 nm and thus signified microporous nature of the polymer (Figure 7a; Inset). **BMOP** showed a CO_2 uptake capacity of 90 mL (18 wt %) at 195 K up to 1 atm (Figure 7b) and 60 mL (12 wt %) at 273 K up to 30 bar (Figure 7b; Inset).

4.3.2 Photophysical Studies

BMOP is a dark green compound in contrast to the white crystalline tris(4-bromo-2,3,5,6-tetramethyl phenyl)boron and 4,4′-diethynylbiphenyl precursors. The absorbance of **BMOP** is broad and features two major UV/Vis absorption bands in the range of 280-350 nm and 410 nm, which can be ascribed to π-π* transition of the linker part and π-p_π(B) electron transition from linker to empty p_π orbital of boron, respectively (Figure 8a). In contrast to the blue emission of the linker and non-emissive behaviour of tris(4-bromo-2,3,5,6-tetramethylphenyl)boron, **BMOP** shows strong green emission with a

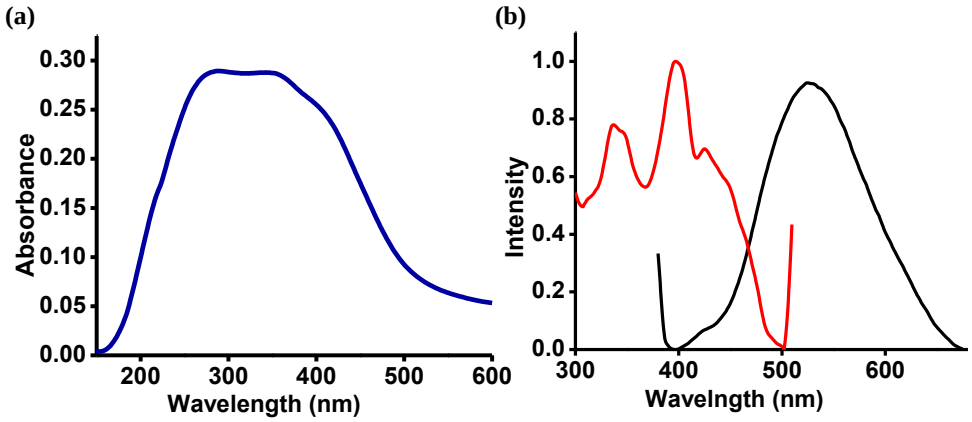

Figure 8. (a) UV/Vis absorption (blue) of **BMOP**. (b) Normalized emission spectra (black) and excitation spectra (red) collected at 520 nm in solid state for **BMOP**.

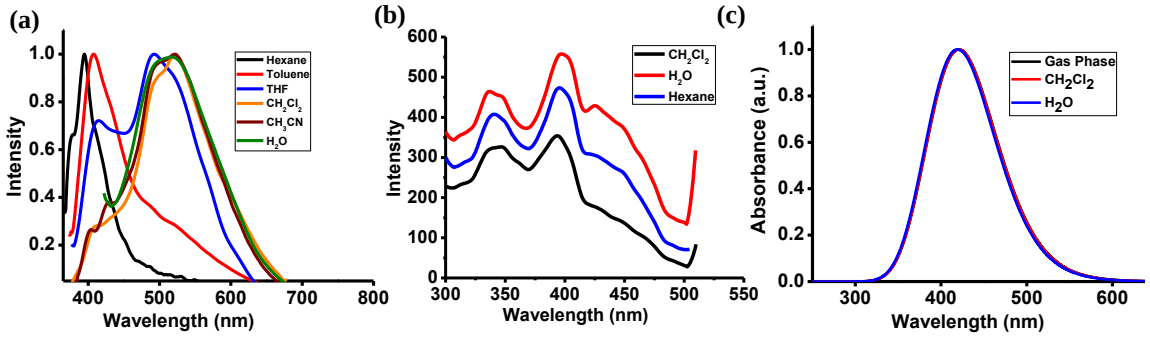

Figure 9. (a) Normalized emission spectra of **BMOP**; emission changes in hexane, toluene, THF, DCM, CH_3CN and water, (b) excitation spectra of **BMOP** (experimental) in different solvent collected at 520 nm and (c) Theoretically calculated normalized UV/Vis absorption spectra of smallest unit of **BMOP** in gas phase and different solvents.

maximum at 520 nm (Figure 8b) and the excitation spectrum shows two resolved bands at 350 and 410 nm. This large redshift in emission of **BMOP** clearly suggests interaction between extended linker (donor) and boron center (acceptor) through ICT via conjugation. The ICT process is validated by solvent-dependent emission features of the polymer (Figure 9a); in a nonpolar solvent like hexane, **BMOP** shows local excited-state

(LE) emission with a maximum at 410 nm originating from the extended linker, whereas in a highly polar solvent such as water (H_2O) the emission maximum is redshifted to 520 nm and assigned to ICT. The dependence of the emission maxima of the polymer on

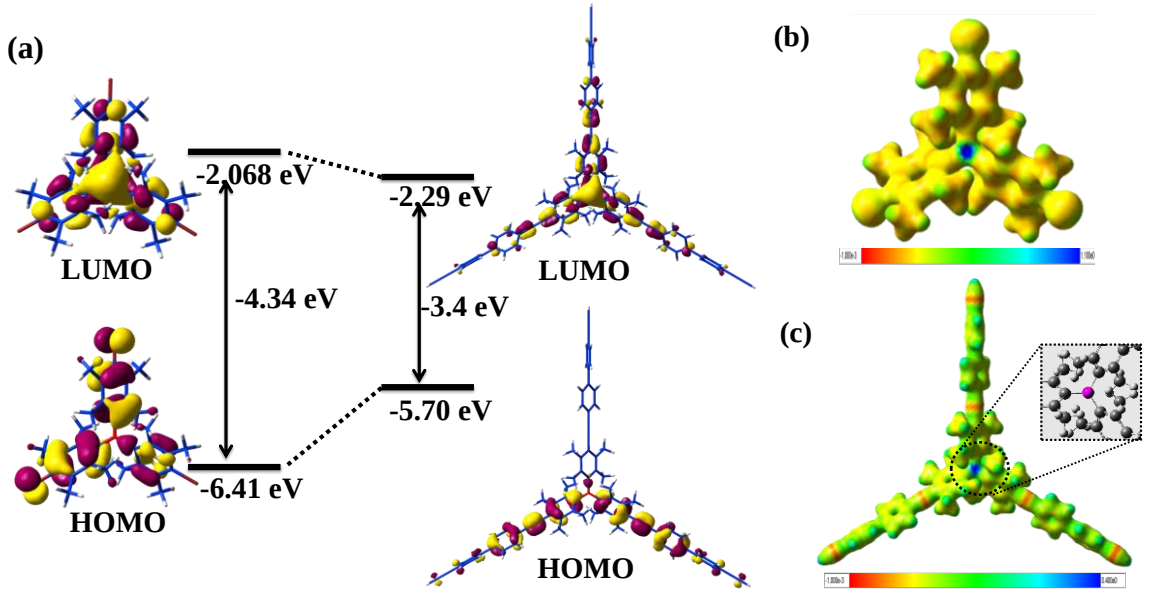

Figure 10. (a) HOMO-LUMO energy level diagram of tris(2,3,5,6-tetramethyl-4-bromophenyl)boron (left) and smallest unit of **BMOP** (right). Electrostatic potential plots of smallest unit of **BMOP**. Electrostatic potential plot of (b) tris(4-bromo-2,3,5,6-tetramethylphenyl)boron and (c) smallest unit of **BMOP** where the central boron is e^- deficient before F^- binding (Inset: Pink, B; Grey, C and silver, H).

solvent polarity demonstrates strong coupling between donor and acceptor in the excited state. This strong dependence of the emission maximum on solvent polarity indicates that the excited state is stabilized by polar solvents due to high dipole moment. Furthermore, no changes in excitation spectra are observed on changing the solvent polarity, and this suggests weak coupling between donor and acceptor in the ground state (Figure 9b, c). The ICT behaviour of **BMOP** is further studied by DFT calculations on boron precursor and the smallest unit of the polymer (Figure 10a) by using the B3LYP functional and 6-31+G(d) basis set, as implemented in Gaussian 09. Molecular orbital plots of the node and smallest unit of **BMOP** show that highest occupied molecular orbital (HOMO) and lowest unoccupied molecular orbital (LUMO) are mainly localized on the phenyl rings and boron center, respectively. TDDFT calculations suggest that the ground state and optically allowed excited state correspond to the HOMO and LUMO, respectively. This clearly suggests that ICT from the linker to the empty p_π orbital of boron occurs. The optical absorption of smallest unit (421.2 nm, f = 1.2151) theoretically predicted by

TDDFT calculations compares fairly well with the experimental value (410 nm), and no changes in absorption maxima are observed with changing solvent polarity (Figure 9c). Furthermore, electrostatic potential (ESP) maps of the smallest unit of **BMOP** clearly reveal that the boron center is highly electron deficient (Figure 10b, 10c).

4.3.3 Fluoride sensing and capture

On the basis of the principle that boron with empty p_π orbital in **BMOP** would accept electrons from anions, which would perturb the ICT process and induce changes in fluorescent signal, we studied the effect of F^- ions on ICT emission of **BMOP**. No visible colour change is observed in the polymer on addition of F^- ions. Initial studies are done on **BMOP** (5 μM) dispersed in THF, and the changes in the emission of **BMOP** on incremental addition of F^- in the form of *tetra-n*-butylammonium fluoride (TBAF, 13 mM) in THF are recorded. As shown in Figure 11a the intensity of the emission band at 520 nm corresponds to ICT decreased on addition of F^- ions, and subsequently a blue

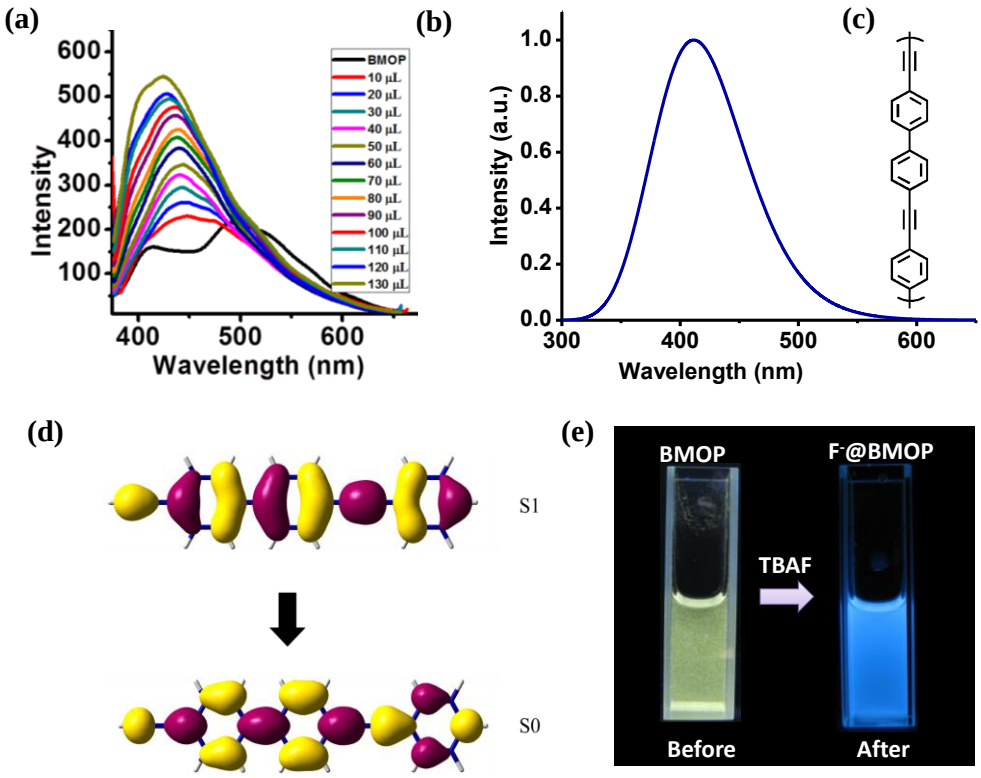

Figure 11. (a) Changes in fluorescence spectrum of **BMOP** on incremental addition of F^- ion in THF, (b) theoretically calculated normalized emission spectrum of modified extended linker, (c) modified extended linker. (d) Orbital plots of modified extended diethynylbiphenyl linker showing the S1 to S0 transition and (e) images of **BMOP** under UV lamp before and after addition of TBAF in THF.

emission band appears at 420 nm and is enhanced with increasing amount of F^- ions. It is expected that, when F^- binds to boron, ICT is blocked and ICT emission decreased; however, excitation of the linker results in π*-π emission localized on the extended linker, that is, tetramethylphenyl-fused 1,4-diethynylbiphenyl unit. To confirm that the blue emission resulted solely from the extended linker, we calculated its excited-state optical properties. The modified extended linker shows an emission peak at 411 nm (1.9820 eV; Figure 11b, c), which is close to experimentally observed blue emission (420 nm). Also, the orbital diagrams (LUMO and HOMO) confirms that this extended linker shows the characteristic π*-π emission peak (S1→ S0; Figure 11d), which further supports the hypothesis that the strong blue emission of F^- loaded **BMOP** (**F^-@ BMOP**) indeed originates from the extended linker, which signifies its importance for turn-on sensing of F^- ions. The emission colour of the solution changes from green to intense blue on F^- binding (Figure 11e). Furthermore, ESP plot suggests that on complexation of F^-,

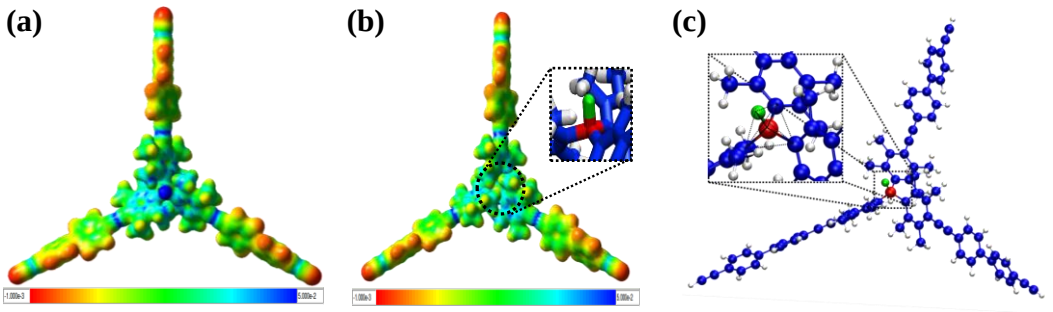

Figure 12. Electrostatic potential plots of smallest unit of **BMOP** (a) after F^- binding (red and blue regions indicate high and low e^- density respectively) (b) **F^-@BMOP** in rear direction where the central boron is observed to be e^- rich after binding of F^- ion (Inset: Green, B; Blue, C and silver, H). (c) Energy minimized structure of **F^-@ BMOP** showing the changes in bonding environment around boron center (Red: B, Blue: C, Green: F, Silver: H).

the boron center loses its electron-deficient character, and F^- becomes the low-electron-density species (Figure 12a, 12b). We calculated the optimized structure for the F^- bound smallest unit (Figure 12c). The F^- ion is indeed strongly bound to the boron center by donating electrons to boron. The 'B-F' distance of 1.47 Å in **F^-@ BMOP** is close to that of BF_4^- (1.43 Å) and suggests strong interaction between B and F and the corresponding geometry shown in Figure 12c. Detection of F^- in water is a challenge. The World Health Organization recommends that F^- ion content in drinking water to be lower than 1.5 ppm. However, **BMOP** does not show significant change in emission spectra on incremental

addition of fluoride ion in pure water due to high hydration enthalpy of F^-(Figure 13a). Hence, further experiments are carried out in aqueous/organic solvent mixtures. Intial experiments are done with **BMOP** (5 μM) dispersed in DMSO/H_2O (8/2) and titrated against TBAF (15 mM in DMSO/H_2O 8/2). Figure 13b shows a gradual decrease of the emission intensity at 520 nm with simultaneous increase in the blue emission intensity at 410 nm on addition of F^-. The blue emission is ascribed to π*-π emission of the extended linker (see above). Nevertheless, the detection limit is observed to be about 20 ppm. Thus, THF/H_2O (9/1) is found to be promising for the detection of lower concentrations of F^- ions. As seen in Figure 13c, similar blockage of ICT emission and enhancement of blue emission from the linker is observed on incremental addition of F^- (3.5 mM) to **BMOP** dispersed in THF/H_2O. Strikingly, similar fluorescence increase in the blue emission intensity at 410 nm on addition of F^-. The blue emission is ascribed to π*-π emission of the extended linker (see above). Nevertheless, the detection limit is observed to be about 20 ppm. On the other hand, THF/H_2O (9/1) is found to be promising for the detection of lower concentrations of F^- ions. As seen in Figure 13c, on incremental addition of F^- (3.5 mM) to **BMOP** dispersed in THF/H_2O, similar blockage of ICT emission and remarkable enhancement of blue emission from the linker is observed. Figure 14a shows the florescence intensity change at 410 nm with fluoride concentration in THF/H_2O (9/1). The detection limit is calculated using 3σ/slope method and it is found to be 2.6 μM. Interestingly, **BMOP** shows appreciable fluorescence response even at lower concentrati-

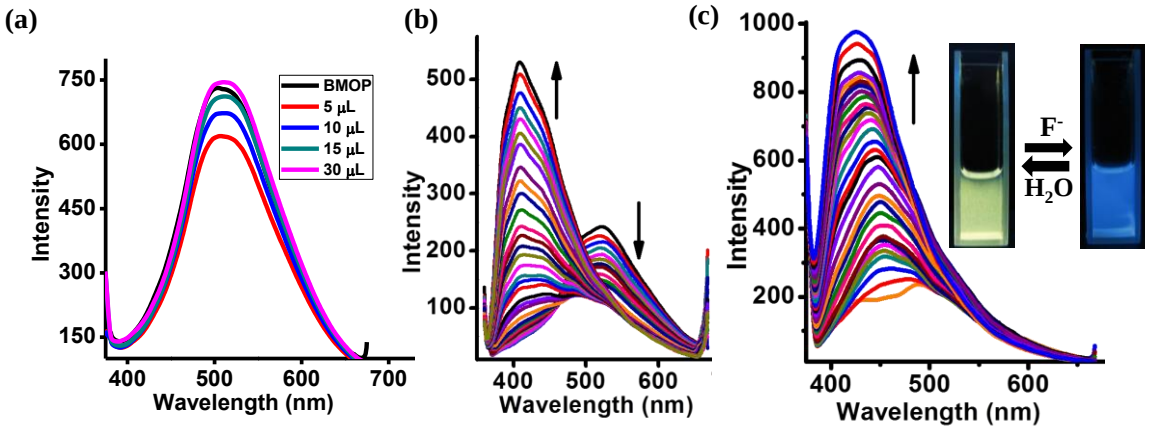

Figure 13. (a) Changes in emission spectra of **BMOP** dispersed in water on incremental addition of TBAF. Changes in fluorescence spectrum of **BMOP** on incremental addition of F^- ion in (b) DMSO/H_2O (8:2) mixture and (c) in THF/H_2O (9:1) mixture (Inset; Images of **BMOP** dispersed in THF/H_2O under UV light before and after F^- addition and its reversibility).

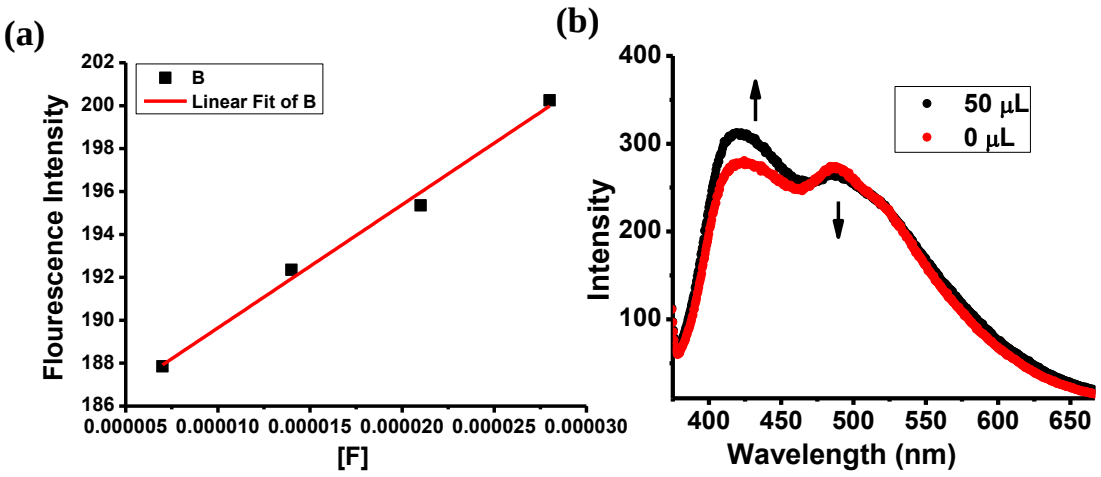

Figure 14. (a) Fluorescence changes of **BMOP** with addition of fluoride; the detection limit is calculated from 3σ/slope method. (b) Spectral changes of **BMOP** emission on addition of 50 µL of F^- ion (final concentration, < 2.6 µM) after 15 min.

ons of F^- ions (final concentration: < 2.6 µM) on soaking F^- with a dispersion of **BMOP** in THF/H_2O for 15 min (Figure 14b). This delayed fluorescence response for such low concentrations of F^- may be attributed to the longer diffusion time of F^- ion to interact with boron present in the polymer. Binding constant for F^- ion to **BMOP** is calculated from fluorescence titration data to be 1×10^4 M^{-1} (Figure 15a). It is noteworthy that **BMOP** is highly selective for F^- ion (Figure 15b) and shows no appreciable fluorescence response to other anions such as Cl^-, Br^-, I^-, NO_3^-, SO_4^{2-}, and CO_3^{2-}. This high selectivity of **BMOP** to F^- ions may be due to the sterically crowded binding environment created by the *ortho*-

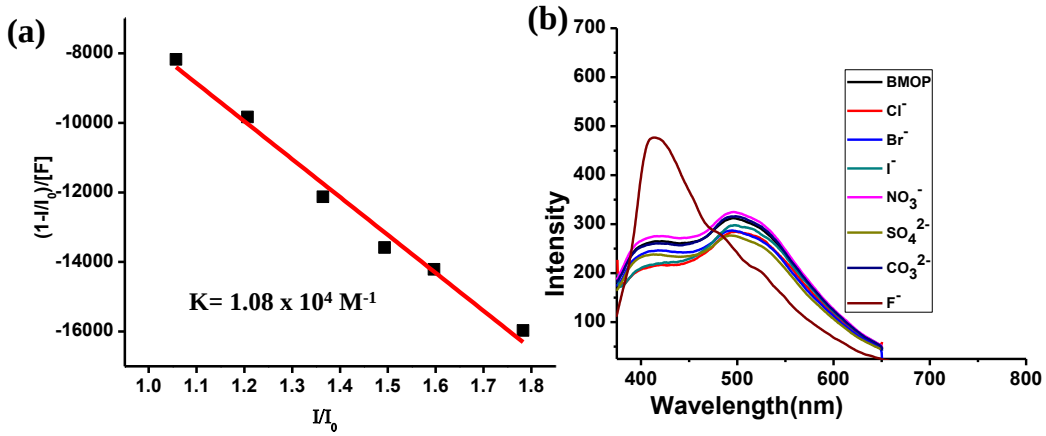

Figure 15. (a) Plot of $(1-I/I_0)/[F]$ vs I/I_0 of **BMOP** fluorescence titration data. (b) Changes in fluorescence spectrum of **BMOP** (black) on addition (100 µL) of anions such as Cl^- (KCl, red), Br^-(KBr, blue), I^-(KI, cyan), NO_3^-(KNO_3, pink), SO_4^{2-}(K_2SO_4, dark yellow), CO_3^{2-}(K_2CO_3 ,navy blue) and F^-(KF, wine red) in THF/H_2O (9:1). 10 mg of each salt is dissolved in 2 mL of THF/H_2O (9:1) mixture.

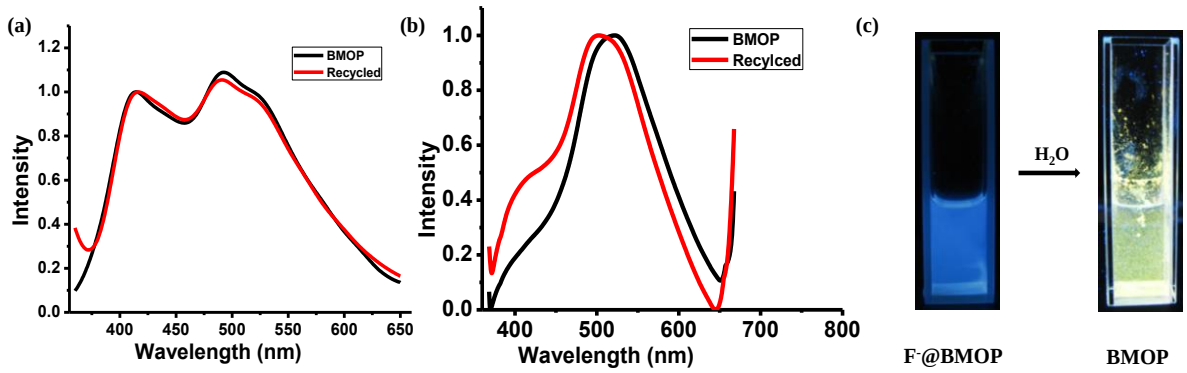

Figure 16. Comparison of emission spectrum of **BMOP** and recycled **BMOP** after sensing of F^- ion (a) recycled from THF/H_2O mixture and (b) recycled from DMSO/H_2O mixture. (c) Images of BMOP dispersion on addition of excess water to F^-**@BMOP** under UV lamp.

methyl groups on phenyls substituents around the boron center.[26] The most striking feature of F^- ion sensing with **BMOP** is its reversibility and sample recovery. Owing to the large hydration enthalpy of F^- ion,[4b] addition of an excess of water to **F^-@BMOP**, regenerates assynthesized polymer with complete restoration of green emission, and it can be recovered by simple centrifugation (Figure 16).

To study the capability of **BMOP** in sequestration of F^-, we carried out ^{19}F-NMR spectroscopy on a solution of TBAF in which **BMOP** is soaked (the insoluble nature of **BMOP** prevented our studying the changes in ^{11}B-NMR spectrum). A solution of TBAF/dmso-d^6 (5 mM) is added to **BMOP** (0.1 mg), the mixture allowed to stand for 60 s, and BMOP removed by centrifugation. The clear solution thus obtained is analyzed for free F^- ions by ^{19}F-NMR spectroscopy (Figure 17). As expected, the signal intensity of free F^- in solution decreased drastically within 60 s, and soaking for a further 60 s resulted in complete loss of F signal in NMR spectrum. This clearly suggests that the F^- ion is indeed captured within the porous polymer, and its coordination to boron center is evident from the blue emission of **BMOP** under UV light (Figure 17, Inset). Furthermore, ^{1}H NMR spectra of the filtrate at different intervals did not show any peaks related to integral parts of the polymer and thus clearly suggested no disintegration of the polymer on F^- ion binding (Figure 18). To further prove the capture of F^- by the polymer, we carried out elemental mapping of **F^-@BMOP** powder isolated by the centrifugation of the dmso-d^6 dispersion. Elemental mapping showed a uniform distribution of 'F' throughout the polymer matrix, which confirms that; the F^- ion is indeed captured by **BMOP** through

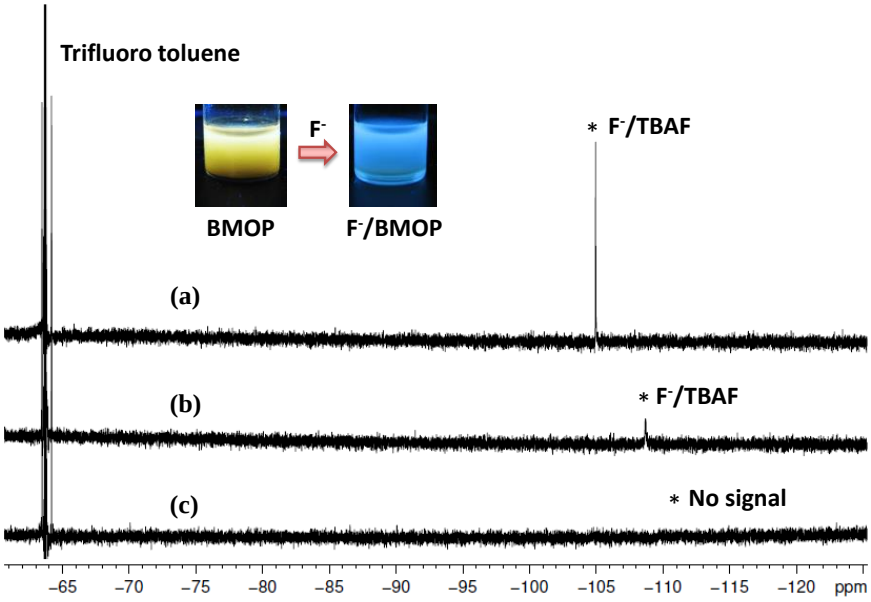

Figure 17. ^{19}F-NMR spectra of TBAF solution in dmso-d^6 (5 *m*M) (a) before and (b) after 60 sec, (c) 120 sec, of soaking with **BMOP** (Trifluorotoluene as standard reference). Inset: Change of emission colour of **BMOP** dispersion to blue after 120 sec under UV lamp.

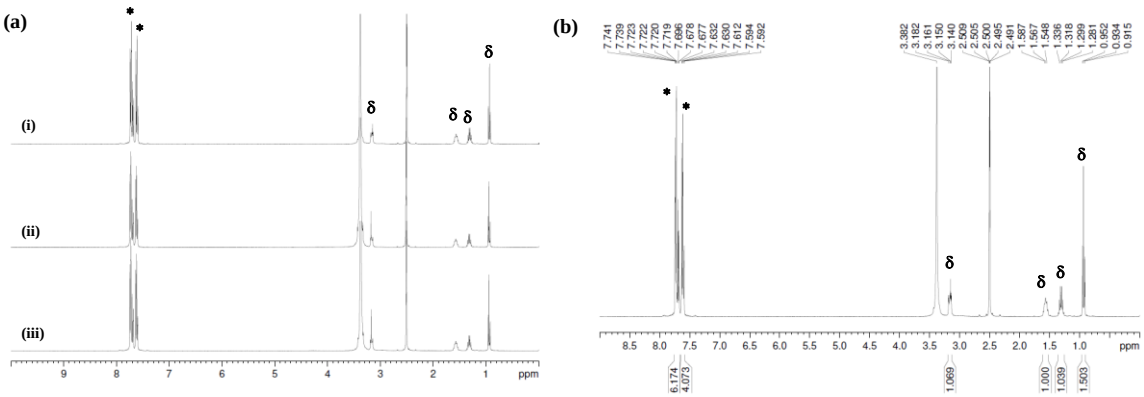

Figure 18. (a) ^{1}H-NMR spectrum of trifluorotoluene and tetrabutylammonium fluoride dmso-d^6 (i) before (stock), (ii) after 60 sec and (iii) after 120 sec of soaking with **BMOP**. ('∗' peaks of trifluorotoluene and 'δ' peaks of tetrabutylammonium cation and other peaks represents dmso-d^6). (b) ^{1}H-NMR spectrum of trifluorotoluene (peaks indicated by '∗') and tetrabutylammonium fluoride (TBAF) (peaks indicated by 'δ') mixture in dmso-d^6.

strong anion-boron interactions in the micropores of the polymer (Figure 19). These results clearly suggest that **BMOP** can not only recognize but also capture F^- ions. This selective recognition and capture or sequestration of F^- ions in a π-conjugated porous polymer is unprecedented, and the detection limits are low in comparison to discrete compounds and porous scaffolds.[27] We have further tested the capability of **BMOP** to

indicate the F^- ions present in Colgate anticavity tooth paste by extracting it with THF/H_2O. As seen in Figure 20, with incremental addition of extract solution, clear enhancement in the blue emission is observed.

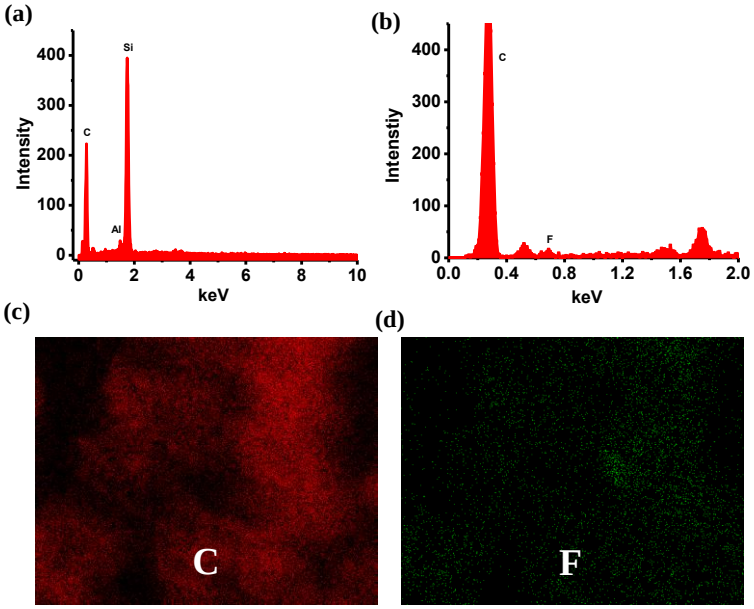

Figure 19. EDAX analysis of (a) **BMOP** and (b) F^-@ **BMOP**, showing the presence of fluoride (F^-) ions in the polymer. Elemental colour mapping of F^-@ **BMOP**; (c) for 'C' and (d) for 'F^-'; showing the presence of carbon and fluoride ion respectively throughout the polymer matrix.

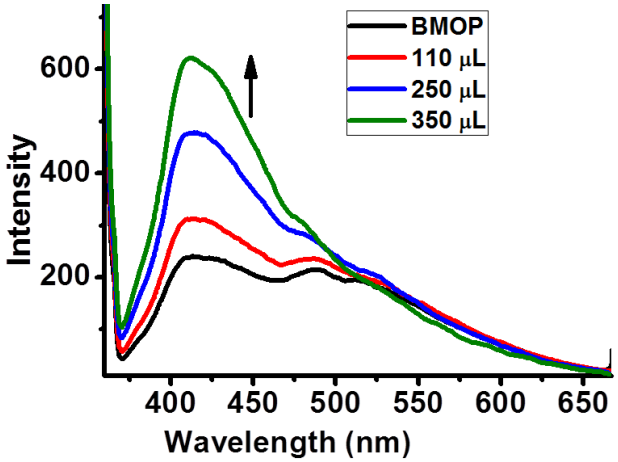

Figure 20. Fluorescence response of **BMOP** on addition of incremental amounts of solution (THF: H_2O, 9:1) obtained from Colgate anticavity toothpaste extract.

4.4 Conclusion

We have demonstrated the rational design and synthesis of a Lewis acidic microporous organic polymer with high density of functional boron centers as recognition sites for selective detection of F^-. The extended conjugation of the

linker through duryl groups facilitated turn-on fluorescent sensing of F^- ion by the obstruction of ICT. **BMOP** shows low detection limit, and strong boron-fluoride interactions allowed facile sequestration of F^- ion. We further believe that **BMOP** with strong ICT emission features could find applications in OLEDs and in sequestration of CO_2 where the boron center interacts with CO_2 through Lewis acid-base interactions.

4.5 References

[1] a) J. Fawell, K. Bailey, J. Chilton, E. Dahi, L. Fewtrell, Y. Magara, World Health Organization (WHO). *Fluoride in Drinking-water*. ISBN: 1900222965, Published by IWA Publishing, London, UK, (**2006**).

[2] a) P. Adler, *Fluorides and health*, World Health Organization, Geneva, **1970**; b) American Public Health Association, American Water Works Association, Water Environment Federation. *Standard methods for the examination of water and wastewater*, American Public Health Association, (**1998**).

[3] a) S. Jagtap, M. K. Yenkie, N. Labhsetwar, S. Rayalu, *Chem. Rev.* **2012**, *112*, 2454; b) B. Pan, J. Xu, B. Wu, Z. Li, X. Liu, *Environ. Sci. Technol.* **2013**, *47*, 9347.

[4] a) Z. M. Hudson, S. Wang, *Acc. Chem. Res.* **2009**, *42*, 1584; b) C. R. Wade, A. E. J. Broomsgrove, S. Aldridge, F. P. Gabbaï, *Chem. Rev.* **2010**, *110*, 3958.

[5] E. Galbraith, T. D. James, *Chem. Soc. Rev.* **2010**, *39*, 3831.

[6] a) T. Liu, A. Nonat, M. Beyler, M. Regueiro-Figueroa, K. Nchimi Nono, O. Jeannin, F. Camerel, F. Debaene, S. Cianférani-Sanglier, R. Tripier, C. Platas-Iglesias, L. J. Charbonnière, *Angew. Chem. Int. Ed.* **2014**, *53*, 7259; b) S. Guha, S. Saha, *J. Am. Chem. Soc.* **2010**, *132*, 17674; c) X. Y. Liu, D. R. Bai, S. Wang, *Angew. Chem. Int. Ed.* **2006**, *45*, 5475; d) P. Bose, P. Ghosh, *Chem. Commun.* **2010**, *46*, 2962; e) R. Hu, J. Feng, D. Hu, S. Wang, S. Li, Y. Li, G. Yang, *Angew. Chem. Int. Ed.* **2010**, *49*, 4915.

[7] a) M. D. Allendorf, C. A. Bauer, R. K. Bhakta, R. J. T. Houk, *Chem. Soc. Rev.* **2009**, *38*, 1330; b) L. E. Kreno, K. Leong, O. K. Farha, M. Allendorf, R. P. Van Duyne, J. T. Hupp, *Chem. Rev.* **2012**, *112*, 1105; c) S. Fischer, J. Schmidt, P. Strauch, A. Thomas, *Angew. Chem. Int. Ed.* **2013**, *52*, 12174; d) X. Liu, Y. Xu, D. Jiang, *J. Am. Chem. Soc.* **2012**, *134*, 8738; e) Y. Cui, Y. Yue, G. Qian, B. Chen, *Chem. Rev.* **2012**, *112*, 1126.

[8] a) F. M. Hinterholzinger, B. Rühle, S. Wuttke, K. Karaghiosoff, T. Bein, *Sci. Rep.* **2013**, *3*, 2562; b) S. Saha, B. Akhuli, I. Ravikumar, P. S. Lakshminarayanan, P. Ghosh, *CrystEngComm* **2014**, *16*, 4796.

[9] a) R. Dawson, E. Stoeckel, J. R. Holst, D. J. Adams, A. I. Cooper, *Energy Environ. Sci.* **2011**, *4*, 4239; b) A. I. Cooper, *Adv. Mater.* **2009**, *21*, 1291; c) H. A. Patel, F. Karadas, J. Byun, J. Park, E. Deniz, A. Canlier, Y. Jung, M. Atilhan, C. T. Yavuz, *Adv. Funct. Mater.* **2013**, *23*, 2270; d) S. Hug, M. E. Tauchert, S. Li, U. E. Pachmayr, B. V. Lotsch, *J. Mater. Chem.* **2012**, *22*, 13956.

[10] J. X. Jiang, F. Su, A. Trewin, C. D. Wood, N. L. Campberll, H. Niu, C. Dickinson, A. Y. Ganin, M. J. Rosseinsky, Y. Z. Khimyak, A. I. Cooper, *Angew. Chem. Int. Ed.* **2008**, *47*, 8574.

[11] a) Z. Chang, D.-S. Zhang, Q. Chen, X. -H. Bu, *Phys. Chem. Chem. Phys.* **2013**, *15*, 5430; b) A. Thomas, *Angew. Chem. Int. Ed.* **2010**, *49*, 8328; c) H. A. Patel, S. H. Je, J.

Park, D. P. Chen, Y. Jung, C. T. Yavuz, A. Coskun, *Nat. Commun.* **2013**, *4*, 1357; d) K. V. Rao, S. Mohapatra, C. Kulkarni, T. K. Maji, S. J. George, *J. Mater. Chem.* **2011**, *21*, 12958; e) K. V. Rao, R. Haldar, T. K. Maji, S. J. George, *Chem. Mater.* **2012**, *24*, 969.

[12] a) V. M. Suresh, S. Bonakala, S. Roy, S. Balasubramanian, T. K. Maji, *J. Phys. Chem. C* **2014**, *118*, 24369; b) K. V. Rao, S. Mohapatra, T. K. Maji, S. J. George, *Chem. Eur. J.* **2012**, *18*, 4505; c) J.-X. Jiang, A. Trewin, D. J. Adams, A. I. Cooper, *Chem. Sci.* **2011**, *2*, 1777; d) L. Chen, Y. Honsho, S. Seki, D. Jiang, *J. Am. Chem. Soc.* **2010**, *132*, 6742; e) S. Ren, R. Dawson, D. J. Adams, A. Cooper, *Polym. Chem.* **2013**, *4*, 5585.

[13] a) G. Cheng, T. Hasell, A. Trewin, D. J. Adams, A. I. Cooper, *Angew. Chem. Int. Ed.* **2012**, *51*, 12727; b) J. Brandt, J. Schmidt, A. Thomas, J. D. Epping, J. Weber, *Polym. Chem.* **2011**, *2*, 1950.

[14] a) N. Matsumi, Y. Chujo, *Polym. J.* **2007**, *40*, 77; b) W.-M. Wan, F. Cheng, F. Jäkle, *Angew. Chem. Int. Ed.* **2014**, *53*, 1; c) P. Chen, F. Jäkle, *J. Am. Chem. Soc.* **2011**, *133*, 20142; e) F. Jäkle, *Chem. Rev.* **2010**, *110*, 3985.

[15] M. J. Frisch, G. W. Trucks, H. B. Schlegel, G. E. Scuseria, M. A. Robb, J. R. Cheeseman, G. Scalmani, V. Barone, B. Mennucci, G. A. Petersson, Gaussian 09, Revision A.02; Gaussian, Inc.: Wallingford, CT, 2009.

[16] A. D. Becke, *J. Chem. Phys.* **1993**, *98*, 5648.

[17] C. Lee, W. Yang, R. G. Parr, *Phys. Rev.* B **1988**, *37*, 785.

[18] R. G. Parr, W. Wang, *Density-Functional Theory of Atoms and Molecules*, Oxford University Press, New York, 1989.

[19] R. E. Stratmann, G. E. Scuseria, M. J. Frisch, *J. Chem. Phys.* **1998**, *109*, 8218.

[20] S. R. K. C. Y. Sharma, B. Arkamita, S. K. Pati, *J. Phys. Chem.* C **2013**, *117*, 23295.

[21] G. Scalmani, M. J. J. Frisch, *Chem. Phys.* **2010**, *132*, 114110.

[22] a) A. P. Cote, A. I. Benin, N. W. Ockwig, M. O'Keeffe, A. J. Matzger, O. M. Yaghi, *Science* **2005**, *310*, 1166; b) R. Dawson, A. Laybourn, Y. Z. Khimyak, D. J. Adams, A. I. Cooper, *Macromolecules* **2010**, *43*, 8524.

[23] a) J.-X. Jiang, F. Su, A. Trewin, C. D. Wood, H. Niu, J. T. A. Jones, Y. Z. Khimyak, A. I. Cooper, *J. Am. Chem. Soc.* **2008**, *130*, 7710; b) J.-X. Jiang, A. Trewin, F. Su, C. D. Wood, H. Niu, J. T. A. Jones, Y. Z. Khimyak, A. I. Cooper, *Macromolecules* **2009**, *42*, 2658.

[24] B. S. Ghanem, M. Hashem, K. D. M. Harris, K. J. Msayib, M. Xu, P. M. Budd, N. Chaukura, D. Book, S. Tedds, A. Walton, N. B. McKeown, *Macromolecules* **2010**, *43*, 5287.

[25] a) C. Ronning, D. Schwen, S. Eyhusen, U. Vetter, H. Hofsäss, *Surf. Coat. Technol.* **2002**, *158*, 382; b) L. Ci, L. Song, C. Jin, D. Jariwala, D. Wu, Y. Li, A. Srivastava, Z. F. Wang, K. Storr, L. Balicas, F. Liu, P. M. Ajayan, *Nat. Mater.* **2010**, *9*, 430; c) A. F. Lee, Z. Chang, S. F. J. Hackett, A. D. Newman, K. Wilson, *J. Phys. Chem. C* **2007**, *111*, 10455.

[26] a) S. Sole,F. P. Gabbai, *Chem. Commun.* **2004**, 1284; b) M. Melaimi, F. P. Gabbai, *J. Am. Chem. Soc.* **2005**, *127*, 9680.

[27] a) N. N. Adarsh, A. Grélard, E. J. Dufourc, P. Dastidar, *Cryst. Growth Des.* **2012**, *12*, 3369; b) B. Chen, L. Wang, F. Zapata, G. Qian, E. B. Lobkovsky, *J. Am. Chem. Soc.* **2008**, *130*, 6718.

Cover Page

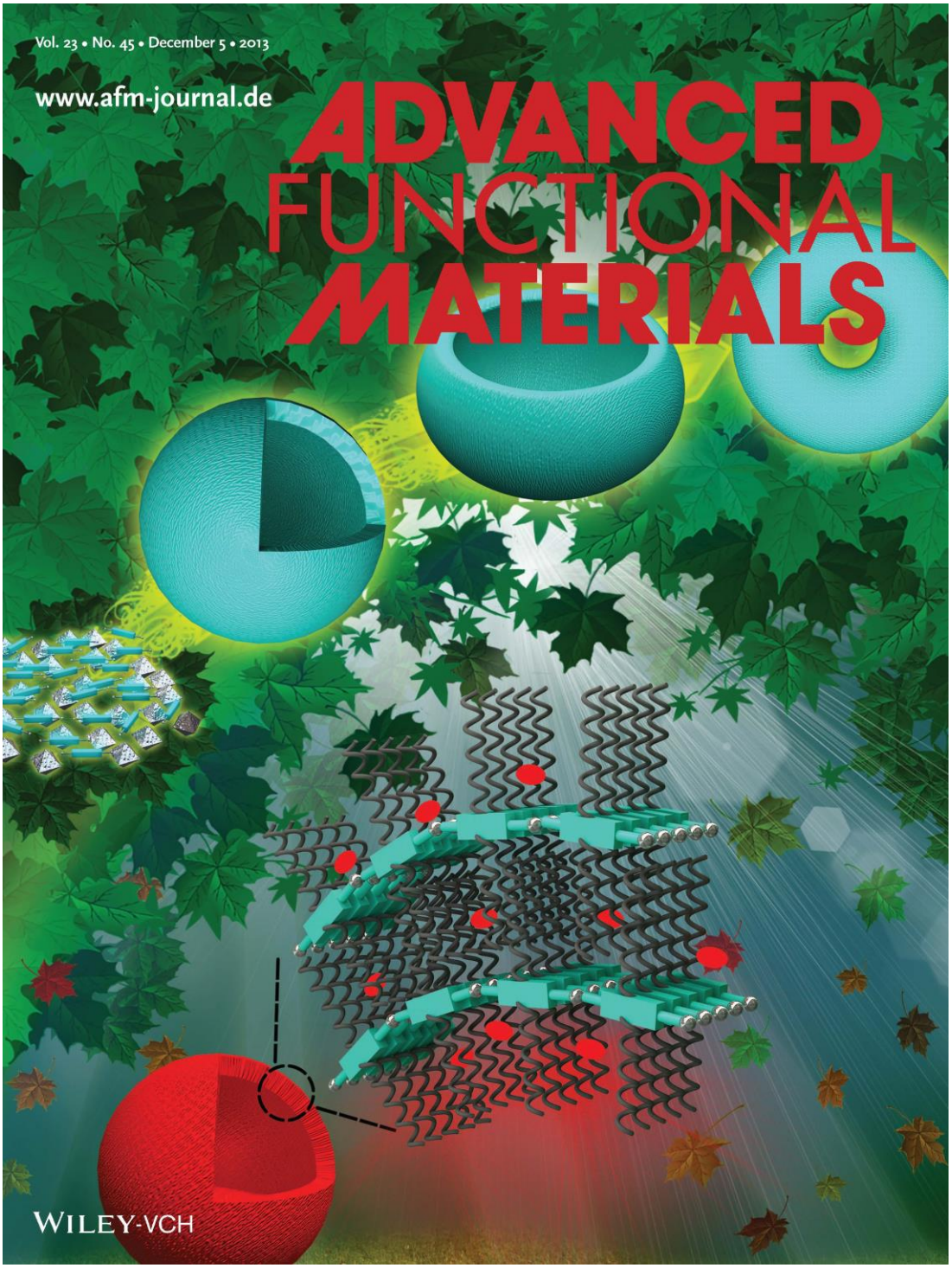
Vol. 23 • No. 45 • December 5 • 2013
www.afm-journal.de
ADVANCED FUNCTIONAL MATERIALS
WILEY-VCH